
# THEORETICAL STUDIES OF SINGLE-SITE CATALYSTS FOR EFFICIENT ELECTROCHEMICAL CO2 REDUCTION

Paulina Pršlja

**Paulina Pršlja**

# Theoretical Studies of Single-Site Catalysts for Efficient Electrochemical $CO_2$ Reduction

DOCTORAL THESIS

Supervised by
Prof. Núria López Alonso

Institute of Chemical Research of Catalonia (ICIQ)
and Rovira i Virgili University (URV)


UNIVERSITAT ROVIRA I VIRGILI

Tarragona
2021

UNIVERSITAT ROVIRA I VIRGILI
THEORETICAL STUDIES OF SINGLE-SITE CATALYSTS FOR EFFICIENT ELECTROCHEMICAL CO2 REDUCTION
Paulina Pršlja

Institut Català d'Investigació Química
Av. Països Catalans, 16
43007 Tarragona (Spain)

Prof. Núria López Alonso, group leader in the Institute of Chemical Research of Catalonia,

I STATE that the present study, entitled "**Efficient Electrochemical $CO_2$ Reduction on Single Site Catalysts"**, presented by Paulina Pršlja for the award of the degree of Doctor in Chemical Science and Technology, has been carried out under our joint supervision at the Institute of Chemical Research of Catalonia and that it fulfills all the requirements to be eligible for the International Doctorate Award.

Tarragona, November 18$^{th}$, 2020

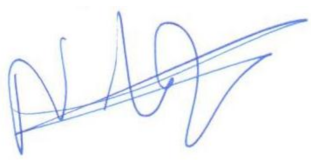

Prof. Núria López Alonso

UNIVERSITAT ROVIRA I VIRGILI
THEORETICAL STUDIES OF SINGLE-SITE CATALYSTS FOR EFFICIENT ELECTROCHEMICAL CO2 REDUCTION
Paulina Pršlja

# Sponsors

The work presented in this PhD thesis has been funded by the European Commission (EC) under the Innovative Training Network (ITN) project ELCOREL-722614 within the Marie Skłodowska-Curie Actions (MSCA) in the framework of the European Research Program Horizon 2020. The generous computer resources provided by the Barcelona Supercomputing Centre (MareNostrum) and the Spanish Supercomputing Network are also acknowledged.


UNIVERSITAT ROVIRA I VIRGILI




UNIVERSITAT ROVIRA I VIRGILI
THEORETICAL STUDIES OF SINGLE-SITE CATALYSTS FOR EFFICIENT ELECTROCHEMICAL CO2 REDUCTION
Paulina Pršlja

# Acknowledgements

I would like to dedicate this thesis to my non ordinary parents and grandparents, that thought me to be faithful, hard working, dedicated, and loyal. Mama in tata vidva sta mi podarila družino, občutek varnosti in srečo, vedno sta bila moja največja podpora. Živeli smo v skromnih okoliščinah, vendar sta vedno verjela v nas in z vašo pomočjo smo vedno dosegli cilje, ki so se zdeli nemogoči. Hvala mojim sestram in bratu, še posebej Antoniji in Katarini. Katarina, hvala, ker si živela z mano en mesec, me spremljala na poti do službe, predvsem zaradi moje zgubljive narave. Največja zahvala gre moji najstarejši sestri, ker mi stojiš ob strani že od četrtega razreda, ker nisi nikoli obupala nad mano in me sprejela takšno, kakršna sem. Hvala za vajino podporo v pomembnih trenutkih življenja. Mojim mlajšim; hvala Mateji, ker si mi pomagala razumeti fizikalne probleme, Mate, ker si me duhovnosti in Ana reda in discipline. Rada bi se zahvalila mojemu svaku Roku za vso pomoč, prav tako mojima nečakoma Erazmu in Jakobu za prijazne nasmeške. Hvala mojim botrom Marici, Nediljku, Jadranki, Zdravku, Simoni, Liljani, Mirku, Marku, Nikolaju, Nikolasu in Anastasiji, ker ste me sprejeli kot svojo. Hvala moji družini na Hrvaškem in Bosni, predvsem mojem stricu Pavi in Željku, teti Dubravki, sestričnam Nataliji, Jasmini in Loreni. Hvala za največje bogastvo, in sicer za vašo ljubezen.

I would like to thank the following people for helping me in my scientific research. First of all, I would like to express my sincere gratitude to my supervisor Prof. Núria López for allowing me the opportunity to work within ELCOREL organization. Thank you for giving me personal support and scientific guidance. Thanks to Edvin for introducing me to VASP and Blender. For help in simulating oxides, I would like to thank Franziska and Marcos. Rodrigo Antonio Nicholas Joaquin Garcia-Mules thank you for endless talks about kpoints, computational electrochemistry, and sharing good Venezuelan chocolate with me. Thanks to Yecheng for all the scientific help. The most I am thankful to Manu for teaching me how to communicate my scientific ideas, participating in chemical conversations with me, and always giving me tactical and thoughtful advice. I would also like to acknowledge my collaborators Jingkun Li and Fredeéric Jaouen from Montpellier University, Javier Perez-Ramírez group from ETH, Tanja Kallio and Noor Hossain from Aalto University.

I would like to thank the rest of my group: Andrea, Albert, Jordi, Sergio, Nathan, Pavle, Julian, and Bob. A special thanks go to my non-biological brother Kosta, thanks for being a really good fake brother. Friendly thanks to Sara, Bruna, Lucía, Enric, and the rest of Maseras's and Bo's group. I wish you all the best in your scientific and personal life. I am grateful for MVPs Martin and Moisés for always helping me with my computer problems and other things that I do not know how to name. Thanks to Núria Vendrell for all the bureaucratic solutions.

I am grateful that I was able to do the short stay in Avantium, Amsterdam. Therefore the biggest thanks go to KlaasJan for welcoming me into the Volta group, for three months I was kind of an experimentalist, I appreciate you for your calm and thoughtful conversations. I am thankful for meeting Julia, for patiently teaching me how to do the GDL's and for answering my scientific questions. Davide and Faezeh for helping me with the experiments. Thanks to BBB wolf pack Bert (the hulk), Bart, and Brian for showing me the Prodock unit (a different world for a theoretician) and making my stay feel nicer. Special thank you goes to the kindest humans I ever meet Mariana and Gil (a bonus colleague). I would like to thank the rest of the Volta group.

I would like to express my gratitude to the Elcorel family: Tugce, Rebecca, DJ Donn, Ricardo, Spiros, Noor, Daniel, Mariana, Chunmiao, Vlad, Davide, and Matt. At last, I would like to say thank you to Federico the Italiano, my ICIQ and Elcorel colleague, friend, thank you so much for all the help. I truly can say I made friends for life. In these three years living in Tarragona, I have met a lot of people, I would like to say thanks to my friends Natalia, Marta, Anna and Jan, and all the people from my climbing group.

UNIVERSITAT ROVIRA I VIRGILI
THEORETICAL STUDIES OF SINGLE-SITE CATALYSTS FOR EFFICIENT ELECTROCHEMICAL CO2 REDUCTION
Paulina Pršlja

UNIVERSITAT ROVIRA I VIRGILI
THEORETICAL STUDIES OF SINGLE-SITE CATALYSTS FOR EFFICIENT ELECTROCHEMICAL CO2 REDUCTION
Paulina Pršlja

**”Nothing in life is to be feared**
**it is only to be understood.**
**Now is the time to understand more,**
**so that we may fear less.”**

**Marie Skłodowska-Curie**

UNIVERSITAT ROVIRA I VIRGILI
THEORETICAL STUDIES OF SINGLE-SITE CATALYSTS FOR EFFICIENT ELECTROCHEMICAL CO2 REDUCTION
Paulina Pršlja

**”Every brilliant experiment,
like every great work of art,
starts with an act of imagination.”**

**Jonah Lehrer**

UNIVERSITAT ROVIRA I VIRGILI
THEORETICAL STUDIES OF SINGLE-SITE CATALYSTS FOR EFFICIENT ELECTROCHEMICAL CO2 REDUCTION
Paulina Pršlja

# Contents

UNIVERSITAT ROVIRA I VIRGILI
THEORETICAL STUDIES OF SINGLE-SITE CATALYSTS FOR EFFICIENT ELECTROCHEMICAL CO2 REDUCTION
Paulina Pršlja

# List of publications

1. **Volcano Trend in Electrocatalytic $CO_2$ Reduction Activity over Atomically Dispersed Metal Sites on Nitrogen-Doped Carbon**. *Li, J.; Pršlja, P.; Shinagawa, T.; Martín Fernández, A. J.; Krumeich, F.; Artyushkova, K.; Atanassov, P.; Zitolo, A.; Zhou, Y.; García-Muelas, R.; López, N.; Perez-Ramírez, J.; Jaouen, F.*, ACS Catal., **2019**, 9 (11), 10426–10439.

2. **Stability and Redispersion of Ni nanoparticles supported on N-doped carbons for the $CO_2$ electrochemical reduction**. *Pršlja, P. and N. López*, ACS Catal., **2020**, 11 (1), 88-94.

3. **Temperature dependent selectivity of $CO_2$ electrochemical reduction on CoTPP/MWCNT catalyst**. *M. N. Hossain, P. Pršlja, C. Flox, N. Muthuswamy, H. Jiang, J. Sainio, A. M. Kannan, N. López, T. Kallio*, Submitted **2020**.

Paulina Pršlja was responsible for the conception of idea design, carried out all calculations and formal analyses, wrote most of the text of all manuscripts, and made all computational figures.

# Abbreviations

| | |
|---|---|
| GHG | Greenhouse Gasses |
| CCUS | Carbon dioxide Capture, Utilization, and Storage |
| CCS | Carbon dioxide Capture, and Storage |
| CCU | Carbon dioxide Capture, and Utilization |
| EOR | Enhanced Oil Recovery |
| e$CO_2$RR | Electrochemical $CO_2$ Reduction Reaction |
| HER | Hydrogen Evolution Reaction |
| OER | Oxygen Evolution Reaction |
| ORR | Oxygen Reduction Reaction |
| GTL | Gas To Liquid |
| CTL | Coal To Liquid |
| SHE | Standard Hydrogen Electrode |
| RHE | Reversible Hydrogen Electrode |
| CHE | Computational Hydrogen Electrode |
| DFT | Density Functional Theory |
| LDA | Local-Density Approximation |
| GGA | Generalized Gradient Approximation |
| VASP | Vienna Ab Initio Simulation Package |
| PAW | Projector-augmented wave pseudopotentials |
| PBE | Perdew-Burke-Ernzerhof density functional |
| RPBE | Revieved Perdew-Burke-Ernzerhof density functional |
| RDS | Rate Determining Step |
| HK | Hohenberg and Kohn |
| SAC | Single-Atom-Catalysis |
| MOF | Metal-Organic Framework |
| M-N-C | Metal-Nitrogen-Carbon catalyst |
| CoTPP | Cobalt(II)-TetraPhenyl Porphine |
| CoPc | Cobalt(II)-Phthalocyanine |
| MWCNT | MultiWalled Carbon NanoTube |
| CNT | Carbon NanoTube |
| MO | Molecular Orbital |

| | |
|---|---|
| M-N-C | Metal-Nitrogen-Carbon catalyst |
| EXAFS | Extended X-ray Absorption Fine Structure |
| XANES | X-ray Absorption Near Edge Structure |
| XPS | X-ray Photoelectron Spectroscopy |
| XAS | X-ray Absorption Spectroscopy |
| HRTEM | High-Resolution Transmission Electron Microscopy |
| SEM | Scanning Electron Microscopy |
| 1H NMR | Proton Nuclear Magnetic Resonance |
| HPLC | High-Performance Liquid Chromatography |
| GC | Gas Chromatography |
| $J_P$ FE | Faradaic Efficiency |
| NPs | Nanoparticles |

# Abstract

Global climate change caused by anthropogenic emission of $CO_2$ is a growing threat to society. Clean $CO_2$ electrochemical conversion ($eCO_2RR$) to produce value-added chemicals and fuels using renewable electricity is a promising strategy for closing the carbon cycle. However, this early-stage technology is challenged by the low activity and selectivity and the competing hydrogen evolution reaction (HER). Thus, it is important to design catalysts with economically viable current density at low overpotential and high selectivity toward certain products. Single-site carbon-based materials are alternative candidates to typical metal catalysts for the $CO_2RR$. This thesis aims to model carbon materials under electrochemical conditions using Density Functional Theory (DFT) for $CO_2$ reduction. DFT can be applied to systems under electrochemical conditions coupled with Computational Hydrogen Electrode (CHE) formalism to investigate their selectivity and activity. The main goal is to establish experimental and theoretical correlations between physicochemical and catalytic properties for the $eCO_2RR$ over different types of catalysts. One of the promising single-site catalysts is metal-nitrogen-carbon (MNC) material with metal atom present as atomically dispersed metal-$N_x$ centers and it was investigated as a model catalyst. The distinct activity for CO formation ($J_{CO}$) observed along the series of catalysts is attributed to the nature of the transition metal in $MN_x$ moieties. Furthermore, I identified the volcano trend between their activity toward CO formation and the CO binding energy for different $MN_x$ sites, with Fe and Co at the top of the volcano. Among the atomically dispersed moieties the Nickel Nitrogen Carbon (NiNC) single-atom catalyst exhibits the highest efficiency for producing CO at different potentials. The variation in the material synthesis produces defects with coordinatively saturated and unsaturated N-doped cavities, and once the metal is placed there these single atoms can present different metal oxidation states depending on the cavity nature. I have computationally evaluated the activity and selectivity of a wide potentially active sites for single atoms and nanoparticles, where the best performing reactivity is found for N-doped models. In addition, the electrochemical stability of the reconstruction and redispersion of supported nanoparticles is addressed. To dissect the possible disintegration of Ni nanoparticles by $Ni(CO)_2$-like species Ostwald formalism was applied. I developed process of Ni nanoparticles reconstruction by forming $Ni(CO)_4$ species that can redisperse into active single atoms at high CO coverages. Moving to different systems, I also unravelled the production of

$C_1$ hydrocarbons with molecular catalysts. I focused on the potential and temperature influence of the product selectivity of $CO_2$ reduction reaction over Cobalt(II)-tetraphenylporphine and Co(II)-phthalocyanine deposited on multiwalled carbon nanotubes and carbon nanotubes. I identified the key differences between the bonding energies of $CH_2O$ via O atom or CHOH via C atom, the binding strength of CO, and the protonation of $^*$CHO. Taken together, this thesis presents a computational understanding of activity and selectivity of single-site carbon-based catalysts for $CO_2$ reduction.

# Chapter 1

# Introduction

## 1.1 Fossil fuels dependency

Fossil fuels (coal, oil, and natural gas) have been the driving force behind the industrialized world and its economic growth. Such energy has grown from insignificant levels in 1800 to an annual output of nearly 10,000 million tons of oil equivalents Mtoe. At present, about 80% of all primary energy in the world is derived from fossil fuels with oil accounting for 32.8%, coal for 27.2%, and natural gas for 20.9%. Combustible biomass and waste (10.2%), nuclear power (5.8%), and hydroelectric dams (2.3%) are the largest contributors to the global energy system after fossil based energy, but they account for only a minor share of the global primary energy supply.[1] Fossil fuels have powered our world for 250 years, they are inexpensive and accessible energy.[2] There are plenty of coalfields and petrol stations, besides they are still used today to make the majority of plastic products.[3] However, such non-renewable sources lead to energy crises and concomitant environmental issues:

- Acid rain is formed by a chemical reaction between sulfur dioxide ($SO_2$) and nitrogen oxides ($NO_x$) combined with water, oxygen ($O_2$), and other chemicals high in the atmosphere. Most of the $SO_2$ originates form coal combustion, while $NO_x$ can be derived from natural gas and motor fuels.[4,5] As $CO_2$ dissolves into carbonic acid, pH of rain is about 5.6, while Acid rain has a pH between 4.2 and 4.4.

- Combustion of coal also enhance the emission of Mercury (Hg), which is toxic and extremely damaging to the environment. The main driving force for increased emissions is the expansion of coal-fired electricity generation in the developing world. From 2008 to 2050 elemental Hg emission will only reduce from 65% to 50-55%.[6]

- The major cause of greenhouse gasses (GHG) emission into the atmosphere is global warming or climate change.[7] The burning of coal is thought to contribute 44% of the world's carbon dioxide emissions. Around the world, petrol (gasoline) alone is said to be responsible for a third of the carbon emissions. Though cleaner than both coal and crude oil, natural gas is responsible for around 20% of our carbon emissions. Since 2015 400ppm of $CO_2$ was relesed into the atmosphere.[8]

Only 0.8% of the world's primary energy is derived from geothermal, wind, solar, or other alternative energy sources. More specifically, wind power accounted for only 0.2% of the global primary energy supply with its 23 Mtoe contribution while direct solar energy accounted for 0.1% with a 12 Mtoe output.[1] Making the switch to clean energy sources will help us to reverse the effects of global warming.

## 1.2 $CO_2$ capture, utilization and storage

$CO_2$ is a greenhouse gas that originates as waste from the burning of fossil fuels, the production of electricity, fertilizers, chemicals, steel, and cement.

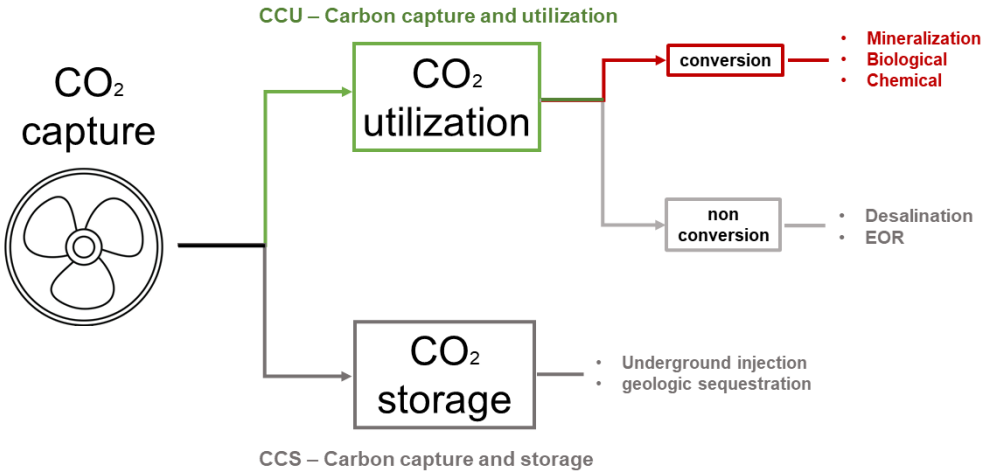


**Figure 1.1: The schematic representation** of carbon capture, utilization and storage (CCUS) concept, adapted from Ref.[9]

Carbon dioxide capture, utilization, and storage (CCUS) is a challenging demending issue, see scheme in the Figure 1.1. The captured $CO_2$ is diluted at about 95% purity, therefore it can be injected underground where the earth can store it. The earth has around 300 billion tons of storage capacity in oil and gas reservoirs, un-mineable coal seams, and deep saline reservoirs. Other than storing $CO_2$ it can also be utilized, where it can be divided into two parts. First, $CO_2$ alone without any conversion has certain uses, such as, enhanced oil recovery (EOR) by $CO_2$ flooding.[10] Indeed, the injection of $CO_2$ into an oil reservoir increases the production due to the high mutual dissolving

capability of supercritical $CO_2$ and hydrophobicity of oil. Also, the increase in pressure lowers the viscosity of the $CO_2$ oil mixture. Consequently, $CO_2$ flooding can raise production by about 15%. The oil containing dissolved $CO_2$ is then brought to the surface and the gases are flashed and $CO_2$ is separated for reinjection. In the second class of utilization, $CO_2$ is converted to chemicals and fuels[9] via carboxylation or electrochemical avenues.

Indeed, using $CO_2$ as a viable feedstock for the chemical industry has been the prediction of visionary scientists and their studies of converting $CO_2$ to $C_1$ building block chemicals, which significant achievements have already been established. Already, around 130 Mt (mega or millions of tons) $CO_2$ are used annually to manufacture urea, salicylic acid, cyclic carbonates, and polycarbonates. Among them, the urea process consumes most of the $CO_2$ industrially. Urea is produced at around 185-190°C and a pressure range of 180-200 atm by reacting $CO_2$ with ammonia. Several other, potentially more sustainable alternatives to fossil fuels are being researched. For example, significant progress is being made in the production of biofuels from algae and woody biomass.[11,12] Wind, solar, and tidal powers are also very popular and expanding rapidly along with increased interest in expanding nuclear energy.[13,14]

## 1.3 Electrochemical $CO_2$ reduction

One of the solutions is an electrochemical conversion of $CO_2$ into useful chemicals (see Figure 1.2). The result is that greenhouse gas is transformed into products that can replace plastics and chemicals that are now produced from fossil feedstock. Heterogeneous electroreduction of carbon dioxide is an important energy conversion reaction of chemical products using renewable energy as an input.[15] Important is that the electricity used for conversion must be renewable, or at least from a carbon-neutral source such as nuclear; otherwise, more $CO_2$ would be emitted in producing the electricity than would be used in the process. A result of $CO_2$ reduction is a variety of possible products such as carbon monoxide (CO),[16–20] formate ($HCOO^-$)[19,21–25] , formaldehyde ($CO_2H$), methane ($CH_4$),[19,26,27] methanol ($CH_3OH$),[28–30] and $C_2$ hydrocarbons[19,31–35] and oxygenates, where these products can be used as commodity chemicals as well as fuels, thus allowing $CO_2$ to be recycled into compounds that can act as energy carriers (see Table 1.1).[15] The cathodic process of the $CO_2RR$ can be coupled to the oxygen evolution reaction at the anode side or to the anodic chlorine production, which is technologically used for $Cl_2$ production from NaCl via aqueous electrolysis.[36]

**Table 1.1:** $CO_2$ reduction products with equilibrium potential $E^0$ in V vs. RHE

| Reaction | $E^0$ |
|---|---|
| $2H^+ + 2e^- \rightarrow H_2(g)$ | 0 |
| $CO_2 + 2H^+ + 2e^- \rightarrow HCOOH(aq)$ | -0.12 |
| $CO_2 + 2H^+ + 2e^- \rightarrow CO(g) + H_2O$ | -0.10 |
| $CO_2 + 6H^+ + 6e^- \rightarrow CH_3OH(aq) + H_2O$ | 0.03 |
| $CO_2 + 8H^+ + 8e^- \rightarrow CH_4(g) + 2H_2O$ | 0.17 |
| $2CO_2 + 12H^+ + 12e^- \rightarrow C_2H_5OH(aq) + 3H_2O$ | 0.09 |
| $2CO_2 + 12H^+ + 12e^- \rightarrow C_2H_4(q) + 4H_2O$ | 0.08 |
| $2CO_2 + 14H^+ + 14e^- \rightarrow C_2H_6(q) + 4H_2O$ | 0.14 |
| $3CO_2 + 18H^+ + 18e^- \rightarrow C_3H_7OH(aq) + 5H_2O$ | 0.10 |

The production of syngas (synthesis gas) will play an important role in the 21st century. Syngas is a fuel gas mixture consisting of hydrogen and carbon monoxide, which can be produced from many sources, including natural gas, coal, biomass, or virtually any hydrocarbon feedstock, by reaction with steam (steam reforming), carbon dioxide (dry reforming), or oxygen (partial oxidation). Syngas is a crucial intermediate resource for the production of hydrogen, ammonia, methanol, and synthetic hydrocarbon fuels. Natural gas to liquid (GTL) and coal to liquid (CTL) technology yield syngas, which is then converted into liquid fuels via the Fischer-Tropsch process. CTL and GTL would allow the use of relatively abundant coal and natural gas to decrease our dependence on imported oil for transportation fuels, however the solution does not address the non-renewable nature of fossil fuels.[15]

For $CO_2$ electrochemical conversion to become feasible, two norms need to satisfy, (i) high energy efficiency and (ii) high reaction rates. The energetic efficiency defines the energy cost of producing the product, where it can be achieved through a combination of high selectivity towards a certain product (Faradaic or current efficiency) and low overpotentials. The equilibrium potentials for most of the carbon dioxide reduction half-reactions are close to 0 V vs. RHE, making the HER an additional competing reaction beyond those toward unwanted carbon-based by-products. The main challenge lays in increasing the energy efficiency, where the limiting step is the formation of a $^{\bullet}CO_2^-$ radical anion intermediate. This step has a standard potential of -1.9 V versus SHE and is the reason for the high overpotentials.[37,38]

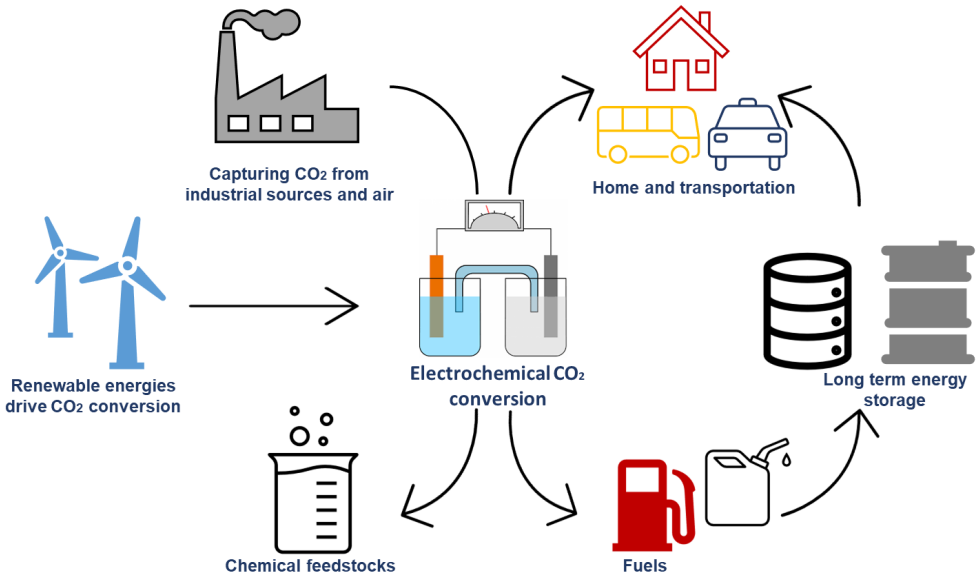


**Figure 1.2: Overall picture** of capturing $CO_2$ to electrochemical converting into commodity chemical feedstocks or fuels. Adapted from Ref.[39]

The major challenge of $CO_2$ utilization is its high thermodynamic stability and so reactions that involve $CO_2$ conversion require high activation energy inputs. Therefore a catalyst is required, so it lowers the kinetic barrier and allow the reaction to occur under reasonable reaction conditions. For this reason focus of this issue is on $CO_2$ catalysis to valorize this waste material into potential new products, and to improve the efficiency of already existing technologies. Research contributions to this issue, have been supplied by some of the leading researchers in this area, considering either heterogeneous or homogeneous catalysis approaches.

## 1.4 Heterogeneous catalysis

In 1835 Baron J. J. Berzelius described catalysis as the property of substances that facilitate chemical reactions without being consumed in them.[40,41] Catalytic reaction controls the changes of the route to equilibrium, where the focus is on reaction kinetics, and not thermodynamics. Catalysts do not change the thermodynamic equilibrium, the reaction thermodynamics describe your energy at your starting point and your destination.[42] Catalysts can be either heterogeneous or homogeneous, depending on whether a catalyst exists in the same phase as the substrate. In heterogeneous catalysis, the catalyst is in a solid phase and then acts on substrates in a gaseous or liquid reaction mixture. The chemical reactions take place at the surface of the material, where at the interphase between the solid surface and the gas or liquid phase, atoms and molecules are exchanged. The catalyst has to be able to: adsorb reactants from the gas phase, make a bond and create a product molecule. And the newly formed molecule has to be able to desorb from the surface. Interaction between

a molecule and a surface can be classified as physisorption and chemisorption. Physisorption is a weak intermolecular (van der Waals) interaction, which do not involve a significant change in the electronic orbital patterns of the species involved. Chemisorption means that atoms form a chemical bond with the surface upon adsorption.

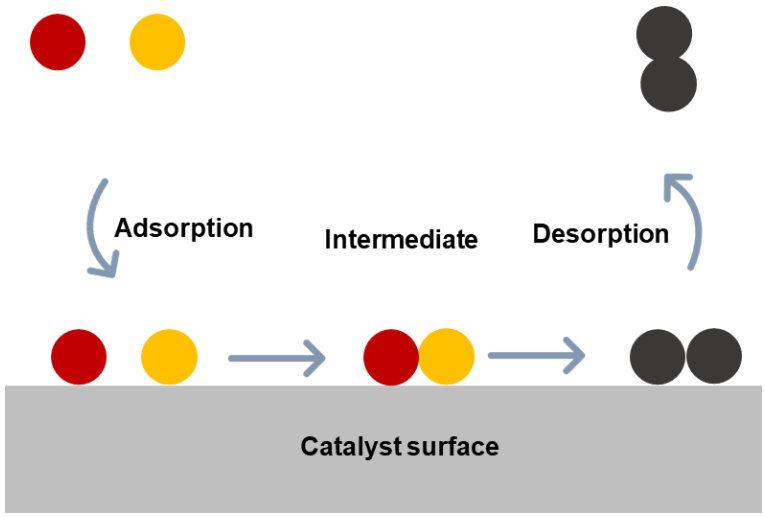


**Figure 1.3: Schematic presentation** of reaction steps in heterogeneous catalysis.

Catalytic reaction only happens on the active sites of the catalyst. A schematic representation is shown in Figure 1.3. Consequently, heterogeneous catalysts should have large surface area. So then, the catalytic materials can be made with a high surface area or the same support, can be used to stabilize active material (nanoparticles). Pure metals and metal oxides are the representatives of typical heterogeneous catalysts. The advantages of heterogeneous catalysis include, amongst others, easy catalyst separation in gas-liquid/solid systems (the catalyst is easily cleaned, or filtered), convenient handling in a fixed-, fluidised- or moving bed reactors, regeneration of catalyst and above all established reactor design principles. These are the reasons why heterogeneous catalysts are important for industry.[43]

## 1.5 Motivation and objectives

The main objective of this thesis is to theoretically study $CO_2$ electrochemical conversion towards CO and higher products over single-site catalysts, in particular well defined and undefined carbon N-doped materials. In particular, I focused on understanding the activity and selectivity of these materials and the possibility of supported Ni nanoparticle reconstruction and disintegration. The objectives for each chapter are detailed below.

**Chapter 3 Single atom catalyst for e$CO_2$RR**
Supported metal nanostructures are the most widely used type of heterogeneous catalyst in industrial processes. The size of metal particles is a key factor in determining the performance of such catalysts. The ultimate small-size limit for metal particles is the single-atom catalyst (SAC), which contains isolated metal atoms singly dispersed on supports. SACs maximize the efficiency of metal atom use, which is particularly important for noble metal catalysts. Moreover, with well-defined and uniform single atom dispersion, SACs offer great potential for achieving high activity and selectivity.

- To describe the importance of single-atom catalysts as an alternative to metal nanoparticles; due to structural motifs, they may increase the selectivity of the $CO_2$RR over the competitive HER.
- To explain the application of coordination chemistry to homogeneous-like defects.

**Chapter 4 Volcano trend in electrocatalytic $CO_2$ reduction activity over atomically dispersed metal sites on Nitrogen-doped carbon**
The development of catalysts for electrochemical reduction of carbon dioxide with high activity and selectivity remains a grand challenge to render the technology usable. As promising candidates, metal-nitrogen-carbon (MNC) catalysts with metal atoms present as atomically-dispersed metal-$N_x$ moieties (M = Mn, Fe, Co, Ni and Cu) were investigated as model catalysts. The distinct activity for CO formation observed along the series of catalysts is attributed to the nature of the transition metal in $MN_x$ moieties, due to otherwise similar composition, structure, and morphology of the carbon matrix.

- To obtain the oxidation states, on which e$CO_2$RR occurs, using computational models of $MN_4$ moties with computed Pourbaix diagram.
- To explain experimental activity with CO binding energy gained from DFT simulations as a descriptor.
- To obtain RDS of calculated e$CO_2$RR to CO Gibbs free reaction energies for each active site.
- To explain selectivity with the relationship between the adsorption($^*CO_2^-$, $^*$H)/desorption (CO) as a function of the d-antibonding occupation at electrochemical conditions.

**Chapter 5 Stability and redispersion of Ni nanoparticles supported on N-doped carbons for the electrochemical $CO_2$ reduction**

Electrocatalysts based on Ni supported on N-doped carbon materials have been computationally analyzed for the reduction of $CO_2$ considering both nanoparticles and single atom supports. In particular, there is a need for understanding the processes that happen under electrochemical conditions.

- To obtain the optimal activity and selectivity over different saturated and unsaturated N-doped carbon materials.
- To obtain surface energies of Ni NPs for nanoparticle shape.
- To investigate if the disintegration of Ni nanoparticles with $Ni(CO)_2$ can happen on studied materials, using Ostwald formalism.
- To develop a mechanism of Ni(211) surface reconstruction that is possible by the formation of $Ni(CO)_4$ species and which could redisperse into active single atoms.
- To study the influence of high CO coverages on the limitation of the HER.

**Chapter 6 Temperature dependent selectivity of $CO_2$ electrochemical reduction on CoTPP/MWCNT catalyst**

Electrochemical reduction of $CO_2$ to hydrocarbons on molecular catalysts is possible due to their structural tunability, selectivity, and low amount of loading on the support. Here we focus on the potential and temperature influence of the $CO_2$ reduction reaction product selectivity over cobalt porphyrin (CoTPP)/multiwalled carbon nanotube (MWCNT) hybrid catalyst.

- To describe the interaction between the CoTPP complex and graphene layer with DFT.
- To obtain Gibbs free reaction energies of calculated $eCO_2RR$ to $CH_3OH$ and $CH_4$ for CoTPP/MWCNT.
- To understand activity and selectivity with DFT simulations, where the difference between the binding energies of $CH_2O$ oxygen bonding, the strength of $^*CO$, and protonation of $^*CHO$ intermediate are analyzed.
- To explain the difference in selectivity with increasing negative potential.
- To explain the temperature influence on the product distribution.

# Chapter 2

# Theoretical methods

## 2.1 Schrödinger equation

The modern approach to describe atomistic properties of systems is based on quantum mechanics, namely molecules and atoms can be described with wave function, where we get the Schrödinger equation solution. It describes how the quantum state of a physical system changes in time and it has form of eigenvalue equation. For a set of atomic nuclei and electrons, according to Born Oppenheimer approximation the motions of nucleus and electrons are treated separately.[44] Thereby a fundamental time independent electronic equation follows as:

$$\hat{H}\Psi = \mathrm{E}\Psi \tag{2.1}$$

Where $\hat{H}$ is the Hamiltonian operator, $\Psi$-many-body wave function depending on the spatial coordinates of the electrons and are a set of solutions ($\Psi_\mathrm{n}$) or eigenstates of the Hamiltonian , E presents electronic energy of the system (to each set of solutions correspond an eigenvalue ($\mathrm{E_n}$)).

Because of the electron - nuclei, and electron - electron interaction the complete Schrödinger equation is written as:

$$\left[-\frac{\hbar^2}{2\mathrm{m_e}}\sum_{i=1}^{N}\nabla_i^2 + \sum_{i=1}^{N}\mathrm{V}(\mathbf{r}_\mathrm{i}) + \sum_{i=1}^{N}\mathrm{U}(\mathbf{r}_\mathrm{i},\mathbf{r}_\mathrm{j})\right]\Psi = \mathrm{E}\Psi \tag{2.2}$$

$\mathrm{m_e}$ - electron mass
1st term - kinetic energy of each electron
2nd term - the interaction energy between electrons and the atomic nuclei
3rd term - the interaction energy between electrons

$\Psi = \Psi_1(\mathbf{r}_1, \mathbf{r}_2, ..., \mathbf{r}_\mathrm{n})$ is the electronic wave function which is a function of each coordinates of all N electrons and can be approximated as a product of individual wave functions. If we want to solve the Schrödinger equation for $CO_2$ molecule, which has N=22 electrons in total, the full wave function is going to be 66 dimensional function. When we adsorb the $CO_2$ molecule to a solid surface with 66 Carbon atoms, the full wave function becomes 1254

dimensional many-body function. Therefore Schrödinger equation still remains a many-body issue which is too complex to solve for a simple catalytic systems. The term that describes the electron-electron interaction is one of the most critical and it is worth realizing that the wave function for any particularly set of coordinates cannot be directly observed and is also difficult to give the wave function any physical significance. A basic idea to simplify the N-electron problem consists in finding some physical quantity that defines the system uniquely without growing in complexity as a function of the number of electrons N. Here is where the Density functional theory is introduced, which focuses on measuring the probability of electron density at a certain position in space. The equation is then written as individual electron wave function:

$$\mathrm{n}(\mathbf{r}) = 2\sum_{i} \psi_{\mathrm{i}}^{*}(\mathbf{r})\psi_{\mathrm{i}}(\mathbf{r}) \tag{2.3}$$

## 2.2 Density Functional Theory

### 2.2.1 The Hohenberg-Kohn approach

In 1964 Density functional theory was developed.[45] The method of applying electron density to solve Schrödinger equation was developed by Hohenberg and Kohn (HK). Thereby the number of variables is reduced from 3N to 3.

**Theorem 1** The first theorem proved by HK is: The ground state energy from Schrödingers equation is a unique functional of the electron density. Restated the ground state energy can be expressed as a functional of the electron density n(r):

$$\mathrm{E}_0 = \mathrm{F}[\mathrm{n}(\mathbf{r})_0] = \mathrm{E}[\mathrm{n}(\mathbf{r})_0] \tag{2.4}$$

Therefore the ground state electron density uniquely determines all properties including the energy and wave function. The theorem says that such a functional F of the electron density exists, but does not tell which mathematical expression it has.

**Theorem 2** The second HK theorem defines a property of the functional: The electron density that minimizes the energy of the overall functional is the true electron density corresponding to the full solution of the Schrödinger equation:

$$\mathrm{E}_0 = \mathrm{minE}[\mathrm{n}(\mathbf{r})] \tag{2.5}$$

### 2.2.2 The Kohn-Sham approach

A convenient way to rewrite a functional described by Hohenberg–Kohn theorem is in terms of single electron wave functions $\Psi_{\mathrm{i}}(\mathbf{r})$.

$$\hat{H}_{\mathrm{KS}}\Psi_{\mathrm{i}} = \mathrm{E}_{\mathrm{i}}\Psi_{\mathrm{i}} \tag{2.6}$$

The energy functional can be now written as:

$$\mathrm{E_{KS}}[\Psi_\mathrm{i}] = -\frac{\hbar^2}{\mathrm{m}}\sum_{i=1}\int \Psi_\mathrm{i}^*\nabla_i^2\Psi_\mathrm{i}\mathrm{d}^3\mathbf{r} + \int V(\mathbf{r})\mathrm{n}(\mathbf{r})\mathrm{d}^3\mathbf{r} + \frac{\mathrm{e}^2}{2}\int\int\frac{\mathrm{n}(\mathbf{r})\mathrm{n}\mathbf{r}^{'})}{|\mathbf{r}-\mathbf{r}^{'}|}\mathrm{d}^3\mathbf{r}\mathrm{d}^3\mathbf{r}^{'} + \mathrm{E_{XC}}[\Psi_\mathrm{i}] \tag{2.7}$$

Where 1st term-is the electron kinetic energy

2nd term-the Coulomb interaction between electrons and nuclei (external potential)

3rd term-the Coulomb interactions between pairs of electrons

$\mathrm{E_{XC}}[\Psi_\mathrm{i}]$ is the exchange correlation functional that include all the many body effects that are not included in the 'known' terms. But however the exact form of the 3rd term in equation 2.8 is not known. This problem could be solved by applying the next approach. Kohn and Sham turn the many body problem to single electron problem.[46] Hence the task of finding the right electron density can be expressed in a way that involves solving a set of equations and each equation only involves a relation for a single electron:

$$[-\frac{\hbar^2}{2\mathrm{m}}\nabla_i^2 + \mathrm{V}(\mathbf{r}) + \mathrm{V_H}(\mathbf{r}) + \mathrm{V_{XC}}(\mathbf{r})]\,\Psi_\mathrm{i}(\mathbf{r}) = \varepsilon_\mathrm{i}\Psi_\mathrm{i}(\mathbf{r}) \tag{2.8}$$

This is similar to equation 2.2 but without summation terms since are single electron wave functions and depend on only three spatial variables.
Where, $\mathrm{V}(\mathbf{r})$-the potential which defines the interaction between an electron and the
atomic nuclei.
$\mathrm{V_H}$-the Coulomb repulsion between the considered electron and the total electron density defined by all electrons in the problem (Hartree potential):

$$\mathrm{V_H}(\mathbf{r}) = \mathrm{e}^2\int\frac{\mathrm{n}(\mathrm{r}^{'})}{|\mathrm{r}-\mathrm{r}^{'}|}\mathrm{d}^3\mathrm{r}^{'} \tag{2.9}$$

Therefore corrections of the many body effects of electrons have to be included in the final potential $\mathrm{V_{XC}}$ which defines exchange and correlation contribution to the single electron equations:

$$\mathrm{V_{XC}}(\mathbf{r}) = \frac{\delta\mathrm{E_{XC}}(\mathbf{r})}{\delta\mathrm{n}(\mathbf{r})} \tag{2.10}$$

### 2.2.3 Exchange correlation energy

In the Kohn Sham scheme the expression for the exchange correlation functional $\mathrm{E_{XC}}$ is unknown, for which several approximations has been developed.

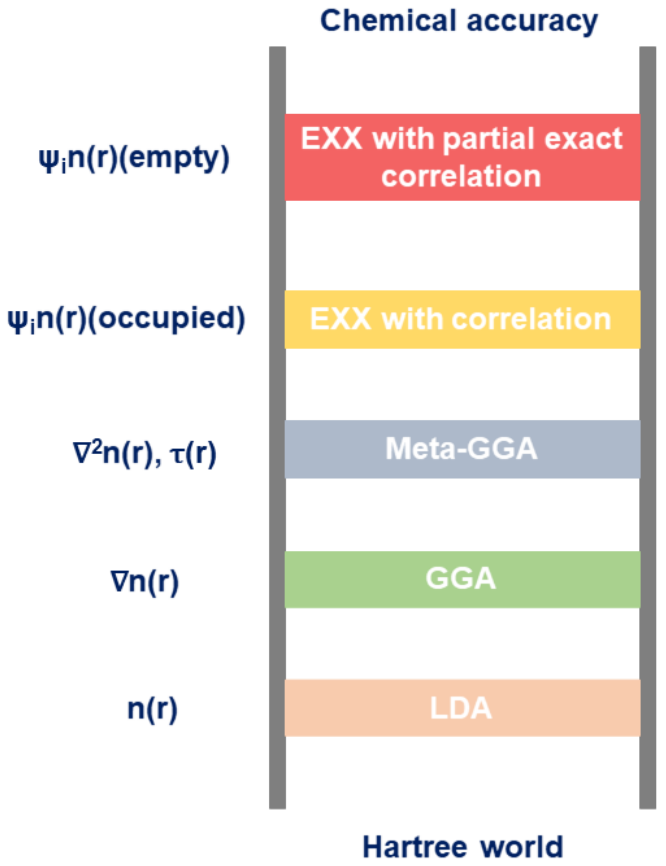


**Figure 2.1:** Perdew's classification ladder of DFT functionals. Adapted from Ref.[45]

In Figure 2.1 the hierarchy of accuracy in the exchange correlation functionals has been defined by John Perdew as "the Jacobs ladder of DFT".[45,47]

**Local density approximation** (LDA), exchange correlation energy is approximated to the one of an homogeneous electron gas, where the electron density is constant at all points in space, $n(\mathbf{r})$. $E_{XC}$ energy can be written as:

$$E_{XC,\,LDA} = \int \varepsilon_{XC}^{hom}(n(\mathbf{r}))n(\mathbf{r})dr \tag{2.11}$$

Where $\varepsilon_{XC}^{hom}(n(\mathbf{r}))$ is the energy of the exchange correlation hole in the homogeneous electron gas of density n. The LDA describes properties such as lattice constants, vibrational frequencies and equilibrium geometries for bulk materials. Other properties such as dissociation energies of molecules, cohesive energies are not very well described using this functional. The spin-polarized version (LSDA) can be applied for magnetic materials.

$$E_{XC,\,LSDA} = \int \varepsilon_{XC}^{hom}(n(\mathbf{r}))n_{\uparrow}, n_{\downarrow}(\mathbf{r})dr \tag{2.12}$$

**Generalized gradient approximation** (GGA), uses information about the local electron density and the local gradient in the electron density. GGA

has a good accuracy and reasonable computational cost, so this approximation is used to describe many systems in homogeneous and heterogeneous catalysis. Also, it corrects the overbinding tendency of LDA functionals. With GGA approach $E_{XC}$ energy can be written as:

$$E_{XC,\,GGA} = \int \varepsilon_{XC}^{hom}(n(\mathbf{r}), \nabla n(\mathbf{r}))dr \tag{2.13}$$

The gradient of the electron density can be included in a GGA functional in different ways, therefore a large number of functionals has been developed. The most widely used functionals for bulk solids and surfaces are Perdew-Wang (PW91),[48] Perdew-Burke-Ernzerhof (PBE)[49,50] and revieved RPBE.[51] For molecules, hybrid functional B3LYP can be used. Thereby the best choice of functional will depend on the system of interest.

**Meta-Generalized gradient approximation** (Meta-GGA), calculations are computationaly demanding, and the improvement of the results from GGA-type functionals is often negligible. $E_{XC}$ energy can be written as:

$$E_{XC,\,GGA} = \int \varepsilon_{XC}^{hom}(n(\mathbf{r}), \nabla n(\mathbf{r}), \nabla^2 n(\mathbf{r}))dr \tag{2.14}$$

### 2.2.4 Implementation of DFT

In order to find the right electron density an iterative method is applied:

1. We start with a trial electron density $n(\mathbf{r})$
2. The trial $n(\mathbf{r})$ is used to solve the Kohn-Sham equations to obtain the single electron wave functions $\Psi_i(r)$.
3. The single electron wave functions is used to calculate an electron density, $n_{KS}(\mathbf{r}) = 2\sum_i \Psi_i^*(\mathbf{r})\Psi_i(\mathbf{r})$
4. Finally the calculated electron density $n_{KS}(\mathbf{r})$ is compared with the trial electron density $n(\mathbf{r})$. If they are different, the trial electron density is updated and the loop is repeated again. If they are the same (with small tolerances), the ground state density is obtained.

### 2.2.5 Periodic systems

#### Plane wave basis sets

A basis set is a set of functions that is used to represent the electronic wave function in density-functional theory. The one-electron Kohn–Sham orbitals $\Psi_i(\mathbf{r})$ (Equation 2.6), can be expanded using different basis:

- spatially localized functions (Slater- or Gaussian-type orbitals)

- spatially extended functions (plane waves)

For the periodic crystalline solids, plane wave approach is used. In order to satisfy Bloch's Theorem,[52] the electronic wave function can be expressed in form of a plane wave $e^{i\cdot\mathbf{kr}}$ with wave vector k multiplied by a periodic function $u_{n\mathbf{k}}(\mathbf{r})$ with the same periodicity as the crystalline lattice:[52,53]

$$\Psi_{i,\,k}(\mathbf{r}) = e^{ik\cdot\mathbf{r}} u_{ik}(\mathbf{r}) \tag{2.15}$$

The cell periodic function ($u_{ik}(\mathbf{r})$) is periodic in space with the same periodicity of the supercell. The electronic wave function is written as a sum of plane waves (Equation 2.16):

$$u_{i,k}(\mathbf{r}) = \sum_{G} C_{i,(k+G)} e^{ik\cdot\mathbf{r}} \tag{2.16}$$

Where $C_{ik+G}$, are the expansion coefficients, k is the wave vector in the first Brillouin zone and G is the reciprocal in the reciprocal wave vectors. The total plane wave expansion can now be writen as:

$$\Psi_{i,\,k}(\mathbf{r}) = C_{i,k+G} e^{ik+G\mathbf{r}} \tag{2.17}$$

**Reciprocal space**

A crystal is defined as a three dimensional periodic structure and can be described as a Bravais lattice, which shows its periodicity as a display of repeated discrete points with lattice vector **R** (Equation 2.18). The lattice vectors $\vec{a}_i$ are linearly independent. The parametres $n_i$ are integer number, because the translations are discrete.[53,54]

$$\vec{R} = i_1\vec{a}_1 + n_2\vec{a}_2 + n_3\vec{a}_3 \tag{2.18}$$

With operations shown in Equation 2.19 we can define reciprocal lattice with cell vectors $\vec{b}_j$ for a Bravais lattice with cell vectors $\vec{a}_j$. Reciprocal space (k-space) is periodic for translations over $\vec{b}_1$, $\vec{b}_2$, and $\vec{b}_3$. The primitive cell of the k-space is known as Brillouin zone.

$$\begin{aligned}
\vec{b}_1 &= 2\pi \frac{\vec{a}_2 \times \vec{a}_3}{\langle \vec{a}_1, \vec{a}_2, \vec{a}_3 \rangle} \\
\vec{b}_2 &= 2\pi \frac{\vec{a}_3 \times \vec{a}_1}{\langle \vec{a}_1, \vec{a}_2, \vec{a}_3 \rangle} \\
\vec{b}_3 &= 2\pi \frac{\vec{a}_1 \times \vec{a}_2}{\langle \vec{a}_1, \vec{a}_2, \vec{a}_3 \rangle}
\end{aligned} \tag{2.19}$$

**k-points**

In order to choose appropriate k-points for calculations of periodic structures, Monkhorst-Pack method should be used.[55,56] Larger lattice vectors in real

space correspond shorter lattice vectors in reciprocal space. Therefore increasing the volume of the cell reduces the number of k-points. Exploring the symmetries in the k-points can significantly reduce the computational time and cost.

### Energy cutoff

Another way to lower computational cost is by limiting the number of plane-waves by setting a kinetic energy cutoff. The kinetic energy of the systems is:

$$\mathrm{E} = -\frac{\hbar^2}{2\mathrm{m}}|\mathrm{k}+\mathrm{G}|^2 \tag{2.20}$$

Next step is to reduce the infinite sum from Equation 2.20 and to include only the solutions that have the kinetic energy lower than a certain value:

$$\mathrm{E}_{\mathrm{cut}} = -\frac{\hbar^2}{2\mathrm{m}}\mathrm{G}_{\mathrm{cut}}^2 \tag{2.21}$$

And the infinite sum from equation (2.21) reduces to:

$$\Psi_{\mathrm{k}}(\mathbf{r}) = \sum_{|G+k|<G_{cut}} C_{k+G}e^{[i(k+G)r]} \tag{2.22}$$

This parameter has to be defined whenever a DFT calculation is performed. Convergence tests should be done for each system. In general many packages provide default values. A key point to remember is whenever a DFT calculation is performed for multiple systems that are going to be compared, the same energy cutoff should be used for all systems.

### Pseudopotentials

Electrons in atoms can be divided into valence and core electrons. Valence electrons responsible for most of the chemical bonding, while the core electrons are tightly bound to the nuclei. Pseudopotential approximation is introduced to replace the electron wave function from a set of core electrons with a smoothed wave function. This is established so as to match various important physical and mathematical properties of the true ion core. This approach is greatly necessary to reduce the computational cost when plane waves are used as basis set. The properties of the core electrons are fixed in all calculations, which is known as the frozen core approximation. In the DFT codes typically a library of pseudopotentials that includes an entry for almost each element in the periodic table is provided. There has to be defined a minimum energy cutoff that has to be used in calculations. Most used families of pseudopotentials are the Vanderbilt ultrasoft pseudopotentials (US-PP)[57] and the Projector Augmented Wave ones (PAW).[58,59] In this thesis PAW approximations are used, as they describe transition metals better.[60]

### General computational details

All electronic structures were performed using spin-polarized Density Functional Theory (DFT) as implemented in the Vienna Ab initio Simulation Package (VASP).[58,61] The GGA PBE-D3 was the functional of choice, where D3 stands for Grimme despersion.[62,63] Core electrons were described by projector augmented wave (PAW),[58,59] and valence electrons were expanded by plane wave basis sets with a kinetic energy cut-off of choice. In each chapter of the thesis the details of calculations are given. They includes the sizes of the unit cell, k-point sampling, kinetic energies cutoffs and the cutoff for the density grid. For all the systems described before, we obtained the energies of the relevant intermediates in the electrochemical environment under $eCO_2RR$ conditions by considering the computational hydrogen electrode (CHE). Gas-phase molecules that were used in the thesis as a reference were calculated with PBE functional. Zero-point, entropic, and heat capacity contributions are shown in Table 2.1.[64] The solvation correction to adsorbate energy was applied to *COOH (-0.25 eV) and *CO (-0.1 eV).[64] Corrections of DFT-based gas-phase errors for standard PBE Gibbs free energies of $CO_2$ ($\varepsilon$=-0.19 eV) and CO ($\varepsilon$=0.24 eV) were applied. The corrections were calculated as:

$$\Delta G^{\circ}_{DFTcorr} = \Delta G^{\circ}_{DFTcorr} - (\sum \varepsilon^{P}_{T} - \sum \varepsilon^{R}_{T}) \tag{2.23}$$

where the $\varepsilon^{R}_{T}$ is the sum of all errors for reactants and $\varepsilon^{P}_{T}$ for the products.[65] solvation and error correction were added for studied materials in Chapters 4 and 5. The optimized structures can be retrieved from ioChem-BD.[66] A unique ioChem-BD link of the DFT calculations for each of the projects will be provided in according chapters.

**Table 2.1:** Zero-point, entropic, and heat capacity contributions (in eV) for gas-phase molecules used as a reference.

| Molecule | ZPE | TS | $C_p$ |
|---|---|---|---|
| **$CO_2$** | 0.31 | -0.66 | 0.10 |
| **CO** | 0.13 | -0.61 | 0.09 |
| **$H_2O$** | 0.57 | -0.67 | 0.10 |
| **$H_2$** | 0.28 | -0.40 | 0.09 |
| **$NiCO_4$** | 0.81 | -0.45 | |

## 2.3 Basic concepts of computational electrochemistry

### 2.3.1 The Computational Hydrogen Electrode

Electrochemical reactions, where electrons and protons are transfered, can be modelled by applying the computational hydrogen electrode (CHE),[67–69] where simplification of combined chemical potential of protons and electrons is applied. Schematic representation of CHE is presented in Figure 2.2. CHE approach is based on the following hypotheses:

1. The Standard Hydrogen Electrode (SHE) is taken as reference electrode and is define as 0 V and pH=0. The chemical potential for the reaction $H^+ + e^-$ can be related to the Gibbs free energy of $\frac{1}{2}H_2$. Therefore, at standard conditions (298 K, 1 bar of gas phase $H_2$)

$$\Delta G_{H^+} = \frac{1}{2} G_{H_2,DFT} \tag{2.24}$$

2. Proton Gibbs free energy is corrected by pH:

$$G_{pH} = -k_B T \ln(H^+) = k_B T \ln 10 \cdot pH \tag{2.25}$$

3. The effect of the electric potential is included adding to a thermodynamic state the energy of each transferred electron, -neU, where U is the applied potential.

4. The electrostatic field caused by the electrical double layer is neglected.

Hydrogen can easily be calculated and then referenced back to the chemical potentials of the electrons and protons in solutions. Once the hydrogen molecule energy is calculated and then add the potential $U_{RHE}$, free energy $G_{CHE}$ can be written as:

$$G_{CHE}(n,U_{RHE}) = \Delta G = \Delta E - T\Delta S + \int_0^T C_p dT + \Delta ZPE - n(\frac{1}{2}\mu_{H_2} - eU_{RHE}), \tag{2.26}$$

where n is the number of proton-electron transferred and $G_{CHE}$ is a function of both potential and proton-electron pair transfers. The thermodynamic contributions to $G_{CHE}$ from the support are typically neglected, and only the contributions from the gas phase and vibrational entropy of the adsorbate are included. The simplicity of the computational hydrogen electrode is obtained by the choice of references and the assumption of electrolyte and electrode in equilibrium. One could include solvation contribution either through explicit water model[68] or implicit model based on solvent dielectric permittivity.[70] As will be shown in the next sections, the CHE is applicable for calculating many

interesting properties in electrochemical reactions, such as surface Pourbaix diagrams and free energy diagrams. The application of CHE model to decouple proton-electron transfers, such as $CO_2$ adsorption, has intrinsic limitations.[71] An alternative model derived from Marcus theory (Ref.[72]) has been proposed to account for the transition between sequential and concerted proton-electron transfer.[73–75]

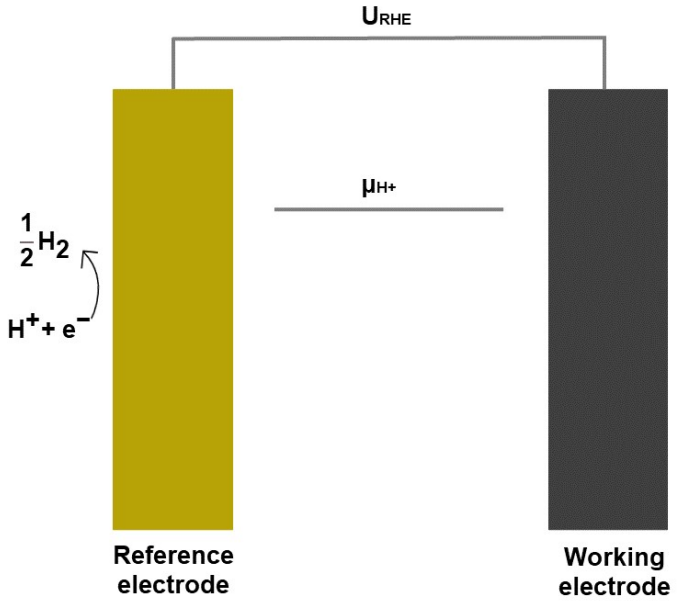


**Figure 2.2:** Schematic representation of the computational hydrogen electrode (CHE). The hydrogen reaction is in equilibrium with the reference electrode. The protons for both the working and the reference electrode have the same chemical potential, while the electrons at the working electrode are affected by the applied potential ($U_{RHE}$). In this case $U_{RHE}$ is negative. Adapted from Ref.[69]

### Pourbaix diagram

Classical Pourbaix diagram, also known as a potential/pH diagram, is a plot of possible thermodynamically stable states of an compound as a function of pH and potential. As noted above, these diagrams are essentially phase diagrams that map these conditions, most typically in aqueous solutions where different redox species are stable (see Figure 2.3).

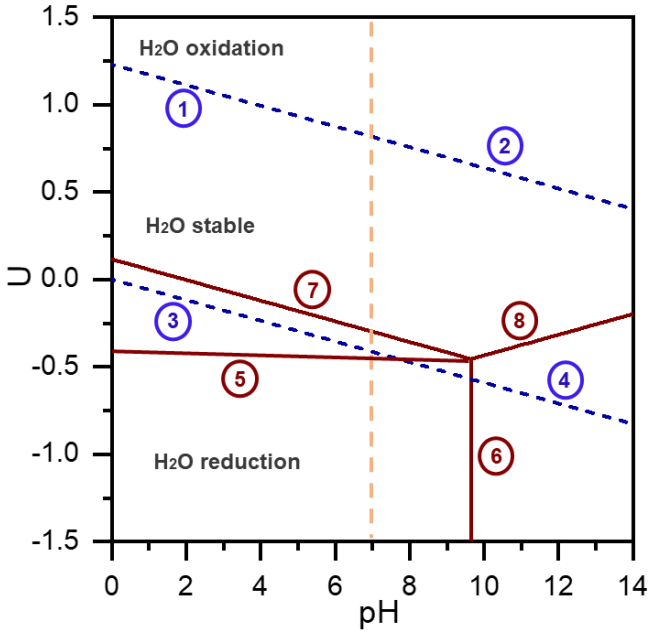


**Figure 2.3: Pourbaix diagram.** The blue lines correspond to the water oxidation and reduction reactions, the red lines separate the different phases, and the orange line corresponds to pH 7.

Areas in the Pourbaix diagram mark regions where a single species is stable, while lines mark places where two species exist in equilibrium. Reaction of numbered lines in Figure 2.3 are presented below;

**(1)** $O_2 + 4H^+ + 4e^- \leftrightarrow H_2O$

**(2)** $O_2 + 2H_2O + 4e^- \leftrightarrow 4OH^-$

**(3)** $2H^+ + 2e^- \leftrightarrow H_2$

**(4)** $2H_2O + 2e^- \leftrightarrow H_2 + 2OH^-$

**(5)** electron reaction: $A \leftrightarrow A^+ + e^-$

**(6)** proton reaction: $AH \leftrightarrow A^- + H^+$

**(7)** and **(8)**: Proton electron reaction: $AH \leftrightarrow {}^*A + H^+ + e^-$

The proton reaction (vertical line) is reaction that only depend on pH. Pure redox reaction (horizontal line) depends on applied potential. The proton-electron reaction depends on pH and potential and has a slope of -0.0592 V/pH (RHE scale). To construct the surface Pourbaix diagram, we take into consideration DFT formation energies of the clean surfaces with according

experimental oxidation states. The aim was to identify the possible oxidation states on which $CO_2$ reduction reaction could happen at experimental condition. Furthermore, the surface Pourbaix diagrams assume that no other reaction occur, for example HER, where on metals such as Au, Ag, or Cu hydrogen gets produced. However on single-site materials, because of their unique structure, HER is limited.

Computed surface Pourbaix diagrams were constructed for $FeN_4$-, $CoN_4$-, and $Ni_4$- species (see Chapter 4). Figure 2.4 shows an example of computed diagram for FeNC catalyst, for which two different oxidation states were observed (2+ and 3+). Therefore, Fe(II)$N_4$-$H_2O$, Fe(II)$N_4$-O, and Fe(III)$N_4$-OH species were chosen.

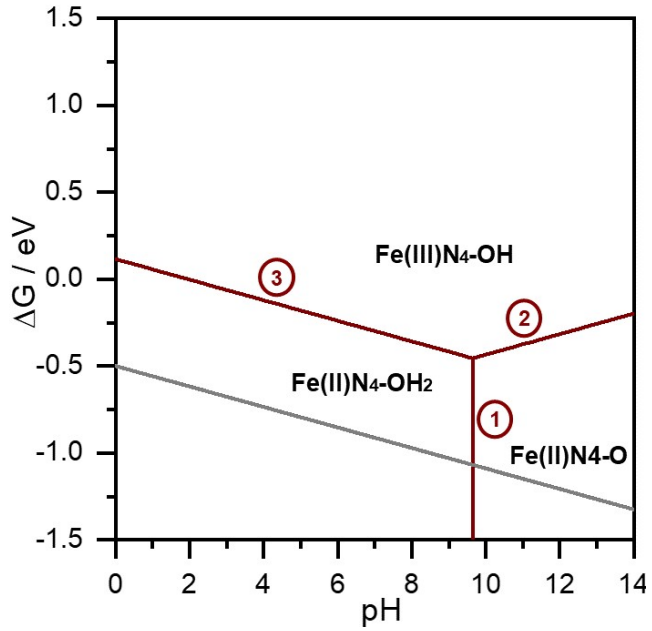


**Figure 2.4: Computed Pourbaix diagram** The red lines separate the different states of $FeN_4$-, and the orange line corresponds to pH 7. Gray line corresponds to -0.5 V vs. RHE.

The oxidation states were determined based on calculated magnetization of the metal using crystal field theory (see Chapter 3). Once the formation energies of the the chosen species were obtained the Pourbaix diagram was build. Numbered reactions in Figure 2.4 are presented below:

**(1)** Fe(II)$N_4$-$H_2O$ $\leftrightarrow$ Fe(II)$N_4$-O + $2H^+$

**(2)** Fe(III)$N_4$-OH + $e^-$ $\leftrightarrow$ Fe(II)$N_4$-O + $H^+$

**(3)** Fe(III)$N_4$-$H_2O$ $\leftrightarrow$ Fe(II)$N_4$-O + $H^+$ + $e^-$

This approach is very simple and in particular it can be applied to screening projects and to study trends. With these trends we show the correlation between experimental and theoretical results.

### 2.3.2 Explanation of electrocatalytic reactions and trends

#### Gibbs free energy diagrams

A way to compare the experimental result with theoretical prediction is the Gibbs free energy diagram. It allows us to interpret different reaction pathways by calculating the reaction intermediates. Once the intermediates for certain reaction are calculated we can get theoretical onset potential, which is numerically equivalent to the additive inverse of the largest positive reaction energy considering electrochemical steps. Onset potential can be calculated by

$$\mathrm{U_{onset}} = -\max(\Delta \mathrm{G_1}, \Delta \mathrm{G_2})/\mathrm{e^-} \tag{2.27}$$

where the $\Delta$G is Gibbs free energy for certain intermediate.[67,76] For constructing free diagram for $CO_2$ reduction towards CO, we can follow two different mechanisms;

- First mechanism, $CO_2$ may be activated by an electron transfer prior to its adsorption, and the adsorbed species is stabilized by a proton close to the surface (one decoupled and coupled proton-electron transfers):[77–81]

  Step 1 : $* + \mathrm{CO_2} + \mathrm{e^-} \rightarrow {}^*\mathrm{CO_2^-}$

  Step 2 : ${}^*\mathrm{CO_2^-} + \mathrm{H^+} \rightarrow {}^*\mathrm{COOH}$

  Step 3 : ${}^*\mathrm{COOH} + \mathrm{H^+} + \mathrm{e^-} \rightarrow {}^*\mathrm{CO} + \mathrm{H_2O}$

  Desorption : ${}^*\mathrm{CO} \rightarrow \mathrm{CO(g)} + *$

- Second mechanism (two coupled proton-electron transfers).[82]

  Step 1 : $* + \mathrm{CO_2} + \mathrm{H^+} + \mathrm{e^-} \rightarrow {}^*\mathrm{COOH}$

  Step 2 : ${}^*\mathrm{COOH} + \mathrm{H^+} + \mathrm{e^-} \rightarrow {}^*\mathrm{CO} + \mathrm{H_2O}$

  Desorption : ${}^*\mathrm{CO} \rightarrow \mathrm{CO(g)} + *$

In order to construct Gibbs free energy diagram (see Figure 2.5), the energy of each reaction step was calculated with respect to the energies of reactants, $CO_2$ and support. $\Delta$G for each step was calculated as shown in Equation 2.26:

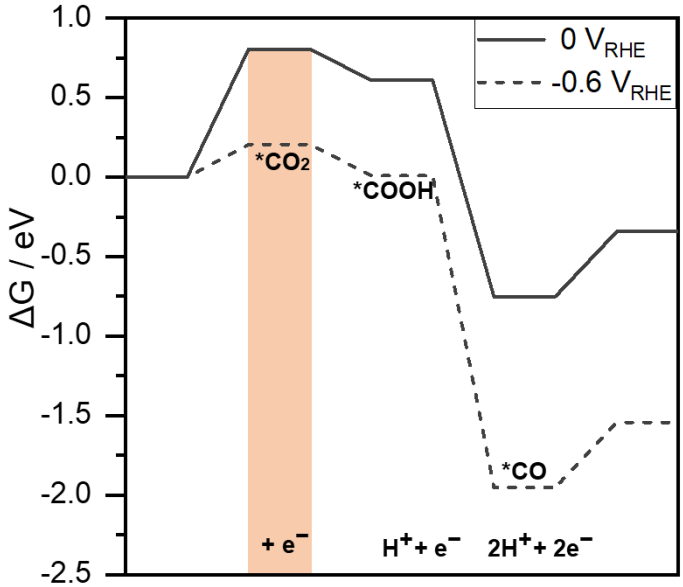


**Figure 2.5:** The Gibbs free energy diagram for $CO_2$ reduction towards CO, at 0 V (solid gray line) and -0.6 V (dashed gray line) vs. RHE. In addition, the light orange area indicates $^*CO_2$ intermediate, which is not part of CHE formalism.

$$G_1 = \Delta G_{^*CO_2} - \Delta G_{CO_2} - \Delta G_* + (eU_{RHE}) \tag{2.28}$$

$$G_2 = \Delta G_{^*COOH} - \Delta G_{CO_2} - \Delta G_* + (\frac{1}{2}H_2 + eU_{RHE}) \tag{2.29}$$

$$G_3 = \Delta G_{^*CO} - \Delta G_{CO_2} - \Delta G_* + (H_2 + 2eU_{RHE}) \tag{2.30}$$

$$G_{des} = \Delta G_{CO} + \Delta G_* - \Delta G_{^*CO} \tag{2.31}$$

Since the modelling of decoupled proton-electron transfers is challenging from a DFT point of view, in this thesis second mechanism was used only when theoretical onset potential was calculated. An example of how it was calculated is shown below:

$$G_{1ons} = \Delta G_3 - \Delta G_2 \tag{2.32}$$

$$G_{2ons} = \Delta G_{des} - \Delta G_3 \tag{2.33}$$

Furthermore, the free energies calculated for the free energy diagram can be used to find scaling relations and construct Sabatier activity volcanoes as a function of reactivity descriptors.

### Scaling relation

Once the adsorption energies of intermediates are calculated, the question is whether different adsorption energies are related to one another and how. One of the solution for understanding relation would be scaling relationship, which corresponds to sets of binding energies through linear functions (example in Figure 2.6), and have been found between C-, N-, S-, and O- derived adsorbates on catalyst surfaces.[83–85] Furthermore scaling relationships are not limited to the binding energies of adsorbed atoms and their hydrogenated species but they hold for a broader group of adsorbates that fulfil certain conditions related to the electronic structure of the surface and the adsorbates.[86]

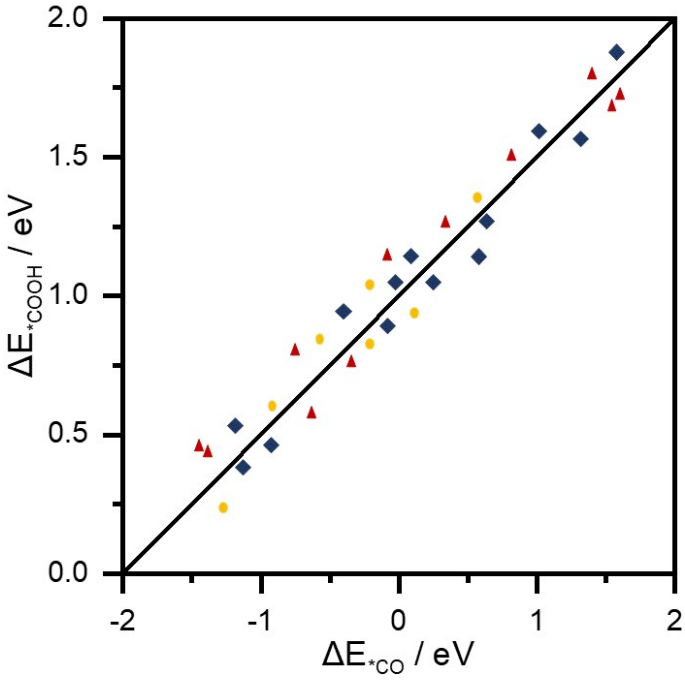


**Figure 2.6: Linear scaling relation** between *COOH and *CO binding energy.

Toward the electrocatalytic $CO_2$RR, it is difficult to attain a low overpotential because of the adsorbate (particularly, *COOH, *CO and *CHO or *COH) scaling relations. Cu electrodes are good example because the protonation of *CO is the rate determining step toward $CH_4$ with the highest free energy change. Protonation from *CO to *CHO or *COH is determined by the electrode surface structure, electrode potential, acidic or alkaline environment, standard strategy to reduce the free energy change of this step is to strengthen the binding energy of *CHO or *COH and weaken the binding strength of *CO. The optimal conversion of $CO_2$ with the lowest limiting potential can be achieved by tuning the free energy change of each elementary reaction to minimum. The way to break the above scaling relations, would be with introducing p states, reducing metal coordination numbers, tethering active ligands, alloying metal catalysts, and designing dual functional sites.[87]

On the other hand, we can use the scaling relations, without breaking them by using single-site catalysts. They have a structural advantages over typical metal and metal oxide catalyst, because intermediate can only bind on the top site of the catalyst. Mostly it can be useful for $eCO_2RR$, as the competitive HER can be limited by lacking the hollow site.[88]

### Volcano plot

French chemist Paul Sabatier qualitatively described the adsorption properties of the optimal catalyst, where the best catalysts should bind adsorbate with an intermediate strength: not too weakly in order to be able to activate the reactants, and not too strongly to be able to desorb the products. Today this statement is known as the Sabatier principle of catalysis,[89] however the quantitative description was portrayed in Balandin-Sabatier volcano-shaped curves, which consider the implication of the rate (catalyst activity) relative to a descriptor of substrate binding.[90,91] Balandin developed a theory mainly concerned with the steric relation between reactant and the surface structure of the catalyst. Figure 2.7 presents illustration of volcano plot, where the top of the volcano corresponds to the highest activity and the intermediate bond strength.

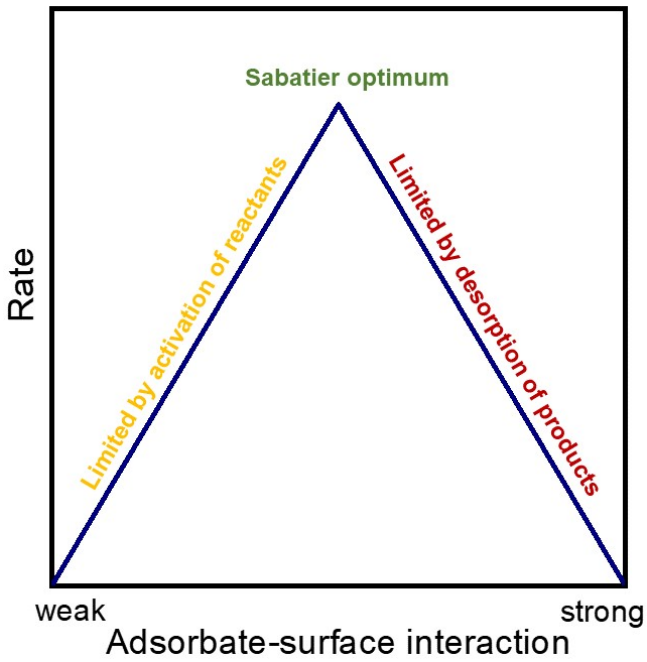


**Figure 2.7: The catalytic volcano plot.** Illustration of the qualitative Sabatier principle.

For electrochemical reactions such as oxygen evolution reaction (OER)/oxygen reduction reaction (ORR) and HER, Sabatier principle coupled with scailing relations can be used to desribe activity with overpotential or current density as fuction of a potential-determining binding energy of intermediates.[43,69,92–99] Volcano trends have been generated for numerous other catalytic reactions such as $NO_x$ decomposition, ammonia synthesis, and CO oxidation.[94]

# Chapter 3

# Carbon based single atom catalyst

The green conversion of $CO_2$ to fine chemicals calls for a new generation of efficient and robust catalysts. Herein I present single-atom catalysts (SACs), in which all metal species are atomically dispersed on a solid support, and which often consist of well-defined mononuclear active sites and enables 100% atom utilization. They are a bridge between homogeneous and heterogeneous catalysts and often show outstanding performance in many industrially important reactions, including thermochemical, electrochemical and photochemical conversions. The relationship between catalytic performance and the active site structure is discussed in terms of the valence state, coordination environment and anchoring chemistry of single atoms to the support, in an effort to guide the rational design of SACs, which has traditionally been dominated by homogeneous catalysis.

## 3.1 Decreasing size particle toward single atom

In heterogeneous catalysis, enormous efforts have been devoted toward improving the performance of supported metal catalysts by downsizing the metal particles. The supported metal particles have multiple active sites with different performances. Such heterogeneity affects the efficient utilization of metal active sites and thus reduces selectivity toward a specific product. The size of metal particles therefore becomes one of the most critical factors determining the reactivity and specificity of supported metal catalysts. The bulk materials can be turned into nanoparticles, subnanoclusters, and finally single metal atoms (see Figure 3.1). The size reduction generates an increase of unsaturated coordination environment of the metal species. Accordingly, the surface free energy of the metal components increases, and the metal sites become more and more active for chemical interactions with the support and adsorbates, which accounts for the size effects of metal nanocatalysts.

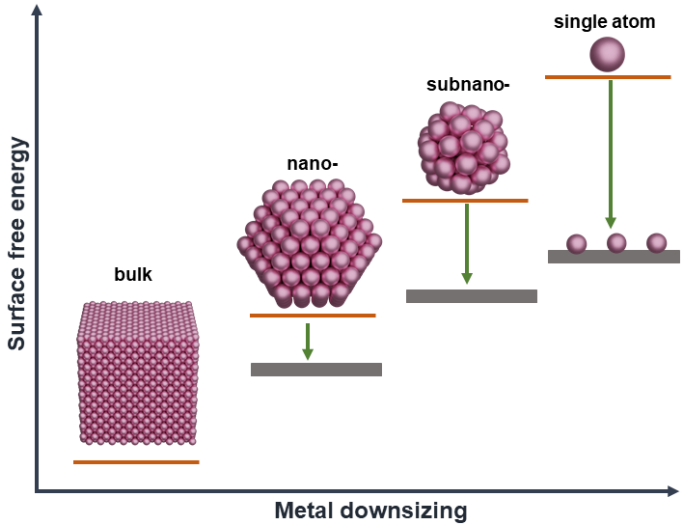


**Figure 3.1:** Schematic diagram illustrates minimizing the metal size from bulk to single atom.

Despite their small sizes, subnanoclusters still contain multiple active centers and are not always the most desirable active sites for specific catalytic processes.[100] Extreme downsize of particles would be SACs, which incorporate many advantageous features of homogeneous and heterogeneous catalysts. Typical homogeneous catalysts have well defined structures but are not easily recycled because they are difficult to separate from reaction media. Heterogeneous catalysts can have high stability and are easily separated from reactants and products. However, their active sites may be non-uniform in nature, and only now there are technologies emerging that enable their in operando study.[101] Thanks to SACs unique structural properties, not only they have a maximal atom utilization efficiency but also offer opportunities for tuning reaction rates and selectivity, thus presenting them as bridge between ho-

mogeneous and heterogeneous catalysts. Therefore, SACs may provide a good platform for understanding structure-activity relationships on an atomic scale. Searching for catalysts with well defined single active centers is necessary for improving the performance and understanding of catalytic mechanisms.

## 3.2 Single sites design for $eCO_2RR$

Ion-exchanged metals supported on porous materials such as metal-organic frameworks (MOFs) and zeolites, as well as organometallic complexes anchored to supports, can also be viewed as SACs.[?,102–104] Furthermore the development of the concept of single-atom catalysis is confirmed with both atomic-resolution characterization techniques and theoretical modelling. The use of these methods provides a clear picture of the dispersion of the atoms, the bonding between single atoms and the support, and even in operando dynamics of single atoms during catalysis. The stabilizing effect of bonding between single transition metal atoms and/or ions and the support is not limited to materials containing oxo ligands. Other donor atoms can also be effective, particularly when carbon-rich supports are concerned. For example, N atoms in carbon-rich supports not only strongly anchor individual metal centres but also modify the electronic properties of the metal (see Figure 3.2). Relative to metals deposited on undoped supports, metal sites on N-doped carbon materials can exhibit higher activity and/or selectivity in a variety of electrocatalytic processes.

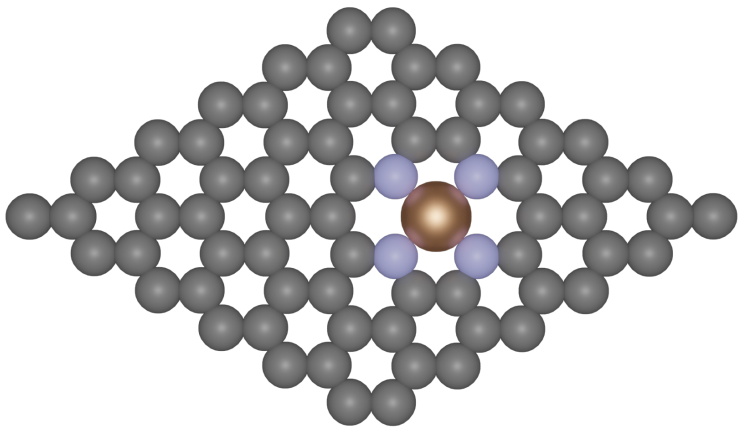

**Figure 3.2:** Model for carbon-rich single-site catalyst, particularly MNC materials.

In this thesis, the research focus on designing the models for (i) defined MOFs, (ii) various unsaturated N-doped carbon based materials, and (iii) molecular catalyst. MOFs have been one of the most researched type of single site catalyst.[105–109] They can be constructed through the periodic coordination of metal ions and organic ligands to form one- to three-dimensional networks. The organic linkers in MOFs are enormously diverse and possess a variety of configurations. In addition, MOFs possess ordered pore structures, uniform

pore sizes and high specifc surface areas, making them ideal substrates for the deposition of single atoms. For the preparation of single atoms, the pyrolysis of MOFs can serve as an important route to fabricate N-doped carbon materials, which are ideal substrates for the dispersion. Such materials were initially developed for catalyzing the oxygen reduction reaction (ORR), in particular in acidic medium, with focus on the $FeN_x$ and $CoN_x$ since other $MN_x$ motives have much lower ORR activity.[106,110,111] This has for a long time impeded the elucidation of the $MN_x$ site structures and their ORR catalytic activities.[106] In the context of $eCO_2RR$, the presence of metal clusters along with $MN_x$ moieties may, depending on the nature of the metal, catalyze the HER,[112–115] and/or other pathways of $eCO_2RR$. This has prevented establishing clear experimental structure-to-property relationships between the nature of the metal in $MN_x$ and their activity and selectivity toward $eCO_2RR$.[116]

Validation of DFT predictions on a reasonably large series of model materials is highly important to speed up the rational identification of more promising MNC candidates for $eCO_2RR$,[117] given that the library of metal demonstrated to form $MN_x$ sites in carbon has been recently expanded also to heavier elements such as Sn,[118] Ru,[119] Pt,[120] Pd,[120] etc. The investigation of model MNC catalysts exclusively comprising atomically-dispersed $MN_x$ sites is thus critical to understand their structure-performance relationships and to identify the proper activity/selectivity descriptor(s). While numerous studies have now reported the $eCO_2RR$ selectivity of some atomically-dispersed MNC catalysts prepared by different synthetic approaches,[120–123] only one single study, to the best of our knowledge, has compared the trends in activity and selectivity for a narrow family of three MNC catalysts prepared identically except for the nature of the metal element.[124] The synthesis leaned on silica templating of o-phenylenediamine and Fe, Co or Ni salts. While metal particles formed in parallel to $MN_x$ sites during the first pyrolysis, they could be removed during subsequent NaOH etching and acid-wash steps. However, the formation of metallic particles during the first pyrolysis lead to markedly different pore size distributions, in particular for CoNC. This rendered the comparison of the materials more complex due to expectedly different utilizations of the $MN_x$ sites for different pore size distributions.

For an example, in Chapter 4 a robust synthesis approach involving a sacrificial Zn(II) zeolitic imidazolate framework and a metal salt (Mn, Fe, Co, Ni and Cu) was applied, which resulted in the complete integration of the metal atoms as atomically-dispersed $MN_x$ moieties in the N-doped carbon matrix derived from the MOF, without formation of metallic particles. Diversity of these ligand pockets changes with a different type of synthesis depending on the reaction precursors and conditions. In addition, in Chapter 5 Ni saturated and unsaturated N-doped materials are investigated, where Ni-N coordination number can be tuned by changing pyrolysis temperatures in which different atomically dispersed Ni catalysts with different $NiN_x$ numbers can be selectively prepared at 923 and 1223°C. Once the metal is embedded in to saturated and unsaturated N-doped cavities these single atoms can present different metal oxidation states depending on the cavity nature. Nickel Nitrogen Car-

bon (NiNC) single-atom catalyst exhibits the highest efficiency for producing CO, at different potentials.[121,125–137] Molecular catalyst with a well-defined metal coordination counts as another type of SACs. Organometallic complexes can be anchored either covalently or non-covalently to the support. Macrocyclic ligands can be divided into different classes, such as phthalocyanine, porphyrin, cyclam, and so on. A number of transition-metal complexes have been utilized as electron-transfer mediators to achieve electrochemical reduction of $CO_2$.[20,138–145] In Chapter 6 a model of Cobalt(II)-tetraphenyl porphine (CoTPP) complex deposited on the multiwalled carbon nanotube (MWCNT) is constructed along whit Cobalt(II)-phthalocyanine (CoPc) anchored to carbon nanotube (CNT).

## 3.3 Basic concept of crystal field theory

Single site carbon materials, which contain homogeneous-like defects, namely $MN_x$ centers, resemble coordination compounds. The d-block metal (Mn, Fe, Co, Ni, Cu, and Zn) complexes can be described by bonding theories that rationalize experimental facts such as electronic spectra and magnetic properties. Once the geometry of the catalyst is determined (see section d-block geometries), computed magnetic data, particularly magnetization of embedded metal atom in SACs material, is used to determine unpaired electrons, where coupled with crystal field theory oxidation state of the metal atom is established. Continuing with the description of bonding in d-block metal complexes can be described with applications of valence bond theory, the electrostatic model and molecular orbital (MO) theory. However valence bond theory may rationalize stereochemical and magnetic properties, but only at a simplistic level. Furthermore, the model implies a distinction between high- and low-spin complexes that is actually misleading and it cannot tell us why certain ligands are associated with those formation. Molecular orbital and the electrostatic model concept differentiated once we move to complexes with ML $\pi$-bonding.

Therefore I used a second approach, the crystal field theory,[146,147] which describes the bonding in coordination compounds of d-block metals. It is an electrostatic model and uses the electrons from the ligands to create an electric field around the metal centre. Ligands are considered as point charges and there are no metal-ligand covalent interactions. This may lead to a change in magnetic properties as well as color. Hybridization schemes are explained for octahedral, square planar, square pyramidal, and trigonal planar geometries, where applications of these hybridization schemes that can be used to describe the bonding in d-block metal complexes. The shapes of the molecular orbitals may be obtained without difficulty from the shapes of the fragment orbitals. Given the greater electronegativity of the ligands, the bonding MOs are more concentrated on them, whereas the antibonding MOs are more concentrated on the metal. Among them, seven involve contributions from the metal d orbitals: the two bonding MO $1e_g$, the three nonbonding $t_{2g}$ MO and the two

antibonding MO $2e_g$. The term 'd block' of an octahedral complex (and also for other types of complexes) is used to refer to the five molecular orbitals that are mainly concentrated on the d orbitals of the metal. The three nonbonding MO of $t_{2g}$ symmetry clearly belong to the d block, since they are formed from pure d orbitals (xy, xz, and yz). For the MO of $e_g$ symmetry, the bonding combinations ($1e_g$) are mainly concentrated on the ligands while the largest coefficient for the antibonding combinations ($2e_g$) is on the metal.

### 3.3.1 d-block geometries

An isolated metal atom has five d orbitals with the same energy. In **octahedral complex** the five fold degeneracy of the d orbitals is lifted, to give three nonbonding degenerate ($t_{2g}$) MO and two antibonding degenerate MO ($e_g$). The three nonbonding orbitals are then xy, xz, and yz, and the two antibonding orbitals are $x^2$-$y^2$ and $z^2$ (see Figure 3.3a). The energy separation ($\Delta^0$) between the $t_{2g}$ orbitals and the $e_g$ orbitals depends on the strength of the $\sigma$ interactions between the metal and the ligands. The value of this energy gap allows us to distinguish, in the family of octahedral complexes, strong field (large $\Delta^0$) from weak-field complexes (small $\Delta^0$). Measurement of the energies of d-d transitions allows us to estimate the value of $\Delta^0$ in a large number of complexes, and to establish a spectrochemical series, in which the ligands are ranked according to the strength of the field (value of $\Delta^0$) that they create:
$I^- < Br^- < Cl^- < F^- < OH^- < O^{2-} < H_2O < NH_3 < NO_2^- < CH_3^- < C_6H_5^- < CN^- < CO$
Organometallic complexes, which contain one or several metal-carbon bonds, are thus strong-field complexes.

One can therefore consider, at least formally, that a **square-planar complex** is formed by removing two ligands from an octahedral complex, for example, those situated on the z-axis (see Figure 3.3b). To establish the structure of the d block, it is convenient to start from the results already obtained for octahedral complexes. Notice that while the three nonbonding orbitals xy, xz, and yz are degenerate from the energetic point of view, only two of them (xz and yz) are degenerate by symmetry. The main difference between the d blocks of octahedral and square planar complexes concerns the number of nonbonding or weakly antibonding orbitals: there are three in the former but four in the latter.

A complex which adopts a **square-based pyramidal** geometry, four ligands are located at the corners of a square which is the base of the pyramid, while the fifth ligand, or apical, is placed on the summit of the pyramid (see Figure 3.3c). In the octahedral complex, the coefficients of the xy, xz, yz, and $x^2$-$y^2$ orbitals are zero for the ligands located on the z-axis. The removal of one of these ligands therefore makes no change to the shape or energy of these four orbitals: in the d block of the square-based pyramidal complex, we therefore find that the three orbitals xy, xz, and yz are nonbonding, while $x^2$-$y^2$ is a strongly antibonding orbital. This result is just the same as that found when studying the square-planar geometry as a derivative of the octahedron.

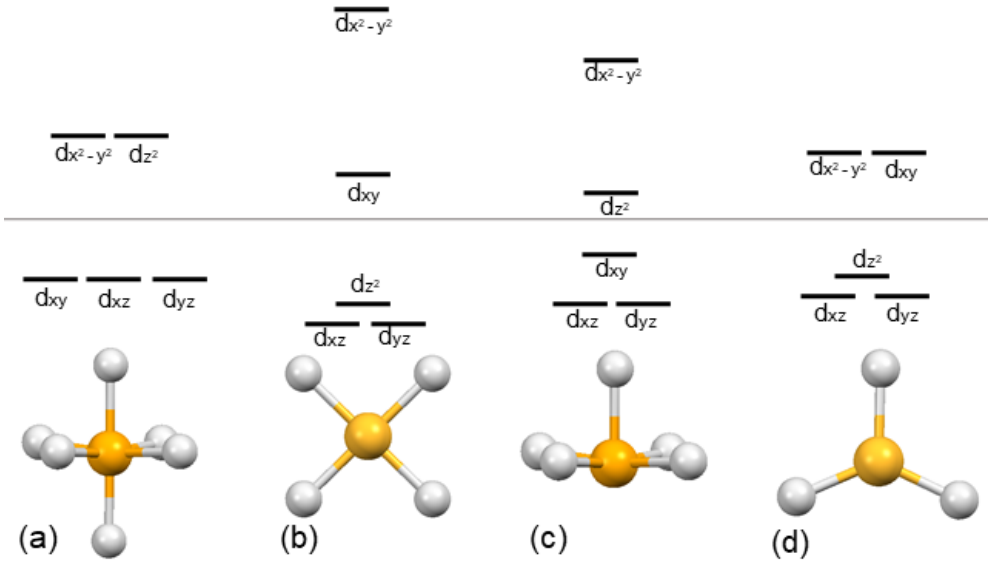


**Figure 3.3:** Derivation of the orbitals of the d block for (a) octahedral (b) square planar (c) square-based pyramidal and (d) trigonal-planar configurations. Gray line shows center of gravity. Ligands are represented with white spheres, and metal with yellow sphere.

The $z^2$ orbital is stabilized by the elimination of one of the two antibonding interactions with the ligands placed on the z-axis. But this stabilization is not as large as that observed when passing from an octahedral to a square-planar complex, since in this latter case, both the antibonding interactions along the z-axis are removed.

A **trigonal-planar** complex can be formed by removing the two axial ligands from a trigonal-bipyramidal complex. The d-block orbitals may therefore be readily deduced from those established in the preceding section. The variations in energy for the five d orbitals are shown in Figure 3.3d. The xz and yz orbitals of a trigonal-bipyramidal complex have zero coefficients on the axial ligands, as do xy and $x^2$-$y^2$. The removal of these two ligands does therefore not change either the shapes or the energies of these four orbitals. But the $z^2$ orbital, which was strongly antibonding due to interactions with the axial ligands, is substantially stabilized by their removal, becoming almost nonbonding. Only three weak antibonding interactions with the ligands in the xy plane are left, and the amplitude of the $z^2$ orbital in this plane is small. The d-block for trigonal-planar geometry thus contains two nonbonding degenerate orbitals (xz and yz), a very weakly antibonding orbital ($z^2$), and two weakly antibonding degenerate orbitals (xy and $x^2$-$y^2$). These five orbitals are sufficiently low in energy to be doubly occupied.

# Chapter 4

# Volcano trend in electrocatalytic $CO_2$ reduction activity over atomically dispersed metal-sites on Nitrogen-doped carbon

In this project, theoretical and experimental results are joint to explain electrochemical carbon dioxide reduction reaction trends for Metal-Nitrogen-Carbon (M-N-C) like catalyst. High-throughput computing for series of atomically dispersed moieties $MN_x$ (M = Mn, Fe, Co, Ni, and Cu) were performed. In order to model oxidation states of metal atoms ligands such as $H_2O$, OH, and O were added. Computational models then led to the identification of $M^{2+}N_4$-$H_2O$ as the most active centers in FeNC and CoNC, whereas $Ni^{1+}N_4$ was predicted as the most active one in NiNC at the experimental potentials of -0.5 and -0.6 V versus the reversible hydrogen electrode. The experimental activity and selectivity could be rationalized from DFT results, identifying in particular the difference between the binding energies for $^*CO_2^-$ and $^*H$ as a descriptor of selectivity toward CO. This work has been published in the Paper I and the optimized structures can be retrieved from ioChem-BD link (https://doi.org/10.19061/iochem-bd-1-115).

## 4.1 Methodology

### 4.1.1 Computational details

The valence electrons were expanded by plane waves basis sets with a kinetic energy cut-off of 500 eV. To model atomically-dispersed $MN_x$ carbon structures, we used graphene layer expanded in a (6×6) supercell replacing four C atoms by nitrogens and removing two C atoms to compensate for the valence. These layers were interleaved by 12 Å vacuum along the Z direction. Various transition metal atoms (M = Mn, Fe, Co, Ni, Cu, Zn) where placed in the cavity left on the carbon sheet. In this configuration, two axial positions are empty. However, most of these atoms prefer octahedral coordinations, and thus ligands (L = none, $H_2O$, OH, O) typically occupy one of the axial positions in aqueous electrolyte, see Figure 4.1. The empty coordination site is then employed to investigate the $eCO_2RR$ and competitive HER. Structures were relaxed with a force threshold of 0.05 eV/Å. The Brillouin zone was sampled using a 3×3×1 k-point mesh generated with the Monkhorst–Pack method.[55] The speciation of the different oxidation states of the metals in the carbon lattice was performed via a Pourbaix diagram derived with Phonopy.[148] The computed extended X-ray absorption fine structure (EXAFS) of MNC models were obtained with Demeter software.[149]

## 4.2 Structural characterization

The Metal-Nitrogen-Carbon (MNC) materials were characterized by different experimental techniques. Multiple areas of the samples were examined, and no metallic particles could be observed. To confirm experimental findings I modelled MNC catalyst, where the single metal atom (M = Mn, Fe, Co, Ni, Cu, and (Zn)) is coordinated with four pyridinic nitrogen atoms, and the ligands (L = none, $H_2O$, OH, O) were used (see Figure 4.1). The (Zn)NC catalyst was used as a control sample and it was synthesized according to used synthesis process, except that no separate metal acetate was added. The models for $ZnN_{-4}$- species did not present low binding energies of $eCO_2RR$ intermediates. Extended X-ray absorption fine structure spectra were fitted with in-plane $MN_4$ structures, with an axial oxygen atom needed to obtain a best-fit only for FeNC, and obtained results were confirmed with computed EXAFS (see Figure 4.2). The metal-nitrogen bond distance and K-edge EXAFS spectra were also calculated ab initio for $MN_4C$ model sites (10 in-plane carbon atoms in the second coordination sphere) in graphene sheets, with or without axial oxygen adsorbate. Considering water coordination via O atom, $MnN_4$ (2.40 Å), $FeN_4$ (2.33 Å), $CoN_4$ (2.31 Å) and $(Zn)N_4$ (2.35 Å) exhibited similar M-O bond distance between 2.31-2.40 Å. No water could be stabilized on the $CuN_4$ and $NiN_4$ models. The DFT-calculated EXAFS spectra shown in Figure 4.2 have characteristic features analogous to those of the experimental FT-EXAFS spectra with a main peak assigned to N or O back-scattering from the first coordination sphere.

The calculated and experimental M-N distances are also in good agreement, except for Fe, for which the EXAFS fitting is complicated by the presence of axial oxygen ligands (see Table 4.1).

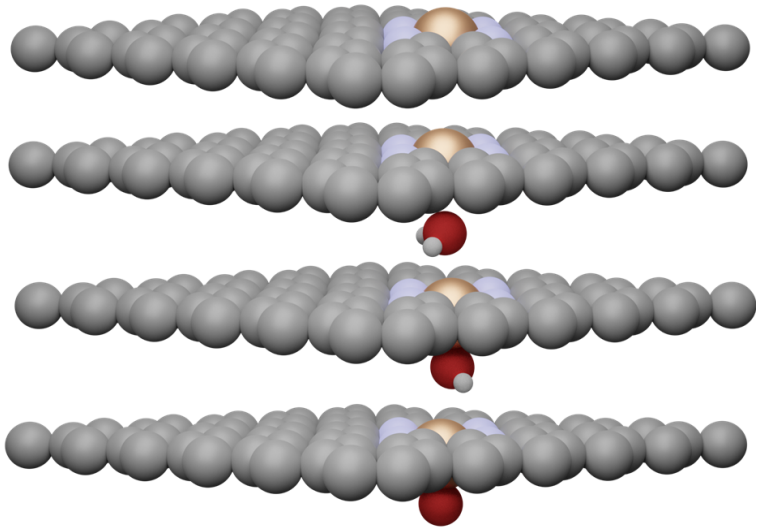

**Figure 4.1: Computational models** for the atomically-dispersed $MN_4$ sites, and when axial ligand is present (L = $H_2O$, OH, O). C is represented by grey spheres, N by purple, the metal in gold, O in red and H in white.

**Table 4.1:** Structural parameters obtained from the analysis with $MN_x$ moieties of the metal K-edge EXAFS spectra and DFT calculations. Errors are given in brackets (1.89(1) means 1.88-1.90). CN stand for coordination number.

| | $\mathbf{R_{(M\text{-}N)}/Å}$ | **CN** | $\mathbf{R_{DFT(M\text{-}N)}/Å}$ | $\mathbf{CN_{DFT}}$ |
|---|---|---|---|---|
| **MnNC** | 1.89(1) | 4 | 1.91 | 4 |
| **FeNC** | 2.01(2) | 5/6 | 1.89 | 5 |
| **CoNC** | 1.96(2) | 3.8(6) | 1.89 | 4 |
| **NiNC** | 1.92(1) | 4.3(3) | 1.88 | 4 |
| **CuNC** | 1.94(1) | 3.9(3) | 1.93 | 4 |
| **ZnNC** | 2.00(1) | 4.1(4) | 1.96 | 4 |

The oxidation state of the atomically-dispersed metal centers before the reaction were investigated with X-ray photoelectron spectroscopy (XPS). They identify the coexistence of $M^{2+}$ and $M^{3+}$ species for FeNC, and the coexistence of $M^{1+}$ and $M^{2+}$ species for CuNC.[150,151] Only the 2+ oxidation state is observed in CoNC, NiNC and ZnNC, while for MnNC, the three different

oxidation states 2+, 3+ and 4+ seem to be present.[152–154] The existence of different oxidation states of the metal in a same catalyst reveals a structural and/or a topological heterogeneity of $MN_x$ moieties. For example, higher oxidation states of the metal cation might be triggered by oxygen ($O_2$, OH) adsorbates, which is possible only for $MN_x$ moieties located on the top surface, while those located in the bulk of the nitrogen-doped carbon matrix are not accessible. Chemical heterogeneity might also lead to different oxidation states for a same structure. For example, while an average $MN_4$ structure was identified from our EXAFS analysis for all materials except FeNC (with additional oxygen adsorbates on top of the $FeN_4$ site itself), EXAFS cannot distinguish between N, O and C atoms in the first coordination sphere, implying that e.g. $MN_2O_2$ moieties or any other combination with a total of 4 in-plane ligating atoms among C, N and/or O are also possible structural candidates from an EXAFS viewpoint. For MnNC in particular, the presence of high valence-state metal (4+) suggests that there might be some O atoms replacing N atoms in $MnN_4$ moieties even during the reaction. This will be re-discussed later.

## 4.3 Selectivity and activity towards $eCO_2RR$

Over all studied MNC catalyst CO was the major $eCO_2RR$ product produced, where the highest FEs were observed over the Fe-, Ni- and Mn-NC materials. High FEs have been reported previously for other FeNC[155–158] and NiNC[121,127,133,159,160] materials synthesized via different approaches but sharing a key common structural feature, namely the atomically dispersed $MN_x$ moieties. Also in agreement with other recently published results, the major product over CoNC is $H_2$.[124,157,161] On the contrary, high selectivity (more than 90%) toward CO in a wide potential range (-0.57 to -0.88 V vs. RHE) over atomically dispersed $CoN_x$ was reported as well[162,163] but with slightly different coordination environment. Since the present series of MNC and (Zn)NC catalysts has, except for the nature of the metal element in $MN_x$ moieties, negligible difference in morphology and structure, the different activity and selectivity toward $eCO_2RR$ to CO can be mainly ascribed to the nature of the metal in $MN_x$ sites. Last, (Zn)NC shows a selectivity for CO being in-between the low value of CoNC and the high values of MnNC, FeNC and NiNC. A catalytic synergy between $MN_x$ and $(Zn)N_4$ moieties is also unlikely when the main considered product of $CO_2$ reduction is CO. The process requires only a 2 electron transfer and the steps are stated in Chapter 2, section explanation of electrocatalytic reactions and trends for reaction steps.

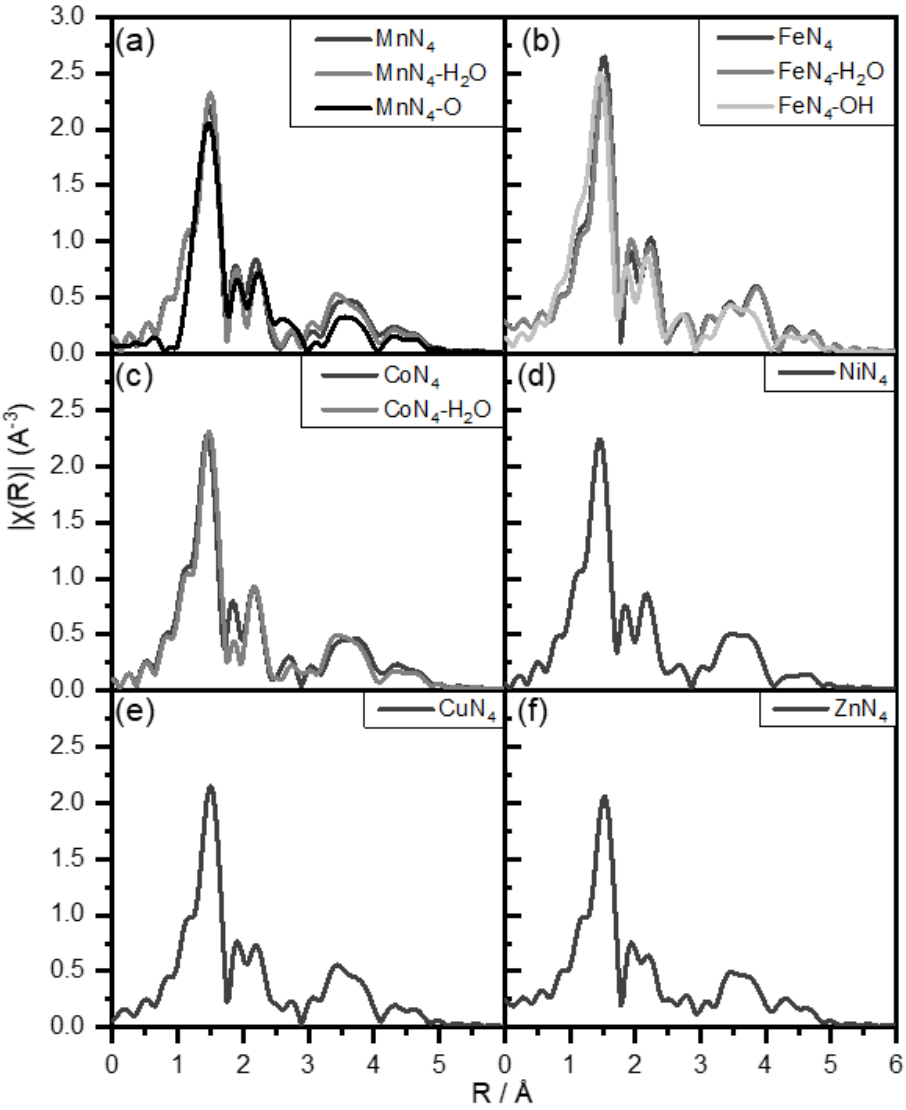


**Figure 4.2: Simulated metal K-edge EXAFS.** (a) MnNC, (b) FeNC, (c) CoNC, (d) NiNC, (e) CuNC, and (f) (Zn)NC. For Mn, Fe, and Co all the relevant computed structures are presented.

If a synergistic effect between $MN_x$ and $(Zn)N_4$ moieties occurs, there are two possibilities: a) $MN_x$ catalyzes step 1 ($* + CO_2 + H^+ + e^- \rightarrow *COOH$) and $(Zn)N_4$ catalyzes step 2 ($*COOH + H^+ + e^- \rightarrow *CO + H_2O$); or b) the opposite. Assuming the synergy case a), the FE for formate on FeNC, CoNC and NiNC should be significantly higher than that on (Zn)NC, which is not the case (Figure 4.3a). Assuming the synergy case b), (Zn)NC should have a $J_{HCOO^-}$ value comparable to $J_{CO}$ observed on the active catalysts NiNC, FeNC and CoNC. However, this is also in contrast with experimental results, where $J_{HCOO^-}$ on (Zn)NC being negligible compared to $J_{CO}$ on NiNC, FeNC and CoNC (Figure 4.3b). Thus, we can rule out any significant catalysis synergy between $MN_x$ and $(Zn)N_4$ moieties.

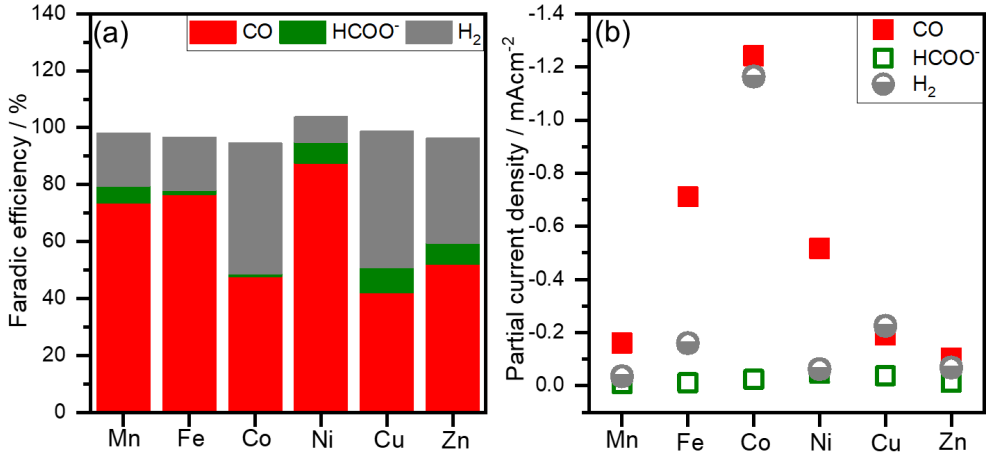


**Figure 4.3: Product analysis over the MNC catalysts (M = Mn, Fe, Co, Ni, and Cu)**, plotted against the embedded metal center sorted by the atomic number. (a) Faradaic efficiency and (b) partial current densities at -0.6 V vs. RHE for CO, $HCOO^-$ and $H_2$ products. The data were obtained by Chronoamperometry (CA) for 90 min, in 0.1 M $KHCO_3$ saturated with $CO_2$ (pH 6.7) at room temperature.

Operando X-ray absorption near edge structure (XANES) spectroscopy was employed to track possible changes in the oxidation state of $MN_x$ sites during $eCO_2RR$. The DFT simulations were performed on the most likely oxidation state and environment for each metal. Combined with the ex situ XPS, we can infer that the oxidation state of Fe was modified from 2+/3+ to only 2+, that of Ni reduced from 2+ to 1+, and that of Cu reduced from 2+/1+ to 0.[161,164] The oxidation state of Mn remained a mixture of 2+/3+/4+, and that of Co remained as 2+, even at -1.0 V vs. RHE. It can further be observed that Fe was reduced from a mix of 2+/3+ to only 2+ already at 0 V vs. RHE, in line with the redox potential identified for FeNC at ca 0.75 V vs. RHE in acidic electrolyte.[165,166] This may explain the high onset potential for $eCO_2RR$ over FeNC, while NiNC is possibly inactive for $eCO_2RR$ as long as it is in 2+ oxidation state. The changes in oxidation states of the three most active MNC catalysts (namely Fe, Co and Ni) with applied potential agree well with the calculated Pourbaix speciation diagrams (see Figure 4.4), which

show that in a pH 7 electrolyte, the oxidation state of Fe and Co in $MN_4$ corresponds to $M^{2+}$ at any potential 0 V vs. RHE, while there is a reduction from $Ni^{2+}$ to $Ni^{1+}$ below 0 V vs. RHE at pH 7, in line with the Ni-reduction experimentally observed between 0 and -0.5 V vs. RHE experimentally (see Figure 4.5).

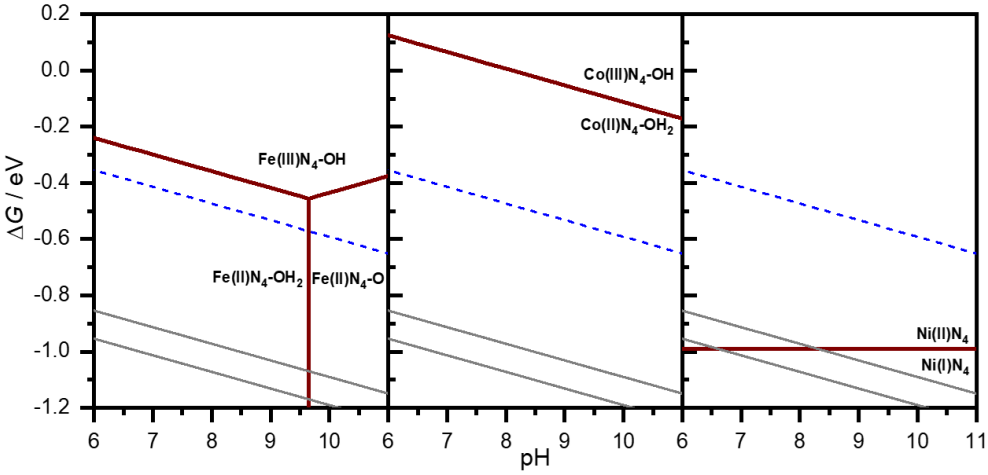


**Figure 4.4: Simulated Pourbaix diagrams.** Computed Pourbaix diagram for $FeN_4$-, $CoN_4$- and $NiN_4$- species. The blue lines corresponding to the water oxidation reactions, the wine red lines separate the different phases, and the area between two gray lines corresponds to the experimental potential window at which $eCO_2RR$ was evaluated (-0.5 and -0.6 V vs. RHE).

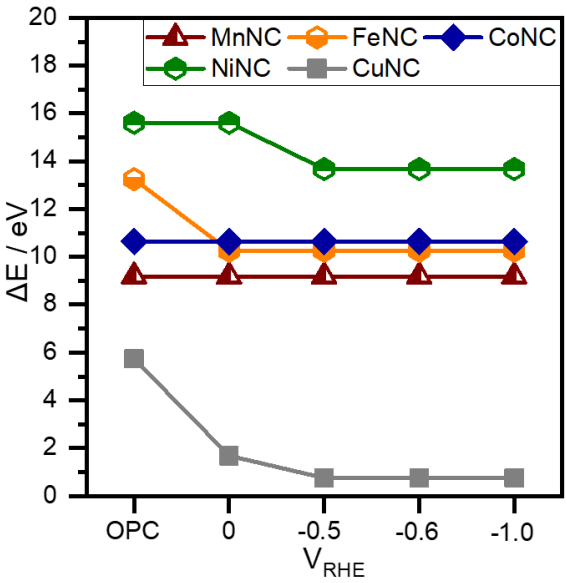


**Figure 4.5: Change in the absorption edge of metal K-edge XANES spectra of MNC catalysts with applied potential.** The electrolyte was $CO_2$-saturated 0.1 M $KHCO_3$, and the OCP was around 0.7 V vs. RHE. The x-axis is the difference between the X-ray energy and the absorption edge of MNC ($E_0$).

## 4.4 Explanation of observed volcano trends

The observation of volcano trends in the electrochemical activity reactions among a series of metal-based catalysts with similar site structures is generally explained by Sabatier's principle. With the binding energy of the metal sites being tuned by the metal's atomic number, and leading to too weak, optimum and too strong binding of the key intermediate adsorbed species when moving in a given direction in the series of transition metal.[167,168] We performed DFT calculations with $MN_4C$ model (M = Mn, Fe, Co, Ni and Cu, with axial oxygen adsorbates for all the metals) with the CHE model at -0.6 V vs. RHE. The reaction energy profiles for each elementary step of $eCO_2RR$ show that the particular transition metal present in the $N_4$ lattice has a tremendous effect on reactivity. I will focus on the Gibbs free energy diagrams at -0.6 vs. RHE (Figure 4.6a and 4.7), potential at which the $eCO_2RR$ activity and selectivity of MNC catalysts are experimentally measured. Overall, the calculated Gibbs free energy diagrams demonstrate that $MnN_4C$ and $FeN_4C$ bind CO too strongly and their CO production rate is determined by the *CO desorption step. In contrast, $NiN_4C$ and $CuN_4C$ have weak CO binding energy, and the $CO_2$ activation and first electron transfer then becomes the RDS (Table 4.2). In this series of model sites, $CoN_4$ shows the optimum balance between the energy barriers for $CO_2$ activation and CO desorption (steps 1 and 4 (desorption) in Table 4.2, respectively).

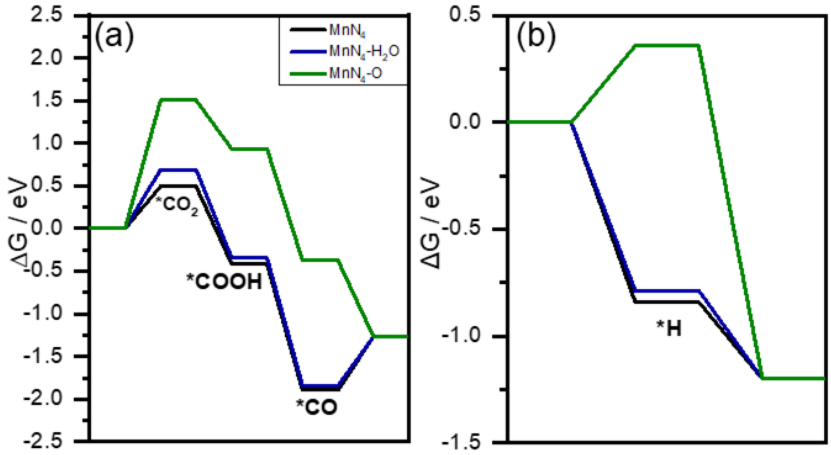


**Figure 4.6: Gibbs free energy profile over $MnN_4$- model** for (a) $eCO_2RR$ and (b) HER at -0.6 V vs. RHE (pH 7) according to the different oxidation state and ligand coordination.

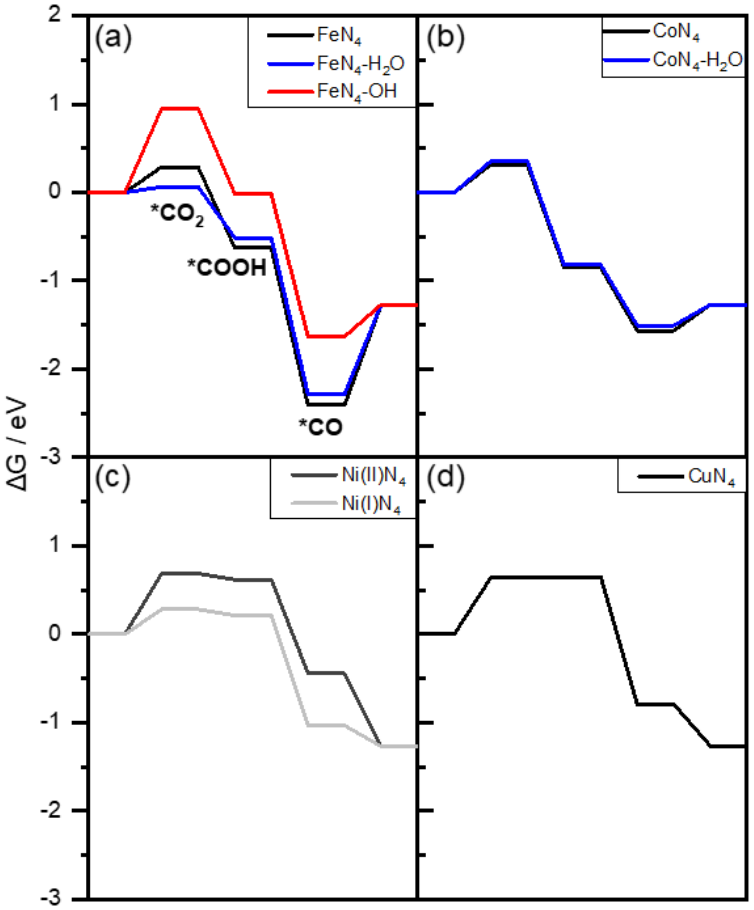


**Figure 4.7: Gibbs free energy profiles for $eCO_2RR$** over (a) $FeN_4$-, (b) $CoN_4$-, (c) $NiN_4$-, and (d) $CuN_4$ model sites at -0.6 V vs. RHE (pH 7) according to the different oxidation state and ligand coordination.

We have also investigated how axial adsorbates ($H_2O$, OH and O) affect the reaction energies on $MnN_4$, $FeN_4$ and $CoN_4$ (no oxygen adsorbates could be stabilized on $CuN_4$ and $NiN_4$). Particularly, the $H_2O$ molecule axially adsorbed on $FeN_4$ lowers the reaction barrier for the first electron transfer to form $^*CO_2^-$ (Figure 4.7a) and thus promotes the $eCO_2RR$ to CO over FeNC. In this case, $FeN_4$ sites are approachable from both axial directions (one side for adsorbing $H_2O$, while the other side for activating $CO_2$ gas molecule). Moreover, for the case of NiNC, $NiN_4C$ with oxidation states of 1+ and 2+ are both used in the DFT simulations, since a reduction of $Ni^{2+}$ to $Ni^{1+}$ was observed from operando X-ray absorption spectroscopy (XAS) (Figure 4.5). In contrast to the high energy barrier for the $CO_2$ activation on $Ni^{2+}N_4C$ (the first step for $eCO_2RR$), $Ni^{1+}N_4C$ binds $CO_2$ more strongly (Figure 4.7c). This explains that the onset potential of $eCO_2RR$ over NiNC is highly correlated to the $Ni^{2+/1+}N_4$ redox potential (Figure 4.5). The $CO_2$ activation energies are also highly correlated to the geometries of the $CO_2$ coordination over $MN_4$ sites, as depicted in Figure 4.8 showing how $CO_2$ is activated in the Fe, Co and

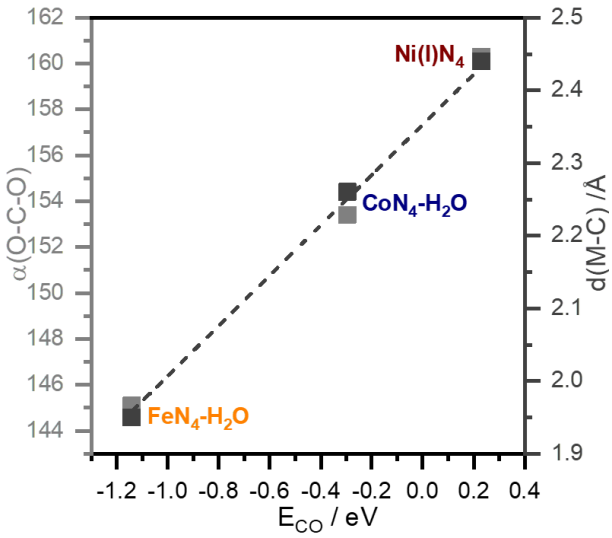


**Figure 4.8: Linear scaling relation.** Linear angle $\alpha$(O-C-O) and distances d(M-C) of $CO_2$ scaling relations for adsorption of CO molecule. Fe presents an $\eta^2$-C,O hapticity, while Co and Ni prefer the $\eta^1$-C configuration.

Ni sites. While both a M-C and a M-O bond can simultaneously form with the $FeN_4$ active site, only a M-C bond appears for the $CoN_4$ and $NiN_4$ sites. In addition, the O-C-O angle departs from the 180° value in the gas phase to only 145° when adsorbed on $FeN_4$-$H_2O$. This explains the lower activation energy of $CO_2$ over FeNC vs. other MNC catalysts and the higher onset potential for FeNC. The activity trends for $CO_2$ reduction to CO can be estimated from DFT calculations on the basis of the exergonic value of the reaction energy at the RDS. Table 4.2 reports the reaction energy calculated for each elementary step for $MN_4$(-$H_2O$) moieties according to the Gibbs free energy profiles for e$CO_2$RR over MNC catalysts (M = Mn, Fe, Co, Ni and Cu) at -0.6 V vs. RHE. For each $MN_4$ site, the structure (with/without $H_2O$ adsorbate) with lowest reaction energy at the RDS is considered in Table 4.2. To compare DFT results to the experimental e$CO_2$RR activity trend, we assumed an Arrhenius type law of the form $Aexp^{(-E_{RDS}/RT)}$, where $E_{RDS}$ is the free energy change at the RDS and A is a pre-exponential factor, assumed the same for all MNC catalysts investigated due to similar metal content and similar carbon porosity, chemistry and morphology.

**Table 4.2:** Gibbs free energies at -0.6 V vs. RHE for the elementary steps of $eCO_2RR$ to CO. The RDS values correspond to energies corrected by CO and $CO_2$ gas entropies. All metal cations in 2+ oxidation state unless otherwise indicated. $FeN_4$-$H_2O$ with a high spin state (S=2) is used

| | **Step 1** | **Step 2** | **Step 3** | **Step 4** | **RDS** |
|---|---|---|---|---|---|
| **$MnN_4$** | 0.49 | -0.91 | -1.48 | 0.63 | 0.63 |
| **$MnN_4$-O** | 1.51 | -0.57 | -1.31 | -0.81 | 1.51 |
| **$FeN_4$-$H_2O$** | 0.06 | -0.58 | -1.77 | 1.02 | 1.02 |
| **$CoN_4$-$H_2O$** | 0.36 | -1.17 | -0.69 | 0.24 | 0.36 |
| **$NiN_4$** | 0.68 | -0.07 | -1.06 | -0.83 | 0.68 |
| **Ni(I)$N_4$** | 0.28 | -0.07 | -1.25 | -0.24 | 0.28 |
| **$CuN_4$** | 0.64 | 0.01 | -1.44 | -0.48 | 0.64 |

Figure 4.9 shows that the trend of reaction rate predicted from DFT according to this approach matches well the experimentally observed volcano trend in the present work, except for $MnN_4$ and $CuN_4$. Among all the $MN_4$(-$H_2O$) active sites, $Ni^{1+}N_4$ is predicted to show the highest activity toward $eCO_2RR$ to CO, with lowest maximum for the free reaction energy at any of the elementary steps. However, the experimental oxidation states of $NiN_4$ sites are most likely in a mix of 1+/2+ at -0.6 V vs. RHE (see Figure 4.5). Thus, the experimental activity of NiNC should fall between those predicted for $Ni^{1+}N_4$ and $Ni^{2+}N_4$. Experimentally, the $eCO_2RR$ activity of NiNC is even lower than that estimated from DFT for $Ni^{2+}N_4$. We assign this to a lower onset potential for NiNC than for CoNC, but once the reaction has started, recent studies have shown that NiNC catalysts with single metal atom sites are the most active and selective MNC catalysts reported to date.[?,133,159,160,169] The calculated activity trends for $MN_4$ sites are as following $FeN_4$-$H_2O$ < $MnN_4$ < $CoN_4$-$H_2O$ < $Ni^{1+}N_4$ > $Ni^{2+}N_4$ ≈ $CuN_4$, with metals on the left hand-side of Co or Ni binding CO too strongly, and metals on the right hand-side binding $CO_2$ too weakly.

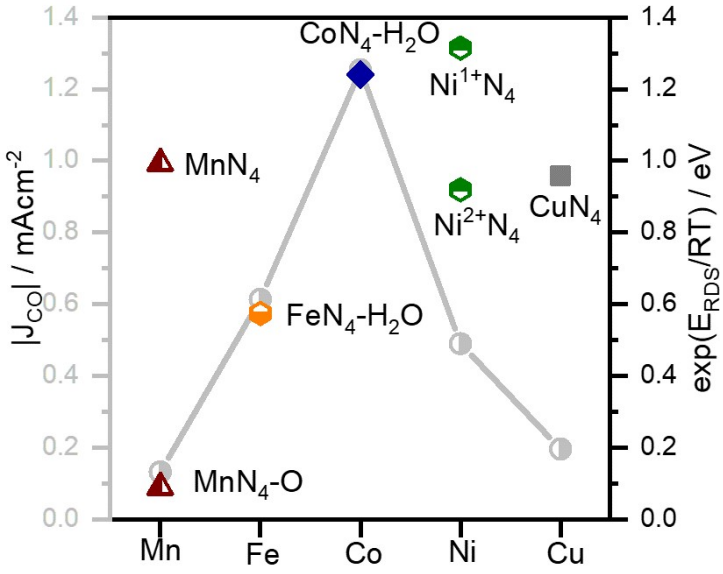


**Figure 4.9: Relation between theoretical and experimental data.** The comparison of CO partial current density at -0.6 V vs. RHE for pyrolyzed MNC materials and DFT calculated trends (at -0.6 V vs. RHE). $E_{RDS}$ is the calculated free reaction energy at the specific RDS of $eCO_2RR$ to CO for each active site (see Table 4.2).

One discrepancy between the experimental and theoretical results is MnNC, for which our experimental data show much lower CO partial current density than FeNC while the DFT calculations predicted that $MnN_4$ and $FeN_4$ sites are both limited by the *CO desorption step, but with lower desorption barrier for $MnN_4$. This results in a predicted $eCO_2RR$ activity higher for $MnN_4$ than $FeN_4$ moieties (Figure 4.9). Given that a higher oxidation state of Mn (a mixture of 4+, 3+ and 2+) was observed by ex situ XPS and operando XANES than can be assumed with a $MN_4$ model site, and given that $MnN_x$ has a higher predicted affinity to oxygen,[150] we re-evaluated the possible active site structure of MnNC. We assumed $MnN_2O_2$ as an alternative model site (Figure 4.10b). Both $MnN_4$ and $MnN_2O_2$ structures converged and optimized under the same conditions, confirming similar energy stabilities of these two structures. Moreover, the experimental FT-EXAFS spectrum of MnNC could be properly fitted with the $MnN_2O_2$ model site, and its DFT calculated EXAFS spectrum exhibits the same characteristic peak at 1.5 Å (Figure 4.10a) assigned to both N and O back-scattering from the first coordination sphere. According to our DFT calculations, this $MnN_2O_2$ model can not coordinate $CO_2$ and is therefore predicted to be inactive toward $eCO_2RR$. Even with a single oxygen adsorbate, the $MnN_4$ site becomes poorly active toward $eCO_2RR$, as indicated by the very high energy barrier for $CO_2$ adsorption for the $MnN_4$-O model (Figure 4.6a). Of all the Mn models investigated, only $Mn^{2+}$ without oxygen ligands can effectively coordinate $CO_2$. However, as identified by ex situ XPS and operando XANES (see Figure 4.5), this species is uncommon at the investigated potentials, explaining why

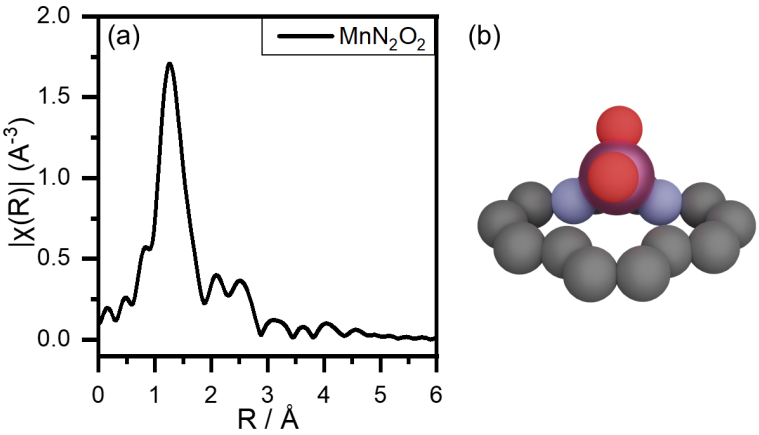


**Figure 4.10: $MnN_2O_2$ site.** (a) Computed simulated metal K-edge EXAFS spectrum and (b) computational model of $MnN_2O_2$ model site.

no activity is experimentally found for MnNC. Last, for CuNC, our operando XANES data show that Cu switches from 2+ to zero oxidation state early on (Figure 4.5), explaining the mismatch between DFT predictions and the experimental CuNC activity. In summary, with the $MnN_4$-O model site for MnNC and $MN_4$(-$H_2O$) model sites for other MNC catalysts (M = Fe, Co, Ni), the experimental volcano trend in the e$CO_2$RR to CO activity of MNC catalysts can be nicely explained by our DFT calculated Gibbs free energy for the RDS (Figure 4.9).

## 4.5 Selectivity toward CO over $MN_4$

As another critical factor for a good e$CO_2$RR catalyst, selectivity is highly correlated to the $^*H$ and $^*CO_2^-$ binding energies over $MN_x$ active sites. Thus, we investigated the Gibbs free energy profiles of HER over $MN_4C$ model sites (M = Mn, Fe, Co, Ni and Cu) at -0.6 V vs. RHE (Figure 4.6b and 4.11). These binding energies can be rationalized from simple coordination chemistry rules. The adsorption behaviour for the metals in the first transition series depends on the occupation of antibonding d-orbitals coming from the crystal field splitting for the resting square pyramidal structure. Therefore, we use the number of d-antibonding electrons (0 for $FeN_4$-$H_2O$, 1 for $CoN_4$-$H_2O$, 2 for $Ni^{1+}N_4$ and 3 for $Ni^{2+}N_4$) to explain the selectivity toward e$CO_2$RR to CO over $MN_4$ sites (Figure 4.12). The population of the antibonding states results from counting the number of electrons in the d-orbitals of the ground state configuration according to the crystal field splitting theory. Figure 4.12 indicates that there is a linear scaling relationship between the $^*CO_2^-$ and $^*CO$ binding energies, which determines the CO activity. Thus, the CO binding energy can serve as a key descriptor for e$CO_2$RR to CO activity.

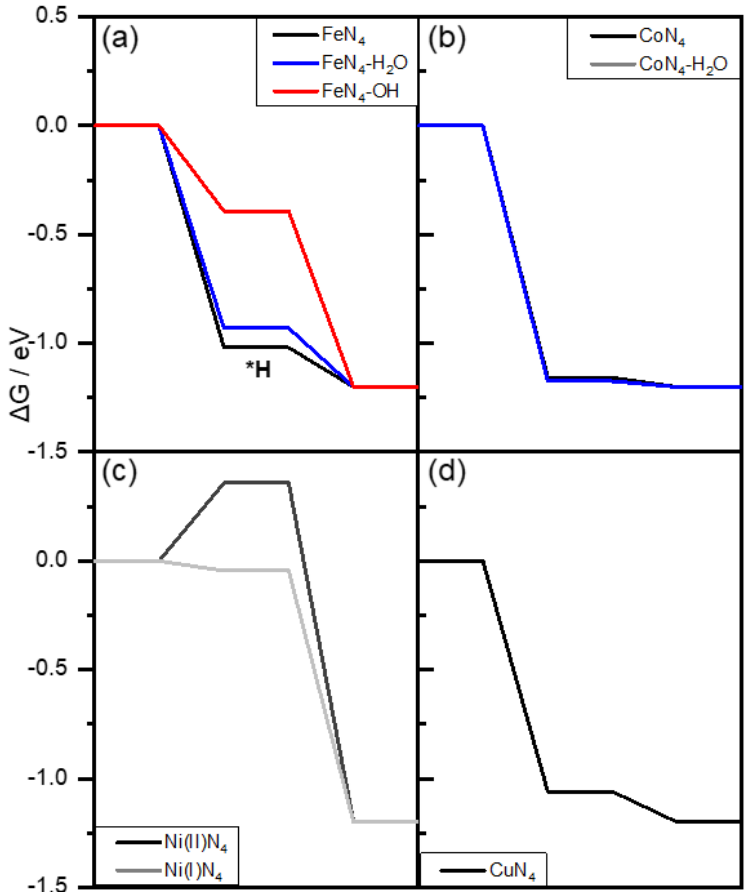


**Figure 4.11: Gibbs free energy profiles for HER** over (a) $FeN_4$-, (b) $CoN_4$-, (c) $NiN_4$-, and (d) $CuN_4$ model sites at -0.6 V vs. RHE (pH 7) according to the different oxidation state and ligand coordination.

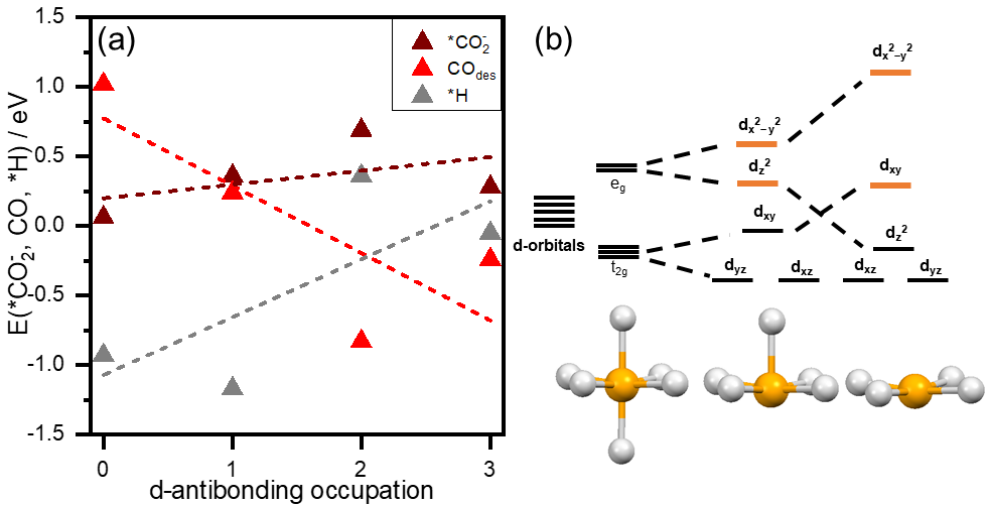


**Figure 4.12: Relationship between the adsorption/desorption energies and the local electronic configurations on the Fe, Co and Ni (1+ and 2+).** (a) $^*CO_2^-$(wine), $^*H$ (grey) adsorption energies and CO (red) desorption (at pH 7 and -0.6V) as a function of the d-antibonding occupation in the active site. In (b) the symmetry descent from the octahedral configuration to either square pyramid or square planar are shown (orange indicates the antibonding states). For the most common Fe species under potential Fe and Co are in $MN_4$-$H_2O$ (square pyramid with 0 and 1 antibonding electrons). Instead Ni is in the square planar configuration with already two electrons in the antibonding state. At high negative potential the highest antibonding $d_{x^2-y^2}$ would be occupied, which could trigger the distortion of the planar pocket ($Ni^{1+}$ state).

The volcano trend with CO binding energy as a descriptor ($J_{CO}$ measured experimentally vs CO binding energy calculated from DFT simulations) is shown in Figure 4.13, with Fe located at the strong binding branch, whereas Ni and Cu are on the weak binding branch. $CoN_4$-$H_2O$ sites possess the optimum binding energies with *CO, which are neither too strong nor too weak. On the other hand, good selectivity toward CO requires high $^*CO_2^-$ binding energy and low *H binding energy (the more negative value in Figure 4.12a, the higher the binding energy). Thus, we utilized the difference of $^*CO_2^-$ and *H binding energies (E($^*CO_2^-$)-E(*H)) as the descriptor for selectivity (Figure 4.14). In that figure, we show only the experimental data for $FeN_4$-$H_2O$, $Ni^{2+/1+}N_4$, and $CoN_4$-$H_2O$ and did not include the other MNC materials, whose $eCO_2RR$ activity and selectivity can originate in whole or in part from metal-free nitrogen functional groups.[170] The $CoN_4$-$H_2O$ site has an optimum binding energy with $^*CO_2^-$, but, unfortunately, the binding energy of *H is much higher than that of $^*CO_2^-$ which leads to a low selectivity toward CO, in line with the experimental result on CoNC (48%, Figure 4.14).

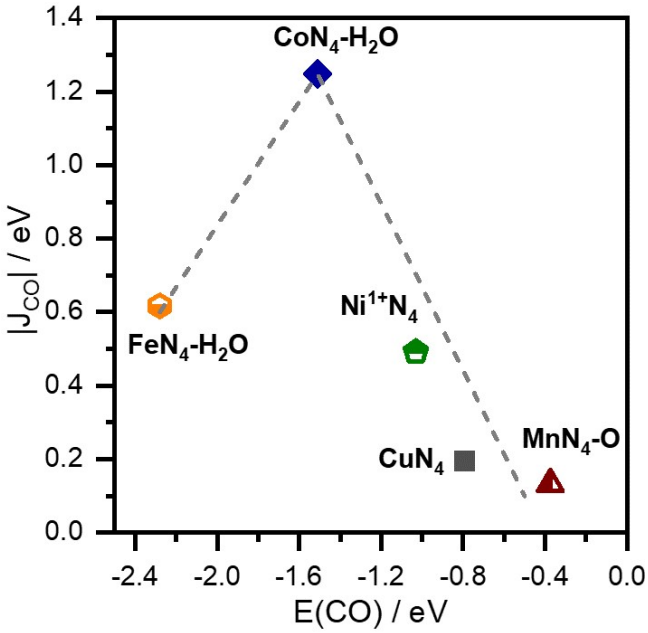


**Figure 4.13: Volcano plot** of CO partial current density at -0.6 V vs. RHE with CO binding energy obtained from DFT simulations as descriptor.

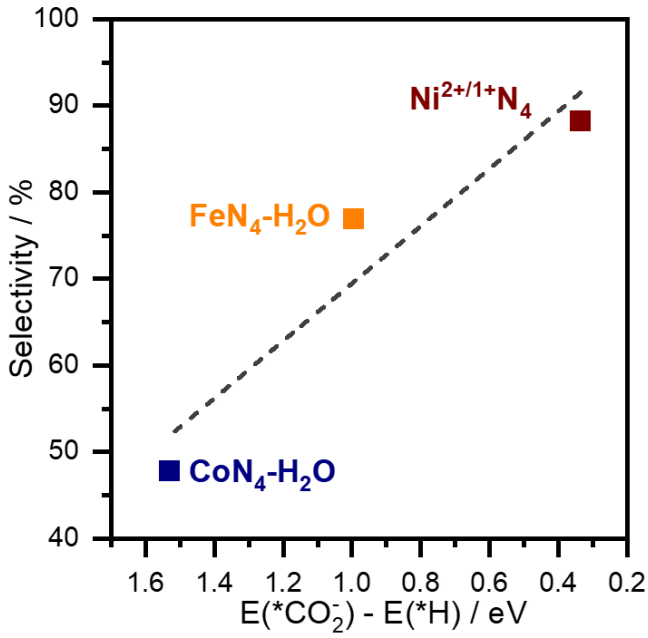


**Figure 4.14: Selectivity analysis**. The experimental selectivity at -0.6 V vs RHE over FeNC, CoNC, and NiNC vs. the DFT simulated E(*$CO_2^-$)-E(*H).

The high selectivity of e$CO_2$RR to CO over $NiN_4$ benefits from the lower *H binding energies compared to other metal $MN_4$ sites (Figure 4.14). For $FeN_4$-$H_2O$, even though the high binding energy to *H suggests a high HER activity (Figure 4.12), the reduction of $CO_2$ to *CO also occurs with zero energy barrier, and the binding energy of *CO on $FeN_4$-$H_2O$ is much stronger than that of *H on $FeN_4$-$H_2O$. Thus the majority of $FeN_4$ sites are occupied by *CO in $CO_2$-saturated electrolyte. This site-blocking effect probably supresses the binding of such active sites with HER related species, resulting in high experimental selectivity toward CO over FeNC. As can be seen in Figure 4.14, the selectivity of e$CO_2$RR toward CO over $MN_x$ moieties can be explained with the DFT-calculated *$CO_2^-$ and *H binding energies, that in turn are highly correlated to the number of d-antibonding electrons. The latter descriptor can thus be used to screen for more promising e$CO_2$RR candidate MNC materials.

## 4.6 Conclusions

We have employed Density Functional Theory to understand experimental results and establish clear correlations between physicochemical and catalytic properties for the $eCO_2RR$ of atomically-dispersed $MN_4$ centres (M = Mn, Fe, Co, Ni, and Cu). With computed Pourbaix diagrams we supported the ex situ XPS and in situ XANES results that were used to identify and monitor changes of the metal oxidation state at rest and under operating conditions, respectively. Mn and Co did not change oxidation state down to -1.0 V vs. RHE while Fe and Ni were partially reduced and Cu was largely reduced to metallic state. Over these highly controlled systems, catalytic tests revealed a volcano-like dependency between $eCO_2RR$ activity and the atomic number of the transition metal, with Fe and Co as the most active centres. Computational models led to the identification of active centres and finally to descriptors rationalizing the distinct activity and selectivity patterns observed. To this end, different configurations were studied according to the speciation of the metal atom, its charge, spin, and coordination sphere. Among the best performing materials, $Fe^{2+}N_4$-$H_2O$ and $Co^{2+}N_4$-$H_2O$ centres were found as the most likely active catalytic centres at considered potentials (-0.5 and -0.6 V vs. RHE), whereas $Ni^{1+}N_4$ was predicted as the most active Ni-based one. The Gibbs free energy change at the RDS accounted for the experimentally determined activity volcano, with Co-, Fe-, and Ni-based systems showing the best compromise between $^*CO$ and $*CO_2^-$ binding energies. Regarding selectivity, the difference between the binding energies for $^*CO_2^-$ and $^*H$, directly related to the number of d-antibonding electrons, described successfully the high selectivity observed on Fe- and Ni catalysts and the more favoured HER observed over the Co-based one.

# Chapter 5

# Stability and redispersion of Ni nanoparticles supported on N-doped carbons for the electrochemical $CO_2$ reduction

The Nickel-Nitrogen-Carbon (Ni-N-C) catalyst exhibits the highest efficiency for producing CO, at different potentials. The variation in the material synthesis produces defects with coordinatively saturated and unsaturated N-doped cavities, and once the metal is placed there these single atoms can present different metal oxidation states depending on the cavity nature. The research in this study was based on experimental findings from aricle[137]. We explored the possibility of Ni nanoparticle redispersion by $Ni(CO)_2$-like disintegration, when supported on saturated and unsaturated N-doped carbon materials. The binding energies of intermediates towards CO on seven different models ($NiN_4$, $NiN_3C$, $NiN_3$, $NiNC_3$, $NiNC_2$, $NiC_4$, $NiC_3$, Ni(100), Ni(111), and Ni(211)) were obtained from DFT taking the most stable conformations for each intermediate on each support. Besides nanoparticle shape was obtained from Ni(100), Ni(111), and Ni(211) facets. This work has been published in the Paper 2 and the optimized structures can be retrieved from ioChem-BD link (http://dx.doi.org/10.19061/iochem-bd-1-168).

## 5.1 Methodology

### 5.1.1 Computational details

This project is divided in two parts. The first part contains calculations of various N-doped carbon materials (see Figure 5.1), were the kinetic energy cut-off was set at 500 eV. N-doped carbon materials are represented with a graphene layer expanded in a (6×6) supercell and replacing carbon atoms by nitrogen atoms to design desired models. These layers were interleaved by 12 Å vacuum along the Z direction. A nickel atom was placed in the cavity left on the carbon sheet. Structures were relaxed with a force threshold of 0.050 eV/Å. The Brillouin zone was sampled using a (3×3×1) k-point mesh generated with the Monkhorst–Pack method.[171]

The second part focuses on Ni nanoparticles represented by three metal surfaces with the lowest Miller indexes Ni(100), Ni(111), and Ni(211). High quality surface energy calculations ((10×10×1) k-point mesh) were performed to build the nanoparticle structure using the Wulff model[172,173] with VESTA.[174] The vacuum between slabs was larger than 10 Å and the structures were relaxed with a force threshold of 0.025 eV/Å. They contained five layers, where the two uppermost were fully relaxed and the rest were fixed to the bulk structure.

CO can adsorb in very dense phases on Ni[175,176] thus different coverages were considered: from 1/12 to 1 ML for Ni(100) and Ni(211) and from 1/16 to 1 ML for Ni(111). The Brillouin zone was sampled using a (3×4×1), (3×3×1) and (5×3×1) k-point meshes for Ni(100), Ni(111) and Ni(211) respectively. The Wulff construction was also employed on the CO-dense phases to explain the restructuring of the nanoparticle. $Ni(CO)_x$ species can be formed in rich CO environments, which can then redisperse and reconstruct the Ni nanoparticle. The Ni(211) surface edge has enough space to accommodate more than one CO molecule, allowing the formation of $Ni(CO)_4$ complexes. We thus calculated the formation and elimination of $Ni(CO)_4$ with different CO coverages on that surface, where the elimination of this species forms a vacancy at the edge of the Ni(211) steps.

### 5.1.2 Ostwald disintegration formalism

We applied the energetic formalism from Ouyang and co-workers[177] to evaluate whether the disintegration of $Ni(CO)_x$ from Ni NPs is possible on N-doped carbon materials.

#### Energetics of Ni nanoparticle

To study this, we start from the energetics of a metal particle in the absence of reactants. Average energy $\Delta E_{NP}$ (per atom) with respect to infinite size particle (bulk) can be calculated by

$$\Delta E_{NP} = \frac{3\Omega\gamma}{R} \tag{5.1}$$

where $\Omega$ is the molar volume of bulk metal atom, $\gamma$ is the overall surface energy of the Ni nanoparticle, and R stands for radius of the nanoparticle. Considering that metal particles may expose different facets i with surface energy $\gamma_i$ and corresponding area ratio $f_i$ over the whole surface area, the overall surface energy $\gamma$ could be rewritten as:

$$\gamma = \sum_i f_i \times \gamma_i \tag{5.2}$$

The chemical potential $\Delta\mu_{NP}$ of the supported metal particle can be derived

$$\Delta\mu_{NP} = \frac{2\Omega\gamma}{R} \tag{5.3}$$

Under reaction conditions, CO may adsorb on the Ni particles, and corresponding Gibbs free energy of the adsorption would reduce the surface energy and stabilize the metal particles. The reduction of surface energy $\Delta\gamma_i$ on the facet i at given temperature T and partial pressure p can be calculated

$$\Delta\gamma_i(T,\, p) = \theta \times [E_{CO}(\theta) - \Delta\mu_{CO}(T,p)]/A_i \tag{5.4}$$

where $\theta$ and $A_i$ is the coverage of adsorbed CO and surface unit area of the facet i. $E_{CO}(\theta)$ is the average binding energy of CO and coverage dependent. The effective surface energy $\gamma'$ of supported metal particles with CO adsorbate becomes

$$\gamma'(T,\, p) = \sum_i f_i[\gamma_i + \Delta\gamma_i(T,\, p)]. \tag{5.5}$$

By substituting $\gamma_i$ in equation 5.1 and 5.3 average energetics $\Delta E'_{NP}$ and chemical potential $\Delta\mu'_{NP}$ of supported metal particles under reactants can be obtained, respectively.

### CO induces disintegration

Following the criteria of reactant induced dynamics, the stability of Ni nanoparticle can be explained by the Gibbs free energy of disintegration ($\Delta G^{dis}_{NP}$). First, we compute the formation energy of isolated metal adatom ($E^{f}_{Ni}$) with respect to Ni bulk reference supported on the different carbon defects by

$$E^{f}_{Ni} = E_{sur\text{-}Ni} - E_{sur} - E_{B} \tag{5.6}$$

where $E_{sur\text{-}Ni}$ is the energy of anchored Ni on the support, $E_{sur}$ is the energy of support, and $E_B$ is the energy of Ni bulk reference. From the results (see Table 5.1), we can see that formation energies are exothermic, as Ni atoms are anchored to a defect. Second, we calculate the energy of the Ni atom coordinated to the N-doped carbon substrate, where they should be able to form a chemical bond with the Ni atom, and corresponding binding energy $E^{f}_{nCO}$ must be negative.

$$E^{f}_{nCO} = E_{sur\text{-}nCO} - E_{sur\text{-}Ni} - n \times E_{CO} \tag{5.7}$$

**Table 5.1:** Formation Energy of Ni anchored atom ($E^{f}_{Ni}$) (with respect to Ni bulk energy), Binding Energy of CO on Ni atom ($E^{f}_{nCO}$), and Formation Energy of the Ni-CO complexes on the support with respect to the infinite size metal particle (CO in gas phase) ($E^{f}_{surf\text{-}nCO}$). All energies in eV.

| | $\mathbf{E^{f}_{Ni}}$ | $\mathbf{E^{f}_{1CO}}$ | $\mathbf{E^{f}_{surf\text{-}1CO}}$ | $\mathbf{E^{f}_{2CO}}$ | $\mathbf{E^{f}_{surf\text{-}2CO}}$ |
|---|---|---|---|---|---|
| $\mathbf{NiN_3}$ | -1.97 | -0.55 | -2.51 | -0.84 | -2.80 |
| $\mathbf{NiNC_2}$ | -2.71 | -0.89 | -3.60 | -1.33 | -4.04 |
| $\mathbf{NiC_3}$ | -3.51 | -0.72 | -4.23 | -0.84 | -4.35 |
| $\mathbf{NiC_3C}$ | -3.52 | 0.21 | -3.31 | 1.81 | -1.76 |
| $\mathbf{NiN_4}$ | -3.00 | 0.77 | -2.24 | 2.18 | -0.82 |
| $\mathbf{NiNC_3}$ | -3.25 | -0.38 | -3.62 | 1.04 | -2.20 |
| $\mathbf{NiC_4}$ | -1.69 | -0.45 | -2.14 | -0.12 | -1.81 |

where n is the number of CO molecules coordinated to the Ni adatom, $E_{sur\text{-}Ni}$ is the total energy of the Ni-CO complexes on support, $E_{sur\text{-}Ni}$ is the total energy of the Ni adatom on support, and $E_{CO}$ is the total energy of CO in gas phase. Furthermore we calculate Gibbs free energy for the CO-decorated nanoparticle, ($\Delta G^{dis}_{NP}$), following the equation:

$$\Delta G^{dis}_{NP}(R,\ T,\ p) = E^{f}_{surf\text{-}nCO} - nCO - n\Delta\mu_{CO}(T,\ p) - \Delta^{'}E_{NP}(R) - TS \quad (5.8)$$

where, $E^{f}_{surf\text{-}CO} = E^{f}_{nCO} + E^{f}_{Ni}$ is the formation energy of the Ni-CO complexes on support with respect to the infinite size metal particle and reactants in gas phase, and $\Delta\mu_{CO}(T,\ p)$ is the excess chemical potential of CO (T, p). In our case, the configurational entropy S was not included because the number of cavities is difficult to assess; however, it will favor dispersed species. Therefore, the values obtained here for the transition correspond to a maximum threshold. The excess chemical potential was set to $\Delta\mu_{CO}(T,\ p)$ = -0.76 eV[178] corresponding to experimental conditions of 300 K and 0.10 mbar. The binding energy of nCO ($E^{f}_{nCO}$) needs to be negative and lower than $\Delta\mu_{CO}(T,\ p)$ = -0.76 eV. When both requirements are fulfilled, nanoparticle disintegration is thermodynamically possible by realising $Ni(CO)_2$ complexes.

## 5.2 Types of N-doped carbon materials

We modelled saturated and unsaturated N-doped carbon materials under reaction conditions. The DFT simulations were performed on a number of N-doped defects where the Ni atoms can be anchored, as well as Ni nanoparticles can be supported, to represent the species characterized in experiments.[137] In the Figure 5.1 we show three families of models: (a) saturated N-doped carbon materials ($NiN_xC$) representing $NiN_4$ and similar undefined N-doped materials made at low doping temperature, (b) unsaturated N-doped ($NiNC_x$) and N-free materials ($NiC_x$) typically occurring for carbons at high doping temperatures, when the nitrogen content decreases, and (c) Ni metal surfaces composing the supported nanoparticles on the unsaturated N-doped supports (NiNP-$NC_x$). This approximation allows us to provide a holistic chain of models that accounts for the complexity of the N-doped carbon support and the metallic nature of the nanoparticle. The ultimate aim is to show the role of the speciation (charge, oxidation state, and coordination environment) on the electrochemical activity and on the dynamic behaviour or the different synthetic preparations.

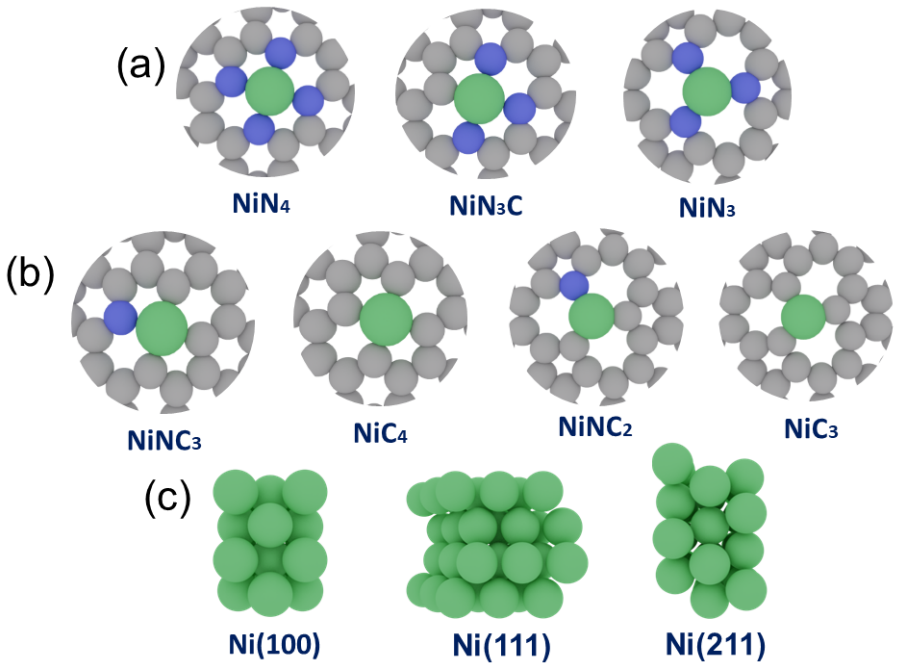


**Figure 5.1: Computational models for different systems.** (a) Saturated N-doped carbon material. (b) Unsaturated N-doped or N-free carbon material. (c) Metal surfaces. C in grey spheres, N in blue, and Ni in green.

## 5.3 Activity and selectivity of the materials

The activity and selectivity of the modelled catalysts can be discussed in terms of the corresponding Gibbs free energy profiles presented in Figure 5.2. The electrochemical activity was analyzed by calculating the binding energies of the intermediates according to the most agreed mechanism for $CO_2$ to CO reduction (see Chapter 2). Notice that once $CO_2$ is adsorbed, activated, and polarized with partial charge transfer (see Table 5.2) from the host material and thus step (i) does not correspond to any extra electron added to the simulation box. In agreement with the previous results, we can see that the highest activity towards CO is shown by unsaturated N-doped materials[125] and metal surfaces, as they bind CO strongly. Regarding the selectivity, it can be discussed by comparison to the competing HER (Figure 5.2d–f). Saturated N-doped materials reach the highest selectivity towards CO, where $NiN_4$ and $NiN_3$ are representative models, while $NiN_3C$ model binds $^*H$ strongly. Therefore, $NiN_3C$ model is ruled out, because it does not account for the experimental selectivity.[137]

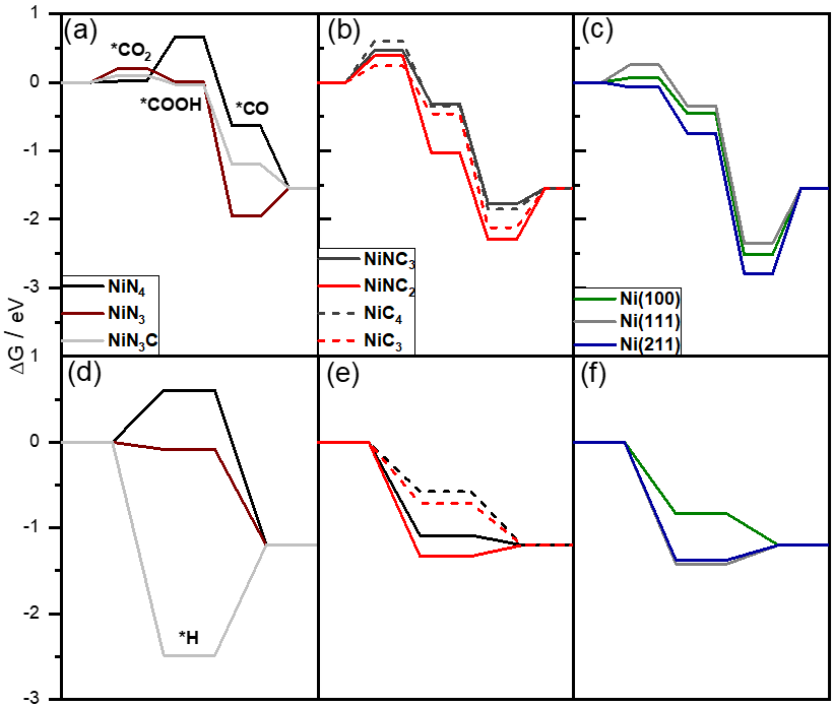


**Figure 5.2: Gibbs free energy profiles for (a, b, and c) eCO$_2$RR and (d, e, and f) HER over different model sites** at -0.6 V vs. RHE (pH 7). (a,d) Saturated nitrogen-doped carbon materials. (b,e) Unsaturated or free N-doped carbon materials. (c,f) Metal surfaces.

For a catalyst to be selective towards CO, the binding of *COOH and *CO$_2$ intermediates needs to be strong to reduce the onset potential. Also, selectivity can be compared with *H binding energy and CO desorption energy. The correlation between adsorption energies of *COOH and *H is shown in Figure 5.3. We can see that NiN$_4$ and NiN$_3$ bind *H weakly, therefore saturated N-doped materials are selective. NiN$_4$ binds *CO$_2$ and *COOH weakly, which means it has a higher onset potential, while the opposite trend is seen for NiN$_3$. The computed onset potentials are presented in Table 5.3, where NiN$_3$ has a lower onset potential than NiN$_4$ because it binds *COOH stronger. Ni(211) and NiNC$_2$ bind strongly *H and *COOH, which means they will not be selective toward CO. Ni(100) would be the best candidate among the metal surfaces as it binds *H weakly and *COOH relatively strongly.

**Table 5.2:** Bader charge of adsorbed $^*CO_2^-$ molecule on all computational model catalysts.

| | $\mathbf{q(CO_2)(\lvert e^- \rvert)}$ |
|---|---|
| **$NiN_4$** | -0.05 |
| **$NiN_3C$** | -0.08 |
| **$NiN_3$** | -0.11 |
| **$NiNC_3$** | -0.34 |
| **$NiC_4$** | -0.09 |
| **$NiNC_2$** | -0.08 |
| **$NiC_3$** | -0.27 |
| **Ni(100)** | -0.59 |
| **Ni(111)** | -0.55 |
| **Ni(211)** | -0.47 |

Figure 5.3b represents a correlation between adsorption energies of $^*CO_2$ and desorption of CO, where $CO_2$ activation can relate to Bader charges of the adsorbed $CO_2$ molecule (see Table 5.2). $NiN_3$, $NiNC_3$, and Ni(100) bind $^*CO_2$ relatively strong, where Ni(100) binds $^*CO$ strongly, which means the rate of CO formation would be low. The strong adsorption energy of $^*H$ for Ni(100) and $NiNC_3$ can be related to low selectivity, where HER and e$CO_2$RR compete. The most interesting systems is $NiN_3$, because of the optimal $^*CO$ binding and the weakly $^*H$ binding. From an electronic structure point of view, the Ni atom in the $NiN_4$ square planar confinement is in the $Ni^{2+}$ oxidation state, while that in the $NiN_3$ trigonal planar configuration is in the $Ni^{1+}$ oxidation state (see Chapter 3).

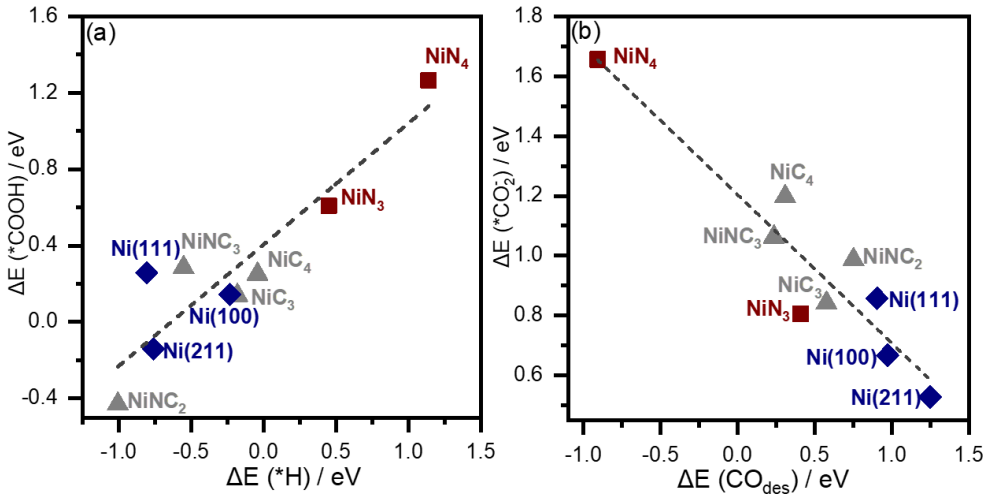


**Figure 5.3: Linear scaling relationship.** (a) Linear COOH binding energy scaling relations for adsorption of H atom. (b) $CO_2$ binding energy and corresponding linear-scaling relationships for desorption of CO molecule. Saturated N-doped carbon materials are represented with red symbols, unsaturated N-doped carbon materials with grey symbols, and metal surfaces with blue symbols.

This special role of $Ni^{1+}$ is long known in organometallic chemistry[179] and even in thermal catalysis.[180] The change in the oxidation state has an impact on the geometries of the activated $CO_2$ intermediate as both the O-C-O angle and Ni-C($CO_2$) distance indicate the degree of activation of the $CO_2$ molecule in the N-doped saturated materials. In Figure 5.4, the linear scaling relationship of $CO_2$ geometry and adsorption of *CO shows that the activation in $NiN_3$ correlates with medium binding of *CO, while the lowest activation appears in $NiN_4$ with a O-C-O angle of 170.2°. All these fingerprints point out to the relevance of understanding the organometallic structures when trying to identify the most suitable defects for a given metal and the importance of the charge state for the encapsulated metal ions.

**Table 5.3:** DFT calculated onset potentials (in eV vs. RHE) for $eCO_2RR$ to CO on N-doped carbon materials and Ni surfaces.

| | $U_{onset}$ |
|---|---|
| **$NiN_4$** | -1.27 |
| **$NiN_3C$** | -0.57 |
| **$NiN_3$** | -0.61 |
| **$NiNC_3$** | -0.29 |
| **$NiC_4$** | -0.31 |
| **$NiNC_2$** | -0.38 |
| **$NiC_3$** | -0.29 |
| **Ni(100)** | -0.49 |
| **Ni(111)** | -0.45 |
| **Ni(211)** | -0.63 |

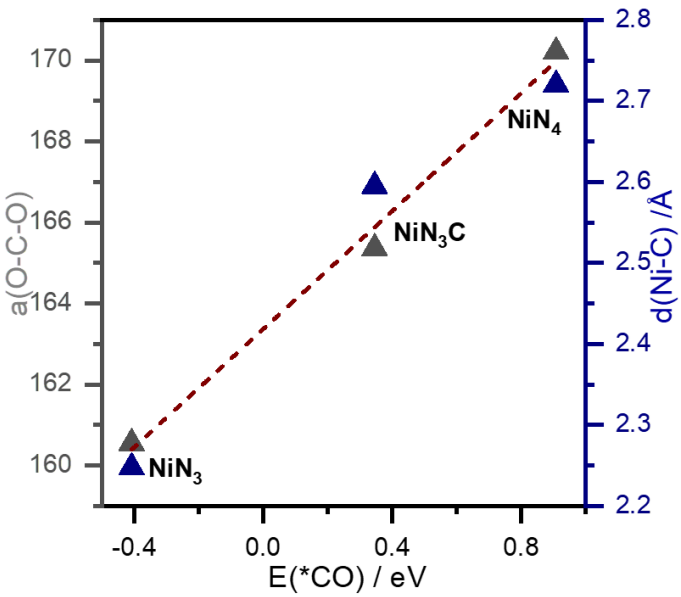


**Figure 5.4: Linear scaling relationship.** Linear angle $\alpha$(O-C-O) and distances d(Ni-C) of $CO_2$ scaling relations for adsorption of CO molecule.

## 5.4 Reconstruction of Ni NPs on N-doped carbon materials

Electrocatalysts can be affected by the presence of different variables. In our case, because of disintegration of $Ni(CO)_2$ complexes later the reconstruction of Ni NPs influences the activity and selectivity. Once the reconstruction happens experimentally, the partial current density of $H_2$ drastically drops compared to that of CO, thus favoring the disintegration process. Such dynamic behavior of electrocatalysts is crucial for their performance and thus we here address these aspects by simplified models. To investigate the role of the reaction products in the stability of the Ni NPs, we model a nanoparticle based on the lowest-energy surfaces through a Wulff construction. This is straightforward for metal nanoparticles and can be extended when adsorbates, like CO, are present.[175,181]In addition, we apply the atomistic version of Ostwald ripening theory[177,182] by the formation of $Ni(CO)_2$-like complexes to show when the disintegration of nanoparticles can occur on such N-doped carbon materials.

### 5.4.1 Nanoparticle shape

To address the role of nanoparticles we first focus on their structure. The size of the synthesized Ni NPs was 2.5 to 7 nm, and thus they can be represented via the Wulff construction that corresponds to the equilibrium structure for a medium-to-large nanoparticle and it is obtained from the surface energies. We calculated the surface energies for three orientations Ni(111), Ni(100), and Ni(211), and, employing the Wulff construction, we then extracted the corresponding areas for each facet (see Figure 5.5). The average surface energy for the nanoparticle is 0.126 eV/Å. In the Table 5.4 surface enrgies and ratios of coresponding facet are presnted. To assess the change in the nanoparticle induced by the environment, we consider CO adsorption on all three facets separately.[175] We calculated average binding energies $E^{'}_{CO}$, for a range of coverages 1/12 to 1 ML for Ni(100) and Ni(211) facets, and Ni(111) from 1/16 to 1 ML (Figure 5.6). In all cases, at low to medium coverages, all the modified surface energies ($\gamma^{'}_{x}$) are smaller, but the reduction in surface energies depends on the particular facet orientation. The detailed balance between adsorption sites and CO-CO repulsion contributes to the surface energy in a non-linear way, as to achieve higher CO densities the molecules need to go to less favourable sites. At 0.25 ML we are left with Ni(100) and Ni(111) surfaces, while at full coverage of 1 ML the extent of Ni(211) facet in the nanoparticle increases and Ni(111) reconstructs (see Appendix Chapter B).

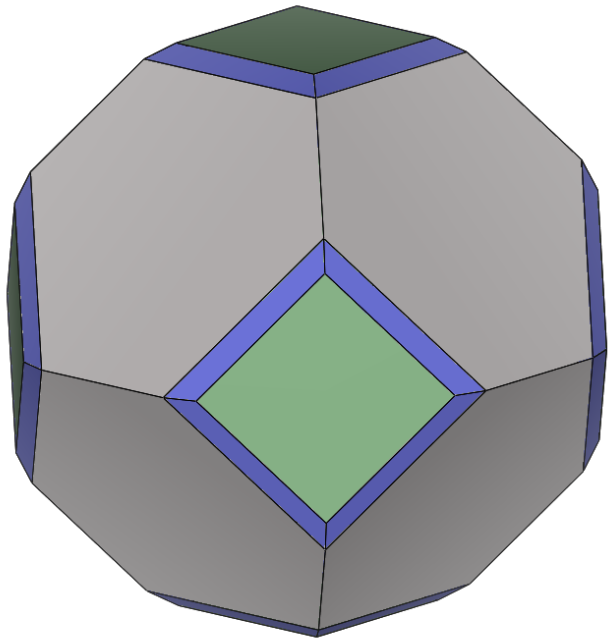

**Figure 5.5: Wulff construction** based on the surface energies calculated by DFT. Surface legend: Ni(100) in green, Ni(111) in gray, and Ni(211) in blue.

In summary, the average surface energy for the decorated nanoparticle ($\gamma^{'}$) at CO coverage 0.25 ML is 0.095 eV/Å$^2$, which is 0.031 eV/Å$^2$ less than for the bare one (see Appendix Chapter B). Therefore, the nanoparticle under product-rich conditions has more surface Ni atoms with less Ni-Ni average coordination.

**Table 5.4:** Calculated surface energies $\gamma_i$ (in eV/Å$^2$ ) of Ni nanoparticle and ratios $f_i$ (in %) of considered facets of infinite size Ni, based on Wulff construction.

| **Facet** | $\gamma_i$ | $f_i$ |
|---|---|---|
| **Ni(100)** | 0.139 | 18 |
| **Ni(111)** | 0.120 | 70 |
| **Ni(211)** | 0.138 | 12 |
| $\gamma^{'}$ **(T,P)** | 0.126 | |

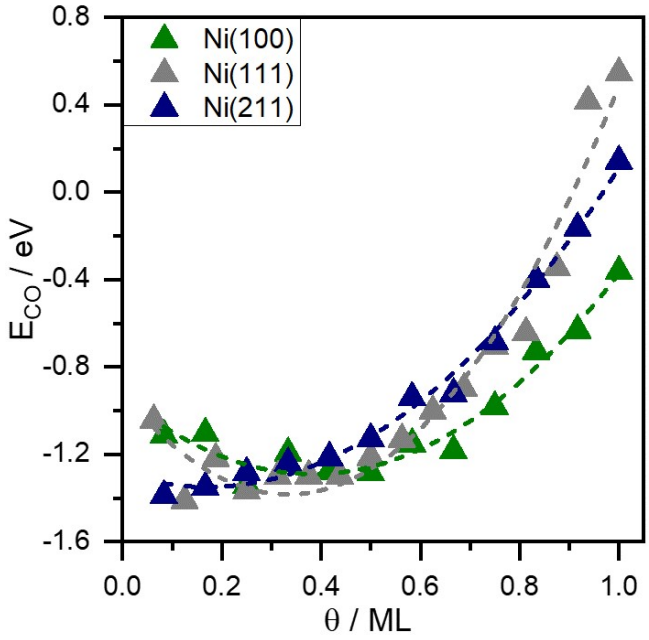


**Figure 5.6: The calculated average binding energy for a CO molecule** on the different Ni surfaces versus CO coverage. The DFT results are polynomial fitted.

In addition, this high product coverage influences the selectivity as it limits the HER reaction. The effect can be explained with the Gibbs free energies of the *H intermediate for the clean and on the CO covered ($\theta$ =0.92ML) Ni surfaces (see Figure 5.7). Once Ni surfaces are covered with CO, *H binds weaker (lowering the selectivity for HER), see Figure 5.8. This agrees with the experimental observations showing a drastic drop of $H_2$ partial current density. Thus, high CO coverage minimizes the HER path and increases selectivity.

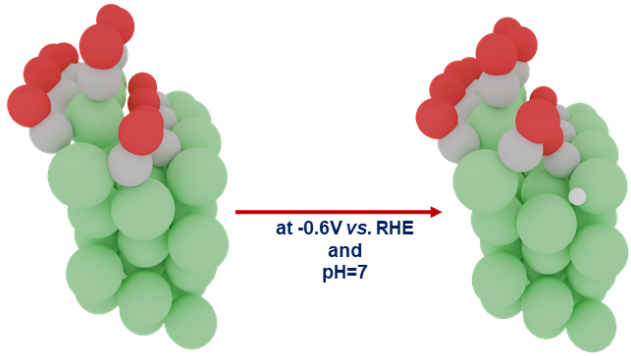


**Figure 5.7: Schematic representation of *H intermediate** on Ni(211) surface at 0.92 ML CO coverage.

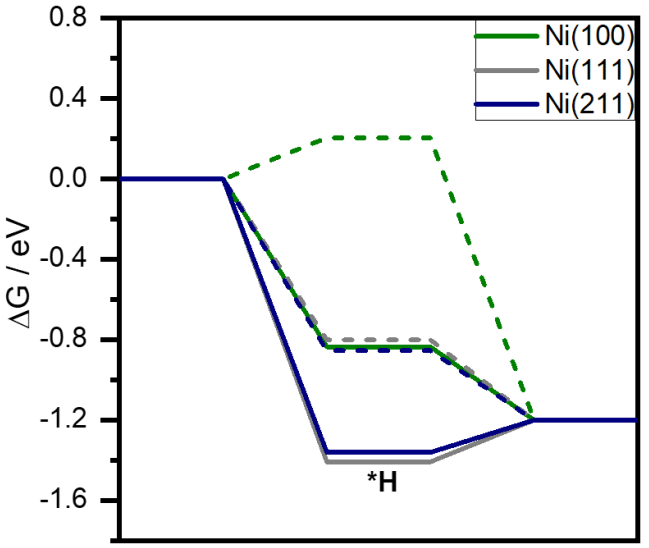


**Figure 5.8: Gibbs free energy profiles for HER over clean metal (solid lines) and 0.92 ML CO coverage (dashed lines) sites** at -0.6 V vs. RHE (pH 7).

### 5.4.2 Gibbs free energy of $Ni(CO)_2$ complexes disintegration on N doped carbon materials

We applied the energetic formalism (see the section Methodology) from Ouyang and co-workers[177] to evaluate whether the disintegration of $Ni(CO)_2$ from Ni NPs is possible on N-doped carbon materials. The nature of the cavities in the support provides a large versatility regarding the stability against disintegration. In our investigations, we have considered all 7 types of defects in Figure 5.1. The anchored Ni atom in saturated N-doped models is coordinated either to pyridinic or pyrrolic N atoms, which are strong ligands able to easily trap metal atoms. This is in line with experiments where they do not observe nanoparticles on those materials. We observe an opposite trend for the unsaturated N-doped materials, where Ni NPs can redisperse into single atom cavities. The reason for that is the decreased N-content and increased C-content in the materials, which makes Ni dynamic and prone to aggregate and disintegrate in the presence of dense CO phases and electrochemical condition. Therefore, single Ni metal atoms with little aggregation are expected in agreement with experiments.[128] Finally, we show that the redispersion of Ni NPs on $NC_2$ defect (unsaturated N-doped model) is thermodynamically possible. $NiNC_2$ is also one of the most active and non-selective $eCO_2RR$ configurations, with strong bindings for *CO, *COOH, and *H intermediates. Once Ni NPs are supported on $NC_2$ they can disintegrate, as the experimentally partial current density drops drastically compared to CO partial current densities. That is how the combination of the two results (activity and stability for dispersion) can support the fact that enhanced Faradaic efficiency was observed when the reaction was performed

five times in a row for nanoparticles supported on unsaturated N-doped carbon materials.[137]

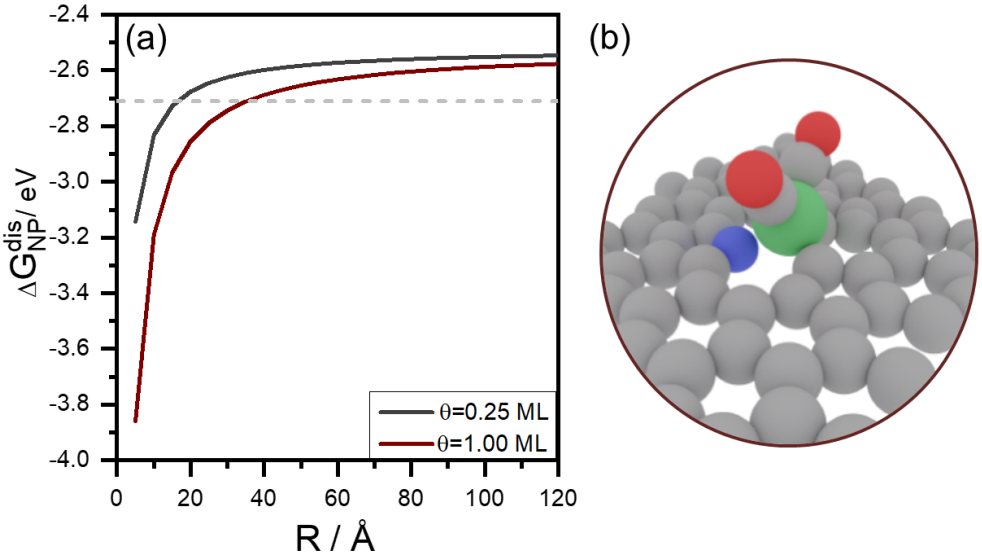


**Figure 5.9: Gibbs free energy of $Ni(CO)_2$ complexes disintegration.** (a) Size dependence of the Gibbs free energy ($\Delta G^{dis}_{NP}$) of $Ni(CO)_2$, when Ni NPs is supported on $NC_2$ at 300 K and 0.1 mbar. The horizontal dashed line indicates the limit for stability. (b) Schematic representation of $Ni(CO)_2$ bound to the $NC_2$ cavity.

Redispersion is thus possible on unsaturated materials; however, the nature of the carrier would affect catalytic performance. The electrochemical cycling from the nanoparticles does enhance the selectivity in unsaturated hosts but not up to the levels found for the saturated materials. To investigate the size (R) dependence of the disintegration induced by CO, we have used NiNP-$NC_2$ model as cavity and have calculated the $\Delta G^{dis}_{NP}$(R, T, p) considering the formation of $Ni(CO)_2$ sitting at these pockets at experimental temperature and pressure. Figure 5.9 presents the $\Delta G^{dis}_{NP}$ corresponding to $Ni(CO)_2$ vs. the radius R of a Ni nanoparticle at two different coverages, 0.25 ML and 1ML (non-wetting conditions for the nanoparticle were considered, thus the Young angle was set to 180°). We found that $\Delta G^{dis}_{NP}$ decreases at smaller R and crosses the reference level (-2.7 eV, adsorption energy of an isolated Ni atom in the cavity) at about 40 Å for 1 ML and 20 Å for 0.25 ML. The lower value found for lower coverage is a direct consequence of the simplicity of the model and shall be taken with caution as kinetic constraints related to the need of concentrating CO molecules to extract the surface atoms could play an important role. At high coverage our results imply that Ni NPs smaller than 4nm will disintegrate into $Ni(CO)_2$ when supported on the $NC_2$ at 300 K and 0.1 mbar.

### 5.4.3 The mechanism for Ni NPs reconstruction

The dense layers that we have identified in section Nanoparticle shape show that after $eCO_2RR$, CO extensively covers the surface and over long times has the potential to increase the fraction of Ni atoms in low-coordinated sites as stepped Ni(211) surfaces. Moreover, the thermodynamic models (see Figure 5.1) indicate that below a certain size, $Ni(CO)_x$ spices can be stable in some particular motifs of the N-doped carbons. To merge these two scenarios, a viable route for decomposition needs to be described. Ni can form volatile species with CO in the form of $Ni(CO)_4$ that can be soluble under the reaction conditions. We have calculated the energy needed for the formation of these species. On nanoparticles, $CO_2$ is reduced to CO at -0.6 V vs. RHE and pH 7, and the resulting CO drives the reconstruction toward Ni(211). Once the reaction is stopped at open circuit potential (OCP), $Ni(CO)_4$ species can be formed as the CO coverage is very high. Thermodynamically, the formation energy of a metal vacancy (with respect to Ni bulk) in Ni(100), Ni(111) and Ni(211) surfaces are 0.59, 1.04 and 0.33 eV, respectively. Strong kinetic limitations can likely appear due to geometric constraints on Ni(111) and Ni(100), but for the fully CO adsorbed Ni(211) surface the step edges can present very high CO concentration. Thus $Ni(CO)_4$ can be formed in this facet with concomitant elimination of Ni atoms. Figure 5.10a presents the average adsorption energy for CO at different coverages (red curve) on the Ni(211) facet and it is compared to the formation-elimination of the $Ni(CO)_4$ complex (gray curve).

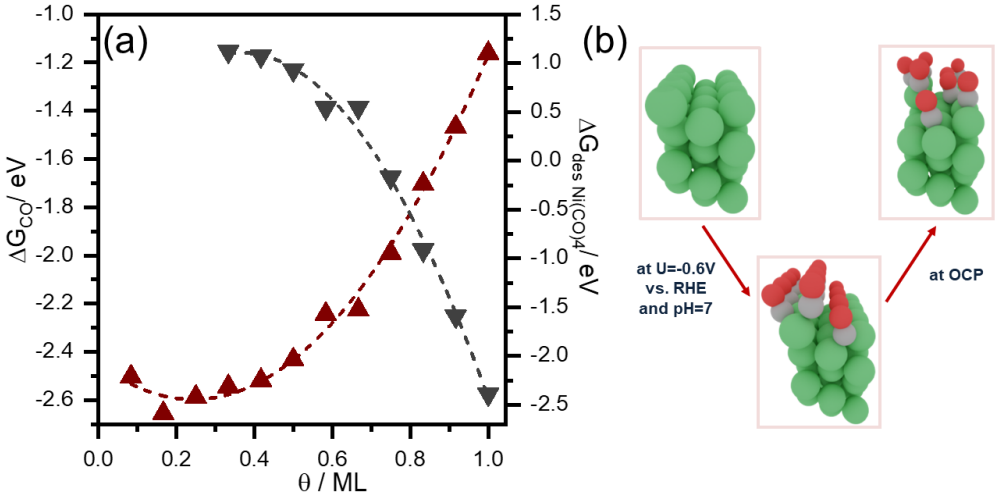


**Figure 5.10: Reconstruction of Ni(211) metal surface.**(a) CO coverage dependence of the average Gibbs free energy (red curve) of CO adsorption at -0.6 V vs. RHE (pH 7) and (gray curve) desorption of $Ni(CO)_4$. (b) Schematic process of clean Ni(211) metal surface fully adsorbing CO at electrochemical conditions. When the reaction is stopped at the open circuit potential (OCP) to assess the material recyclability, $Ni(CO)_4$-like complexes can desorb.

The crossing between these two lines can be interpreted as the coverage at which the elimination of Ni atoms in the form of the species becomes viable. Therefore, high CO coverages would affect the stability of the edge sites starting around 0.78 ML coverage promoting the formation of the species that can then redisperse on the cavities of the N-doped carbon. The process of reconstruction is sketched in Figure 5.10b. All the data is presented in Appendix Chapter B. Once the reaction is under electrochemical potential again, these complexes react with non-occupied defects on the unsaturated N-doped carbon (NiNP-$NC_2$) and effectively redisperse. This process could potentially lead to higher activity, as shown in the experiments.[137]

## 5.5 Conclusions

Electrocatalysts based on Ni supported on N-doped carbon materials have been computationally analyzed for the reduction of $CO_2$ considering both nanoparticles and single atoms. The optimal activity and selectivity are found for $NiN_3$ model, in which Ni is in $Ni^{1+}$ oxidation state. $NiN_3$ exhibits theoretically low onset potential in agreement with experiments and high rate towards CO. However, rather saturated N-doped materials are more selective towards CO formation. As single atoms can be prepared from nanoparticles, we show through the Oswald formalism that disintegration of $Ni(CO)_x$ can happen if Ni nanoparticles are supported on N-doped unsaturated support such as $NC_2$. We present a mechanism of Ni(211) surface reconstruction that is possible only at high CO coverages around 8/12 ML by the formation of $Ni(CO)_4$ species, which then redisperse into active single atoms. The complete understanding of the Ni-N-C materials points towards a very dynamic behavior where considering the full complexity of the material in terms of Ni nuclearity and environment is needed. This is likely a common feature for such type of electrocatalysts.

# Chapter 6

# Temperature dependent distribution of $CO_2$ electrochemical reduction on CoTPP/MWCNT catalyst

Among the various classes of catalytic materials, molecular catalysts that consist of ligands bound to metal ions have chemically modifiable structures that allow their activity to be tuned quite precisely. In this chapter DFT was used to understand experimental findings on the selectivity of molecular catalyst, Cobalt(II)-tetraphenyl porphine (CoTPP)/multiwalled carbon nanotube (MWCNT) towards different $eCO_2RR$ products. Cobalt(II)-phthalocyanine (CoPc) deposited on carbon nanotube (CNT) and $FeN_4C$ models were used to benchmark the obtained results. Calculations for HER were performed for all three materials while intermediates toward $CH_2OH$, and $CH_4$ were performed for CoTPP/MWCNT, toward $CH_3OH$ for CoPc/CNT and toward $CH_4$ for the $FeN_4C$.

## 6.1 Methodology

### 6.1.1 Computational details

To model CoTPP/MWCNT and CoPc/CNT catalysts, a graphene layer expanded in a (9×9) supercell was used and embedded complexses. These layers were interleaved by 18 Å vacuum along the Z-direction. In order to model atomically-dispersed $FeN_4C$ carbon structures, graphene layer expanded in a (6×6) supercell replacing four C atoms by nitrogens and removing two C atoms. These layers were interleaved by 12 Å vacuum along the Z direction. The kinetic energy cutoff was set at 500 eV for all the models. We investigated competitive $eCO_2RR$ and HER, where structures were relaxed with a force threshold of 0.05 eV/Å. The Brillouin zone was sampled using a 2×2×1 k-point mesh for CoTPP/MWCNT and CoPc/CNT, and 3×3×1 k-point mesh for $FeN_4C$ generated with the Monkhorst–Pack method.[55]

## 6.2 Characterization of CoTPP/MWCNT catalyst

The CoTPP/MWCNT catalyst was characterized by high-resolution transmission electron microscopy (HRTEM) and scanning electron microscopy (SEM). Both methods suggest a strong interaction existing between MWCNT and CoTPP as intended. Raman spectroscopy was employed for further characterization of the CoTPP/MWCNT catalyst. The Raman spectra of MWCNT exhibit two characteristic peaks the D-band (ca. 1314 $cm^{-1}$) is assigned to the $sp^3$ hybridized carbon or the disordered nanotube structure[183,184] and the G-band (ca. 1575 $cm^{-1}$) correspond to the $sp^2$ hybridized carbon atoms which are generated by tangential vibrational mode of the nanotubes. CoTPP peaks in a range of 300-1600 $cm^{-1}$ are visible and originate from the symmetric and asymmetric stretching and bending molecular vibrational modes of chemical species.[185] The existence of such interactions can also be experimentally proven with 1H NMR.[186] In that study a Ru complex, with aromatic ligands, was deposited on MWCNT, where the experimental and DFT results show existence of CH-$\pi$ interactions, therefore we suggest a similar behavior for our system. The formation of the catalyst is observed from the change in the intensity ratio ($I_D/I_G$), which are 0.40 and 0.46 for pristine MWCNT and the catalyst, respectively. The intensity ratio of the D band to the G band ($I_D/I_G$) corresponds to the amount of $sp^3$-hybridized carbon atoms on the $sp^2$ conjugated carbon materials.[187]

Co in CoTPP is in a square planar configuration, while phenyl groups are in perpendicular configuration, where hydrogen atoms of the phenyl rings interact with the $\pi$ system of the MWCNT forming multiple CH–$\pi$ interactions[186,188,189] (see Figure 6.1a). Each of the four aromatic rings form two CH-$\pi$ interactions, where the H···C distances go from 2.65Å to 3.33Å. In order to benchmark experimental findings over CoTPP/MWCNT catalyst, CoPc/CNT[190](see Figure 6.1b) and $FeN_4C$ (see Figure 4.1) are modelled. CoPc complex is in a square planar configuration; where phenyl rings interact

with the $\pi$ system of the MWCNT forming multiple $\pi$–$\pi$ interactions. Interaction between both $\pi$ systems are around 3.5Å, adsorption energies of clean CoTPP and CoPc complexes on the graphen layer are -1.94 eV and -2.28 eV, respectively.

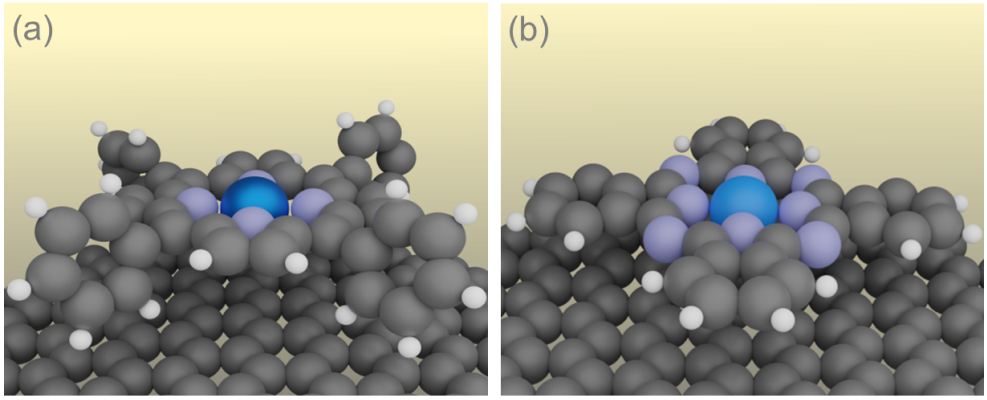


**Figure 6.1: Computational models.** Structures of the (a) CoTPP/MWCNT catalyst and (b) CoPc/CNT, where C is in grey, N in purple, Co in blue, and H in white.

## 6.3 Catalytic performance of CoTPP/MWCNT catalyst

From the experimental results we can conclude that the CoTPP is active toward $CO_2$ reduction reaction when deposited on MWCNT. From Cyclic voltamograms is evident that water reduction is occurring at elevated temperature and increased potential. As a result of simultaneous electrocatalytic reduction of $CO_2$, $H_2O$, and subsequent reduction of CO the gas chromatography (GC) detected $H_2$, CO and $CH_4$ as gaseous products. At the end of the controlled potential electrolysis, catholyte was collected and analyzed with high-performance liquid chromatography (HPLC). In these measurements, $HCOO^-$ and $CH_3OH$ were detected as liquid products. $HCOO^-$ is generated with a low Faradaic efficiency, and thus low partial current density, therefore formate is excluded from the discussion. Furthermore, CV experiments were performed at room temperature (20°C), 30°C, 40°C and 50°C in $N_2$ and $CO_2$ saturated electrolytes to elucidate the direct proton and $H_2O$ reduction mechanism. At 40°C and 50°C $H_2O$ reduction becomes predominant.[191]

Regarding the selectivity in terms of Faradaic efficiencies, we noticed two trends in the product distribution influenced by the temperature over CoTPP/MWCNT catalyst. With increasing temperature, the formation of $H_2$ is increasing, while for the $CH_3OH$, CO, and $CH_4$ the opposite trend is observed. An exception is observed at -0.6 V vs. RHE, where FE of CO is increasing with the temperature until 40°C and at 50°C when it decreases. Figure 6.2 shows the FE of detected products, while partial current densities are shown in Figure 6.3. FE and partial current density of $H_2$ both increase

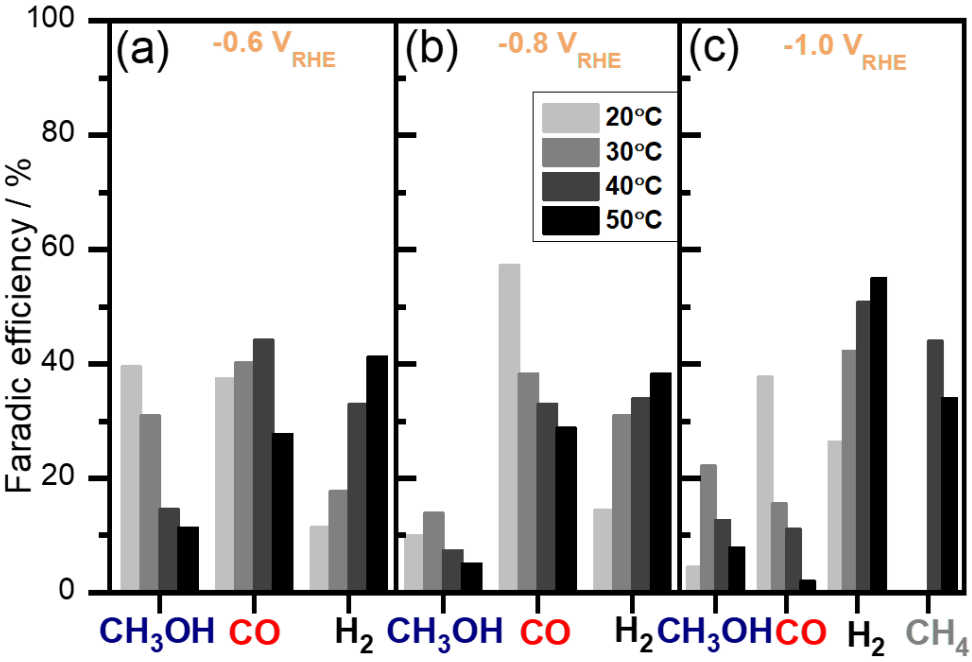


**Figure 6.2: Product analysis.** Faradaic efficiency of the detected products at studied temperatures at (a) -0.6 V, (b) -0.8 V, and (c) -1.0 V vs. RHE over the CoTPP/MWCNT catalyst, plotted against the obtained products. The data were obtained by CA for 4 hours, performed in 0.1 M $KHCO_3$ aqueous electrolyte saturated with $CO_2$ (pH 6.8).

with temperature and potential, with FE being close to 60% at 50°C and -1.0 V vs. RHE. One of the reasons could be solubility which is a function of the temperature, where $CO_2$ with increasing temperature is getting less soluble in water, while the solubility of $H_2$ is constant and low.[192]

Consenquently, the $H_2$ formation is increasing beacuse of the low $CO_2$ solubility in water. A large contribution to the current generation comes from the direct reduction of $H^+$ and/or $H_2O$ to $H_2$. The highest CO formation was observed at room temperature and -0.8 V vs. RHE with FE of 57%. Syngas was produced at 30°C and higher temperatures and at -0.8 V vs. RHE, where the ratios of CO and $H_2$ are close to 1:1. The temperature influence could be a way to control ratios for syn-gas formation. Significantly in the design of metgas plants, ratios of CO and $H_2$ are accommodated to be 1:2 to drive $CH_3OH$ synthesis.[?,193] At room temperature and -0.6 V vs. RHE the main product is $CH_3OH$, while at the same potential production of $CH_3OH$ is decreasing with increasing temperature. e$CO_2$RR proceeds in such a way that adsorbed $CO_2$ reduces via parallel pathways to liquid and gaseous products $CH_3OH$ and CO. Therefore, a considerable amount of CO is desorbed from the electrocatalyst surface before further reduction and it is suggested to be an intermediate species during the formation of the liquid products. An interesting trend occurs with decreasing the potential, at -0.6 V the FE of $CH_3OH$ and CO is relatively the same, 40% and 38% respectively. Once the potential decreases to -0.8 V vs. RHE, the FE for $CH_3OH$ reduces to 10%, while for CO enlarges to 57 %. The formation of $CH_4$ was observed only at -1.0V vs. RHE and elevated temperatures (40°C and 50°C), with FE being more than 35%.

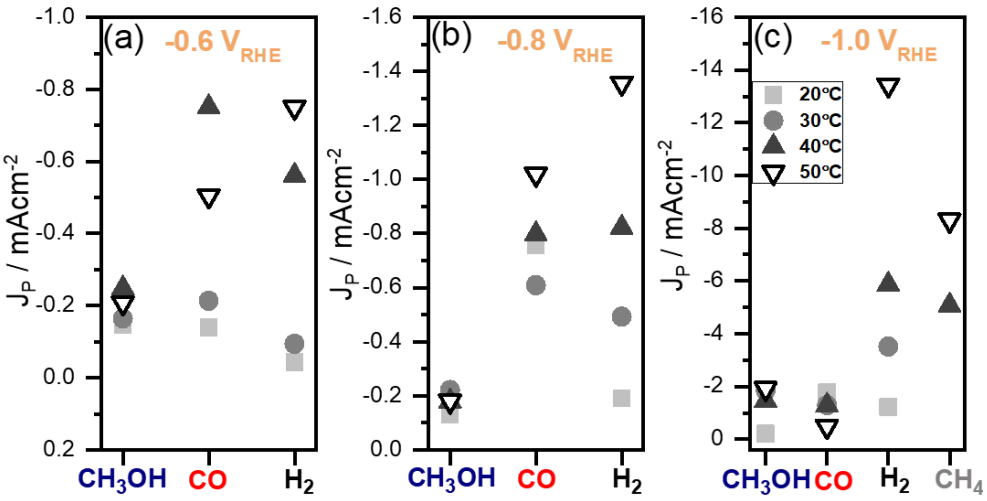


**Figure 6.3: Partial current analysis.** Partial current densities of the detected products at studied temperatures at (a) -0.6 V, (b) -0.8 V, and (c) -1.0 V vs. RHE over the CoTPP/MWCNT catalyst, plotted against the obtained products. The data were obtained by CA for 4 hours, performed in 0.1 M $KHCO_3$ aqueous electrolyte saturated with $CO_2$ (pH 6.8).

## 6.4 $CO_2$ reduction pathway

Upon adsorption and reduction of $CO_2$, the first main intermediate is *CO (Figure 6.4a). Releasing CO would regenerate the catalyst; otherwise, *CO can further hydrogenate to *CHO. This is a key intermediate from which different products can be obtained. On the one hand, hydrogenation of the C atom yields formaldehyde $^*CH_2O$ through a O–M bond, which can either desorb or keep reacting to eventually form $CH_3OH$ (Figure 6.4b). On the other hand, hydrogenation of the O atom produces *CHOH via a C–M bond, which can evolve to $CH_3OH$ (two proton and electron transfers) or $CH_4$ and $H_2O$ (four proton and electron transfers) depending on the hydrogenation pathway (Figure 6.4c). Alternatively, the initial *CO could also hydrogenate to *COH (Figure 6.4d). Additional hydrogenation with concomitant water elimination could produce *C.[194] This intermediate can accept up to four protons and electrons to finally yield $CH_4$. However, this mechanism is not chemically possible for single atom metals as carbon needs to form four bonds.

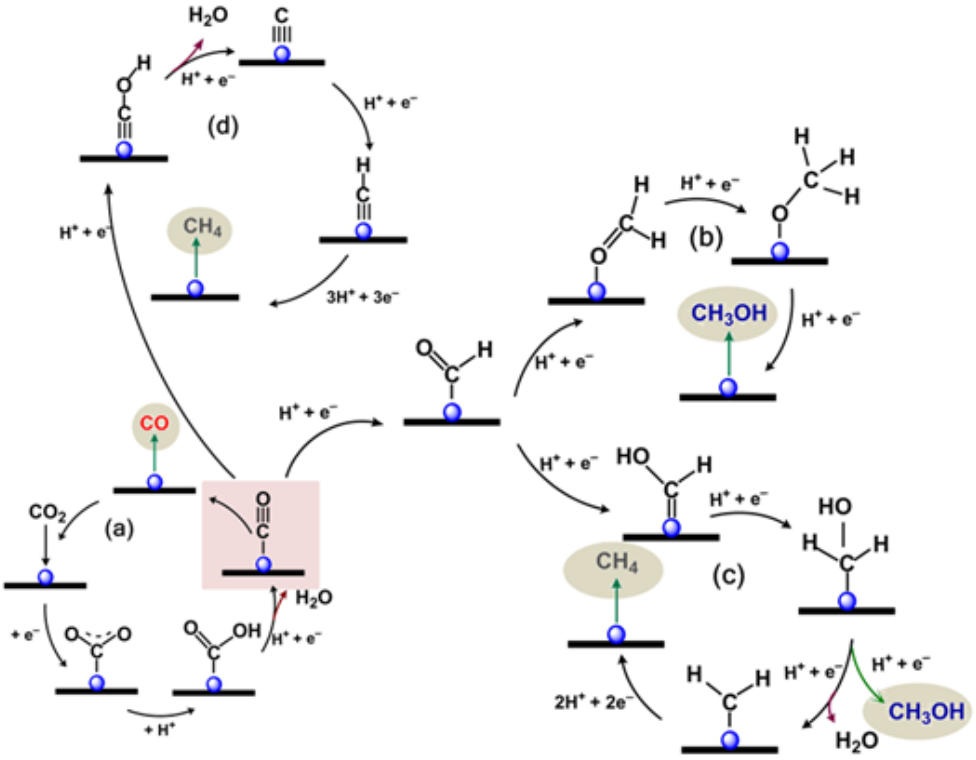


**Figure 6.4: Electrochemical $CO_2$ reduction network.** Reaction mechanism towards (a) CO, (b) $CH_3OH$, (c) $CH_4$ and side product $CH_3OH$, and (d) $CH_4$ on CoTPP/MWCNT.

## 6.5 Understanding product selectivity

There are ways to understand product selectivity based on the DFT results. One way would be to determine the oxophilicity of the catalyst, which correlates with the binding energy of $O_{ads}$, and is the main descriptor for selectivity between $CH_4$ and $CH_3OH$.[195] In that work, the authors studied selectivity over transition metals. $CH_3OH$ was detected on the poorly oxophilic Au metal surface, while $CH_4$ was found for the strongly oxophilic Fe. To benchmark this approach we applied this theory to our case, CoTPP/MWCNT and a reference $FeN_4$ catalyst, see Figure 6.5. The bonding energy of $^*O$ to CoTPP/MWCNT is -2.65 eV, and to the reference $FeN_4$ model is 1.18 eV more exothermic. Indeed, on $FeN_4$ active sites the formation of $CH_4$ was detected[196] thus reinforcing the validity of the approach. A second descriptor for selectivity corresponds to energy of oxygen bonding $^*OCH_2$, where the most exothermic energy has CoTPP/MWCNT. All three materials have exothermic $^*H$ binding energy with CoTPP/MWCNT having the lowest -1.07 eV at -0.6 V vs. RHE. From all of this findings we can conclude that CoTPP/MWCNT and CoPc/CNT are able to produce $CH_3OH$, while $FeN_4$ forms $CH_4$.

**Table 6.1:** Gibbs free energies of $^*OCH_2$, $^*OCH_3$, $^*CHOH$, and $^*CH_2OH$ at -0.6 V vs. RHE , where energies were obtained with the respect to reactants ($CO_2$ and support($*$)). $OCH_2$ binding energy was calculated respect to $OCH_2$ molecule and $*$.(colored row)

| | **CoTPP/MWCNT** | **CoPc/CNT** | **$FeN_4$** |
|---|---|---|---|
| $^*\mathbf{OCH_2}$ | -4.26 | -2.26 | -2.98 |
| $^*\mathbf{OCH_3}$ | -4.52 | -3.36 | -4.55 |
| $^*\mathbf{CHOH}$ | -3.09 | -1.47 | -3.87 |
| $^*\mathbf{CH_2OH}$ | -5.41 | -4.31 | -4.68 |
| $^*\mathbf{OCH_2}$ | -1.21 | -0.32 | -0.37 |

Furthermore to investigate the product formation pathway, electrolysis of HCOOH acid and $CH_2O$ was performed. Interestingly, when HCOOH was reduced only $H_2$ formation is observed, while $CH_2O$ is producing both $CH_3OH$ and $CH_4$. From $CH_2O$ reduction, we get $^*OCH_3$, where oxygen bonding gives alcohols while $^*CH_2OH$ the carbon bonding leads to fully reduced hydrocarbons.[197] The difference in these systems can be noticed between oxygen bonding $^*OCH_2$ and carbon bonding $^*CHOH$ intermediates. For CoTPP/MWCNT and CoPc/CNT the $^*OCH_2$ is more exothermic than $^*CHOH$, while for $FeN_4$ the opposite trend is observed (see Table 6.1). Furthermore the electrochemical activity and selectivity were analyzed by calculating the binding energies of the possible intermediates. The Gibbs free energy network for the different

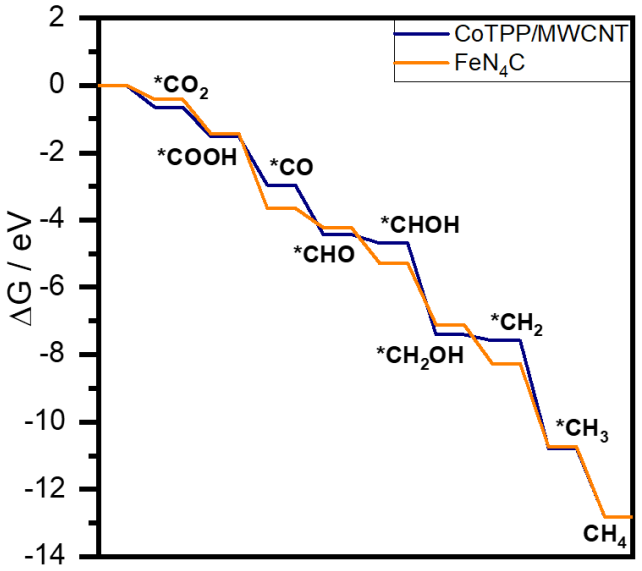


**Figure 6.5: Gibbs free energy profiles** for $eCO_2RR$ over CoTPP/MWCNT and $FeN_4$ towards $CH_4$ at -1.0 V vs. RHE (pH 6.8).

product pathways is presented in Figure 6.6. Compared to previous results in the literature, at room temperature different Co complexes predominately produce CO, except for the CoPc/CNT[190] catalyst which produces $CH_3OH$. When the CoTPP was used but supported in a different material, CNT insted of MWCNT, CoTPP/CNT[198] 90% of CO production at -0.68 V vs. RHE were reported.

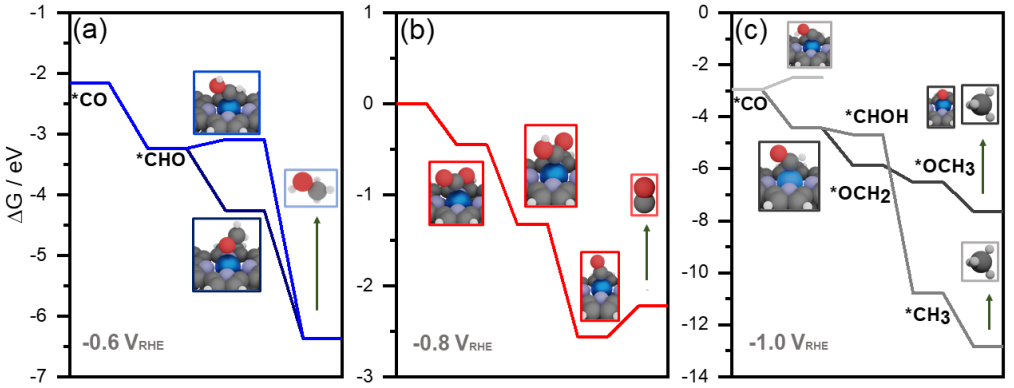


**Figure 6.6: Gibbs free energy profiles.** Energy diagrams for $eCO_2RR$ over CoTPP/MWCNT. (a) Towards $CH_3OH$ at -0.6 V vs. RHE, (b) CO and at -0.8 V vs. RHE, and (c) $CH_4$ at -1.0 V vs. RHE (pH 6.8).

In contrast, in this study at room temperature (20°C) and -0.6 V vs. RHE we observe the production of $CH_3OH$. From simulations, *CO is determining intermediate to produce higher value products and in Figure 6.6b the pathway towards CO is shown at -0.8 V. In the Figure 6.5 we can see that CoTPP/MWCNT binds CO weaker than $FeN_4C$ does.

At the lower potential region, desorption of CO is accelerated by higher temperature as indicated by the increasing total yield of CO (total current times FE) with the temperature.[185,199] The protonation of *CO to *CHO is exothermic for CoTPP/MWCNT catalyst, which makes CO easier to protonate towards $CH_3OH$. As mentioned at room temperature with reducing potential, FE and J of CO increases at -0.8 V comparing to -0.6 V vs. RHE. According to the DFT at -0.8 V vs. RHE, more exothermic, which means it would make CO harder to desorb (Figure 6.7). The reason for a difference in results could be a structural change of an active site during the reaction, porphyrin complexes have a reductive decomposition of the macrocycle.[200,201] The influence of structural features of catalytic sites, meaning the number of coordinated N atoms, and configuration of phenyl groups, plays an important role. The results for $CO_2$ reduction obtained over CoPc/CNT catalyst[190] show that at -0.82 V around 80 % of CO gets produced, and at -0.94 V vs. RHE around 44% of $CH_3OH$ is formed (see Figure 6.8). Figure 6.7 presents Gibbs free energy diagram for CoTPP/MWCNT and CoPC/CNT molecular catalysts at -0.6 V vs. RHE. Comparing *CO binding energies between systems, a difference of 2.43 eV. CoTPP/MWCNT catalyst binds CO stronger than CoPc/CNT, that is the reason why at -0.6 V $CH_3OH$ gets produced. According to binding energy of *CO to CoPc/CNT at -0.8 V potential. CO gets desorbed rather than going further to produce $CH_3OH$.

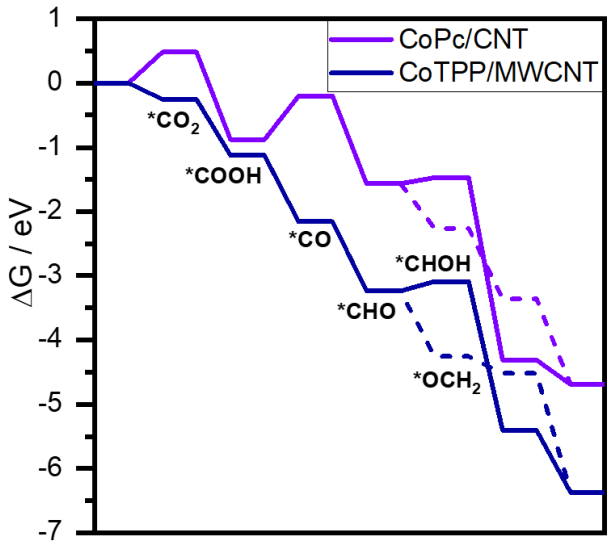


**Figure 6.7: Gibbs free energy profile** for $eCO_2RR$ over CoTPP/MWCNT and CoPc/CNT towards $CH_4$ at -0.6 V vs. RHE (pH 6.8).

In the Figure 6.6a the pathways towards forming $CH_3OH$ are presented for CoTPP/MWCNT. As we confirmed the oxygen bonding of $CH_2O$ is more favourable for CoTPP/MWCNT catalyst, the reduction will continue through $^*OCH_3$ intermediate. Based on our result the $^*OCH_3$ and $^*CH_2OH$ are similar in energy, thereby both possibilities would be possible. In the case of $CH_4$ formation (Figure 6.4d), we can go through $^*COH$ or $^*CHO$ intermediate, where the $^*COH$ intermediate is higher in energy by 1.94 eV, therefore the pathway is excluded. As $CH_4$ is traced at elevated temperatures and low potential, there is a way it can be produced from reduction of $CH_3OH$ or can be reduced to $CH_4$ through $^*CH_2OH$ and $^*CH_3$ intermediates.

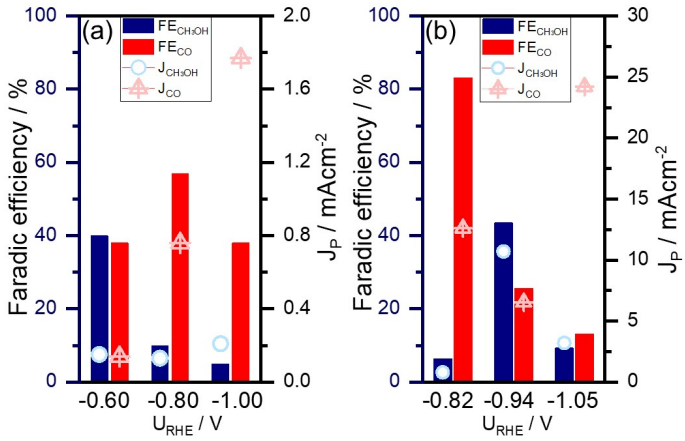


**Figure 6.8: Comparison of catalytic performance.** Product selectivity (FE) and partial current densities of $CH_3OH$ and CO over (a) CoTPP/MWCNT and (b) CoPc/CNT (Ref.[190]) at different potentials.

Increasing temperature to 30°C seems to favor the production of CO and $CH_3OH$, because the mass transport of $CO_2$ can be improved by increasing its solubility by adjusting the pressure and the temperature.[202] Mass transfer can be enhanced with the modulation of the $H_2O$ surface tension that occurs at elevated temperatures. The modulation of surface tension may help to increase the wettability of the electrode surface, which may contribute to decrease of the diffusion layer thickness and hence the mass transfer.[203]

## 6.6 Conclusions

In this chapter, study supported with both experimental and theoretical results is presented which helped to unravel two interesting features (i) the improved activity for the liquid product formation compared to earlier published studies, and (ii) the temperature dependent products distribution favouring hydrogen production at elevated temperatures. It has been shown that improved activity of the hybrid catalyst is due to the interaction between the CoTPP catalytic active centers and electron conducting MWCNTs. Furthermore comparing the structure of the CoTPP and CoPc complex plays an important role in activity of the catalyst. Temperature affects both the gaseous and liquid product formation, making differences in the balance of energy of the different routes in the mechanism that impact product distribution. Notably, FE of $CH_3OH$ decreases with temperature and in contrary FE of CO increases which indicates that the temperature enhances the desorption of CO before further reduction. CoTPP/MWCNT is poorly oxophilic comparing to $FeN_4$, indeed it has an affinity to produce $CH_3OH$. Also, the efficiency of the competing HER increases with the increasing temperature and overpotential. It is suggested from CVs that the $H_2$ is produced from both direct proton and $H_2O$ reduction. The outstanding methanol production observed at room temperature and low potential points toward a interface design to improve product selectivity.

# Chapter 7

# General conclusions

Electrocatalysis plays an important role in clean energy conversion, because it would allow sustainable production of a broad range of chemicals and fuels. Electrochemical $CO_2$ reduction reaction over single site catalysts was investigated using DFT simulations coupled with Computational Hydrogen Electrode formalism. In Chapter 3 I described the importance of understanding the fundamental mechanisms of single-atom catalysis to design systems with improved performance and stability. In addition the crystal field theory within coordination chemistry is explained for anchored homogeneous-like $MN_x$ centers. In Chapter 4 I establish experimental and theoretical correlations between physiochemical and catalytic properties for the $CO_2$ reduction towards CO for MNC catalyst. In Chapter 5 I explained the process of Ni nanoparticles reconstruction by the disintegration of $Ni(CO)_2$ complex, by applying Oswald formalism, on N-doped carbon materials. Finally, in Chapter 6 I unravelled the $CO_2$ reduction product influenced by changing potential and the temperature over modelled CoTPP/MWCNT catalyst. The conclusions specified by Chapter are summarized below.

With respect to the volcano trend in electrocatalytic $CO_2$ reduction activity over atomically dispersed metal sites on Nitrogen-doped Carbon:

- Among the best performing materials, $Fe^{2+}N_4$-$H_2O$ and $Co^{2+}N_4$-$H_2O$ catalyst were theoretically found as the most likely active catalytic centers at studied potentials, whereas $Ni^{1+}N_4$ was predicted as the most active Ni-based one.

- The Gibbs free energy change at the RDS accounted for the experimentally determined activity volcano, with Co-, Fe-, and Ni-based systems showing the best compromise between $^*CO$ and $^*CO_2^-$ binding energies.

- Regarding selectivity, the difference between the binding energies for $^*CO_2^-$ and $^*H$, directly related to the number of d-antibonding electrons, described successfully the high selectivity observed on Fe and Ni catalysts and the more favoured HER observed over the Co based one.

With respect to the stability and redispersion of Ni nanoparticles supported on N-doped carbons for the electrochemical $CO_2$ reduction

- The optimal activity and selectivity are found for $NiN_3$ model, in which Ni is in $Ni^{1+}$ oxidation state.
- $NiN_3$ exhibits theoretically low onset potential in agreement with CO high rates.
- Saturated N-doped materials are selective towards CO formation.
- Redispersion of Ni nanoparticles happens by disintegration of $Ni(CO)_2$-like complex, when Ni nanoparticles are supported on N-doped unsaturated support such as $NC_2$.
- A mechanism of Ni(211) surface reconstruction was developed. Reconstruction is possible only at high CO coverages around 8/12 ML by the formation of $Ni(CO)_4$ species.
- At 0.92ML CO coverage ($\Theta$=0.92ML) Ni surfaces bind $^*H$ weaker, which means the selectivity for HER is decreasing.

With respect to the temperature dependent selectivity of $CO_2$ electrochemical reduction on CoTPP/MWCNT catalyst

- The improved activity of $CH_3OH$ at lower overpotential (-0.6 V vs. RHE) is achieved.
- Increasing temperature to 30°C favours production of CO and $CH_3OH$, while $H_2$ formation gets produce at elevated temperatures.
- Employing temperature could be a way of controlling the ratio of CO and $H_2$ for syngas production.
- The CoTPP/MWCNT catalyst is poorly oxophilic, which correlates with the binding energy of $O_{ads}$, thus making the catalyst selective towards $CH_3OH$.
- The $^*OCH_2$ intermediate is for -1.17 eV more exothermic than $^*CH_2OH$.

# Appendices

UNIVERSITAT ROVIRA I VIRGILI
THEORETICAL STUDIES OF SINGLE-SITE CATALYSTS FOR EFFICIENT ELECTROCHEMICAL CO2 REDUCTION
Paulina Pršlja

# Appendix A

# Structural characterization data

## A.1 Structural parameters for studied models

Tables A.1-A.3 list structural parameter such as distance between metal and local environment for $MN_4$-, Ni saturated and unsaturated N-doped, CoTPP, and CoPc materials. The label $R_{M\text{-}N}$ or $R_{M\text{-}C}$, stands for distance between certain metal and Nitrogen or Carbon atom.

**Table A.1:** Structural metal-nitrogen/oxygen distances obtained for $MN_4$- calculated model structures (in Å).

| | $\mathbf{R_{M\text{-}N}}$ | $\mathbf{R_{M\text{-}O}}$ |
|---|---|---|
| **$MnN_4$-$H_2O$** | 1.91 | 2.40 |
| **$FeN_4$-$H_2O$** | 1.89 | 2.33 |
| **$CoN_4$-$H_2O$** | 1.89 | 2.31 |
| **$ZnN_4$-$H_2O$** | 1.97 | 2.35 |
| **$FeN_4$-OH** | 1.90 | 1.81 |
| **$MnN_4$-O** | 1.95 | 1.58 |

**Table A.2:** Structural Ni-nitrogen/carbon distances obtained for Ni saturated and unsaturated N-doped calculated model structures (in Å).

| | $\mathbf{R_{Ni\text{-}N/C}}$ |
|---|---|
| $\mathbf{NiN_4}$ | 1.88 |
| $\mathbf{NiN_3}$ | 1.80 |
| $\mathbf{NiN_3C}$ | 1.89 |
| $\mathbf{NiC_4}$ | 1.88 |
| $\mathbf{NiNC_3}$ | 1.89 |
| $\mathbf{NiC_3}$ | 1.74 |
| $\mathbf{NiNC_2}$ | 1.77 |

**Table A.3:** Structural Co-nitrogen distances obtained for CoTPP and CoPc calculated model structures (in Å).

| | $\mathbf{R_{Co\text{-}N}}$ |
|---|---|
| **CoTPP** | 1.97 |
| **CoPc** | 1.91 |

## A.2 Oxidation sate of embedded metals

### A.2.1 Magnetization and Bader charge

Tables A.4-A.6 list magnetization and Bader charges of the embedded metal in studied materials such as $MN_4$-, Ni saturated and unsaturated N-doped, CoTPP/MWCNT, and CoPc/CNT.

**Table A.4:** Magnetisation and Bader charges for $MN_4$-like catalysts.

| | | * | *$CO_2^-$ | *COOH | *CO | *$H^+$ |
|---|---|---|---|---|---|---|
| **$MnN_4$** | $\mu_n$ | 2.89 | 2.89 | 2.08 | 1.14 | 2.12 |
| | q(Mn)(\|$e^-$\|) | 1.36 | 1.36 | 1.35 | 1.35 | 1.33 |
| **$FeN_4$** | $\mu_n$ | 1.82 | 0.00 | 0.81 | 0.00 | 0.92 |
| | q(Fe)(\|$e^-$\|) | 1.13 | 1.11 | 1.09 | 1.06 | 1.07 |
| **$CoN_4$** | $\mu_n$ | 0.82 | 0.57 | 0.00 | 0.00 | 0.00 |
| | q(Co)(\|$e^-$\|) | 0.94 | 0.95 | 0.94 | 0.96 | 0.93 |
| **Ni(I)$N_4$** | $\mu_n$ | 0.78 | 0.00 | 0.38 | 0.89 | 0.37 |
| | q(Ni)(\|$e^-$\|) | 0.75 | 0.82 | 0.93 | 0.92 | 0.89 |
| **$NiN_4$** | $\mu_n$ | 0.00 | 0.00 | 0.38 | 0.00 | 0.37 |
| | q(Ni)(\|$e^-$\|) | 0.86 | 0.82 | 0.93 | 0.88 | 0.89 |
| **$CuN_4$** | $\mu_n$ | 0.54 | 0.44 | 0.00 | 0.54 | 0.52 |
| | q(Cu)(\|$e^-$\|) | 0.95 | 0.93 | 0.90 | 0.96 | 1.05 |
| **$ZnN_4$** | $\mu_n$ | 0.00 | 0.00 | 0.00 | 0.00 | 0.00 |
| | q(Zn)(\|$e^-$\|) | 1.14 | 1.08 | 1.17 | 1.16 | 0.97 |
| **$MnN_4$-$H_2O$** | $\mu_n$ | 2.96 | 1.58 | 2.04 | 1.12 | 2.11 |
| | q(Mn)(\|$e^-$\|) | 1.42 | 1.33 | 1.39 | 1.32 | 1.41 |
| **$FeN_4$-$H_2O$** | $\mu_n$ | 0.00 | 0.00 | 0.01 | 0.00 | 0.90 |
| | q(Fe)(\|$e^-$\|) | 1.19 | 1.11 | 1.19 | 1.06 | 1.14 |
| **$CoN_4$-$H_2O$** | $\mu_n$ | 0.88 | 0.61 | 0.00 | 0.40 | 0.00 |
| | q(Co)(\|$e^-$\|) | 1.05 | 0.96 | 1.02 | 1.03 | 0.99 |
| **$MnN_4$-O** | $\mu_n$ | 0.46 | 0.45 | 2.07 | 2.03 | 0.02 |
| | q(Mn)(\|$e^-$\|) | 1.57 | 1.54 | 1.46 | 1.64 | 1.49 |
| **$FeN_4$-OH** | $\mu_n$ | 1.04 | 0.29 | 0.86 | 0.00 | 0.92 |
| | q(Fe)(\|$e^-$\|) | 1.28 | 1.26 | 1.30 | 1.24 | 1.22 |

**Table A.5:** Magnetisation and Bader charges for $MN_4$-like catalysts.

| | | * | $^*CO_2^-$ | *COOH | *CO | $^*H^+$ |
|---|---|---|---|---|---|---|
| $NiN_4$ | $\mu_n$ | 0.00 | 0.00 | 0.00 | 0.96 | 0.34 |
| | q(Ni)(\|e$^-$\|) | 0.86 | 0.85 | 0.93 | 0.92 | 0.90 |
| $NiN_3C$ | $\mu_n$ | 0.02 | 0.01 | 0.00 | 0.10 | 0.12 |
| | q(Ni)(\|e$^-$\|) | 0.75 | 0.72 | 0.86 | 0.82 | 0.87 |
| $NiN_3$ | $\mu_n$ | 1.27 | 1.23 | 0.74 | 1.10 | 0.73 |
| | q(Ni)(\|e$^-$\|) | 0.84 | 0.93 | 1.05 | 0.72 | 0.88 |
| $NiC_4$ | $\mu_n$ | 0.00 | 0.00 | 0.00 | 0.00 | 0.10 |
| | q(Ni)(\|e$^-$\|) | 0.64 | 0.61 | 0.65 | 0.64 | 0.61 |
| $NiNC_3$ | $\mu_n$ | 0.36 | 0.19 | 0.00 | 0.00 | 0.00 |
| | q(Ni)(\|e$^-$\|) | 0.67 | 0.68 | 0.72 | 0.70 | 0.65 |
| $NiC_3$ | $\mu_n$ | 0.00 | 0.00 | 0.00 | 0.00 | 0.10 |
| | q(Ni)(\|e$^-$\|) | 0.58 | 0.63 | 0.49 | 0.48 | 0.45 |
| $NiNC_2$ | $\mu_n$ | 1.26 | 0.00 | 0.00 | 0.00 | 0.00 |
| | q(Ni)(\|e$^-$\|) | 0.72 | 0.56 | 0.72 | 0.73 | 0.53 |

**Table A.6:** Magnetisation and Bader charges for CoTPP/MWCNT catalysts.

| | $\mu_n$ | q(Co)(\|e$^-$\|) |
|---|---|---|
| * | 0.98 | 1.12 |
| ***H** | 0.00 | 1.01 |
| ***CO$_2$** | 0.84 | 1.09 |
| ***COOH** | 0.00 | 1.02 |
| ***CO** | 0.70 | 1.10 |
| ***CHO** | 0.00 | 0.99 |
| ***OCH$_2$** | 0.97 | 1.14 |
| ***OCH$_3$** | 1.34 | 1.23 |
| ***CHOH** | 0.26 | 1.07 |
| ***H$_2$CHO** | 0.00 | 1.03 |
| ***COH** | 0.00 | 0.98 |
| ***C** | 0.79 | 0.99 |
| ***CH** | 0.39 | 1.06 |
| ***CH$_2$** | 0.00 | 1.14 |
| ***CH$_3$** | 0.00 | 1.06 |
| ***O** | 1.75 | 1.36 |
| ***OH** | 1.41 | 1.28 |

### A.2.2 Determining oxidation state

The computed magnetization of embedded metal and geometry of chosen defect becomes useful to determine oxidation state of the metal using crystal field theory. Figures A.1-A.3 present the crystal field energy splitting for the studied materials.

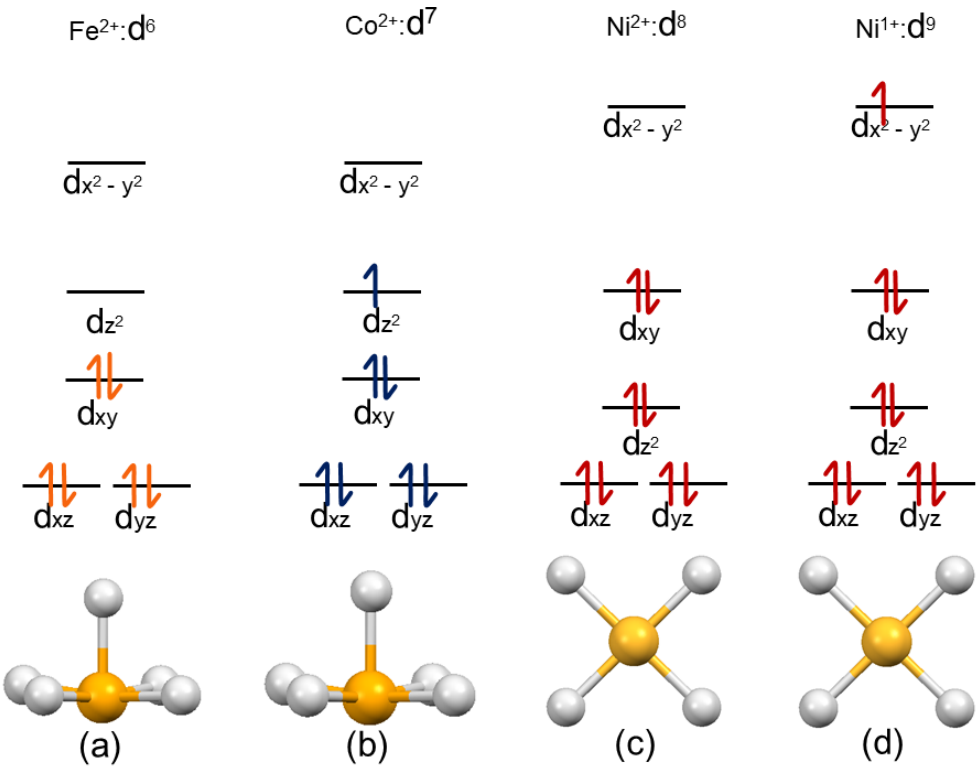


**Figure A.1:** The crystal field theory splitting of the metal d block for (a) $FeN_4$-$H_2O$ (square-based pyramidal) (b) $CoN_4$-$H_2O$ (square-based pyramidal) (c) Ni(II)$N_4$ (square planar) and (d) Ni(I)$N_4$ (square planar). Ligands are represented with white spheres, and metal with yellow sphere.

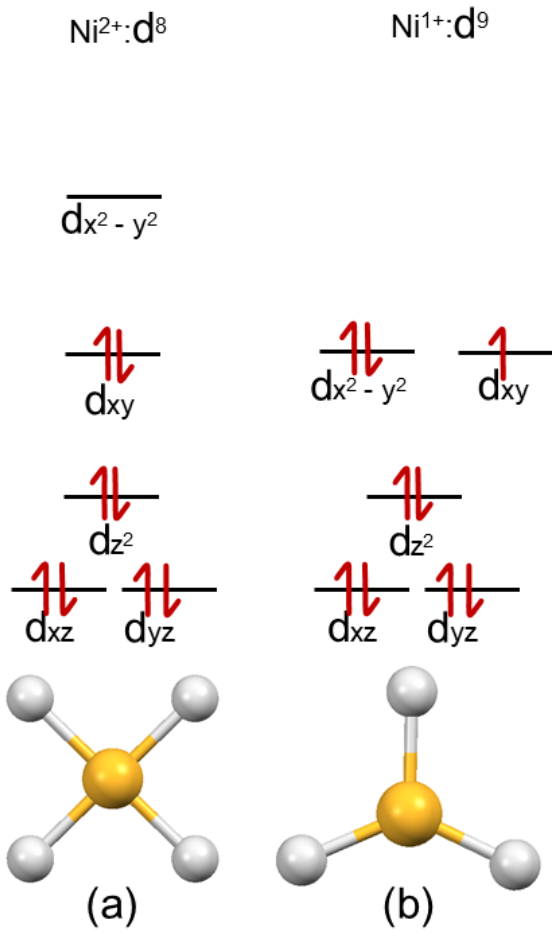


**Figure A.2:** The crystal field theory splitting of the metal d block for (a) Ni(II)$N_4$ (square planar) and (b) Ni(I)$N_4$ (trigonal planar). Ligands are represented with white spheres, and metal with yellow sphere.

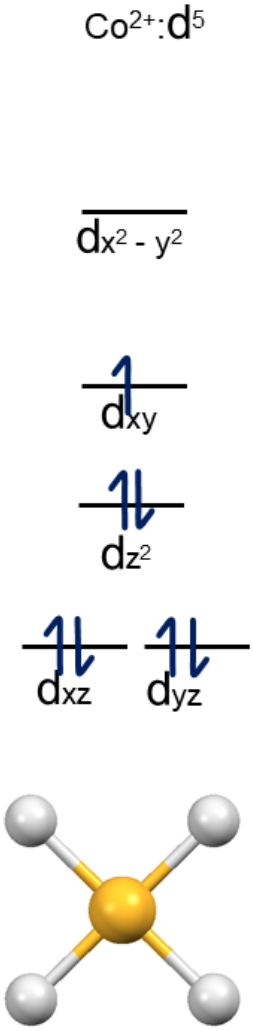


**Figure A.3:** The crystal field theory splitting of the metal d block for CoTPP and CoPc complexes (square planar). Ligands are represented with white spheres, and metal with yellow sphere.

# Appendix B

# Additional methodological details

## B.1 Construction of Ni nanoparticle at different CO coverages

In order to calculate surface energy of Ni NPs at certain CO coverage, than CO adsorption should be considered on all three facets separately. Therefore I calculated average binding energies $E'_{CO}$ for all three facets at 0.25 ML, 0.50 ML, 0.75 ML, and 1 ML CO coverage (see Table B.1). Table B.2 lists the reduction of surface energy $\Delta\gamma_i$ and effective surface energy $\gamma'_i$ of supported Ni particles with CO adsorbate. Once the the reduction of surface energies is calculated, than the surface energy of Ni NPs at certain CO coverage can be calculated by

$$\gamma'(T, p) = \sum_i f_i[\gamma_i + \Delta\gamma_i(T, p)]. \quad (B.1)$$

Table B.3 lists the surface energy and ratios at certain CO coverage of the facetes and surface energy of the Ni NP. Figure B.1 presents Wullf construction of Ni NP at CO coverages 0.25 ML, 0.50 ML, 0.75 ML, and 1.00 ML.

**Table B.1:** Average adsorption energies of CO (in eV/CO molecule) for different coverages and surface unit area of the facet "i" (in $Å^2$)

| | **Ni(100)** | **Ni(111))** | **Ni(211)** |
|---|---|---|---|
| **A** | 74.44 | 85.95 | 60.84 |
| $\mathbf{A_i}$ | 6.20 | 5.37 | 5.07 |
| $\mathbf{E_{CO\text{-}0.25\ ML}}$ | -1.34 | -1.37 | -1.28 |
| $\mathbf{E_{CO\text{-}0.50\ ML}}$ | -1.29 | -1.21 | -1.13 |
| $\mathbf{E_{CO\text{-}0.75\ ML}}$ | -0.98 | -0.71 | -0.69 |
| $\mathbf{E_{CO\text{-}1.00\ ML}}$ | -0.36 | 0.55 | 0.14 |

**Table B.2:** Calculated surface energies of Ni particle before $\gamma_i$ and after CO adsorption $\gamma_i^{'}$ and ratio $f_i$, $f_i^{'}$ of considered facets of infinite size Ni based on Wulff construction. Ratios are presented in (%) and $\gamma_i$ in (eV/$Å^2$)

| $\theta$ | **0.25 ML** | **0.50 ML** | **0.75 ML** | **1.00 ML** |
|---|---|---|---|---|
| $\Delta\gamma_{100}\mathbf{(T,p)}$ | -0.024 | -0.042 | -0.027 | 0.064 |
| $\Delta\gamma_{111}\mathbf{(T,p)}$ | -0.028 | -0.042 | 0.007 | 0.243 |
| $\Delta\gamma_{211}\mathbf{(T,p)}$ | -0.024 | -0.036 | 0.011 | 0.178 |
| $\gamma_{100}^{'}\mathbf{(T,p)}$ | 0.016 | 0.015 | 0.068 | 0.201 |
| $\gamma_{111}^{'}\mathbf{(T,p)}$ | 0.078 | 0.067 | 0.050 | 0.000 |
| $\gamma_{211}^{'}\mathbf{(T,p)}$ | 0.000 | 0.000 | 0.000 | 0.004 |

**Table B.3:** Calculated surface energies of Ni facets after CO adsorption $\gamma_i^{'}$ and ratio $f_i^{'}$ of considered facets of infinite size Ni based on Wulff construction. Ratios are presented in (%) and $\gamma_i$ in (eV/Å$^2$)

| $\theta$ | **0.25 ML** | | **0.5 ML** | | **0.75 ML** | | **1.00 ML** | |
|---|---|---|---|---|---|---|---|---|
| | $\gamma_i$ | $f_i$ | $\gamma_i$ | $f_i$ | $\gamma_i$ | $f_i$ | $\gamma_i$ | $\gamma_i$ |
| **Ni(100)** | 0.116 | 14 | 0.102 | 15 | 0.149 | 61 | 0.203 | 99 |
| **Ni(111)** | 0.092 | 86 | 0.078 | 85 | 0.127 | 39 | 0.363 | 0 |
| **Ni(211)** | 0.114 | 0 | 0.102 | 0 | 0.149 | 0 | 0.316 | 1 |
| $\gamma^{'}$ **(T,P)** | 0.095 | | 0.081 | | 0.118 | | 0.204 | |

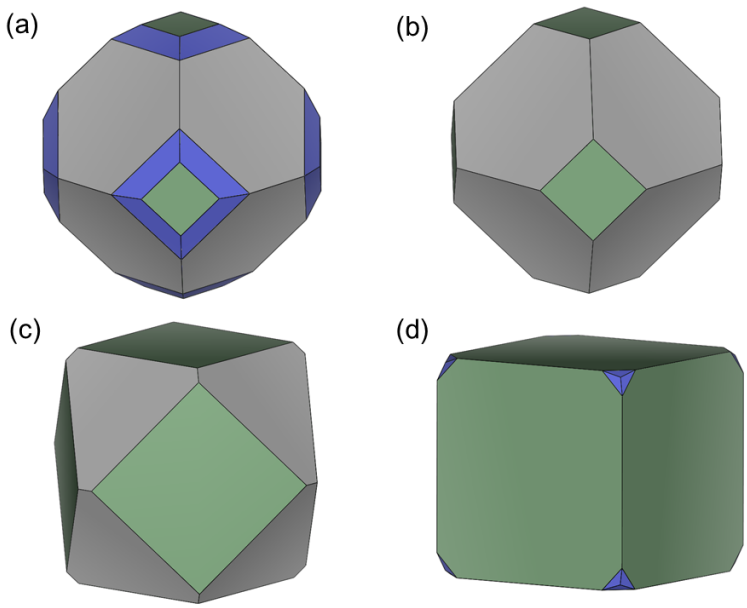


**Figure B.1:** Wulff construction based on the surface energies calculated by first principle theory. (a) Ni nanoparticle with 0.25 ML coverage of CO. (b) Ni nanoparticle with 0.5 ML coverage of CO. (c) Ni nanoparticle with 0.75 ML coverage of CO. (d) Ni nanoparticle with 1.0 ML coverage of CO. Ni(100) surface is represented in green color, Ni(111) surface with gray color, and Ni(211) surface with blue color.

## B.2 Reconstruction of Ni(211)

Tables B.4 and B.5 present Gibbs free energies of CO molecule adsorption and desorption, while desorption energies of $Ni(CO)_4$ compound are presented in Table B.6. CO adsorption follows as $* + nCO + n2H^+ + n2e^- \rightarrow {}^*CO + nH_2O$ and is calculated with applied CHE formalism as:

$$\Delta G_{DFT} = nG(^*CO) + nG(H_2O) - nG(*) - nG(CO_2) - nG(H_2) \qquad (B.2)$$

**Table B.4:** Gibbs free energies of CO molecule adsorption depending on the coverage of Ni(211) metal surface at -0.6 V vs. RHE and pH 7. All energies in eV.

| | $\theta$ **(ML)** | $\Delta G_{\mathbf{a\text{-}nCO}}$ | $\Delta G_{\mathbf{a\text{-}nCOave}}$ |
|---|---|---|---|
| $\Delta G_{\mathbf{a\text{-}1CO}}$ | 0.08 | -2.50 | -2.50 |
| $\Delta G_{\mathbf{a\text{-}2CO}}$ | 0.17 | -5.31 | -2.66 |
| $\Delta G_{\mathbf{a\text{-}3CO}}$ | 0.25 | -7.76 | -2.59 |
| $\Delta G_{\mathbf{a\text{-}4CO}}$ | 0.33 | -10.18 | -2.54 |
| $\Delta G_{\mathbf{a\text{-}5CO}}$ | 0.42 | -12.59 | -2.52 |
| $\Delta G_{\mathbf{a\text{-}6CO}}$ | 0.50 | -14.59 | -2.43 |
| $\Delta G_{\mathbf{a\text{-}7CO}}$ | 0.58 | -15.70 | -2.24 |
| $\Delta G_{\mathbf{a\text{-}8CO}}$ | 0.67 | -17.80 | -2.23 |
| $\Delta G_{\mathbf{a\text{-}9CO}}$ | 0.75 | -17.90 | -1.99 |
| $\Delta G_{\mathbf{a\text{-}10CO}}$ | 0.83 | -17.04 | -1.70 |
| $\Delta G_{\mathbf{a\text{-}11CO}}$ | 0.92 | -16.13 | -1.47 |
| $\Delta G_{\mathbf{a\text{-}12CO}}$ | 1.00 | -13.94 | -1.16 |

**Table B.5:** Gibbs free energies of CO molecule desorption depending on the coverage of Ni(211) metal surface at -0.6 V vs. RHE and pH 7. All energies in eV.

| | $\theta$ (ML) | $\Delta G_{d\text{-}nCO}$ | $\Delta G_{d\text{-}nCOave}$ |
|---|---|---|---|
| $\Delta G_{d\text{-}1CO}$ | 0.08 | 1.15 | 1.15 |
| $\Delta G_{d\text{-}2CO}$ | 0.17 | 2.22 | 1.11 |
| $\Delta G_{d\text{-}3CO}$ | 0.25 | 3.13 | 1.04 |
| $\Delta G_{d\text{-}4CO}$ | 0.33 | 4.00 | 1.00 |
| $\Delta G_{d\text{-}5CO}$ | 0.42 | 4.87 | 0.97 |
| $\Delta G_{d\text{-}6CO}$ | 0.50 | 5.33 | 0.89 |
| $\Delta G_{d\text{-}7CO}$ | 0.58 | 4.90 | 0.70 |
| $\Delta G_{d\text{-}8CO}$ | 0.67 | 5.45 | 0.68 |
| $\Delta G_{d\text{-}9CO}$ | 0.75 | 4.01 | 0.45 |
| $\Delta G_{d\text{-}10CO}$ | 0.83 | 1.61 | 0.16 |
| $\Delta G_{d\text{-}11CO}$ | 0.92 | -0.84 | 0.08 |
| $\Delta G_{d\text{-}12CO}$ | 1.00 | -4.58 | -0.38 |

**Table B.6:** Gibbs free desorption energies of $Ni(CO)_4$ (in eV).

| $\theta$ (ML) | $\Delta G_{Ni(CO)_4}$ | $\Delta G_{Ni(CO)_4}$ava |
|---|---|---|
| 0.09 | 4.29 | 1.07 |
| 0.18 | 3.73 | 0.93 |
| 0.27 | 2.16 | 0.54 |
| 0.36 | 2.19 | 0.55 |
| 0.45 | -0.69 | -0.17 |
| 0.55 | -3.66 | -0.91 |
| 0.64 | -6.37 | -1.59 |
| 0.73 | -9.57 | -2.39 |

# Bibliography

[1] Höök, M.; Tang, X. Depletion of fossil fuels and anthropogenic climate change-A review, *Energy Policy* **2013,** *52,* 797–809.

[2] Olah, G. A. Towards oil independence through renewable methanol chemistry, *Angew. Chemie-Int. Ed.* **2013,** *52,* 104–107.

[3] Eriksson, O.; Finnveden, G. Plastic waste as a fuel $CO_2$ neutral or not?, *Energy Environ. Sci.* **2009,** *2,* 907–914.

[4] Baselga, J. *et al.* Europe and the century of biomedical discovery and implementation, *The Lancet* **2011,** *377,* 719–720.

[5] Krug, E. C.; Frink, C. R. Acid rain on acid soil: A new perspective, *Science* **1983,** *221,* 520–525.

[6] Streets, D. G.; Zhang, Q.; Wu, Y. Projections of global mercury emissions in 2050, *Environ. Sci. Technol.* **2009,** *43,* 2983–2988.

[7] Ramanathan, V.; Carmichael, G. Global and regional climate changes due to black carbon, *Nat. Geosci.* **2008,** *1,* 221–227.

[8] Adamu, A.; Russo-Abegao, F.; Boodhoo, K. Process intensification technologies for $CO_2$ capture and conversion-a review, *BMC Chemical Engineering* **2020,** *2,* 1–18.

[9] Alper, E.; Yuksel Orhan, O. $CO_2$ utilization: Developments in conversion processes, *Petroleum* **2017,** *3,* 109–126.

[10] Dai, Z.; Middleton, R.; Viswanathan, H.; Fessenden-Rahn, J.; Bauman, J.; Pawar, R.; Lee, S. Y.; McPherson, B. An integrated framework for optimizing $CO_2$ sequestration and enhanced oil recovery, *Environ. Sci. Technol. Lett.* **2013,** *1,* 49–54.

[11] Fasihi, M.; Efimova, O.; Breyer, C. Techno-economic assessment of $CO_2$ direct air capture plants, *J. Clean. Prod.* **2019,** *224,* 957–980.

[12] Jiang, Z.; Xiao, T.; Kuznetsov, V. L.; Edwards, P. P. Turning carbon dioxide into fuel, *Philos. Trans. R. Soc. A Math. Phys. Eng. Sci.* **2010,** *368,* 3343–3364.

[13] Bajamundi, C. J. E.; Koponen, J.; Ruuskanen, V.; Elfving, J.; Kosonen, A.; Kauppinen, J.; Ahola, J. Capturing $CO_2$ from air: Technical performance and process control improvement, *J. $CO_2$ Util.* **2019,** *30,* 232–239.

[14] Soltani, S. M.; Fennell, P. S.; Mac Dowell, N. A parametric study of $CO_2$ capture from gas-fired power plants using monoethanolamine (MEA), *Int. J. Greenh. Gas Control* **2017,** *63,* 321–328.

[15] Whipple, D. T.; Kenis, P. J. Prospects of $CO_2$ utilization via direct heterogeneous electrochemical reduction, *J. Phys. Chem. Lett.* **2010,** *1,* 3451–3458.

[16] Nielsen, I. M.; Leung, K. Cobalt-porphyrin catalyzed electrochemical reduction of carbon dioxide in water. 1. A density functional study of intermediates, *J. Phys. Chem. A* **2010,** *114,* 10166–10173.

[17] Leung, K.; Nielsen, I. M.; Sai, N.; Medforth, C.; Shelnutt, J. A. Cobalt-porphyrin catalyzed electrochemical reduction of carbon dioxide in water. 2. Mechanism from first principles, *J. Phys. Chem. A* **2010,** *114,* 10174–10184.

[18] Yamamoto, T.; Tryk, D. A.; Fujishimal, A.; Ohata, H. Production of syngas plus oxygen from $CO_2$ in a gas-diffusion electrode-based electrolytic cell, *Electrochim. Acta* **2002,** *47,* 3327–3334.

[19] Hori, Y.; Wakebe, H.; Tsukamoto, T.; Koga, O. Electrocatalytic process of CO selectivity in electrochemical reduction of $CO_2$ at metal electrodes in aqueous media, *Electrochim. Acta* **1994,** *39,* 1833–1839.

[20] Furuya, N.; Koide, S. Electroreduction of carbon dioxide by metal phthalocyanines, *Electrochim. Acta* **1991,** *36,* 1309–1313.

[21] Azuma, M.; Hashimoto, K.; Hiramoto, M.; Watanabe, M.; Sakata, T. Electrochemical reduction of carbon dioxide on various metal electrodes in low-temperature aqueous $KHCO_3$ Media, *J. Electrochem. Soc.* **1990,** *137,* 1772–1778.

[22] Furuya, N.; Yamazaki, T.; Shibata, M. High performance Ru-Pd catalysts for $CO_2$ reduction at gas-diffusion electrodes, *J. Electroanal. Chem.* **1997,** *431,* 39–41.

[23] Ikeda, S.; Takagi, T.; Ito, K. Selective formation of formic acid, oxalic acid, and carbon monoxide by electrochemical reduction of carbon dioxide, *Bull. Chem. Soc. Jpn.* **1987,** *60,* 2517–2522.

[24] Mahmood, M. N.; Masheder, D.; Harty, C. J. Use of gas-diffusion electrodes for high-rate electrochemical reduction of carbon dioxide. I. Reduction at lead, indium- and tin-impregnated electrodes, *J. Appl. Electrochem.* **1987,** *17,* 1159–1170.

[25] Udupa, K. S.; Subramanian, G. S.; Udupa, H. V. K. The electrolytic reduction of carbon dioxide to formic acid, *Electrochim. Acta* **1971,** *16,* 1593–1598.

[26] Hara, K.; Sonoyama, N.; Sakata, T. Electrocatalytic Fischer-Tropsch reactions. Formation of hydrocarbons and Oxygen-containing compounds from CO on a Pt gas diffusion electrode, *Bull. Chem. Soc. Jpn.* **1997,** *70,* 745–754.

[27] Kaneco, S.; Katsumata, H.; Suzuki, T.; Ohta, K. Electrochemical reduction of $CO_2$ to methane at the Cu electrode in methanol with sodium supporting salts and its comparison with other alkaline salts, *Energy and Fuels* **2006,** *20,* 409–414.

[28] Arai, G.; Harashina, T.; Yasumori, I. Selective electrocatalytic reduction of carbon dioxide to Methanol on Ru-modified electrode, *Chem. Lett.* **1989,** *18,* 1215–1218.

[29] Summers, D. P.; Leach, S.; Frese, K. W. The electrochemical reduction of aqueous carbon dioxide to methanol at molybdenum electrodes with low overpotentials, *J. Electroanal. Chem. Interfacial Electrochem.* **1986,** *205,* 219–232.

[30] Qu, J.; Zhang, X.; Wang, Y.; Xie, C. Electrochemical reduction of $CO_2$ on $RuO_2/TiO_2$nanotubes composite modified Pt electrode, *Electrochim. Acta* **2005,** *50,* 3576–3580.

[31] Cook, R. L.; MacDuff, R. C.; Sammells, A. F. High rate gas phase $CO_2$ reduction to ethylene and methane using gas diffusion electrodes, *Electrochem. Soc.* **1990,** *137,* 607–608.

[32] Hori, Y.; Murata, A.; Takahashi, R. Formation of hydrocarbons in the electrochemical reduction of carbon dioxide at a copper electrode in aqueous solution, *J. Chem. Soc. Faraday Trans. 1 Phys. Chem. Condens. Phases* **1989,** *85,* 2309–2326.

[33] Hori, Y.; Takahashi, R.; Yoshinami, Y.; Murata, A. Electrochemical reduction of CO at a copper electrode, *J. Phys. Chem. B* **1997,** *101,* 7075–7081.

[34] Kuhl, K. P.; Cave, E. R.; Abram, D. N.; Jaramillo, T. F. New insights into the electrochemical reduction of carbon dioxide on metallic copper surfaces, *Energy Environ. Sci.* **2012,** *5,* 7050–7059.

[35] Peterson, A. A.; Nørskov, J. K. Activity descriptors for $CO_2$ electroreduction to methane on transition-metal catalysts, *J. Phys. Chem. Lett.* **2012,** *3,* 251–258.

[36] Varela, A. S.; Ju, W.; Strasser, P. Correction to: Molecular nitrogen-carbon catalysts, solid metal organic framework catalysts, and solid

metal/nitrogen-doped carbon (MNC) catalysts for the electrochemical $CO_2$ reduction , *Adv. Energy Mater.* **2018,** *8,* 2017–2018.

[37] T., D. A.; F., A. Electrochemists enlisted in war on global warming: The carbon dioxide reduction battle, *Electrochem. Soc. interface* **2001,** *10,* 32–36.

[38] Chaplin, R. P.; Wragg, A. A. Effects of process conditions and electrode material on reaction pathways for carbon dioxide electroreduction with particular reference to formate formation, *J. Appl. Electrochem.* **2003,** *33,* 1107–1123.

[39] De Luna, P.; Hahn, C.; Higgins, D.; Jaffer, S. A.; Jaramillo, T. F.; Sargent, E. H. What would it take for renewably powered electrosynthesis to displace petrochemical processes?, *Science* **2019,** *364,*.

[40] G. Ertl, H. Knozinger, and J. Weitkamp, publisher = Wiley, t. . H. y. . .

[41] Deutschmann, O.; Knözinger, H.; Kochloefl, K.; Turek, T. Heterogeneous catalysis and solid catalysts, *Ullmann's Encyclopedia of Industrial Chemistry* **2009,** .

[42] Rothenberg, G. *Catalysis:Concepts and Green Applications;* 2008.

[43] Nørskov JK, Studt F, Abild-Pedersen F Bligaard T, y. . . p. . W. *Fundamental concepts in heterogeneous catalysis.;*.

[44] Terme, D.; Beitrag, S.; Grund, D.; Standpunkte, V. Zur Quantentheorie der Molekeln, **1927,** .

[45] David S. Sholl, J. A. S. *Density Functional Theory: A Practical Introduction;* Wiley & Sons: 2009.

[46] Kohn, W.; Sham, L. J. Self-consistent equations including exchange and correlation effects, *Phys. Rev.* **1965,** *140,* 1133–1138.

[47] López, N.; Almora-Barrios, N.; Carchini, G.; Błoński, P.; Bellarosa, L.; García-Muelas, R.; Novell-Leruth, G.; García-Mota, M. State-of-the-art and challenges in theoretical simulations of heterogeneous catalysis at the microscopic level, *Catal. Sci. Technol.* **2012,** *2,* 2405–2417.

[48] Wang, Y.; Perdew, J. P. Correlation hole of the spin-polarized electron gas, with exact small-wave-vector and high-density scaling, *Phys. Rev. B* **1991,** *44,* 13298–13307.

[49] Ernzerhof, M.; Scuseria, G. E. Assessment of the Perdew-Burke-Ernzerhof exchange-correlation functional, *J. Chem. Phys.* **1999,** *110,* 5029–5036.

[50] Perdew, J. P.; Burke, K.; Ernzerhof, M. Generalized gradient approximation made simple, *Phys. Rev. Lett.* **1996,** *77,* 3865–3868.

[51] Hammer, B.; Hansen, L. B.; Norskov, J. K. Improved adsorption energetics within density-functional theory using revised Perdew-Burke-Ernzerhof functionals, *Phys. Rev. B* **1999,** *59,* 7413–7421.

[52] Bloch, F. Über die quantenmechanik der elektronen in kristallgittern, *Zeitschrift für Physik* **1929,** *52,* 555–600.

[53] Ashcroft, N. W. and Mermin N. D., publisher = Harcourt College Publishers, y. . . *Solid State Physics;*.

[54] Groß, A. *Theoretical surface science;* Springer: 2014.

[55] Monkhorst, H. J.; Pack, J. D. Special points for Brillouin-zone integrations, *Phys. Rev. B* **1976,** *13,* 5188–5192.

[56] Chadi, D. J.; Cohen, M. L. Special points in the Brillouin zone, *Phys. Rev. B* **1973,** *8,* 5747–5753.

[57] Vanderbilt, D. Soft self-consistent pseudopotentials in a generalized eigenvalue formalism, *Phys. Rev. B* **1990,** *41,* 7892.

[58] Joubert, D. From ultrasoft pseudopotentials to the projector augmented-wave method, *Phys. Rev. B* **1999,** *59,* 1758–1775.

[59] Blöchl, P. E. Projector augmented-wave method, *Phys. Rev. B* **1994,** *50,* 17953–17979.

[60] Kresse, G.; Joubert, D. From ultrasoft pseudopotentials to the projector augmented-wave method, *Phys. Rev. B* **1999,** *59,* 1758–1775.

[61] Kresse, G.; Furthmüller, J. Efficiency of ab-initio total energy calculations for metals and semiconductors using a plane-wave basis set, *Comput. Mater. Sci.* **1996,** *6,* 15–50.

[62] Grimme, S.; Antony, J.; Ehrlich, S.; Krieg, H. A consistent and accurate ab initio parametrization of density functional dispersion correction (DFT-D) for the 94 elements H-Pu, *J. Chem. Phys.* **2010,** *132,*.

[63] Perdew, J. P.; Burke, K.; Ernzerhof, M. Generalized gradient approximation made simple, *Phys. Rev. Lett.* **1996,** *77,* 3865–3868.

[64] Chan, K.; Tsai, C.; Hansen, H. A.; Nørskov, J. K. Molybdenum sulfides and selenides as possible electrocatalysts for $CO_2$ reduction, *ChemCatChem* **2014,** *6,* 1899–1905.

[65] Granda-Marulanda, L. P.; Rendón-Calle, A.; Builes, S.; Illas, F.; Koper, M. T.; Calle-Vallejo, F. A semiempirical method to detect and correct DFT-based gas-phase errors and its application in electrocatalysis, *ACS Catal.* **2020,** *10,* 6900–6907.

[66] Álvarez-Moreno, M.; De Graaf, C.; López, N.; Maseras, F.; Poblet, J. M.; Bo, C. Managing the computational chemistry big data problem: The ioChem-BD platform, *J. Chem. Inf. Model.* **2015,** *55,* 95–103.

[67] Peterson, A. A.; Abild-Pedersen, F.; Studt, F.; Rossmeisl, J.; Nørskov, J. K. How copper catalyzes the electroreduction of carbon dioxide into hydrocarbon fuels, *Energy Environ. Sci.* **2010,** *3,* 1311–1315.

[68] Nørskov, J. K.; Rossmeisl, J.; Logadottir, A.; Lindqvist, L.; Kitchin, J. R.; Bligaard, T.; Jónsson, H. Origin of the overpotential for oxygen reduction at a fuel-cell cathode, *J. Phys. Chem. B* **2004,** *108,* 17886–17892.

[69] Bagger, A.; Castelli, I. E.; Hansen, M. H.; Rossmeisl, J. Fundamental atomic insight in electrocatalysis BT-Handbook of materials modeling: Applications: Current and emerging materials. In ; Springer International Publishing: 2020.

[70] Garcia-Ratés, M.; López, N. Multigrid-based methodology for implicit solvation models in periodic DFT, *J. Chem. Theory Comput.* **2016,** *12,* 1331–1341.

[71] Birdja, Y. Y.; Pérez-Gallent, E.; Figueiredo, M. C.; Göttle, A. J.; Calle-Vallejo, F.; Koper, M. T. Advances and challenges in understanding the electrocatalytic conversion of carbon dioxide to fuels, *Nat. Energy* **2019,** *4,* 732–745.

[72] Marcus, R. A. On the theory of electron-transfer reactions. VI. Unified treatment for homogeneous and electrode reactions, *J. Chem. Phys.* **1965,** *43,* 679–701.

[73] Göttle, A. J.; Koper, M. T. Proton-coupled electron transfer in the electrocatalysis of $CO_2$ reduction: prediction of sequential vs. concerted pathways using DFT, *Chem. Sci.* **2016,** *8,* 458–465.

[74] Koper, M. T. Theory of multiple proton-electron transfer reactions and its implications for electrocatalysis, *Chem. Sci.* **2013,** *4,* 2710–2723.

[75] Koper, M. T. Theory of the transition from sequential to concerted electrochemical proton-electron transfer, *Phys. Chem. Chem. Phys.* **2013,** *15,* 1399–1407.

[76] Granda-Marulanda, L. P.; Rendón-Calle, A.; Builes, S.; Illas, F.; Koper, M. T.; Calle-Vallejo, F. A Semiempirical method to detect and correct DFT-based gas-phase errors and its application in electrocatalysis, *ACS Catal.* **2020,** *10,* 6900–6907.

[77] Akhade, S. A.; McCrum, I. T.; Janik, M. J. The impact of specifically adsorbed ions on the Copper-catalyzed electroreduction of $CO_2$ , *J. Electrochem. Soc.* **2016,** *163,* F477–F484.

[78] Pérez-Gallent, E.; Marcandalli, G.; Figueiredo, M. C.; Calle-Vallejo, F.; Koper, M. T. Structure- and potential-dependent cation effects on CO reduction at Copper single-crystal electrodes, *J. Am. Chem. Soc.* **2017,** *139,* 16412–16419.

[79] Ringe, S.; Clark, E. L.; Resasco, J.; Walton, A.; Seger, B.; Bell, A. T.; Chan, K. Understanding cation effects in electrochemical $CO_2$ reduction, *Energy Environ. Sci.* **2019,** *12,* 3001–3014.

[80] Singh, M. R.; Kwon, Y.; Lum, Y.; Ager, J. W.; Bell, A. T. Hydrolysis of electrolyte cations enhances the electrochemical reduction of $CO_2$ over Ag and Cu, *J. Am. Chem. Soc.* **2016,** *138,* 13006–13012.

[81] Resasco, J.; Chen, L. D.; Clark, E.; Tsai, C.; Hahn, C.; Jaramillo, T. F.; Chan, K.; Bell, A. T. Promoter effects of alkali metal cations on the electrochemical reduction of carbon dioxide, *J. Am. Chem. Soc.* **2017,** *139,* 11277–11287.

[82] Hansen, H. A.; Varley, J. B.; Peterson, A. A.; Nørskov, J. K. Understanding trends in the electrocatalytic activity of metals and enzymes for $CO_2$ reduction to CO, *J. Phys. Chem. Lett.* **2013,** *4,* 388–392.

[83] Abild-Pedersen, F.; Greeley, J.; Studt, F.; Rossmeisl, J.; Munter, T. R.; Moses, P. G.; Skúlason, E.; Bligaard, T.; Nørskov, J. K. Scaling properties of adsorption energies for hydrogen-containing molecules on transition-metal surfaces, *Phys. Rev. Lett.* **2007,** *99,* 4–7.

[84] Jones, G.; Studt, F.; Abild-Pedersen, F.; Nørskov, J. K.; Bligaard, T. Scaling relationships for adsorption energies of $C_2$ hydrocarbons on transition metal surfaces, *Chem. Eng. Sci.* **2011,** *66,* 6318–6323.

[85] Fernández, E. M.; Moses, P. G.; Toftelund, A.; Hansen, H. A.; Martínez, J. I.; Abild-Pedersen, F.; Kleis, J.; Hinnemann, B.; Rossmeisl, J.; Bligaard, T.; Nørskov, J. K. Scaling relationships for adsorption energies on transition metal oxide, sulfide, and nitride surfaces, *Angew. Chemie* **2008,** *120,* 4761–4764.

[86] Calle-Vallejo, F.; Martínez, J. I.; García-Lastra, J. M.; Rossmeisl, J.; Koper, M. T. Physical and chemical nature of the scaling relations between adsorption energies of atoms on metal surfaces, *Phys. Rev. Lett.* **2012,** *108,* 1–5.

[87] Ouyang, Y.; Shi, L.; Bai, X.; Li, Q.; Wang, J. Breaking scaling relations for efficient $CO_2$ electrochemical reduction through dual-atom catalysts, *Chem. Sci.* **2020,** *11,* 1807–1813.

[88] Ju, W.; Bagger, A.; Hao, G. P.; Varela, A. S.; Sinev, I.; Bon, V.; Roldan Cuenya, B.; Kaskel, S.; Rossmeisl, J.; Strasser, P. Understanding activity and selectivity of metal-nitrogen-doped carbon catalysts for electrochemical reduction of $CO_2$, *Nat. Commun.* **2017,** *8,* 1–9.

[89] Sabatier, F. *La catalyse en chimie organique;* Berange, Paris, 1920.

[90] Balandin, A. A. The multiplet theory of catalysis, *Energy Factors Catal.* **1964,** *33,* 519–579.

[91] A. A. Balandin, V. A. F.; Tolstopyatova, A. A. The activity of Cadmium oxide as a catalyst for hydrogen dehydrogenation, *Div. Chem. Sci.* **1960,** *9,* 1630–1636.

[92] Medford, A. J.; Vojvodic, A.; Hummelshøj, J. S.; Voss, J.; Abild-Pedersen, F.; Studt, F.; Bligaard, T.; Nilsson, A.; Nørskov, J. K. From the Sabatier principle to a predictive theory of transition-metal heterogeneous catalysis, *J. Catal.* **2015,** *328,* 36–42.

[93] Calle-Vallejo, F.; Koper, M. T. First-principles computational electrochemistry: Achievements and challenges, *Electrochim. Acta* **2012,** *84,* 3–11.

[94] Ardagh, M. A.; Abdelrahman, O. A.; Dauenhauer, P. J. Principles of dynamic heterogeneous catalysis: Surface resonance and turnover frequency response, *ACS Catal.* **2019,** *9,* 6929–6937.

[95] Greeley, J.; Jaramillo, T. F.; Bonde, J.; Chorkendorff, I.; Nørskov, J. K. Computational high-throughput screening of electrocatalytic materials for hydrogen evolution, *Nat. Mater.* **2006,** *5,* 909–913.

[96] Quaino, P.; Juarez, F.; Santos, E.; Schmickler, W. Volcano plots in hydrogen electrocatalysis-uses and abuses, *Beilstein J. Nanotechnol.* **2014,** *5,* 846–854.

[97] Busch, M.; Halck, N. B.; Kramm, U. I.; Siahrostami, S.; Krtil, P.; Rossmeisl, J. Beyond the top of the volcano?-A unified approach to electrocatalytic oxygen reduction and oxygen evolution, *Nano Energy* **2016,** *29,* 126–135.

[98] Man, I. C.; Su, H. Y.; Calle-Vallejo, F.; Hansen, H. A.; Martínez, J. I.; Inoglu, N. G.; Kitchin, J.; Jaramillo, T. F.; Nørskov, J. K.; Rossmeisl, J. Universality in Oxygen Evolution Electrocatalysis on Oxide Surfaces, *ChemCatChem* **2011,** *3,* 1159–1165.

[99] Nørskov, J. K.; Bligaard, T.; Logadottir, A.; Kitchin, J. R.; Chen, J. G.; Pandelov, S.; Stimming, U. Trends in the exchange current for hydrogen evolution, *J. Electrochem. Soc.* **2005,** *152,* J23.

[100] Yang, X. F.; Wang, A.; Qiao, B.; Li, J.; Liu, J.; Zhang, T. Single-atom catalysts: A new frontier in heterogeneous catalysis, *Acc. Chem. Res.* **2013,** *46,* 1740–1748.

[101] Wang, A.; Li, J.; Zhang, T. Heterogeneous single-atom catalysis, *Nat. Rev. Chem.* **2018,** *2,* 65–81.

[102] Flytzani-Stephanopoulos, M.; Gates, B. C. Atomically dispersed supported metal catalysts, *Annu. Rev. Chem. Biomol. Eng.* **2012,** *3,* 545-574.

[103] Ranocchiari, M.; Lothschütz, C.; Grolimund, D.; Van Bokhoven, J. A. Single-atom active sites on metal-organic frameworks, *Proc. R. Soc. A Math. Phys. Eng. Sci.* **2012,** *468,* 1985-1999.

[104] Thomas, J. M.; Raja, R.; Lewis, D. W. Single-site heterogeneous catalysts, *Angew. Chemie - Int. Ed.* **2005,** *44,* 6456–6482.

[105] Single-atom dispersed Co-N-C catalyst: structure identification and performance for hydrogenative coupling of nitroarenes,.

[106] Zitolo, A.; Goellner, V.; Armel, V.; Sougrati, M.-T.; Mineva, T.; Stievano, L.; Fonda, E.; Jaouen, F. Identification of catalytic sites for oxygen reduction in iron- and nitrogen-doped graphene materials.,.

[107] Zitolo, A.; Ranjbar-Sahraie, N.; Mineva, T.; Li, J.; Jia, Q.; Stamatin, S.; Harrington, G. F.; Lyth, S. M.; Krtil, P.; Mukerjee, S.; Fonda, E.; Jaouen, F. Identification of catalytic sites in cobalt-nitrogen-carbon materials for the oxygen reduction reaction, *Nat. Commun.* **2017,** *8,* 1–10.

[108] Zhang, L.; Wang, A.; Wang, W.; Huang, Y.; Liu, X.; Miao, S.; Liu, J.; Zhang, T. Co-N-C catalyst for C-C coupling reactions: On the catalytic performance and active sites, *ACS Catal.* **2015,** *5,* 6563–6572.

[109] Liu, W.; Zhang, L.; Liu, X.; Liu, X.; Yang, X.; Miao, S.; Wang, W.; Wang, A.; Zhang, T. Discriminating catalytically active $FeN_x$ species of atomically dispersed Fe-N-C catalyst for selective oxidation of the C-H bond, *J. Am. Chem. Soc.* **2017,** *139,* 10790–10798.

[110] Zitolo, A.; Ranjbar-Sahraie, N.; Mineva, T.; Li, J.; Jia, Q.; Stamatin, S.; Harrington, G. F.; Lyth, S. M.; Krtil, P.; Mukerjee, S.; Fonda, E.; Jaouen, F. Identification of catalytic sites in cobalt-nitrogen-carbon materials for the oxygen reduction reaction., *Nat. Commun.* **2017,** *8,* 957.

[111] Proietti, E.; Jaouen, F.; Lefévre, M.; Larouche, N.; Tian, J.; Herranz, J.; Dodelet, J.-P. Iron-based cathode catalyst with enhanced power density in polymer electrolyte membrane fuel cells, *Nat. Commun.* **2011,** *2,* 416.

[112] Fan, X.; Peng, Z.; Ye, R.; Zhou, H.; Guo, X. $M_3C$ (M: Fe, Co, Ni) Nanocrystals encased in graphene nanoribbons: An active and stable bifunctional electrocatalyst for oxygen reduction and hydrogen evolution reactions, *ACS Nano* **2015,** *9,* 7407–7418.

[113] Jin, Q.; Ren, B.; Li, D.; Cui, H.; Wang, C. In situ promoting water dissociation kinetic of Co based electrocatalyst for unprecedentedly enhanced hydrogen evolution reaction in alkaline media, *Nano Energy* **2018,** *49,* 14–22.

[114] Jiang, H.; Lin, Y.; Chen, B.; Zhang, Y.; Liu, H.; Duan, X.; Chen, D.; Song, L. Ternary interfacial superstructure enabling extraordinary hydrogen evolution electrocatalysis, *Mater. Today* **2018,** *21,* 602–610.

[115] Huan, T. N.; Ranjbar, N.; Rousse, G.; Sougrati, M.; Zitolo, A.; Mougel, V.; Jaouen, F.; Fontecave, M. Electrochemical reduction of $CO_2$ catalyzed by Fe-N-C materials: A structure-selectivity study, *ACS Catal.* **2017,** *7,* 1520–1525.

[116] Ma, D.-D.; Zhu, Q.-L. MOF-based atomically dispersed metal catalysts: Recent progress towards novel atomic configurations and electrocatalytic applications, *Coord. Chem. Rev.* **2020,** *422,* 213483.

[117] Larrazábal, G. O.; Martín, A. J.; Pérez-Ramírez, J. Building blocks for high performance in electrocatalytic $CO_2$ reduction: Materials, optimization strategies, and device engineering, *J. Phys. Chem. Lett.* **2017,** *8,* 3933–3944.

[118] Zhao, Y.; Liang, J.; Wang, C.; Ma, J.; Wallace, G. G. Tunable and efficient Tin modified Nitrogen-doped carbon nanofibers for electrochemical reduction of aqueous carbon dioxide, *Adv. Energy Mater.* **2018,** *8,* 1702524.

[119] Zhang, C. *et al.* Single-atomic Ruthenium catalytic sites on Nitrogen-doped Graphene for Oxygen reduction reaction in acidic medium, *ACS Nano* **2017,** *11,* 6930–6941.

[120] Wei, S. *et al.* Direct observation of noble metal nanoparticles transforming to thermally stable single atoms, *Nat. Nanotechnol.* **2018,** *13,* 856–861.

[121] Li, X.; Bi, W.; Chen, M.; Sun, Y.; Ju, H.; Yan, W.; Zhu, J.; Wu, X.; Chu, W.; Wu, C.; Xie, Y. Exclusive Ni-$N_4$ sites realize near-unity CO selectivity for electrochemical $CO_2$ reduction, *J. Am. Chem. Soc.* **2017,** *139,* 14889–14892.

[122] Cheng, Y.; Zhao, S.; Johannessen, B.; Veder, J.-P.; Saunders, M.; Rowles, M. R.; Cheng, M.; Liu, C.; Chisholm, M. F.; De Marco, R.; Cheng, H.-M.; Yang, S.-Z.; Jiang, S. P. *Adv. Mater.* **2018,** *30,* 1706287.

[123] Pan, F.; Zhang, H.; Liu, K.; Cullen, D.; More, K.; Wang, M.; Feng, Z.; Wang, G.; Wu, G.; Li, Y. Unveiling active sites of $CO_2$ reduction on Nitrogen-coordinated and atomically dispersed Iron and Cobalt catalysts, *ACS Catal.* **2018,** *8,* 3116–3122.

[124] Hu, X.-M.; Hval, H. H.; Bjerglund, E. T.; Dalgaard, K. J.; Madsen, M. R.; Pohl, M.-M.; Welter, E.; Lamagni, P.; Buhl, K. B.; Bremholm, M.; Beller, M.; Pedersen, S. U.; Skrydstrup, T.; Daasbjerg, K. Selective $CO_2$ reduction to CO in water using earth-abundant metal and nitrogen-doped carbon electrocatalysts, *ACS Catal.* **2018,** *8,* 6255–6264.

[125] Möller, T.; Ju, W.; Bagger, A.; Wang, X.; Luo, F.; Ngo Thanh, T.; Varela, A. S.; Rossmeisl, J.; Strasser, P. Efficient $CO_2$ to CO electrolysis on solid Ni-N-C catalysts at industrial current densities, *Energy Environ. Sci.* **2019,** *12,* 640–647.

[126] Zheng, T.; Jiang, K.; Ta, N.; Hu, Y.; Zeng, J.; Liu, J.; Wang, H. Large-scale and highly selective $CO_2$ electrocatalytic reduction on Nickel single-atom catalyst, *Joule* **2019,** *3,* 265–278.

[127] Jiang, K.; Siahrostami, S.; Zheng, T.; Hu, Y.; Hwang, S.; Stavitski, E.; Peng, Y.; Dynes, J.; Gangisetty, M.; Su, D.; Attenkofer, K.; Wang, H. Isolated Ni single atoms in graphene nanosheets for high-performance $CO_2$ reduction, *Energy Environ. Sci.* **2018,** *11,* 893–903.

[128] Wen, C. F.; Mao, F.; Liu, Y.; Zhang, X. Y.; Fu, H. Q.; Zheng, L. R.; Liu, P. F.; Yang, H. G. Nitrogen-stabilized low-valent Ni motifs for efficient $CO_2$ electrocatalysis, *ACS Catal.* **2020,** *10,* 1086–1093.

[129] Koshy, D. M.; Chen, S.; Lee, D. U.; Stevens, M. B.; Abdellah, A. M.; Dull, S. M.; Chen, G.; Nordlund, D.; Gallo, A.; Hahn, C.; Higgins, D. C.; Bao, Z.; Jaramillo, T. F. Understanding the origin of highly selective $CO_2$ electroreduction to CO on Ni,N-doped carbon catalysts, *Angew. Chemie Int. Ed.* **2020,** *59,* 4043-4050.

[130] Yang, H.; Lin, Q.; Zhang, C.; Yu, X.; Cheng, Z.; Li, G.; Hu, Q.; Ren, X.; Zhang, Q.; Liu, J.; He, C. Carbon dioxide electroreduction on single-atom nickel decorated carbon membranes with industry compatible current densities, *Nat. Commun.* **2020,** *11,* 1–8.

[131] Yan, C.; Li, H.; Ye, Y.; Wu, H.; Cai, F.; Si, R.; Xiao, J.; Miao, S.; Xie, S.; Yang, F.; Li, Y.; Wang, G.; Bao, X. Coordinatively unsaturated Nickel-nitrogen sites towards selective and high-rate $CO_2$ electroreduction, *Energy Environ. Sci.* **2018,** *11,* 1204–1210.

[132] Su, P.; Iwase, K.; Nakanishi, S.; Hashimoto, K.; Kamiya, K. Nickel-nitrogen-modified graphene: An efficient electrocatalyst for the reduction of carbon dioxide to carbon monoxide, *Small* **2016,** *12,* 6083–6089.

[133] Yang, H. B. *et al.* Atomically dispersed Ni(i) as the active site for electrochemical $CO_2$ reduction, *Nat. Energy* **2018,** *3,* 140-147.

[134] Ma, S.; Su, P.; Huang, W.; Jiang, S. P.; Bai, S.; Liu, J. Atomic Ni species anchored N-doped carbon hollow spheres as nanoreactors for efficient electrochemical $CO_2$ reduction, *ChemCatChem* **2019,** *11,* 6092–6098.

[135] Zhao, C.; Dai, X.; Yao, T.; Chen, W.; Wang, X.; Wang, J.; Yang, J.; Wei, S.; Wu, Y.; Li, Y. Ionic exchange of metal-organic frameworks to access single Nickel sites for efficient electroreduction of $CO_2$, *J. Am. Chem. Soc.* **2017,** *139,* 8078–8081.

[136] Yang, J.; Qiu, Z.; Zhao, C.; Wei, W.; Chen, W.; Li, Z.; Qu, Y.; Dong, J.; Luo, J.; Li, Z.; Wu, Y. In situ thermal atomization to convert supported Nickel nanoparticles into surface-bound Nickel single-atom catalysts, *Angew. Chemie Int. Ed.* **2018,** *57,* 14095–14100.

[137] Büchele, S.; Martín, A. J.; Mitchell, S.; Krumeich, F.; Collins, S. M.; Xi, S.; Borgna, A.; Pérez-Ramírez, J. Structure sensitivity and evolution of Nickel-bearing Nitrogen-doped carbons in the electrochemical reduction of $CO_2$, *ACS Catal.* **2020,** *10,* 3444–3454.

[138] Kelly, C. A.; Blinn, E. L.; Camaioni, N.; D'Angelantonio, M.; Mulazzani, Q. G. Mechanism of $CO_2$ and $H^+$ reduction by Ni(cyclam)$^+$ in aqueous solution. A pulse and continuous radiolysis study, *Inorg. Chem.* **1999,** *38,* 1579–1584.

[139] Sullivan, B. P.; Bolinger, C. M.; Conrad, D.; Vining, W. J.; Meyer, T. J. One- and two-electron pathways in the electrocatalytic reduction of $CO_2$ by fac-Re(bpy)$(CO)_3$Cl (bpy=2,2'-bipyridine), *J. Chem. Soc. Chem. Commun.* **1985,** 1414–1416.

[140] Meshitsuka, S.; Ichikawa, M.; Tamaru, K. Electrocatalysis by metal phthalocyanines in the reduction of carbon dioxide, *J. Chem. Soc. Chem. Commun.* **1974,** 158–159.

[141] Birdja, Y. Y.; Shen, J.; Koper, M. T. M. Influence of the metal center of metalloprotoporphyrins on the electrocatalytic $CO_2$ reduction to formic acid, *Catal. Today* **2017,** *288,* 37–47.

[142] Manbeck, G. F.; Fujita, E. A review of iron and cobalt porphyrins, phthalocyanines and related complexes for electrochemical and photochemical reduction of carbon dioxide, *J. Porphyr. Phthalocyanines* **2015,** *19,* 45–64.

[143] Lin, S.; Diercks, C. S.; Zhang, Y.-B.; Kornienko, N.; Nichols, E. M.; Zhao, Y.; Paris, A. R.; Kim, D.; Yang, P.; Yaghi, O. M.; Chang, C. J. Covalent organic frameworks comprising cobalt porphyrins for catalytic $CO_2$ reduction in water, *Science* **2015,** *349,* 1208–1213.

[144] Aga, H.; Aramata, A.; Hisaeda, Y. The electroreduction of carbon dioxide by macrocyclic cobalt complexes chemically modified on a glassy carbon electrode, *J. Electroanal. Chem.* **1997,** *437,* 111–118.

[145] Collin, J. P.; Sauvage, J. P. Electrochemical reduction of carbon dioxide mediated by molecular catalysts, *Coord. Chem. Rev.* **1989,** *93,* 245–268.

[146] Jean, Y. *Molecular orbitals of transition metal complexes;* Oxford: 2005.

[147] Roger G. Burns, *Mineralogical applications of crystal field theory;* Cambridge: 1993.

[148] Togo, A.; Tanaka, I. First principles phonon calculations in materials science, *Scripta Materialia* **2015,** *108,* 1–5.

[149] Ravel, B.; Newville, M. ATHENA, ARTEMIS, HEPHAESTUS: data analysis for X-ray absorption spectroscopy using IFEFFIT., *J. Synchrotron Radiat.* **2005,** *12,* 537–541.

[150] Zagal, J. H.; Koper, M. T. Reactivity descriptors for the activity of molecular $MN_4$ catalysts for the oxygen reduction reaction, *Angew. Chemie - Int. Ed.* **2016,** *55,* 14510–14521.

[151] Lefévre, M.; Dodelet, J. P.; Bertrand, P. Molecular oxygen reduction in PEM fuel cell conditions: ToF-SIMS analysis of Co-based electrocatalysts, *J. Phys. Chem. B* **2005,** *109,* 16718–16724.

[152] Lalande, G.; Cóté, R.; Guay, D.; Dodelet, J. P.; Weng, L. T.; Bertrand, P. Is nitrogen important in the formulation of Fe-based catalysts for oxygen reduction in solid polymer fuel cells?, *Electrochim. Acta* **1997,** *42,* 1379–1388.

[153] Xu, H.; Cheng, D.; Cao, D.; Zeng, X. C. A universal principle for a rational design of single-atom electrocatalysts, *Nat. Catal.* **2018,** *1,* 339–348.

[154] Grosvenor, A. P.; Kobe, B. A.; Biesinger, M. C.; McIntyre, N. S. Investigation of multiplet splitting of Fe 2p XPS spectra and bonding in iron compounds, *Surf. Interface Anal.* **2004,** *36,* 1564–1574.

[155] Huan, T. N.; Ranjbar, N.; Rousse, G.; Sougrati, M.; Zitolo, A.; Mougel, V.; Jaouen, F.; Fontecave, M. Electrochemical reduction of $CO_2$ catalyzed by Fe-N-C materials: A structure-selectivity study, *ACS Catal.* **2017,** *7,* 1520–1525.

[156] Varela, A. S.; Kroschel, M.; Leonard, N. D.; Ju, W.; Steinberg, J.; Bagger, A.; Rossmeisl, J.; Strasser, P. pH effects on the selectivity of the electrocatalytic $CO_2$ reduction on Graphene-embedded Fe-N-C motifs: Bridging concepts between molecular homogeneous and solid-state heterogeneous catalysis, *ACS Energy Lett.* **2018,** *3,* 812–817.

[157] Pan, F.; Zhang, H.; Liu, K.; Cullen, D.; More, K.; Wang, M.; Feng, Z.; Wang, G.; Wu, G.; Li, Y. Unveiling active sites of $CO_2$ reduction on Nitrogen-coordinated and atomically dispersed Iron and Cobalt catalysts, *ACS Catal.* **2018,** *8,* 3116–3122.

[158] Kattel, S.; Atanassov, P.; Kiefer, B. Stability, electronic and magnetic properties of in-plane defects in graphene: A first-principles study, *J. Phys. Chem. C* **2012,** *116,* 8161–8166.

[159] Cheng, Y.; Zhao, S.; Johannessen, B.; Veder, J. P.; Saunders, M.; Rowles, M. R.; Cheng, M.; Liu, C.; Chisholm, M. F.; De Marco, R.; Cheng, H. M.; Yang, S. Z.; Jiang, S. P. Atomically dispersed transition metals on carbon nanotubes with ultrahigh loading for selective electrochemical carbon dioxide reduction, *Adv. Mater.* **2018,** *30,* 1–7.

[160] Zhao, C.; Dai, X.; Yao, T.; Chen, W.; Wang, X.; Wang, J.; Yang, J.; Wei, S.; Wu, Y.; Li, Y. Ionic exchange of metal-organic frameworks to access single Nickel sites for efficient electroreduction of $CO_2$ , *J. Am. Chem. Soc.* **2017,** *139,* 8078–8081.

[161] Ju, W.; Bagger, A.; Hao, G. P.; Varela, A. S.; Sinev, I.; Bon, V.; Roldan Cuenya, B.; Kaskel, S.; Rossmeisl, J.; Strasser, P. Understanding activity and selectivity of metal-nitrogen-doped carbon catalysts for electrochemical reduction of $CO_2$, *Nat. Commun.* **2017,** *8,* 1–9.

[162] Lefévre, M.; Proietti, E.; Jaouen, F.; Dodelet, J.-P. Iron-based catalysts with improved oxygen reduction activity in polymer electrolyte fuel cells, *Science* **2009,** *324,* 71–74.

[163] Jaouen, F.; Lefévre, M.; Dodelet, J.-P.; Cai, M. Heat-treated Fe-N-C catalysts for $O_2$ electroreduction: Are active sites hosted in micropores?,.

[164] Wang, X.; Chen, Z.; Zhao, X.; Yao, T.; Chen, W.; You, R.; Zhao, C.; Wu, G.; Wang, J.; Huang, W.; Yang, J.; Hong, X.; Wei, S.; Wu, Y.; Li, Y. Regulation of coordination number over single Co sites: Triggering the efficient electroreduction of $CO_2$, *Nat. Rev. Chem.* **2018,** *57,* 1944–1948.

[165] Göttle, A. J.; Koper, M. T. M. Determinant role of electrogenerated reactive nucleophilic species on selectivity during reduction of $CO_2$ catalyzed by metalloporphyrins, *Journal of the American Chemical Society* **2018,** *140,* 4826–4834.

[166] Li, J.; Ghoshal, S.; Liang, W.; Sougrati, M.-T.; Jaouen, F.; Halevi, B.; McKinney, S.; McCool, G.; Ma, C.; Yuan, X.; Ma, Z.-F.; Mukerjee, S.; Jia, Q. Structural and mechanistic basis for the high activity of Fe-N-C catalysts toward oxygen reduction, *Energy Environ. Sci.* **2016,** *9,* 2418–2432.

[167] Siahrostami, S.; Jiang, K.; Karamad, M.; Chan, K.; Wang, H.; Nørskov, J. Theoretical investigations into defected Graphene for electrochemical reduction of $CO_2$ , *ACS Sustainable Chemistry & Engineering* **2017,** *5,* 11080–11085.

[168] Weng, Z.; Wu, Y.; Wang, M.; Jiang, J.; Yang, K.; Huo, S.; Wang, X.-F.; Ma, Q.; Brudvig, G. W.; Batista, V. S.; Liang, Y.; Feng, Z.; Wang, H. Active sites of copper-complex catalytic materials for electrochemical carbon dioxide reduction, *Nat. Commun.* **2018,** *9,* 415.

[169] Jiang, K.; Siahrostami, S.; Zheng, T.; Hu, Y.; Hwang, S.; Stavitski, E.; Peng, Y.; Dynes, J.; Gangisetty, M.; Su, D.; Attenkofer, K.; Wang, H. Isolated Ni single atoms in graphene nanosheets for high-performance $CO_2$ reduction, *Energy Environ. Sci.* **2018,** *11,* 893–903.

[170] Hursa, D.; Angelika, A.; Asset, T.; Atanassov, P. Morphological attributes govern carbon dioxide reduction on N-doped carbon electrodes, *Joule* **2019,** *3,* 1719–1733.

[171] Pack, J. D.; Monkhorst, H. J. "special points for Brillouin-zone integrations"-a reply, *Phys. Rev. B* **1977,** *16,* 1748–1749.

[172] Barmparis, G. D.; Lodziana, Z.; Lopez, N.; Remediakis, I. N. Nanoparticle shapes by using Wulff constructions and first-principles calculations, *Beilstein J. Nanotechnol.* **2015,** *6,* 361–368.

[173] Wulff, G. Zur frage der geschwindigkeit des wachsthums und der auflösung der krystallflächen, *Zeitschrift für kristallographie-crystalline materials* **1901,** *34,* 449–530.

[174] Momma, K.; Izumi, F. VESTA3 for three-dimensional visualization of crystal, volumetric and morphology data, *J. Appl. Crystallogr.* **2011,** *44,* 1272-1276.

[175] Barmparis, G. D.; Remediakis, I. N. Dependence on CO adsorption of the shapes of multifaceted gold nanoparticles: A density functional theory, *Phys. Rev. B-Condens. Matter Mater. Phys.* **2012,** *86,* 1–7.

[176] Loffreda, D.; Simon, D.; Sautet, P. Dependence of stretching frequency on surface coverage and adsorbat-adsorbate interactions: A density-functional theory approach of CO on Pd(111), *Surf. Sci.* **1999,** *425,* 68–80.

[177] Ouyang, R.; Liu, J. X.; Li, W. X. Atomistic theory of ostwald ripening and disintegration of supported metal particles under reaction conditions, *J. Am. Chem. Soc.* **2013,** *135,* 1760–1771.

[178] Berkó, A.; Solymosi, F. Adsorption-induced structural changes of Rh supported by $TiO_2$ (110)-(1×2): An STM study, *Study. J. Catal.* **1999,** *183,* 91–101.

[179] Beley, M.; Collin, J. P.; Ruppert, R.; Sauvage, J. P. Electrocatalytic reduction of $CO_2$ by Ni Cyclam$^{2+}$ in water: Study of the factors affecting the efficiency and the selectivity of the process, *ChemInform* **1987,** *18,* 7461–7467.

[180] Millet, M.-M.; Algara-Siller, G.; Wrabetz, S.; Mazheika, A.; Girgsdies, F.; Teschner, D.; Seitz, F.; Tarasov, A.; Levchenko, S. V.; Schlögl, R.; Frei, E. Ni single atom catalysts for $CO_2$ activation, *J. Am. Chem. Soc.* **2019,** *141,* 2451–2461.

[181] Li, Q.; Rellán-Pineiro, M.; Almora-Barrios, N.; Garcia-Ratés, M.; Remediakis, I. N.; López, N. Shape control in concave metal nanoparticles by etching, *Nanoscale* **2017,** *9,* 13089–13094.

[182] Voorhees, P. W. The theory of Ostwald ripening, *J. Stat. Phys.* **1985,** *38,* 231–252.

[183] Dresselhaus, M. S.; Dresselhaus, G.; Saito, R.; Jorio, A. Raman spectroscopy of carbon nanotubes, *Phys. Rep.* **2005,** *409,* 47–99.

[184] Jorio, A.; Pimenta, M. A.; Filho, A. G. S.; Saito, R.; Dresselhaus, G.; Dresselhaus, M. S. Characterizing carbon nanotube samples with resonance Raman scattering, *New J. Phys.* **2003,** *5,* 139.

[185] Herrero, E.; Feliu, J. M.; Blais, S.; Radovic-Hrapovic, Z.; Jerkiewicz, G. Temperature dependence of CO chemisorption and its oxidative desorption on the Pt (111) electrode, *Langmuir* **2000,** *16,* 4779–4783.

[186] Hoque, M. A. *et al.* Water oxidation electrocatalysis using ruthenium coordination oligomers adsorbed on multiwalled carbon nanotubes, *Nat. Chem.* **2020,** *12,* 1060-1066.

[187] Zhao, D.; Zhu, G.; Ding, Y.; Zheng, J. Construction of a different polymer chain structure to study $\pi$-$\pi$ interaction between polymer and reduced graphene oxide, *Polymers* **2018,** *10,* 716.

[188] Nishio, M. The CH/$\pi$ hydrogen bond in chemistry. Conformation, supramolecules, optical resolution and interactions involving carbohydrates, *Phys. Chem. Chem. Phys.* **2011,** *13,* 13873–13900.

[189] Neel, A. J.; Hilton, M. J.; Sigman, M. S.; Toste, F. D. Exploiting noncovalent $\pi$ interactions for catalyst design, *Nature* **2017,** *543,* 637–646.

[190] Wu, Y.; Jiang, Z.; Lu, X.; Liang, Y.; Wang, H. Domino electroreduction of $CO_2$ to methanol on a molecular catalyst, *Nature* **2019,** *575,* 639–642.

[191] Monteiro, M. C. O.; Jacobse, L.; Touzalin, T.; Koper, M. T. M. Mediator-free SECM for probing the diffusion layer pH with functionalized gold ultramicroelectrodes, *Anal. Chem.* **2020,** *92,* 2237–2243.

[192] Wiebe, R.; Gaddy, V. L. The solubility of hydrogen in water at 0, 50, 75 and 100° from 25 to 1000 atmospheres, *J. Am. Chem. Soc.* **1934,** *56,* 76–79.

[193] Olah, G. A. Towards oil independence through renewable methanol chemistry, *Angew. Chemie - Int. Ed.* **2013,** *52,* 104–107.

[194] Nie, X.; Esopi, M. R.; Janik, M. J.; Asthagiri, A. Selectivity of $CO_2$reduction on Copper electrodes: The role of the kinetics of elementary steps, *Angew. Chemie* **2013,** *125,* 2519–2522.

[195] Kuhl, K. P.; Hatsukade, T.; Cave, E. R.; Abram, D. N.; Kibsgaard, J.; Jaramillo, T. F. Electrocatalytic conversion of carbon dioxide to methane and methanol on transition metal surfaces, *J. Am. Chem. Soc.* **2014,** *136,* 14107–14113.

[196] Ju, W.; Bagger, A.; Wang, X.; Tsai, Y.; Luo, F.; Möller, T.; Wang, H.; Rossmeisl, J.; Varela, A. S.; Strasser, P. Unraveling mechanistic reaction pathways of the electrochemical $CO_2$ Reduction on Fe-N-C single-site catalysts, *ACS Energy Lett.* **2019,** *4,* 1663–1671.

[197] Bagger, A.; Ju, W.; Varela, A. S.; Strasser, P.; Rossmeisl, J. Electrochemical $CO_2$ reduction: A classification problem, *ChemPhysChem* **2017,** *18,* 3266–3273.

[198] Hu, X. M.; Rønne, M. H.; Pedersen, S. U.; Skrydstrup, T.; Daasbjerg, K. Enhanced catalytic activity of Cobalt Porphyrin in $CO_2$ electroreduction upon immobilization on carbon materials, *Angew. Chemie - Int. Ed.* **2017,** *56,* 6468–6472.

[199] Marković, N. M.; Schmidt, T. J.; Grgur, B. N.; Gasteiger, H. A.; Behm, R. J.; Ross, P. N. Effect of temperature on surface processes at the Pt (111)-liquid interface: Hydrogen adsorption, oxide formation, and CO oxidation, *J. Phys. Chem. B* **1999,** *103,* 8568–8577.

[200] Grodkowski, J.; Behar, D.; Neta, P.; Hambright, P. Iron porphyrin-catalyzed reduction of $CO_2$. Photochemical and radiation chemical studies, *J. Phys. Chem. A* **1997,** *101,* 248–254.

[201] Behar, D.; Dhanasekaran, T.; Neta, P.; Hosten, C. M.; Ejeh, D.; Hambright, P.; Fujita, E. Cobalt porphyrin catalyzed reduction of $CO_2$. Radiation chemical, photochemical, and electrochemical studies, *J. Phys. Chem. A* **1998,** *102,* 2870–2877.

[202] König, M.; Vaes, J.; Klemm, E.; Pant, D. Solvents and supporting electrolytes in the ectrocatalytic reduction of $CO_2$, *Science* **2019,** *19,* 135–160.

[203] Lim, C. F.; Harrington, D. A.; Marshall, A. T. Effects of mass transfer on the electrocatalytic $CO_2$ reduction on Cu, *Electrochim. Acta* **2017,** *238,* 56–63.

# Publications

UNIVERSITAT ROVIRA I VIRGILI
THEORETICAL STUDIES OF SINGLE-SITE CATALYSTS FOR EFFICIENT ELECTROCHEMICAL CO2 REDUCTION
Paulina Pršlja

ACS Catalysis
Research Article
Cite This: ACS Catal. 2019, 9, 10426−10439
pubs.acs.org/acscatalysis

# Volcano Trend in Electrocatalytic $CO_2$ Reduction Activity over Atomically Dispersed Metal Sites on Nitrogen-Doped Carbon

Jingkun Li,[†] Paulina Pršlja,[‡] Tatsuya Shinagawa,[§,▽] Antonio José Martín Fernández,[§] Frank Krumeich,[∥] Kateryna Artyushkova,[⊥] Plamen Atanassov,[#] Andrea Zitolo,[¶] Yecheng Zhou,[‡] Rodrigo García-Muelas,[‡] Núria López,[‡] Javier Pérez-Ramírez,[§] and Frédéric Jaouen*[,†]

[†]Institut Charles Gerhardt Montpellier, UMR 5253, CNRS, Université Montpellier, ENSCM, Place Eugène Bataillon, 34095 Montpellier Cedex 5, France
[‡]Institute of Chemical Research of Catalonia, ICIQ, The Barcelona Institute of Science and Technology, Av. Països Catalans, 16, 43007 Tarragona, Spain
[§]Institute for Chemical and Bioengineering, Department of Chemistry and Applied Biosciences and [∥]Laboratory of Inorganic Chemistry, Department of Materials, ETH Zurich, Vladimir-Prelog-Weg 1, 8093 Zurich, Switzerland
[⊥]The Department of Chemical and Biological Engineering, Center for Micro-Engineered Materials (CMEM), University of New Mexico, Albuquerque, New Mexico 87131, United States
[#]Chemical and Biomolecular Engineering, University of California Irvine, Irvine, California 92697, United States
[¶]Synchrotron SOLEIL, L'Orme des Merisiers, BP 48 Saint Aubin, 91192 Gif-sur-Yvette, France

Supporting Information

**ABSTRACT:** The development of catalysts for electrochemical reduction of carbon dioxide ($eCO_2RR$) with high activity and selectivity remains a grand challenge to render the technology useable. As promising candidates, metal−nitrogen−carbon (MNC) catalysts with metal atoms present as atomically dispersed metal−$N_x$ moieties ($MN_x$, M = Mn, Fe, Co, Ni, and Cu) were investigated as model catalysts. The distinct activity for CO formation observed along the series of catalysts is attributed to the nature of the transition metal in $MN_x$ moieties because of otherwise similar composition, structure, and morphology of the carbon matrix. We identify a volcano trend between their activity toward CO formation and the nature of the transition metal in $MN_x$ sites, with Fe and/or Co at the top of the volcano, depending on the electrochemical potential. Regarding selectivity, FeNC, NiNC, and MnNC had Faradaic efficiency for CO >80%. To correctly model the active sites in operando conditions, experimental operando X-ray absorption near edge structure spectroscopy was performed to follow changes in the metal oxidation state with electrochemical potential. Co and Mn did not change the oxidation state with potential, whereas Fe and Ni were partially reduced and Cu largely reduced to Cu(0). Computational models then led to the identification of $M^{2+}N_4$−$H_2O$ as the most active centers in FeNC and CoNC, whereas $Ni^{1+}N_4$ was predicted as the most active one in NiNC at the considered potentials of −0.5 and −0.6 V versus the reversible hydrogen electrode. The experimental activity and selectivity could be rationalized from our density functional theory results, identifying in particular the difference between the binding energies for $CO_2^{*-}$ and H* as a descriptor of selectivity toward CO. This in-depth understanding of the activity and selectivity based on the speciation of the metals for $eCO_2RR$ over atomically dispersed $MN_x$ sites provides guidelines for the rational design of MNC catalysts toward $eCO_2RR$ for their application in high-performance devices.

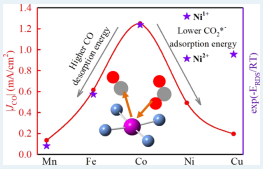


**KEYWORDS:** *$CO_2$ electroreduction, $CO_2$ activation, MNC catalyst, single-atom catalyst, metal−$N_4$, electrocatalysis*

## 1. INTRODUCTION

Global climate change triggered by anthropogenic emission of $CO_2$ is a growing threat to society. Direct electrochemical reduction of $CO_2$ ($eCO_2RR$) to produce value-added chemicals and fuels using renewable electricity is a promising strategy for closing the carbon cycle. However, this early-stage technology is challenged by the low activity and selectivity because of the extremely stable C═O bond (806 kJ $mol^{-1}$) in $CO_2$ and the competing hydrogen evolution reaction (HER) in aqueous electrolytes.[1,2] Thus, it is of paramount importance to identify robust catalysts with economically viable current density at low overpotential and high selectivity toward $eCO_2RR$.

Large ensembles of crystallographically ordered metal atoms (reduced metals, metal-oxides, chalcogenides, metal-oxide@metal core@shell, etc.) have hitherto been the most studied

Received: June 20, 2019
Revised: September 5, 2019
Published: October 2, 2019

  

DOI: 10.1021/acscatal.9b02594
ACS Catal. 2019, 9, 10426−10439

family of $eCO_2RR$ catalytic sites. They can be categorized into four types, according to their main $eCO_2RR$ products and/or selectivity:[3−5] (1) formate or formic acid for catalytic sites with low binding energy for $CO_2^{*-}$ (typical examples are ensembles based on Sn or Pb); (2) CO for catalytic sites with strong COOH* binding but weak CO* binding (typical examples are metallic surfaces such as Au, Ag); (3) products corresponding to 4−12 electron reduction (HCHO, $CH_3OH$, $CH_4$, $C_2H_4$, $C_2H_5OH$) for catalytic sites with less weak CO* binding energy (metallic Cu is an outstanding material for achieving this); (4) catalytic sites with low selectivity toward $eCO_2RR$, with $H_2$ as the main product (such as Pt or Ni metallic surfaces).

A second family of $eCO_2RR$ catalysts involves active sites based on a single metal-atom coordinated only with nonmetal elements. In this family, the subgroup of molecular catalysts with a well-defined metal coordination have been studied since the 1970s and have shown promising properties for $eCO_2RR$.[5] In particular, some transition-metal phthalocyanines and porphyrins with well-defined square-planar $MN_4$ structure presented high selectivity toward CO formation.[6−9] The electroreduction of $CO_2$ to CO ($CO_2 + 2H^+ + 2e^- \rightarrow CO + H_2O$) with standard electrochemical potential of −0.11 V versus a reversible hydrogen electrode (RHE) is attractive as it requires the transfer of only two electrons, leading to lower activation barriers than for hydrocarbon formation.[4] Together with formic acid, CO has thus been identified as the economically most appealing product of $eCO_2RR$.[2,4] Moreover, the simultaneous production of CO and $H_2$ (syngas) in appropriate composition during $eCO_2RR$ on surfaces with multiple catalytic sites may be used to prepare synthetic fuels via a downstream Fischer−Tropsch process.[10] Molecular catalysts however have several disadvantages, such as cost related to their synthesis, lower operando stability because of metal leaching or chemical degradation, and poor electrical connection with the conductive support, impeding reaching high current densities in a $CO_2$/water electrolyzer.[11,12]

As a second subgroup of catalysts with single metal-atom sites for $eCO_2RR$, metal−nitrogen−carbon (MNC) materials exclusively comprising atomically dispersed transition-metal cations covalently bonded with nitrogen atoms ($MN_x$ moieties) hold promise to overcome the above disadvantages of molecular catalysts while retaining high activity and selectivity toward CO formation.[13−21] The metal-ion coordination in MNC materials resembles the local patterns existing in metal−$N_4$ macrocycles. Such materials were initially developed for catalyzing the oxygen reduction reaction (ORR), in particular in acidic medium, with focus on the $FeN_x$ and $CoN_x$ as other $MN_x$ motives have a much lower ORR activity.[22−25] MNC materials are prepared via the self-assembly of metal, nitrogen, and carbon atoms at a high temperature. However, the elevated temperature and excess of metal often lead to the formation of clusters of metal atoms (metallic, metal-oxide, metal-carbide, etc.) along with the $MN_x$ sites.[26−28] This has for a long time impeded the elucidation of the $MN_x$ site structures and their ORR catalytic activities.[25] In the context of $eCO_2RR$, the presence of metal clusters along with $MN_x$ moieties may, depending on the nature of the metal, catalyze the HER[10,29−31] and/or other pathways of $eCO_2RR$. This has prevented establishing clear experimental structure-to-property relationships between the nature of the metal in $MN_x$ and their activity and selectivity toward $eCO_2RR$. In addition, the presence of even a minute amount of metallic clusters in MNC catalysts also impedes a reliable comparison between experimental $eCO_2RR$ activity/selectivity trends for such materials and density functional theory (DFT) results obtained on $MN_4$ sites.[32−34] Validation of DFT predictions on a reasonably large series of model materials is highly important to speed up the rational identification of more promising MNC candidates for $eCO_2RR$,[2] given that the library of metals demonstrated to form $MN_x$ sites in carbon has been recently expanded also to heavier elements such as Sn,[35] Ru,[36] Pt,[37] Pd,[37] and so on. The investigation of model MNC catalysts exclusively comprising atomically dispersed $MN_x$ sites is thus critical to understand their structure−performance relationships and to identify the proper activity/selectivity descriptor(s). Whereas numerous studies have now reported the $eCO_2RR$ selectivity of some atomically dispersed MNC catalysts prepared by different synthetic approaches,[13,16,20,38] a single study has, to the best of our knowledge, compared the trends in activity and selectivity for a narrow family of three atomically dispersed MNC catalysts prepared identically except for the nature of the metal element.[21] The synthesis leaned toward silica templating of *o*-phenylenediamine and Fe, Co, or Ni salts. Whereas metal particles formed in parallel to $MN_x$ sites during the first pyrolysis, they could be removed during subsequent NaOH etching and acid-wash steps. However, the formation of metallic particles during the first pyrolysis leads to markedly different pore size distributions, in particular for CoNC. This rendered the comparison of the materials more complex because of expectedly different utilizations of the $MN_x$ sites for different pore size distributions.

Herein, we applied a robust synthesis approach involving a sacrificial Zn-based metal−organic framework (MOF) and a metal salt (Mn, Fe, Co, Ni, or Cu) that resulted in the complete integration of the metal atoms as atomically dispersed $MN_x$ moieties in the N-doped carbon matrix derived from the MOF, without formation of metallic particles. With this series of five model MNC catalysts, a volcano trend in their catalytic activity toward $CO_2$ electroreduction to CO could be revealed for the first time, with the $CoN_4$ moieties exhibiting the highest intrinsic activity at −0.6 V versus RHE. Our operando spectroscopy characterization and DFT models further reveal the importance of the speciation of the metal center under reaction conditions in order to correctly interpret and predict the competition between $CO_2$ activation, CO and H adsorption, thus providing a more accurate understanding of the activity of $eCO_2RR$ toward CO over $MN_x$ motives.

## 2. EXPERIMENTAL METHODS

**2.1. Catalyst Synthesis.** All catalyst precursors were prepared via dry ball-milling of the Zn(II) zeolitic imidazolate framework (Basolite Z1200 from BASF, labeled ZIF-8), $M^{2+}$ acetate (M = Mn, Fe, Co, Ni, and Cu), and 1,10-phenanthroline. 1,10-phenanthroline (200 mg), 800 mg of ZIF-8, and a certain amount of $M^{2+}$ acetate corresponding to 0.5 wt % transition metal in the total precursor were weighed and poured into a $ZrO_2$ crucible with 100 zirconium-oxide balls of 5 mm diameter. The $ZrO_2$ crucible was then sealed under air and placed in a planetary ball-miller (Fritsch Pulverisette 7 Premium, Fritsch, Idar-Oberstein, Germany). The powders were milled for four cycles of 30 min at 400 rpm milling speed. The catalyst precursors resulting from the milling were pyrolyzed at 1050 °C in Ar for 1 h. The obtained catalysts were labeled MNC. A control sample was also



DOI: 10.1021/acscatal.9b02594
ACS Catal. 2019, 9, 10426−10439

synthesized according to this process, except that no separate metal acetate was added (labeled (Zn)NC).

**2.2. Scanning Transmission Electron Microscopy.** For the scanning transmission electron microscopy (STEM) investigations, the material was dispersed in ethanol and a few drops of the suspension deposited onto a perforated carbon foil supported on a copper grid. After evaporation of the ethanol, the grid was mounted on the single tilt holder of the microscope. STEM images were recorded on an aberration-corrected HD2700CS (Hitachi) with a high-angle annular dark-field detector (HAADF). CuNC was measured on a Mo grid to avoid the Cu stray radiation from the TEM grid. STEM combined with energy-dispersive X-ray (EDX) spectroscopy was performed on a Talos F200X microscope (ThermoFisher) with a high brightness field emission gun operated at an acceleration potential of 200 kV. The EDX system of this microscope consists of four silicon drift detectors, which enables one to record EDX maps with good signal to noise ratio in a relatively short collection time (here 10−20 min).

**2.3. X-ray Diffraction.** X-ray diffraction (XRD) patterns were obtained using a PANanalytical X'Pert Pro powder X-ray diffractometer with Cu K$\alpha$ radiation.

**2.4. X-ray Absorption Spectroscopy.** Metal K-edge X-ray absorption spectroscopy (XAS) was conducted at room temperature at SAMBA beamline (Synchrotron SOLEIL). The beamline is equipped with a sagittally focusing Si 220 monochromator and two Pd-coated mirrors that were used to remove X-rays harmonics. The catalysts were pelletized as disks of 10 mm diameter with 1 mm thickness using Teflon powder (1 $\mu$m particle size) as a binder. The detailed analysis method for the extended X-ray absorption fine structure (EXAFS) data can be found elsewhere.[24,25]

For operando XAS measurements, catalyst inks were prepared by mixing 10 mg of catalyst with 50 $\mu$L of deionized water and 100 $\mu$L of 5 wt % Nafion solution with ultrasound. A 50 $\mu$L aliquot was then pipetted on a ∼3 $cm^2$ circular area of a 100 $\mu$m thick graphite foil (Goodfellow cat. C 000200/2), resulting in a catalyst loading of ∼1 mg $cm^{-2}$. The graphite foil then served as a working electrode, and was installed in an electrochemical cell[24] (PECC2, from Zahner) with an Ag/AgCl (saturated KCl) reference electrode, a Pt counter electrode, and $CO_2$-saturated 0.1 M $KHCO_3$ electrolyte. Operando measurements were performed by recording the K$\alpha$ X-ray fluorescence of Fe with a Canberra 35-elements monolithic planar Ge pixel array detector.

**2.5. X-ray Photoelectron Spectroscopy.** X-ray photoelectron spectroscopy (XPS) spectra were acquired on a Kratos Axis DLD Ultra-X-ray photoelectron spectrometer using an Al K$\alpha$ source monochromatic operating at 150 W with no charge compensation. The base pressure was about $2 \times 10^{-10}$ Torr and the operating pressure was around $2 \times 10^{-9}$ Torr. Survey and high-resolution spectra were obtained at pass energies of 80 and 20 eV, respectively. Acquisition times were 2 min for survey spectra, 3 min for C 1s spectra, and 40 min for N 1s and M 2p spectra. Data analysis and quantification were performed using CasaXPS software. A linear background subtraction was used for quantification of C 1s, O 1s, and N 1s spectra, whereas a Shirley background was applied to the M 2p spectra. Sensitivity factors provided by the manufacturer were utilized to obtain atomic percentages of Fe, N, C, and O present in samples, and the elemental percentage reported was the average of five spots per sample. A 70% Gaussian/30% Lorentzian line shape was utilized in the curve fitting. Averages from three areas per sample were presented. N 1s spectra were fitted with a set of components with a fixed energy position, in accordance with a previous study.[39] The fitting components are assigned to pyridinic N (398.8 eV), N in $MN_x$ moieties (398.8−399.9 eV), pyrrolic and hydrogenated N (400.7 eV), graphitic N (401.8 and 402.7 eV), and N-oxide (404.3 and 405.6 eV).

**2.6. Scanning Electron Microscopy.** Scanning electron microscopy (SEM) micrographs were obtained with a Hitachi S-4800 apparatus (Hitachi, Tokyo, Japan).

**2.7. $N_2$ Physisorption.** $N_2$ physisorption analysis was performed at liquid nitrogen temperature (77 K) with a Micromeritics ASAP 2020 instrument. Prior to the measurements, MNC materials were degassed at 200 °C for 5 h in flowing nitrogen to remove guest molecules or moisture.

**2.8. Raman Spectroscopy.** Raman spectra were collected using a LabRAM ARAMIS Raman microscope with a 473 nm laser.

**2.9. Linear Scan Voltammetry.** Catalyst powders were deposited on glassy carbon as the working electrode. Catalyst inks were prepared by dispersing 10 mg of catalyst in a mixture of Millipore water (36.5 $\mu$L, 18.2 MΩ cm) and ethanol (300 $\mu$L, Sigma-Aldrich, 99.8%), into which 5 wt % Nafion solution (108.5 $\mu$L, Sigma-Aldrich) was added as a binder. The ink was sonicated for 60 min, and an aliquot of 7 $\mu$L was dropcast onto glassy carbon (0.196 $cm^2$, Pine instrument), to reach 800 $\mu$g $cm^{-2}$ loading. The resulting working electrode was used in a three-electrode cell setup connected to a bipotentiostat (Biologic SP 300) and rotator (Pine Instruments). A graphite rod and Ag/AgCl (saturated KCl) were used as counter and reference electrodes, respectively. e$CO_2$RR activity was measured in $CO_2$-saturated 0.1 M $KHCO_3$ (pH = 6.7), and a 0.1 M $N_2$-saturated $KH_2PO_4/K_2HPO_4$ buffer solution (pH = 6.7) was used as $CO_2$-free blank. Linear scan voltammetry (LSV) was carried out from −0.6 to −1.4 V versus Ag/AgCl with a scan rate of 5 mV $s^{-1}$ at 1600 rpm. The change of potential scale versus RHE was done according to the following equation

$$E(\text{V vs RHE}) = E(\text{V vs Ag/AgCl}) + E(\text{V of Ag/AgCl vs NHE}) + 0.059 \times \text{pH} \quad (1)$$

where $E$ (V of Ag/AgCl vs NHE) = 0.199 V.

**2.10. Chronoamperometry and Product Analysis.** Catalysts were deposited on carbon gas diffusion layers (GDLs) by airbrushing. The ink was prepared by dispersing 50 mg of catalyst powder in a mixture of Millipore water (4 mL, 18.2 MΩ cm) and 2-propanol (4 mL, Sigma-Aldrich, 99.8%), into which 5 wt % Nafion solution (50 $\mu$L, Sigma-Aldrich) was added as a binder. The ink was sonicated for 15 min, and then sprayed onto the GDL (Sigracet 39BC, SGL Group) with an airbrush (Iwata Eclipse HP-SBS) at 353 K. The loading was 0.64 mg $cm^{-2}$ in average, with a standard deviation of 0.03 for all prepared electrodes.

A custom gas-tight glass cell with two compartments separated by a Nafion 212 membrane (Alfa Aesar, 0.05 mm thickness) was employed for the electrochemical study. Both catholyte and anolyte chambers were filled with 40 $cm^3$ of a 0.1 M $KHCO_3$ solution (Sigma-Aldrich, 99.95% trace metals basis) prepared with ultrapure water. Before (20 min) and



DOI: 10.1021/acscatal.9b02594
ACS Catal. 2019, 9, 10426−10439

during the measurement, $CO_2$ (Messer, purity 4.8) was supplied to the catholyte at a flow rate of 20 $cm^3$ $min^{-1}$, resulting in a pH level of 6.7. A Pt wire and an Ag/AgCl (3.0 M KCl) electrode were used as counter and reference electrodes, respectively. The geometric surface area of the working electrodes was in the range of 1−6 $cm^2$, accurately quantified for each electrode with the ImageJ image processing and analysis software (Wayne Rasband, National Institutes of Health). All measurements were performed using an Autolab PGSTAT302N potentiostat at room temperature. The double layer capacitance of the electrodes was assessed by cyclic voltammetry (CV) at varying scan rates in the potential range of open circuit potential (OCP) ±15 mV and performing a linear fit only in the region of scan rates where a straight line between electric charge and scan rate is observed. The performance of the prepared electrodes for $eCO_2RR$ was investigated by chronoamperometry (CA) at −0.5 and −0.6 V versus RHE for 1.5 h. These potentials were chosen because they result in sufficient currents to quantify the formed $eCO_2RR$ products with high precision while at the same time avoiding excessive Faradaic reduction currents, which would otherwise lead to mass-transport limitations and local pH changes, implying that the measured current would not only be controlled by electrochemical kinetics but by other factors as well.[40] CAs were performed with the *i*R compensation function set at 85% of the uncompensated resistance ($R_u$), which was determined before the start of the CAs and updated every 10 min by potentiostatic electrochemical impedance spectroscopy at the electrolysis potential (100 kHz, 10 mV amplitude). The remaining 15% of the *i*R loss was corrected manually by the $R_u$ measured by the impedance spectroscopy. Current densities were normalized by the geometric surface area.

Gaseous products were analyzed using an on-line gas chromatograph (SRI 8610C, Multi-Gas #3 configuration) with Ar as a carrier gas, which was equipped with a HayeSep D column and a Molecular Sieve 13× column. Gas samples were injected through a sampling loop and analyzed 10 min after the start of the electrolysis and thereafter every 15 min. The Faradaic efficiency (FE) for the gaseous products was calculated with the following equation

$$\mathrm{FE} = \frac{\text{gas flow through the cell} \times \text{concentration of the product}}{\text{electric current at sampling time}/nF} \times 100 \quad (2)$$

Liquid products were examined with a high-performance liquid chromatograph in a Merck LaChrom system equipped with a Bio-Rad Aminex HPX-87H column heated at 333 K and a refractive index detector (Hitachi Chromaster 5450), using 5 mM $H_2SO_4$ as eluent. The FE for the liquid products was quantified by analyzing the catholyte after the test using the following equation

$$\mathrm{FE} = \frac{\text{catholyte volume} \times \text{concentration of the product}}{\text{total charge passed during the electrolysis}/nF} \times 100 \quad (3)$$

In the above equations, $n$ is the number of electrons transferred and $F$ is the Faraday constant.

**2.11. Computational Details.** All calculations were performed using spin-polarized DFT as implemented in the Vienna Ab initio Simulation Package (VASP).[41,42] The GGA PBE-D3 was the functional of choice.[43,44] Core electrons were described by the projector augmented wave,[42,45] and valence electrons were expanded by plane wave basis sets with a kinetic energy cut-off of 500 eV. To model atomically dispersed metal−$N_x$ carbon structures, we used graphene layer expanded in a (6 × 6) supercell replacing four C atoms by nitrogens and removing two C atoms to compensate for the valence. These layers were interleaved by 12 Å vacuum along the $z$ direction. Various transition metal atoms (M = Mn, Fe, Co, Ni, Cu, Zn) were placed in the cavity left on the carbon sheet. In this configuration, two axial positions are empty. However, most of these atoms prefer octahedral coordinations,[46] and thus water-derived ligands (L = none, $H_2O$, OH, O) typically occupy one of the axial positions in aqueous electrolytes. The empty coordination site is then employed to investigate the competitive $eCO_2RR$ and HER. Structures were relaxed with a force threshold of 0.05 eV/Å. The Brillouin zone was sampled using a 3 × 3 × 1 *k*-point mesh generated with the Monkhorst−Pack method.[47] To obtain the energies of the relevant intermediates in the electrochemical environment, the computational hydrogen electrode (CHE) was used.[48,49] The speciation of the different oxidation states of the metals in the carbon lattice was performed via a Pourbaix diagram derived with Phonopy.[50] The optimized structures can be retrieved from ioChem-BD.[51,52]

## 3. RESULTS

**3.1. Structural Characterization of Pristine Catalysts.** Leaning on the synthetic route developed by our group for the preparation of FeNC and CoNC materials that exclusively comprise $MN_x$ moieties,[24,25] we expanded it to prepare MnNC, NiNC, and CuNC materials. A control sample was synthesized by the same approach without the addition of divalent metal acetate, and was labeled (Zn)NC, with (Zn) indicating the possible presence of residual Zn from ZIF-8, as discussed later. The MNC materials were first characterized by HAADF-STEM. Multiple areas of the samples were examined, and no metallic particles could be observed (Figure 1). The absence of crystalline metallic species in as-prepared MNC materials was further confirmed by powder XRD (Figure S1), exhibiting only two broad reflection peaks typical for nanometric graphite-like domains present in amorphous N-doped carbon materials. Elemental mapping with EDX spectroscopy showed a homogenous distribution of the metal, C and N atoms in the catalysts, revealing also the presence of residual Zn from ZIF-8 in all five MNC catalysts (Figure S2). These STEM and EDX analyses indicate that the metals are probably atomically dispersed in the nitrogen-doped carbon matrix. However, because of limited resolution of the EDX mapping, nano- or sub-nano-sized metal clusters cannot be excluded at this stage.

In order to unambiguously demonstrate the absence of metal clusters and to identify the metal coordination and bond distances in atomically dispersed $MN_x$ sites, we resorted to EXAFS spectroscopy (Figure 2). The Fourier transform (FT) of the ex situ EXAFS spectra [$\kappa^2$ weighted $\chi(\kappa)$] of all MNC catalysts at their respective metal K-edge energy exhibited a major peak at ∼1.5 Å, attributed to the backscattering by light atoms (C, N, or O) situated in the first coordination shell of the absorbing metal. The secondary peak(s) at 2−3 Å is associated with the contribution of carbon (or N, O) atoms in the second coordination sphere of the metal center. The FT-EXAFS spectra of the MNC catalysts agree well with those of



DOI: 10.1021/acscatal.9b02594
ACS Catal. 2019, 9, 10426−10439

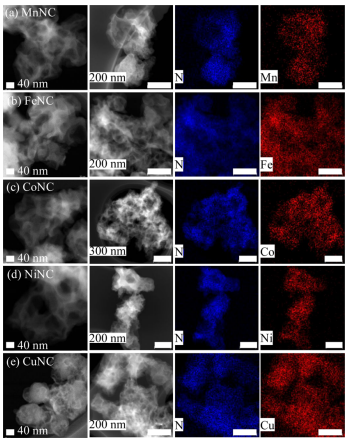


**Figure 1.** MNC catalyst morphology: high-resolution TEM characterization. TEM images and EDX elemental mappings for N and the respective metal derived from the metal-acetate precursor of (a) MnNC, (b) FeNC, (c) CoNC, (d) NiNC, and (e) CuNC.

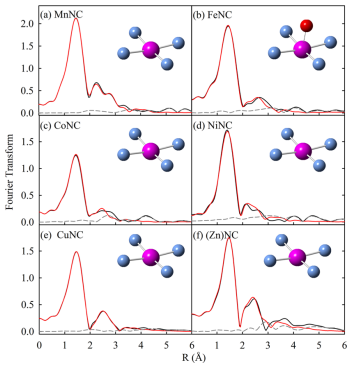


**Figure 2.** Atomically dispersed $MN_x$ sites: metal K-edge EXAFS analysis. (a) MnNC, (b) FeNC, (c) CoNC, (d) NiNC, (e) CuNC, and (f) (Zn)NC. The black curves represent the experimental spectra, whereas the red curves represent calculated spectra based on the depicted structures. The dashed gray curves are the difference between experimental and calculated spectra. Metal, nitrogen, and oxygen atoms are represented in purple, blue, and red, respectively (carbon atoms in the second coordination sphere are not shown). No phase-shift correction was applied to the FTs.

some atomically dispersed MNC materials previously reported by other groups.[13,20]

The metal K-edge EXAFS spectra were then fitted with the model structures depicted in the insets of Figure 2. For CoNC, NiNC, and CuNC, a variable number of in-plane nitrogen atoms binding the metal−cation center were allowed for the fitting, while the spectra of FeNC and MnNC were fitted assuming the presence of four in-plane nitrogen atoms, and either one or two oxygen atoms as axial ligands. This approach was used to reduce the number of EXAFS parameters in the fit, as $FeN_x$ and $MnN_x$ moieties have a higher affinity to oxygen compared to other metal−$N_4$ moieties.[53] The structural parameters obtained from the fittings are shown in Table 1, including the coordination number (CN) and M−N bond distances. The best-fit results show a CN-value of ∼4 for MnNC, CoNC, NiNC, and CuNC, suggesting that the vast majority of metal cations in these catalysts could be involved in $MN_4$ moieties. EXAFS alone however cannot distinguish between N, C, and O atoms, which means that the CN value of 4 may also be acceptable, from a structural viewpoint, with a mix of N, C, and O atoms. From a chemical viewpoint however, metal−nitrogen bonds in the first coordination sphere are more likely than metal−carbon or metal−oxygen ones. For Fe and Co, time-of-flight secondary-ion mass spectroscopy revealed the major presence of $MN_2C_y^+$, $MN_4C_y^+$.[54] Experimentally, it has also been shown that nitrogen is critical for the formation of single Fe atom site in a carbon support during pyrolysis, only metallic Fe particles being observed in the absence of nitrogen in the synthesis.[55] For other metals of the 3d row, although less experimental characterization has been reported yet, DFT predicts higher energy stability for metal−$N_4$ defects in graphene than metal−$C_4$ defects.[56] For those reasons, we started by investigating in-plane $MN_4$ sites in our DFT study to explain the reactivity, as reported in Section 4.2. With the starting hypothesis of the in-plane $FeN_4$ site, the higher average CN-value of 5−6 for FeNC[22,25] strongly suggests that one or two axial O atoms are adsorbed on top of $FeN_4$ moieties, resulting in coordinatively saturated iron cations, in line with the high oxophilicity of Fe.

It should be noted that $ZnN_x$ moieties with an average CN of ∼4 are present not only in the control sample (Zn)NC (Figure 2f and Table 1) but also in all five MNC samples. The Zn K-edge X-ray absorption near edge structure (XANES) and EXAFS spectra of the five samples are identical to that recorded for (Zn)NC (Figure S3), implying that the $ZnN_x$ coordination is unaffected by the presence of a second metal. The coexistence of $ZnN_x$ and $MN_x$ moieties is another indication that the metal content (from metal acetate) is not saturating the material, explaining the absence of metallic particles. In summary, the EXAFS spectra were fitted with in-plane $MN_4$ structures, with an axial oxygen atom needed to obtain a best-fit only for FeNC. Most important, no M−M backscattering signal was needed to get an excellent EXAFS fit, unambiguously indicating the isolated nature of the metal centers.

The metal−nitrogen bond distance and K-edge EXAFS spectra were also calculated ab initio for $MN_4C_{10}$ model sites (10 in-plane carbon atoms in the second coordination sphere) in graphene sheets, with or without axial oxygen adsorbates (Figure S4). Considering water as an oxygen ligand, $MnN_4$ (2.40 Å), $FeN_4$ (2.33 Å), $CoN_4$ (2.31 Å), and $ZnN_4$ (2.35 Å) exhibited similar M−O bond distance between 2.31 and 2.40 Å (Table S1). No water could be stabilized on the $CuN_4$ and $NiN_4$ models. The DFT-calculated EXAFS spectra shown in Figure S5 have characteristic features analogous to those of the experimental FT-EXAFS spectra in Figure 2 with a main peak assigned to N or O back-scattering from the first coordination sphere. The calculated and experimental M−N distances are


DOI: 10.1021/acscatal.9b02594
ACS Catal. 2019, 9, 10426−10439

**Table 1. Structural Parameters Obtained from the Analysis with $MN_x$ Moieties of the Metal K-Edge EXAFS Spectra and DFT Calculations**[a]

| | MnNC | FeNC | CoNC | NiNC | CuNC | (Zn)NC |
|---|---|---|---|---|---|---|
| $R_{M-N}$ (Å) | 1.89(1) | 1.99(2)/2.01(2) | 1.96(2) | 1.92(1) | 1.94(1) | 2.00(1) |
| $\sigma^2$ (Å$^2$) | 0.0033(4) | 0.008(2) | 0.008(2) | 0.007(1) | 0.0072(7) | 0.0056(3) |
| CN | 4 | 5/6 | 3.8(6) | 4.3(3) | 3.9(3) | 4.1(4) |
| $R^e_{M-N}$ (Å) | 1.91 | 1.89 | 1.89 | 1.88 | 1.93 | 1.96 |

[a] $R_{M-N}$ is the metal−nitrogen bond distance, $\sigma^2$ the Debye−Waller factor, and CN the coordination number, obtained from EXAFS fitting, whereas $R^e_{M-N}$ is the DFT simulated metal−nitrogen bond distance for $MN_4C_{10}$ model sites. Errors are given in brackets, for example, 1.89(1) means 1.88−1.90.

also in good agreement, except for Fe, for which the EXAFS fitting is complicated by the presence of axial oxygen ligands (Tables 1 and S1).

The oxidation state of the atomically dispersed metal centers was then investigated with XPS. No signal related to metal(0) state could be observed in the M 2p spectra. The narrow-scan spectra in the binding energy regions corresponding to the M $2p_{3/2}$ spin−orbit couplings are shown in Figure 3. They

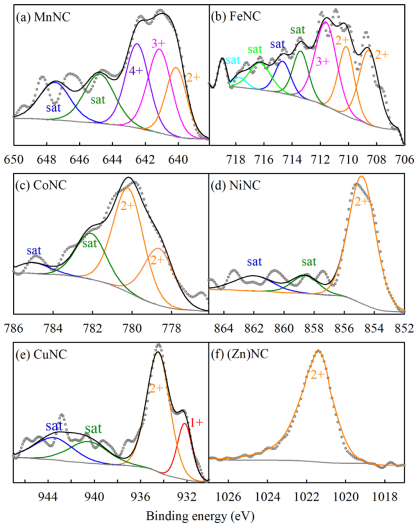


**Figure 3.** XPS characterization. Metal 2p spectra of (a) MnNC, (b) FeNC, (c) CoNC, (d) NiNC, (e) CuNC, and (f) (Zn)NC.

identify the coexistence of $M^{2+}$ and $M^{3+}$ species for FeNC, and the coexistence of $M^+$ and $M^{2+}$ species for CuNC.[57,58] Only the 2+ oxidation state is observed in CoNC, NiNC, and (Zn)NC, whereas for MnNC, the three different oxidation states 2+, 3+, and 4+ seem to be present.[59−61] The existence of different oxidation states of the metal in a same catalyst reveals a structural and/or a topological heterogeneity of $MN_x$ moieties. For example, higher oxidation states of the metal−cation might be triggered by oxygen ($O_2$, OH) adsorbates, which is possible only for $MN_x$ moieties located on the top surface, whereas those located in the bulk of the nitrogen-doped carbon matrix are not accessible. Chemical heterogeneity might also lead to different oxidation states for a same structure. For example, whereas an average $MN_4$ structure was identified from our EXAFS analysis for all materials except FeNC (with additional oxygen adsorbates on top of the $FeN_4$ site itself), EXAFS cannot distinguish between N, O, and C atoms in the first coordination sphere, implying that, for example, $MN_2O_2$ moieties or any other combination with a total of four in-plane ligating atoms among C, N, and/or O are also possible structural candidates from an EXAFS viewpoint. Whereas the energetic stability of such moieties is usually lower than $MN_4$,[62,63] their existence as minor species cannot be excluded. For MnNC in particular, the presence of high valence-state metal (4+) suggests that there might be some O atoms replacing N atoms in $MnN_4$ moieties. This will be re-discussed later.

The elemental content of the catalysts was quantified from XPS signals. All MNC catalysts have similar C, N, and O absolute contents, whereas the metal contents are in the range 0.16−0.27 at. %, except Zn in the range of 0.11 to 0.38 at. % (Table S2). The average nitrogen chemistry is similar for all five MNC catalysts with similar relative concentrations of different N species observed, as shown in Figure S6 and Table S3. Nitrogen−transition metal interactions are being expressed as a singular peak in the N 1s fine resolution spectra. Interactions of transition metal with 2, 3, or 4 co-planar N atoms are indistinguishable within the resolution of the peak composition analysis, as well as different transition metals studied here produce a de-facto identical shift, and the spectral component is commonly addressed here as $M-N_x$ (Figure S6). Nevertheless, a positive correlation was found between the N content and the total metal content of selected samples (Figure S7), with the linear fitting results for selected samples CuNC, ZnNC, NiNC and CoNC. MnNC was not included as we demonstrate that the first sphere coordination of Mn probably involves both O and N atoms (details will be discussed in Section 4.2), and FeNC was excluded from the linear fitting as it is, for an unknown reason, an outlier. Most interestingly, the fitted line in Figure S7 has a slope of 3.34 N atoms per metal atom, nicely supporting the fixation of close to four nitrogen atoms during pyrolysis per each single metal atom, and the major presence of $MeN_4$ sites for the (Zn)NC, CoNC, NiNC, and CuNC materials. The position of MnNC data point below the line also supports the mix of O and N in the first coordination sphere of Mn.

SEM (Figure S8) and $N_2$ physisorption isotherms (Figure S9) indicate a similar porous carbon structure in the six materials. The isotherm shape indicates a high microporosity (vertical rise at low $P/P_0$) and the existence of small mesopores that are responsible for the hysteresis. Similar porous structures had been observed on analogous ZIF-8-derived materials,[22,23]



DOI: 10.1021/acscatal.9b02594
ACS Catal. 2019, 9, 10426−10439

and micropores were shown to be important to host $MN_x$ active sites.[64,65] The Brunauer−Emmett−Teller surface areas of the catalysts are similar, in the range of 220−330 $m^2\ g^{-1}$ (Table S4). Similar double layer capacitances according to CV further confirm that MNC and (Zn)NC materials possess a similar electrochemical surface area (Figure S10 and Table S4). As shown in Figure S1, the XRD patterns of the MNC catalysts revealed only two broad reflection peaks attributed to the (002) and (101) facets of nanometric graphitic structures.[22,66] In the Raman spectra (Figure S11), all samples showed the same ratio of D to G band intensity ($I_D/I_G \approx 0.8$), suggesting the same degree of disorder of the carbon phase. In summary, the five MNC catalysts have similar structure and composition, with the only significant difference being the nature of the metal and its exact coordination and oxidation state in $MN_x$ moieties.

### 3.2. Selectivity and Activity of $MN_x$ Sites for $eCO_2RR$.

The catalytic activities of MNC and (Zn)NC toward $eCO_2RR$ were first screened with LSV. The five MNC materials and also (Zn)NC exhibit higher current densities in $CO_2$-saturated 0.1 M $KHCO_3$ than in $N_2$-saturated 0.1 M $K_2HPO_4/KH_2PO_4$ buffer electrolyte (Figure S12). The onset potential is highest for FeNC, whereas the current density reached with NiNC surpassed that reached with FeNC below −0.8 V versus RHE (the reasons for the high onset of FeNC will be discussed later).[14] CoNC shows even higher current density than NiNC at a low potential but, because of similarity in the polarization curves in $CO_2$-saturated and $CO_2$-free electrolytes (Figure S12c), this might mostly be attributed to HER. These trends agree with previous reports.[14,15,20,21] The identification and quantification of the $eCO_2RR$ products were then carried out under potentiostatic control. The FEs obtained from CA at −0.5 and −0.6 V versus RHE vary with the embedded metal center, as shown in Figure 4. Although CO was the major

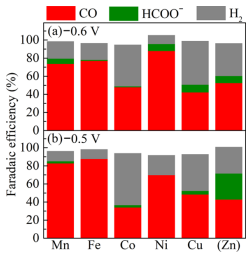


**Figure 4.** Product analysis. FE at (a) −0.6 V and (b) −0.5 V vs RHE obtained over the MNC catalysts (M = Mn, Fe, Co, Ni, and Cu), plotted against the embedded metal center sorted by the atomic number. The data were obtained by CA for 90 min, performed in 0.1 M $KHCO_3$ aqueous electrolyte saturated with $CO_2$ (pH 6.7) at room temperature.

$eCO_2RR$ product over all MNC, the highest FEs were observed over the Fe−, Ni− and Mn−NC materials. High FEs have been reported previously for other FeNC[10,17,20,67] and NiNC[13,16,18,19,38] materials synthesized via different approaches but sharing a key common structural feature, namely, the atomically dispersed $MN_x$ moieties. Also, in agreement with other recently published results, the major product over CoNC is $H_2$.[14,15,20,21] On the contrary, high selectivity (more than 90%) toward $CO_2$ reduction to CO in a wide potential range (−0.57 to −0.88 V vs RHE) over atomically dispersed $CoN_x$ was reported as well,[68,69] but with slightly different coordination environment. As the present series of MNC and (Zn)NC catalysts has, except for the nature of the metal element in $MN_x$ moieties, negligible difference in morphology and structure, the different activity and selectivity toward $eCO_2RR$ to CO can be mainly ascribed to the nature of the metal in $MN_x$ sites. Last, (Zn)NC shows a selectivity for CO being in-between the low value of CoNC and the high values of MnNC, FeNC, and NiNC.

Although Figure 4 indicates the relative fraction of all products formed during CA on each of the catalysts, it does not convey any information on the rate at which these products formed. Therefore, the partial current densities for each of the products (CO, $HCOO^-$, and $H_2$) were calculated from the CA data, and are reported in Figure 5. They were

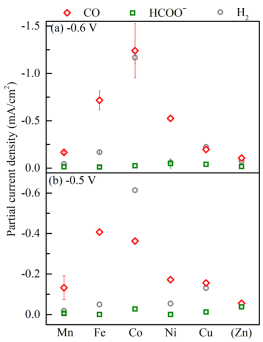


**Figure 5.** Volcano trend in $eCO_2RR$ activity. Partial current densities at (a) −0.6 V and (b) −0.5 V vs RHE over the MNC catalysts for CO, $HCOO^-$, and $H_2$ products. The data were obtained by CA for 90 min, in 0.1 M $KHCO_3$ saturated with $CO_2$ (pH 6.7) at room temperature.

calculated from the knowledge of (i) the average current density on each catalyst during the CA experiment and (ii) the product quantification averaged during the CA (see Experimental Methods). Looking at the results obtained at −0.6 V versus RHE (Figure 5a), it should first be noted that, whereas (Zn)NC shows non-zero activity toward $CO_2$ reduction, it is negligible compared to the activity observed for FeNC, CoNC, and NiNC. The low activity of (Zn)NC is attributed to $ZnN_4$ moieties[8,70] and/or nitrogen groups not bonded to any metal.[71,72] Given that MNC catalysts and (Zn)NC share a similar carbon matrix with similar amounts of $ZnN_4$ moieties and nitrogen functionalities, we assign the higher partial current densities for CO formation ($J_{CO}$) of MNC samples to the presence of $MN_x$ moieties (Fe-, Co-, and $NiN_x$ moieties in particular). A catalytic synergy between $MN_x$ and $ZnN_4$ moieties is also unlikely when the main considered product of $CO_2$ reduction is CO (only two electrons transferred, with COOH* as the only possible intermediate species). There are generally three steps for the $eCO_2RR$ to CO: (i) $CO_2 + H^+ + e^- \rightarrow$ COOH* (this first electron and proton transfer can be



DOI: 10.1021/acscatal.9b02594
ACS Catal. 2019, 9, 10426−10439

further decoupled into two steps: (i-a) $CO_2 + e^- \rightarrow CO_2^{\bullet-}$, and (i-b) $CO_2^{\bullet-} + H^+ \rightarrow COOH^*$, as discussed in the following DFT simulations), (ii) $COOH^* + H^+ + e^- \rightarrow CO^* + H_2O$ and (iii) $CO^*$ desorption. If a synergistic effect between $MN_x$ and $ZnN_4$ moieties occurs, there are two possibilities: (a) $MN_x$ catalyzes step (i) and $ZnN_4$ catalyzes step (ii); or (b) the opposite. Assuming the synergy case (a), the FE for formate on FeNC, CoNC and NiNC should be significantly higher than that on (Zn)NC, which is not the case (Figure 4). Assuming the synergy case (b), (Zn)NC should have a $J_{HCOO^-}$ value comparable to $J_{CO}$ observed on the active catalysts NiNC, FeNC, and CoNC. However, this is also in contrast with experimental results, where $J_{HCOO^-}$ on (Zn)NC is negligible compared to $J_{CO}$ on NiNC, FeNC, and CoNC (Figure 5). Thus, we can rule out any significant catalysis synergy between $MN_x$ and $ZnN_4$ moieties.

Interestingly, with increasing atomic number from Mn to Co, $J_{CO}$ monotonically increases, whereas with further increasing atomic number of the metal, the $J_{CO}$ value decreases (Figure 5a). A volcano-shaped trend is thus identified in the electrocatalytic activity for the reduction of $CO_2$ to CO. A similar volcano trend is also apparent at −0.5 V versus RHE, but with FeNC exhibiting a slightly higher $J_{CO}$ value than CoNC at this potential (Figure 5b). The same volcano trends are observed if $J_{CO}$ is normalized by the electrochemical double layer capacitance (Figure S13b) or by the metal content obtained from XPS (Figure S13c). These observations indicate that $MN_x$ moieties embedded in the nitrogen-doped carbon matrix exhibit not only different selectivity but also distinct activities toward $eCO_2RR$. Herein, we for the first time reveal a volcano-shaped trend in the electrocatalytic activity for the $CO_2$ to CO reduction over a series of pyrolyzed MNC catalysts, with CoNC and FeNC located at the volcano peak at −0.6 and −0.5 V versus RHE, respectively. The underlying reasons for this volcano-trend are discussed in the next section.

The DFT simulations were performed on the most likely oxidation state and environment for each of the metals. Although it was characterized via ex situ XPS, the oxidation state under operating conditions might be very different.[24,67] We therefore resorted to operando XANES spectroscopy to track possible changes in the oxidation state of $MN_x$ sites during $eCO_2RR$. The overlapping XANES spectra at OCP before and after CA at 0.0, −0.5, −0.6 and −1.0 V versus RHE demonstrate that no irreversible structural change occurred for the $MN_x$ sites during $eCO_2RR$ (Figure 6a), in agreement with operando XAS results on other MNC catalysts previously reported.[24,67] The position of the absorption edge at the metal K-edge XANES spectra is generally recognized to correlate, for a given coordination environment of the metal, to the metal oxidation state. The absorption edge position was therefore determined as the maximum of the first derivative of the XANES spectra, and is shown as a function of the electrochemical potential in Figure 6b. The figure indicates that a reduction occurred for Fe, Ni, and Cu sites when decreasing the potential from OCP to −0.5 V versus RHE, whereas the oxidation state of Mn and Co sites remained the same. Combined with the ex situ XPS oxidation state identification, we can infer that the oxidation state of Fe was modified from 2+/3+ to only 2+, that of Ni reduced from 2+ to 1+, and that of Cu reduced from 2+/1+ to 0.[14,73] The oxidation state of Mn remained a mixture of 2+/3+/4+, and that of Co remained as 2+, even at −1.0 V versus RHE. It can further be observed that Fe was reduced from a mix of 2+/3+ to only 2+ already at 0 V versus RHE, in line with the redox potential identified for FeNC at ca. 0.75 V versus RHE in acidic electrolyte.[22,74] This may explain the high onset potential for $eCO_2RR$ over FeNC, whereas NiNC is possibly inactive for $eCO_2RR$ as long as it is in 2+ oxidation state (discussed later in combination with DFT). The changes in oxidation states of the three most active MNC catalysts (namely Fe, Co, and Ni) with applied potential agree well with the calculated Pourbaix speciation diagrams, which shows that in a pH = 7 electrolyte, the oxidation state of Fe and Co in $MN_4$ corresponds to $Co^{2+}$ at any potential < 0 V versus RHE, whereas there is a reduction from $Ni^{2+}$ to $Ni^{1+}$ below 0 V versus RHE at pH = 7 (Figure S14), in line with the Ni-reduction experimentally observed between 0 and −0.5 V versus RHE experimentally (Figure 6b). It should be noted that XAS is a bulk technique and therefore the signal and values reported in Figure 6 are an average of all metal atoms of the same nature in the sample, regardless of whether they are on the surface (sensitive to the electrochemical potential) or in the bulk (possibly insensitive to the electrochemical potential).

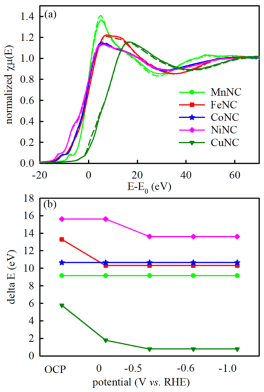


**Figure 6.** (a) Metal K-edge XANES spectra of MNC catalysts at OCP before and after the CA measurements at different potentials (solid curve: before; dashed curve: after), and (b) change in the absorption edge of metal K-edge XANES spectra of MNC catalysts with applied potential. The electrolyte was $CO_2$-saturated 0.1 M $KHCO_3$, and the OCP was around 0.7 V vs RHE. In (a), the *x*-axis is the difference between the X-ray energy and the absorption edge of MNC ($E_0$). In (b), the *y*-axis ($\Delta E$) is ($E_0 - E_{0,metal}$).

## 4. DISCUSSION

**4.1. Explanation for the Slightly Different Volcano Trends at −0.5 and −0.6 V Versus RHE.** Figure 5 reveals that the most active catalyst for $eCO_2RR$ to CO depends on the electrochemical potential. In the general case, such a potential-dependent volcano trend can be expected, as the electrochemical kinetics of even a simple one-electron reaction is governed by at least two parameters, namely, the exchange current density ($i_0$) and the Tafel slope. Only if the Tafel slope for $eCO_2RR$ to CO is the same on all MNC catalysts can one expect a potential-independent activity trend. This is clearly shown in Figure S15, constructed from Tafel laws and



DOI: 10.1021/acscatal.9b02594
ACS Catal. 2019, 9, 10426−10439

assuming different $i_0$ values and either a common Tafel slope (Figure S15a) or slightly different Tafel slopes (Figure S15b). The plot of the kinetic current density versus potential show the same trends at −0.5 and −0.6 V versus RHE when the Tafel slope is assumed to be the same for all three catalysts (Figure S15c), whereas the trends differ when different Tafel slopes are assumed (Figure S15d). Thus, the simplest explanation to account for the slightly different volcano trends in Figure 5a,b is a variation of the $eCO_2RR$ Tafel slope from one catalyst to another. This may, in turn, be related to different rate-determining steps of $eCO_2RR$ on those different catalysts. From the theory of electrokinetics of multielectron reactions, higher Tafel slopes are generally expected when the rate-determining step (RDS) is the first electron transfer than when it is the second electron transfer or any reaction step after the second electron transfer.[75]

**4.2. Underlying Reason for the Volcano Trends.** The observation of volcano trends in the electrochemical activity for various reactions among a series of metal-based catalysts with similar site structures is generally explained by Sabatier's principle, with the binding energy of the metal sites being tuned by the metal's atomic number, and leading to too weak, optimum, and too strong binding of the key intermediate-adsorbed species when moving in a given direction in the series of transition metal.[76,77] We then performed DFT calculations with $MN_4C_{10}$ model (M = Mn, Fe, Co, Ni, and Cu, with axial oxygen adsorbates for some of the metals) with the CHE model at $U = -0.6$, −0.5, and 0.0 V versus RHE, to investigate the binding energy of the key reaction intermediates for HER and $eCO_2RR$ according to the following elementary steps

Step A: $CO_2(g) + e^- \rightarrow CO_2^{\bullet-}$
Step B: $CO_2^{\bullet-} + H^+ \rightarrow COOH^*$
Step C: $COOH^* + e^- + H^+ \rightarrow CO^* + H_2O$
Step D: $CO^* \rightarrow CO(g)$

The reaction energy profiles for each elementary step of $eCO_2RR$ (Figure 7 ($U = -0.6$ and −0.5 V vs RHE), Figure S16 ($U = 0.0$ V vs RHE) and Tables S5−S7) show that the particular transition metal present in the $N_4$ lattice has a tremendous effect on reactivity. As $eCO_2RR$ does not occur at $U = 0.0$ V versus RHE, we focus in our discussion on the free energy diagrams at $U = -0.6$ and −0.5 V versus RHE (Figure 7), potentials at which we experimentally measured the $eCO_2RR$ activity and selectivity of MNC catalysts. Overall, the calculated Gibbs free energy diagrams demonstrate that $MnN_4$ and $FeN_4$ bind CO too strongly and their CO production rate is determined by the CO* desorption step. In contrast, $NiN_4$ and $CuN_4$ have weak CO binding energy, and the $CO_2$ activation and first electron transfer then becomes the RDS (Table S8). In this series of model sites, $CoN_4$ shows the optimum balance between the energy barriers for $CO_2$ activation and CO desorption (steps A and D in Table S8, respectively).

We also investigated how axial adsorbates ($H_2O$, OH, and O) affect the reaction energies on $MnN_4$, $FeN_4$, and $CoN_4$ (no oxygen adsorbates could be stabilized on $CuN_4$ and $NiN_4$). Particularly, the $H_2O$ molecule axially adsorbed on $FeN_4$ lowers the reaction barrier for the first electron transfer to form $CO_2^{\bullet-}$ (Figures 7b and S14) and thus promotes the $eCO_2RR$ to CO over FeNC. In this case, $FeN_4$ sites are approachable from both axial directions (one side for adsorbing $H_2O$, and the other side for activating $CO_2$ gas molecule). Moreover, for the case of NiNC, $NiN_4C_{10}$ with oxidation states of 1+ and 2+ are both used in the DFT

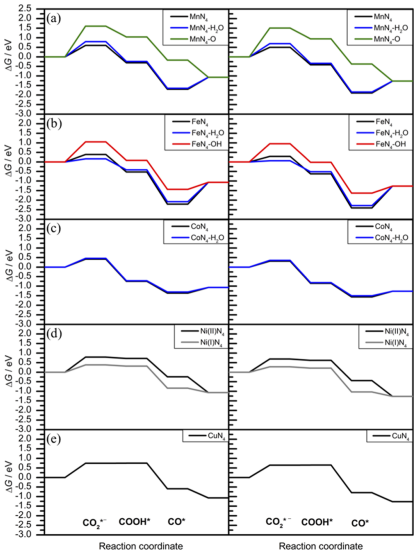


**Figure 7.** Gibbs free energy profiles for $eCO_2RR$ over $MN_4$ model sites ((a−e) M = Mn, Fe, Co, Ni, and Cu) at $U = -0.5$ V (left) and −0.6 V (right) vs RHE (pH = 7) according to the different metal speciation (oxidation state and ligand coordination).

simulations, as a reduction of $Ni^{2+}$ to $Ni^{1+}$ was observed from operando XAS (Figure 6). In contrast to the high energy barrier for the $CO_2$ activation on $Ni^{2+}N_4C_{10}$ (the first step for $eCO_2RR$), $Ni^{1+}N_4C_{10}$ binds $CO_2$ more strongly (Figure 7d). This explains that the onset potential of $eCO_2RR$ over NiNC is highly correlated to the $Ni^{2+/1+}N_4$ redox potential (Figures 6b and S11d). The $CO_2$ activation energies are also highly correlated to the geometries of the $CO_2$ coordination over $MN_4$ sites, as depicted in Figure S17 showing how $CO_2$ is activated in the Fe, Co, and Ni sites. Whereas both a M−C and a M−O bonds can simultaneously form with the $FeN_4$ active site, only a M−C bond appears for the $CoN_4$ and $NiN_4$ sites. In addition, the O−C−O angle departs from the 180° value in the gas phase to only 145° when adsorbed on $FeN_4$. This explains the lower activation energy of $CO_2$ over FeNC versus other MNC catalysts and the higher onset potential for FeNC.

The activity trends for $CO_2$ reduction to CO can be estimated from DFT calculations on the basis of the exergonic value of the reaction energy at the RDS. Table S8 reports the reaction energy calculated for each elementary step for $MN_4(-H_2O)$ moieties according to the Gibbs free energy profiles for $eCO_2RR$ over MNC catalysts (M = Mn, Fe, Co, Ni, and Cu) at $U = -0.6$ V versus RHE. For each $MN_4$ site, the structure (with/without $H_2O$ adsorbate) with lowest reaction energy at the RDS is considered in Table S8. To compare DFT results to the experimental $eCO_2RR$ activity trend, we assumed an Arrhenius type law of the form $A \exp(-E_{RDS}/RT)$, where $E_{RDS}$ is the free energy change at the RDS and $A$ is a pre-


DOI: 10.1021/acscatal.9b02594
ACS Catal. 2019, 9, 10426−10439

exponential factor, assumed the same for all MNC catalysts investigated because of similar metal content and similar carbon porosity, chemistry, and morphology. Figure 8 shows

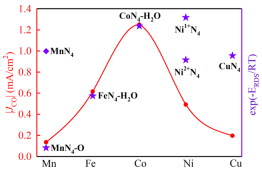


**Figure 8.** Comparison of experimental CO partial current density at −0.6 V vs RHE for pyrolyzed MNC materials and DFT calculated trends ($U$ = −0.6 V vs RHE). $E_{RDS}$ is the calculated free reaction energy at the specific RDS of $eCO_2RR$ to CO for each active site (see Table S8).

that the trend of reaction rate predicted from DFT according to this approach matches well the experimentally observed volcano trend in the present work, except for $MnN_4$ and $CuN_4$, which will be discussed later. Among all the $MN_4(-H_2O)$ active sites, $Ni^{1+}N_4$ is predicted to show the highest activity toward $eCO_2RR$ to CO, with lowest maximum for the free reaction energy at any of the elementary steps. However, the experimental oxidation states of $NiN_4$ sites are most likely in a mix of 1+/2+ at −0.6 V versus RHE (Figures 6 and S12). Thus, the experimental activity of NiNC should fall between those predicted for $Ni^{1+}N_4$ and $Ni^{2+}N_4$. Experimentally, the $eCO_2RR$ activity of NiNC is even lower than that estimated from DFT for $Ni^{2+}N_4$ however. We assign this to a lower onset potential for NiNC than for CoNC, but once the reaction has started, recent studies have shown that NiNC catalysts with single metal atom sites are the most active and selective MNC catalysts reported to date.[13,16,18,19,38] The calculated activity trends for $MN_4$ sites are as following $FeN_4{-}H_2O$ < $MnN_4$ < $CoN_4{-}H_2O$ < $Ni^{1+}N_4$ > $Ni^{2+}N_4$ ≈ $CuN_4$, with metals on the left-hand side of Co or Ni binding CO too strongly, and metals on the right-hand side binding $CO_2$ too weakly.

One discrepancy between the present experimental results and theoretical results is MnNC, for which our experimental results show much lower CO partial current density than FeNC, whereas the DFT calculations predicted that $MnN_4$ and $FeN_4$ sites are both limited by the CO* desorption step, but with lower desorption barrier for $MnN_4$. This results in a predicted $eCO_2RR$ activity higher for $MnN_4$ than $FeN_4$ moieties (Figure 8).

Given that a higher oxidation state of Mn (a mixture of 4+, 3+, and 2+) was observed by ex situ XPS and operando XANES than can be assumed with a $MN_4$ model site, and given that $MnN_x$ has a higher predicted affinity to oxygen,[53] we re-evaluated the possible active site structure of MnNC. We assumed $MnN_2O_2$ as an alternative model site (Figure S18a). Both $MnN_4$ and $MnN_2O_2$ structures converged and optimized under the same conditions, confirming similar energy stabilities of these two structures. Moreover, the experimental FT-EXAFS spectrum of MnNC could be properly fitted with the $MnN_2O_2$ model site (Figure S18b), and its DFT calculated EXAFS spectrum (Figure S18c) exhibits the same characteristic peak at ∼1.5 Å assigned to both N and O back-scattering from the first coordination sphere. According to our DFT

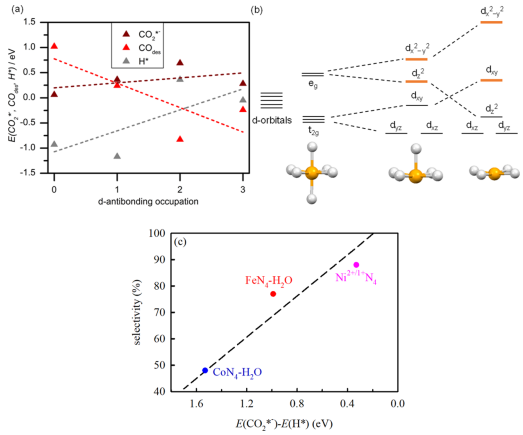


**Figure 9.** Relationship between the adsorption/desorption energies and the local electronic configurations on the Fe, Co, and Ni (1+ and 2+). (a) $CO_2^{*-}$ (wine), H* (gray) adsorption energies and CO (red) desorption (at pH = 7, $U$ = −0.6 V) as a function of the d-antibonding occupation in the active site. In (b), the symmetry descent from the octahedral configuration to either square pyramid or square planar is shown (orange indicates the antibonding states). For the most common Fe species under potential Fe and Co are in $MN_4{-}H_2O$ (square pyramid with 0 and 1 antibonding electrons). Instead, Ni is in the square planar configuration with already two electrons in the antibonding state. At high negative potential the highest antibonding $d_{x^2-y^2}$ would be occupied, which could trigger the distortion of the planar pocket ($Ni^{1+}$ state). (c) The experimental selectivity at −0.6 V vs RHE over FeNC, CoNC, and NiNC vs the DFT-simulated $E(CO_2^{*-}) - E(H^*)$.



DOI: 10.1021/acscatal.9b02594
ACS Catal. 2019, 9, 10426−10439

calculations, this $MnN_2O_2$ model can however not coordinate $CO_2$ and is therefore predicted to be inactive toward $eCO_2RR$. Even with a single oxygen adsorbate, the $MnN_4$ site becomes poorly active toward $eCO_2RR$, as indicated by the very high energy barrier for $CO_2$ adsorption calculated by DFT for the $MnN_4$−O model (Figure 7a). Of all the Mn models investigated, only $Mn^{2+}$ without oxygen ligands can effectively coordinate $CO_2$. However, as identified by ex situ XPS and operando XANES (Figures 3 and 6), this species is uncommon at the investigated potentials, explaining why no activity is experimentally found for MnNC. Last, for CuNC, our operando XANES data show that Cu switches from 2+ to 0 oxidation state early on (Figure 6), explaining the mismatch between DFT predictions and the experimental CuNC activity. In summary, with the $MnN_4$−O model site for MnNC and $MN_4C_{10}(-H_2O)$ model sites for other MNC catalysts (M = Fe, Co, Ni), the experimental volcano trend in the $eCO_2RR$ to CO activity of MNC catalysts can be nicely explained by our DFT-calculated Gibbs free energy for the RDS (Figure 8).

The volcano-shaped trend in $eCO_2RR$ activity to CO over various MNC catalysts could not be identified in other reports, where CoNC exhibited lower $J_{CO}$ values relative to other $MN_x$ moieties (Ni and Fe in particular) in a broad potential range.[14,15,21] The reason for this seems to be that previous reports either lacked evidence for the exclusive atomically dispersed nature of transition metals (the XRD for some of the MNC catalysts exhibited sharp peaks arising from metallic nanoparticles, which might alter the carbon structure),[14,15] or studied the activity of MNC catalysts varying not only in the nature of the transition metal but also in the carbon matrix structure (as shown in XRD and/or $N_2$ adsorption/desorption isotherms).[21]

**4.3. Selectivity toward CO over $MN_4$.** As another critical factor for a good $eCO_2RR$ catalyst, selectivity is highly correlated to the H* and $CO_2^{*-}$ binding energies over $MN_x$ active sites. Thus, we investigated the Gibbs free energy profiles of HER over $MN_4C_{10}$ model sites (M = Mn, Fe, Co, Ni, and Cu) at −0.5 and −0.6 V versus RHE (Figure S19).

These binding energies can be rationalized from simple coordination chemistry rules. The adsorption behavior for the metals in the first transition series depends on the occupation of antibonding d-orbitals coming from the crystal field splitting for the resting square pyramidal structure. Therefore, we use the number of d-antibonding electrons (0 for $FeN_4$−$H_2O$, 1 for $CoN_4$−$H_2O$, 2 for $Ni^{1+}N_4$, and 3 for $Ni^{2+}N_4$) to explain the selectivity toward $eCO_2RR$ to CO over $MN_4$ sites (Figure 9). The population of the antibonding states results from counting the number of electrons in the d-orbitals of the ground-state configuration according to the crystal field splitting theory. Figure 9a indicates that there is a linear scaling relationship between the $CO_2^{*-}$ and CO* binding energies (Figure S20), which determines the CO activity. Thus, the CO binding energy can serve as a key descriptor for $eCO_2RR$ to CO activity. The volcano trend with CO binding energy as a descriptor ($J_{CO}$ measured experimentally vs CO binding energy calculated from DFT simulations) is shown in Figure S21, with Fe located at the strong binding branch, whereas Ni and Cu are on the weak binding branch. $CoN_4$−$H_2O$ sites possess the optimum binding energies with CO*, which are neither too strong nor too weak. On the other hand, good selectivity toward CO requires high $CO_2^{*-}$ binding energy and low H* binding energy (the more negative value in Figure 9a, the higher the binding energy). Thus, we utilized the difference of $CO_2^{*-}$ and H* binding energies ($E(CO_2^{*-}) - E(H^*)$) as the descriptor for selectivity (Figure 9c). In that figure, we show only the experimental data for FeNC, NiNC, and CoNC and did not include the other MNC materials, whose $eCO_2RR$ activity and selectivity can originate in whole or in part from metal-free nitrogen functional groups.[78] The $CoN_4$−$H_2O$ site has an optimum binding energy with $CO_2^{*-}$, but, unfortunately, the binding energy of H* is much higher than that of $CO_2^{*-}$, which leads to a low selectivity toward CO, in line with the experimental result on CoNC (48%, Figure 9c). The high selectivity of $eCO_2RR$ to CO over $NiN_4$ benefits from the lower H* binding energies compared to other $MN_4$ sites (Figure 9c). For $FeN_4$−$H_2O$, even though the high binding energy to H* suggests a high HER activity (Figure 9a), the reduction of $CO_2$ to CO* also occurs with zero energy barrier, and the binding energy of CO* on $FeN_4$−$H_2O$ is much stronger than that of H* on $FeN_4$−$H_2O$. Thus, the majority of $FeN_4$ sites are occupied by CO* in $CO_2$-saturated electrolyte. This site-blocking effect probably suppresses the binding of such active sites with HER-related species, resulting in high experimental selectivity toward CO over FeNC. As can be seen in Figure 9c, the selectivity of $eCO_2RR$ toward CO over $MN_x$ moieties can be explained with the DFT-calculated $CO_2^{*-}$ and H* binding energies, that in turn are highly correlated to the number of d-antibonding electrons. The latter descriptor can thus be used to screen for more promising $eCO_2RR$ candidate MNC materials.

## 5. CONCLUSIONS

The careful integration of experimental and theoretical methods allowed us to establish clear correlations between physicochemical and catalytic properties for the $eCO_2RR$ of atomically dispersed $MN_4$ centres (M = Mn, Fe, Co, Ni, and Cu). The ex situ characterization demonstrates the incorporation of the metal exclusively in $MN_4$ centers over otherwise similar nitrogen-doped carbon matrices. Ex situ XPS and in situ XANES were applied to identify and monitor changes of the metal oxidation state at rest and under operating conditions, respectively. Mn and Co did not change oxidation state down to −1.0 V versus RHE, whereas Fe and Ni were partially reduced and Cu was largely reduced to a metallic state. Over these highly controlled systems, catalytic tests revealed a volcano-like dependency between $eCO_2RR$ activity and the atomic number of the transition metal, with Fe and Co as the most active centers. In contrast, no clear trend was observable for the FE toward CO, for which Fe, Mn, and Ni-based materials showed the highest values (>80%). Computational models led to the identification of active centers and finally to descriptors rationalizing the distinct activity and selectivity patterns observed. To this end, different configurations were studied according to the speciation of the metal atom, its charge, spin, and coordination sphere. Among the best performing materials, $Fe^{2+}N_4$−$H_2O$ and $Co^{2+}N_4$−$H_2O$ centers were found as the most likely active catalytic centers at considered potentials (−0.5 and −0.6 V vs RHE), whereas $Ni^{1+}N_4$ was predicted as the most active Ni-based one. The Gibbs free energy change at the RDS accounted for the experimentally determined activity volcano, with Co-, Fe-, and Ni-based systems showing the best compromise between CO* and $CO_2^{*-}$ binding energies. Regarding selectivity, the difference between the binding energies for $CO_2^{*-}$ and H*, directly related to the number of d-antibonding electrons, described successfully the high selectivity observed on Fe- and



DOI: 10.1021/acscatal.9b02594
ACS Catal. 2019, 9, 10426−10439

Ni catalysts and the more favored HER observed over the Co-based one. All in all, these results describe the influence of the particular metal species existing at relevant potentials on the catalytic activity and selectivity, laying down the path for a rational optimization of single-atom catalysts for $eCO_2RR$.

## ■ ASSOCIATED CONTENT

### Supporting Information

The Supporting Information is available free of charge on the ACS Publications website at DOI: 10.1021/acscatal.9b02594.

Physical (XRD, (S)TEM, EDX, XAS, XPS, SEM, $N_2$ physisorption, and Raman) and electrochemical (CV, LSV) characterizations of MNC catalysts, the calculated electrochemical potential versus logarithm of the reaction rate with simplified Tafel laws, and the DFT calculated Gibbs free energy diagrams of $eCO_2RR$ to CO and HER (PDF)

## ■ AUTHOR INFORMATION

### Corresponding Author

*E-mail: frederic.jaouen@umontpellier.fr.

### ORCID

Jingkun Li: 0000-0002-8679-9612
Tatsuya Shinagawa: 0000-0002-5240-7342
Frank Krumeich: 0000-0001-5625-1536
Kateryna Artyushkova: 0000-0002-2611-0422
Plamen Atanassov: 0000-0003-2996-472X
Andrea Zitolo: 0000-0002-2187-6699
Rodrigo García-Muelas: 0000-0002-2219-5027
Núria López: 0000-0001-9150-5941
Javier Pérez-Ramírez: 0000-0002-5805-7355
Frédéric Jaouen: 0000-0001-9836-3261

### Present Address

[▽]School of Engineering, Department of Chemical System Engineering, The University of Tokyo, 7-3-1 Hongo, Bunkyo-ku, 113-8656, Tokyo, Japan.

### Author Contributions

J.L. and F.J. designed, synthesized, and physically characterized the materials. T.S., A.J.M.F., and J.P.-R. performed the $eCO_2RR$ electrochemical measurements and product analysis. P.P., Y.Z., R.G.-M., and N.L. performed the DFT simulations. F.K. conducted the (S)TEM and EDX characterizations. A.Z. conducted the XAS analysis and computation. K.A. and P.A. conducted the XPS measurement and analysis. J.L. and F.J. wrote and edited the paper with input from all authors. All authors read and approved the final version of the paper.

### Funding

The research leading to these results has received funding from the A-LEAF Project, which is funded by the European Union's H2020 Programme under grant agreement no. 732840. We thank the BSC-RES for providing generous computational resources. Additionnal financial suppport was generously provided by the MCIU/AEI/FEDER/UE RTI2018-101394-B-I00 and AGAUR 2017-SGR-90 projects. P.P. thanks ITN-ELCOREL (funded by the European Union's H2020 Programme under grant agreement No. 722614) for a predoctoral grant.

### Notes

The authors declare no competing financial interest.

## ■ ACKNOWLEDGMENTS

We acknowledge Synchrotron SOLEIL (Gif-sur Yvette, France) for provision of synchrotron radiation facilities at beamline SAMBA (proposal number 20180635) and the Scientific Center for Optical and Electron Microscopy (ScopeM) of ETH Zurich for access to its facilities.

## ■ REFERENCES

(1) Zheng, T.; Jiang, K.; Wang, H. Recent Advances in Electrochemical $CO_2$ to CO Conversion on Heterogeneous Catalysts. *Adv. Mater.* **2018**, *30*, 1802066.
(2) Larrazábal, G. O.; Martín, A. J.; Pérez-Ramírez, J. Building Blocks for High Performance in Electrocatalytic $CO_2$ Reduction: Materials, Optimization Strategies, and Device Engineering. *J. Phys. Chem. Lett.* **2017**, *8*, 3933−3944.
(3) Wang, Y.; Liu, J.; Wang, Y.; Al-Enizi, A. M.; Zheng, G. Tuning of $CO_2$ Reduction Selectivity on Metal Electrocatalysts. *Small* **2017**, *13*, 1701809.
(4) Martín, A. J.; Larrazábal, G. O.; Pérez-Ramírez, J. Towards Sustainable Fuels and Chemicals Through the Electrochemical Reduction of $CO_2$: Lessons from Water Electrolysis. *Green Chem.* **2015**, *17*, 5114−5130.
(5) Zhang, W.; Hu, Y.; Ma, L.; Zhu, G.; Wang, Y.; Xue, X.; Chen, R.; Yang, S.; Jin, Z. Progress and Perspective of Electrocatalytic $CO_2$ Reduction for Renewable Carbonaceous Fuels and Chemicals. *Adv. Sci.* **2018**, *5*, 1700275.
(6) Lin, S.; Diercks, C. S.; Zhang, Y.-B.; Kornienko, N.; Nichols, E. M.; Zhao, Y.; Paris, A. R.; Kim, D.; Yang, P.; Yaghi, O. M.; Chang, C. J. Covalent Organic Frameworks Comprising Cobalt Porphyrins for Catalytic $CO_2$ Reduction in Water. *Science* **2015**, *349*, 1208−1213.
(7) Zhang, Z.; Xiao, J.; Chen, X. J.; Yu, S.; Yu, L.; Si, R.; Wang, Y.; Wang, S.; Meng, X.; Wang, Y.; Tian, Z. Q.; Deng, D. Reaction Mechanisms of Well-Defined Metal-$N_4$ Sites in Electrocatalytic $CO_2$ Reduction. *Angew. Chem., Int. Ed.* **2018**, *57*, 16339−16342.
(8) Wu, Y.; Jiang, J.; Weng, Z.; Wang, M.; Broere, D. L.; Zhong, Y.; Brudvig, G. W.; Feng, Z.; Wang, H. Electroreduction of $CO_2$ Catalyzed by a Heterogenized Zn−Porphyrin Complex with a Redox-Innocent Metal Center. *ACS Cent. Sci.* **2017**, *3*, 847−852.
(9) Costentin, C.; Drouet, S.; Robert, M.; Savéant, J.-M. A Local Proton Source Enhances $CO_2$ Electroreduction to CO by a Molecular Fe Catalyst. *Science* **2012**, *338*, 90−94.
(10) Huan, T. N.; Ranjbar, N.; Rousse, G.; Sougrati, M.; Zitolo, A.; Mougel, V.; Jaouen, F.; Fontecave, M. Electrochemical Reduction of $CO_2$ Catalyzed by Fe-NC Materials: A Structure−Selectivity Study. *ACS Catal.* **2017**, *7*, 1520−1525.
(11) Han, N.; Wang, Y.; Ma, L.; Wen, J.; Li, J.; Zheng, H.; Nie, K.; Wang, X.; Zhao, F.; Li, Y.; Fan, J.; Zhong, J.; Wu, T.; Miller, D. J.; Lu, J.; Lee, S.-T.; Li, Y. Supported Cobalt Polyphthalocyanine for High-Performance Electrocatalytic $CO_2$ Reduction. *Chem* **2017**, *3*, 652−664.
(12) Manbeck, G. F.; Fujita, E. A Review of Iron and Cobalt Porphyrins, Phthalocyanines and Related Complexes for Electrochemical and Photochemical Reduction of Carbon Dioxide. *J. Porphyrins Phthalocyanines* **2015**, *19*, 45−64.
(13) Yang, H. B.; Hung, S.-F.; Liu, S.; Yuan, K.; Miao, S.; Zhang, L.; Huang, X.; Wang, H.-Y.; Cai, W.; Chen, R.; Gao, J.; Yang, X.; Chen, W.; Huang, Y.; Chen, H. M.; Li, C. M.; Zhang, T.; Liu, B. Atomically Dispersed Ni(I) as the Active Site for Electrochemical $CO_2$ Reduction. *Nat. Energy* **2018**, *3*, 140−147.
(14) Ju, W.; Bagger, A.; Hao, G.-P.; Varela, A. S.; Sinev, I.; Bon, V.; Cuenya, B. R.; Kaskel, S.; Rossmeisl, J.; Strasser, P. Understanding Activity and Selectivity of Metal-Nitrogen-Doped Carbon Catalysts for Electrochemical Reduction of $CO_2$. *Nat. Commun.* **2017**, *8*, 944.
(15) Pan, F.; Deng, W.; Justiniano, C.; Li, Y. Identification of Champion Transition Metals Centers in Metal and Nitrogen-Codoped Carbon Catalysts for $CO_2$ Reduction. *Appl. Catal., B* **2018**, *226*, 463−472.



DOI: 10.1021/acscatal.9b02594
*ACS Catal.* 2019, 9, 10426−10439

(16) Li, X.; Bi, W.; Chen, M.; Sun, Y.; Ju, H.; Yan, W.; Zhu, J.; Wu, X.; Chu, W.; Wu, C.; Xie, Y. Exclusive Ni−$N_4$ Sites Realize Near-Unity CO Selectivity for Electrochemical $CO_2$ Reduction. *J. Am. Chem. Soc.* **2017**, *139*, 14889−14892.
(17) Varela, A. S.; Kroschel, M.; Leonard, N. D.; Ju, W.; Steinberg, J.; Bagger, A.; Rossmeisl, J.; Strasser, P. pH Effects on the Selectivity of the Electrocatalytic $CO_2$ Reduction on Graphene-Embedded Fe−N−C Motifs: Bridging Concepts Between Molecular Homogeneous and Solid-State Heterogeneous Catalysis. *ACS Energy Lett.* **2018**, *3*, 812−817.
(18) Jiang, K.; Siahrostami, S.; Zheng, T.; Hu, Y.; Hwang, S.; Stavitski, E.; Peng, Y.; Dynes, J.; Gangisetty, M.; Su, D.; Attenkofer, K.; Wang, H. Isolated Ni Single Atoms in Graphene Nanosheets for High-Performance $CO_2$ Reduction. *Energy Environ. Sci.* **2018**, *11*, 893−903.
(19) Zhao, C.; Dai, X.; Yao, T.; Chen, W.; Wang, X.; Wang, J.; Yang, J.; Wei, S.; Wu, Y.; Li, Y. Ionic Exchange of Metal−Organic Frameworks to Access Single Nickel Sites for Efficient Electroreduction of $CO_2$. *J. Am. Chem. Soc.* **2017**, *139*, 8078−8081.
(20) Pan, F.; Zhang, H.; Liu, K.; Cullen, D.; More, K.; Wang, M.; Feng, Z.; Wang, G.; Wu, G.; Li, Y. Unveiling Active Sites of $CO_2$ Reduction on Nitrogen-Coordinated and Atomically Dispersed Iron and Cobalt Catalysts. *ACS Catal.* **2018**, *8*, 3116−3122.
(21) Hu, X.-M.; Hval, H. H.; Bjerglund, E. T.; Dalgaard, K. J.; Madsen, M. R.; Pohl, M.-M.; Welter, E.; Lamagni, P.; Buhl, K. B.; Bremholm, M.; Beller, M.; Pedersen, S. U.; Skrydstrup, T.; Daasbjerg, K. Selective $CO_2$ Reduction to CO in Water Using Earth-Abundant Metal and Nitrogen-Doped Carbon Electrocatalysts. *ACS Catal.* **2018**, *8*, 6255−6264.
(22) Li, J.; Ghoshal, S.; Liang, W.; Sougrati, M.-T.; Jaouen, F.; Halevi, B.; McKinney, S.; McCool, G.; Ma, C.; Yuan, X.; Ma, Z.-F.; Mukerjee, S.; Jia, Q. Structural and Mechanistic Basis for the High Activity of Fe−N−C Catalysts Toward Oxygen Reduction. *Energy Environ. Sci.* **2016**, *9*, 2418−2432.
(23) Proietti, E.; Jaouen, F.; Lefèvre, M.; Larouche, N.; Tian, J.; Herranz, J.; Dodelet, J.-P. Iron-based cathode catalyst with enhanced power density in polymer electrolyte membrane fuel cells. *Nat. Commun.* **2011**, *2*, 416.
(24) Zitolo, A.; Ranjbar-Sahraie, N.; Mineva, T.; Li, J.; Jia, Q.; Stamatin, S.; Harrington, G. F.; Lyth, S. M.; Krtil, P.; Mukerjee, S.; Fonda, E.; Jaouen, F. Identification of Catalytic Sites in Cobalt-Nitrogen-Carbon Materials for the Oxygen Reduction Reaction. *Nat. Commun.* **2017**, *8*, 957.
(25) Zitolo, A.; Goellner, V.; Armel, V.; Sougrati, M.-T.; Mineva, T.; Stievano, L.; Fonda, E.; Jaouen, F. Identification of Catalytic Sites for Oxygen Reduction in Iron-and Nitrogen-Doped Graphene Materials. *Nat. Mater.* **2015**, *14*, 937−942.
(26) Kramm, U. I.; Lefèvre, M.; Larouche, N.; Schmeisser, D.; Dodelet, J.-P. Correlations Between Mass Activity and Physicochemical Properties of Fe/N/C Catalysts for the ORR in PEM Fuel Cell via $^{57}$Fe Mossbauer Spectroscopy and Other Techniques. *J. Am. Chem. Soc.* **2014**, *136*, 978−985.
(27) Xia, Z.; An, L.; Chen, P.; Xia, D. Non-Pt Nanostructured Catalysts for Oxygen Reduction Reaction: Synthesis, Catalytic Activity and Its Key Factors. *Adv. Energy Mater.* **2016**, *6*, 1600458.
(28) Gewirth, A. A.; Varnell, J. A.; DiAscro, A. M. Nonprecious Metal Catalysts for Oxygen Reduction in Heterogeneous Aqueous Systems. *Chem. Rev.* **2018**, *118*, 2313−2339.
(29) Jiang, H.; Lin, Y.; Chen, B.; Zhang, Y.; Liu, H.; Duan, X.; Chen, D.; Song, L. Ternary Interfacial Superstructure Enabling Extraordinary Hydrogen Evolution Electrocatalysis. *Mater. Today* **2018**, *21*, 602−610.
(30) Jin, Q.; Ren, B.; Li, D.; Cui, H.; Wang, C. In Situ Promoting Water Dissociation Kinetic of Co Based Electrocatalyst for Unprecedentedly Enhanced Hydrogen Evolution Reaction in Alkaline Media. *Nano Energy* **2018**, *49*, 14−22.
(31) Fan, X.; Peng, Z.; Ye, R.; Zhou, H.; Guo, X. $M_3C$ (M: Fe, Co, Ni) Nanocrystals Encased in Graphene Nanoribbons: An Active and Atable Bifunctional Electrocatalyst for Oxygen Reduction and Hydrogen Evolution Reactions. *ACS Nano* **2015**, *9*, 7407−7418.
(32) Tripkovic, V.; Vanin, M.; Karamad, M.; Björketun, M. E.; Jacobsen, K. W.; Thygesen, K. S.; Rossmeisl, J. Electrochemical $CO_2$ and CO Reduction on Metal-Functionalized Porphyrin-Like Graphene. *J. Phys. Chem. C* **2013**, *117*, 9187−9195.
(33) Bagger, A.; Ju, W.; Varela, A. S.; Strasser, P.; Rossmeisl, J. Single Site Porphyrine-Like Structures Advantages Over Metals for Selective Electrochemical $CO_2$ Reduction. *Catal. Today* **2017**, *288*, 74−78.
(34) Chan, Y.-T.; Tsai, M.-K. $CO_2$ Reduction Catalysis by Tunable Square-Planar Transition-Metal Complexes: A Theoretical Investigation Using Nitrogen-Substituted Carbon Nanotube Models. *Phys. Chem. Chem. Phys.* **2017**, *19*, 29068−29076.
(35) Zhao, Y.; Liang, J.; Wang, C.; Ma, J.; Wallace, G. G. Tunable and Efficient Tin Modified Nitrogen-Doped Carbon Nanofibers for Electrochemical Reduction of Aqueous Carbon Dioxide. *Adv. Energy Mater.* **2018**, *8*, 1702524.
(36) Zhang, C.; Sha, J.; Fei, H.; Liu, M.; Yazdi, S.; Zhang, J.; Zhong, Q.; Zou, X.; Zhao, N.; Yu, H.; Jiang, Z.; Ringe, E.; Yakobson, B. I.; Dong, J.; Chen, D.; Tour, J. M. Single-Atomic Ruthenium Catalytic Sites on Nitrogen-Doped Graphene for Oxygen Reduction Reaction in Acidic Medium. *ACS Nano* **2017**, *11*, 6930−6941.
(37) Wei, S.; Li, A.; Liu, J.-C.; Li, Z.; Chen, W.; Gong, Y.; Zhang, Q.; Cheong, W.-C.; Wang, Y.; Zheng, L.; Xiao, H.; Chen, C.; Wang, D.; Peng, Q.; Gu, L.; Han, X.; Li, J.; Li, Y. Direct Observation of Noble Metal Nanoparticles Transforming to Thermally Stable Single Atoms. *Nat. Nanotechnol.* **2018**, *13*, 856−861.
(38) Cheng, Y.; Zhao, S.; Johannessen, B.; Veder, J.-P.; Saunders, M.; Rowles, M. R.; Cheng, M.; Liu, C.; Chisholm, M. F.; De Marco, R.; Cheng, H.-M.; Yang, S.-Z.; Jiang, S. P. Atomically Dispersed Transition Metals on Carbon Nanotubes with Ultrahigh Loading for Selective Electrochemical Carbon Dioxide Reduction. *Adv. Mater.* **2018**, *30*, 1706287.
(39) Artyushkova, K.; Matanovic, I.; Halevi, B.; Atanassov, P. Oxygen Binding to Active Aites of Fe−N−C ORR Electrocatalysts Observed by Ambient-Pressure XPS. *J. Phys. Chem. C* **2017**, *121*, 2836−2843.
(40) Gupta, N.; Gattrell, M.; MacDougall, B. Calculation for the Cathode Surface Concentrations in the Electrochemical Recudtion of $CO_2$ in $KHCO_3$ solutions. *J. Appl. Electrochem.* **2006**, *36*, 161−172.
(41) Kresse, G.; Furthmüller, J. Efficiency of Ab-Initio Total Energy Calculations for Metals and Semiconductors Using a Plane-Wave Basis Set. *Comput. Mater. Sci.* **1996**, *6*, 15−50.
(42) Kresse, G.; Joubert, D. From Ultrasoft Pseudopotentials to the Projector Augmented-Wave Method. *Phys. Rev. B: Condens. Matter Mater. Phys.* **1999**, *59*, 1758−1775.
(43) Grimme, S.; Antony, J.; Ehrlich, S.; Krieg, H. A Consistent and Accurate Ab Initio Parametrization of Density Functional Dispersion Correction (DFT-D) for the 94 Elements H-Pu. *J. Chem. Phys.* **2010**, *132*, 154104.
(44) Perdew, J. P.; Burke, K.; Ernzerhof, M. Generalized Gradient Approximation Made Simple. *Phys. Rev. Lett.* **1996**, *77*, 3865−3868.
(45) Blöchl, P. E. Projector Augmented-Wave Method. *Phys. Rev. B: Condens. Matter Mater. Phys.* **1994**, *50*, 17953−17979.
(46) Greenwood, N. N.; Earnshaw, A. *Chemistry of the Elements*; Elsevier: Oxford, 2012.
(47) Monkhorst, H. J.; Pack, J. D. Special Points for Brillouin-Zone Integrations. *Phys. Rev. B: Solid State* **1976**, *13*, 5188−5192.
(48) Peterson, A. A.; Abild-Pedersen, F.; Studt, F.; Rossmeisl, J.; Nørskov, J. K. How Copper Catalyzes the Electroreduction of Carbon Dioxide into Hydrocarbon Fuels. *Energy Environ. Sci.* **2010**, *3*, 1311−1315.
(49) Nørskov, J. K.; Rossmeisl, J.; Logadóttir, A.; Lindqvist, L.; Kitchin, J. R.; Bligaard, T.; Jónsson, H. Origin of the Overpotential for Oxygen Reduction at a Fuel-Cell Cathode. *J. Phys. Chem. B* **2004**, *108*, 17886−17892.
(50) Togo, A.; Tanaka, I. First Principles Phonon Calculations in Materials Science. *Scr. Mater.* **2015**, *108*, 1−5.


DOI: 10.1021/acscatal.9b02594
*ACS Catal.* 2019, 9, 10426−10439

(51) Álvarez-Moreno, M.; de Graaf, C.; Lopez, N.; Maseras, F.; Poblet, J. M.; Bo, C. Managing the Computational Chemistry Big Data Problem: the ioChem-BD Platform. *J. Chem. Inf. Model.* **2015**, *55*, 95−103.
(52) Pršlja, P. https://doi.org/10.19061/iochem-bd-1-115 (accessed Jun 14, 2019).
(53) Zagal, J. H.; Koper, M. T. M. Reactivity Descriptors for the Activity of Molecular $MN_4$ Catalysts for the Oxygen Reduction Reaction. *Angew. Chem., Int. Ed.* **2016**, *55*, 14510−14521.
(54) Lefèvre, M.; Dodelet, J. P.; Bertrand, P. Molecular Oxygen Reduction in PEM Fuel Cell Conditions: ToF-SIMS Analysis of Co-Based Electrocatalysts. *J. Phys. Chem. B* **2005**, *109*, 16718−16724.
(55) Lalande, G.; Cote, R.; Guay, D.; Dodelet, J. P.; Weng, L. T.; Bertrand, P. Is Nitrogen Important in the Formulation of Fe-based Catalysts for Oxygen Reduction in Solid Polymer Fuel Cells? *Electrochim. Acta* **1997**, *42*, 1379−1388.
(56) Xu, H.; Cheng, D.; Cao, D.; Zeng, X. C. A Universal Principle for a Rational Design of Single-Atom Electrocatalysts. *Nat. Catal.* **2018**, *1*, 339.
(57) Grosvenor, A. P.; Kobe, B. A.; Biesinger, M. C.; McIntyre, N. S. Investigation of Multiplet Splitting of Fe 2p XPS Spectra and Bonding in Iron Compounds. *Surf. Interface Anal.* **2004**, *36*, 1564−1574.
(58) Kuang, M.; Tao Li, T.; Chen, H.; Mao Zhang, S.; Li Zhang, L.; Xin Zhang, Y. Hierarchical $Cu_2O/CuO/Co_3O_4$ Core-Shell Nanowires: Synthesis and Electrochemical Properties. *Nanotechnology* **2015**, *26*, 304002−304011.
(59) Weidler, N.; Schuch, J.; Knaus, F.; Stenner, P.; Hoch, S.; Maljusch, A.; Schäfer, R.; Kaiser, B.; Jaegermann, W. X-ray Photoelectron Spectroscopic Investigation of Plasma-Enhanced Chemical Vapor Deposited $NiO_x$, $NiO_x(OH)_y$, and $CoNiO_x(OH)_y$: Influence of the Chemical Composition on the Catalytic Activity for the Oxygen Evolution Reaction. *J. Phys. Chem. C* **2017**, *121*, 6455−6463.
(60) Pervaiz, E.; Tareen, A. K.; Yang, M. Bimetallic Oxide Nanoflowers Decorated Graphene Oxide Nanosheets as Novel Nanohybrids for 4-Nitrophenol Removal at Room Temperature. *Nanoscale Adv.* **2017**, *2*, 1−7.
(61) Jeon, H. S.; Ahn, S. J.; Jee, M. S.; Yoon, S. S.; Hwang, Y. J.; Min, B. K. Water Oxidation by Manganese Oxide Electrocatalytic Films Synthesized by Chemical Solution Deposition Method. *J. Electrochem. Soc.* **2016**, *163*, F3113−F3118.
(62) Kattel, S.; Atanassov, P.; Kiefer, B. Catalytic Activity of Co−$N_x$/C Electrocatalysts for Oxygen Reduction Reaction: A Density Functional Theory Study. *Phys. Chem. Chem. Phys.* **2013**, *15*, 148−153.
(63) Kattel, S.; Atanassov, P.; Kiefer, B. Stability, Electronic and Magnetic Properties of In-Plane Defects in Graphene: A First-Principles Study. *J. Phys. Chem. C* **2012**, *116*, 8161−8166.
(64) Lefèvre, M.; Proietti, E.; Jaouen, F.; Dodelet, J.-P. Iron-Based Catalysts with Improved Oxygen Reduction Activity in Polymer Electrolyte Fuel Cells. *Science* **2009**, *324*, 71−74.
(65) Jaouen, F.; Lefèvre, M.; Dodelet, J.-P.; Cai, M. Heat-Treated Fe/N/C Catalysts for $O_2$ Electroreduction: Are Active Sites Hosted in Micropores? *J. Phys. Chem. B* **2006**, *110*, 5553−5558.
(66) Varela, A. S.; Ranjbar Sahraie, N.; Steinberg, J.; Ju, W.; Oh, H.-S.; Strasser, P. Metal-Doped Nitrogenated Carbon as an Efficient Catalyst for Direct $CO_2$ Electroreduction to CO and Hydrocarbons. *Angew. Chem., Int. Ed.* **2015**, *54*, 10758−10762.
(67) Leonard, N.; Ju, W.; Sinev, I.; Steinberg, J.; Luo, F.; Varela, A. S.; Roldan Cuenya, B.; Strasser, P. The Chemical Identity, State and Structure of Catalytically Active Centers During the Electrochemical $CO_2$ Reduction on Porous Fe−Nitrogen−Carbon (Fe−N−C) Materials. *Chem. Sci.* **2018**, *9*, 5064−5073.
(68) Pan, Y.; Lin, R.; Chen, Y.; Liu, S.; Zhu, W.; Cao, X.; Chen, W.; Wu, K.; Cheong, W.-C.; Wang, Y.; Zheng, L.; Luo, J.; Lin, Y.; Liu, Y.; Liu, C.; Li, J.; Lu, Q.; Chen, X.; Wang, D.; Peng, Q.; Chen, C.; Li, Y. Design of Single-Atom Co−$N_5$ Catalytic Site: A Robust Electrocatalyst for $CO_2$ Reduction with nearly 100% CO Selectivity and Remarkable Stability. *J. Am. Chem. Soc.* **2018**, *140*, 4218−4221.
(69) Wang, X.; Chen, Z.; Zhao, X.; Yao, T.; Chen, W.; You, R.; Zhao, C.; Wu, G.; Wang, J.; Huang, W.; Yang, J.; Hong, X.; Wei, S.; Wu, Y.; Li, Y. Regulation of Coordination Number Over Single Co Sites: Triggering the Efficient Electroreduction of $CO_2$. *Angew. Chem.* **2018**, *130*, 1962−1966.
(70) Göttle, A. J.; Koper, M. T. M. Determinant Role of Electrogenerated Reactive Nucleophilic Species on Selectivity During Reduction of $CO_2$ Catalyzed by Metalloporphyrins. *J. Am. Chem. Soc.* **2018**, *140*, 4826−4834.
(71) Wang, R.; Sun, X.; Ould-Chikh, S.; Osadchii, D.; Bai, F.; Kapteijn, F.; Gascon, J. Metal-Organic-Framework-Mediated Nitrogen-Doped Carbon for $CO_2$ Electrochemical Reduction. *ACS Appl. Mater. Interfaces* **2018**, *10*, 14751−14758.
(72) Siahrostami, S.; Jiang, K.; Karamad, M.; Chan, K.; Wang, H.; Nørskov, J. Theoretical Investigations into Defected Graphene for Electrochemical Reduction of $CO_2$. *ACS Sustainable Chem. Eng.* **2017**, *5*, 11080−11085.
(73) Weng, Z.; Wu, Y.; Wang, M.; Jiang, J.; Yang, K.; Huo, S.; Wang, X.-F.; Ma, Q.; Brudvig, G. W.; Batista, V. S.; Liang, Y.; Feng, Z.; Wang, H. Active Sites of Copper-Complex Catalytic Materials for Electrochemical Carbon Dioxide Reduction. *Nat. Commun.* **2018**, *9*, 415.
(74) Li, J.; Alsudairi, A.; Ma, Z.-F.; Mukerjee, S.; Jia, Q. Asymmetric Volcano Trend in Oxygen Reduction Activity of Pt and Non-Pt Catalysts: In Situ Identification of the Site-Blocking Effect. *J. Am. Chem. Soc.* **2017**, *139*, 1384−1387.
(75) Fletcher, S. Tafel Slopes from First Principles. *J. Solid State Electrochem.* **2009**, *13*, 537−549.
(76) Stamenkovic, V. R.; Mun, B. S.; Arenz, M.; Mayrhofer, K. J. J.; Lucas, C. A.; Wang, G.; Ross, P. N.; Markovic, N. M. Trends in Electrocatalysis on Extended and Nanoscale Pt-Bimetallic Alloy Surfaces. *Nat. Mater.* **2007**, *6*, 241−247.
(77) Stamenkovic, V.; Mun, B. S.; Mayrhofer, K. J. J.; Ross, P. N.; Markovic, N. M.; Rossmeisl, J.; Greeley, J.; Nørskov, J. K. Changing the activity of electrocatalysts for oxygen reduction by tuning the surface electronic structure. *Angew. Chem.* **2006**, *118*, 2963−2967.
(78) Hursán, D.; Samu, A. A.; Janovák, L.; Artyushkova, K.; Asset, T.; Atanassov, P.; Janáky, C. Morphological Attributes Govern Carbon Dioxide Reduction on N-Doped Carbon Electrodes. *Joule* **2019**, *3*, 1719−1733.



DOI: 10.1021/acscatal.9b02594
*ACS Catal.* 2019, 9, 10426−10439

UNIVERSITAT ROVIRA I VIRGILI
THEORETICAL STUDIES OF SINGLE-SITE CATALYSTS FOR EFFICIENT ELECTROCHEMICAL CO2 REDUCTION
Paulina Pršlja

ACS Catalysis

pubs.acs.org/acscatalysis Viewpoint

# Stability and Redispersion of Ni Nanoparticles Supported on N-Doped Carbons for the $CO_2$ Electrochemical Reduction

Paulina Prslja and Núria López*

Cite This: ACS Catal. 2021, 11, 88−94 Read Online

ACCESS | Metrics & More | Article Recommendations | Supporting Information



## 1. INTRODUCTION

Single-metal nitrogen carbon materials (M−N−C) have been proposed as one of the most attractive catalysts for electrocatalytic $CO_2$ reduction reaction ($eCO_2RR$). Furthermore, with maximum atom efficiency and low coordination metal centers, they show high selectivity toward producing CO[1−4] even with the competing hydrogen evolution reaction (HER). Combined products or syngas can be used to produce liquid hydrocarbons via Fischer−Tropsch synthesis. Moreover, the M−N−C materials can further reduce CO to hydrocarbons.[3,5,6] The experimentally most studied example of these types of materials, even proposed to be industrially efficient, comes from Ni−N−C, which is highly selective to producing CO.[7−20]

The efficiency of these materials can be controlled by synthetic and postsynthetic treatments. Their nitrogen content can be controlled in several ways, such as changing the doping temperature.[20] All these approaches change the nature of the cavities present both in terms of size and coordination environment. Therefore, we can classify the hosts according to these cavities as saturated and unsaturated N-doped carbon materials. Homogenous-like confinement of the metal in the cavities plays an important role in preventing the migration as the material goes through high-temperature carbonization.[21] The vacancies can be synthetically tailored by employing MOF scaffolds,[4,22] by oxidizing carbon materials and further doping with nitrogen to form undefined motifs,[20,23] and by depositing porphyrin-like complexes.[5,24−26] The ultimate (i) size and structure of the defect in which the metal is embedded; (ii) the nitrogen content which can be controlled with the doping temperature;[20] and (iii) the reaction conditions determine the nature of the metal sites, their coordination environment, and the size of the metal nanoparticles, thus affecting the electronic structure of the active metal. Targeting activity and selectivity require adapting the anchoring sites to the metal electronic properties so that they can synergistically act.

To understand the efficiency and selectivity of the materials, different types of catalysts were synthesized and tested under electrochemical $eCO_2RR$.[20] To be concrete, these catalysts include (i) Ni nanoparticles supported on carbon material, (ii) single metal atom in saturated N-doped carbon material, (iii) sample containing both particles and single atoms, and (iv) Ni nanoparticles supported on unsaturated N-doped carbon materials. Importantly, significant changes in efficiency and product distribution were observed when repeating the electrochemical reaction five times in a row. This effect was particularly acute for the Ni-containing colloidal nanoparticle samples on the unsaturated N-doped materials. With the colloidal particle method, the size and particle loading can be controlled, and this preparation method is crucial for the stability of the catalyst and depends on the support. High efficiency can also be seen in the Ni single atoms induced by thermal atomization in N-doped carbon, but it does not occur over pure carbon support.[19] Ni particles and Ni single active sites supported on carbon nitrides[27] featured high selectivity toward CO. These authors demonstrated that the materials can boost the conversion of $CO_2$ into CO.[10] All these works highlight the role of the nature of the support and how its detailed characterization allows fine-tuning the chemical properties of these materials.

To shed light and rationalize such catalytic behavior, we turn to simulations at the atomic level to explore different N-doped carbon materials, both saturated and unsaturated, as reported in previous experiments.[20] Then we compute the activity of Ni catalysts for $eCO_2RR$, both as a nanoparticle and as single atoms embedded in different coordination environments. Furthermore, we report a model nanoparticle to link the possible reconstruction and redispersion under electrochemical conditions when supported on unsaturated N-doped carbon materials.

## 2. COMPUTATIONAL DETAILS

All simulations were performed using spin-polarized density functional theory (DFT) as implemented in the vienna ab initio simulation package (VASP)[28,29] using the GGA PBE-D3 density functional.[30,31] Core electrons were described by projector augmented wave (PAW),[29,32] while valence electrons were expanded by plane wave basis sets with a kinetic energy cutoff of at least 500 eV.

N-doped carbon materials are represented with a graphene layer expanded in a (6 × 6) supercell and replacing carbon atoms by nitrogen atoms to design saturated and unsaturated N-doped carbon models. These layers were interleaved by a 12 Å vacuum along the z direction. A nickel atom was placed in the cavity left on the carbon sheet. Structures were relaxed with

Received: April 29, 2020





https://dx.doi.org/10.1021/acscatal.0c01909
ACS Catal. 2021, 11, 88−94

a force threshold of 0.050 eV/Å. The Brillouin zone was sampled using a (3 × 3 × 1) *k*-point mesh generated with the Monkhorst−Pack method.[33]

Ni nanoparticles were represented using three metal surfaces with the lowest Miller indexes (and thus lowest surface energies) Ni(100), Ni(111), and Ni(211). High-quality surface-energy calculations ((10 × 10 × 1) *k*-point mesh) were performed to build the nanoparticle structure using the Wulff model[34,35] with VESTA.[36] The vacuum between slabs was larger than 10 Å, and the structures were relaxed with a force threshold of 0.025 eV/Å. They contained five layers, where the two uppermost were fully relaxed and the rest were fixed to the bulk structure.

CO can adsorb in very dense phases on Ni,[37,38] and thus, different coverages were considered: from 1/12 to 12/12 ML for Ni(100) and Ni(211) and from 1/16 to 16/16 ML for Ni(111). The Brillouin zone was sampled using a (3 × 4 × 1), (3 × 3 × 1), and (5 × 3 × 1) *k*-point meshes for Ni(100), Ni(111), and Ni(211) respectively. The Wulff construction was also employed on the CO-dense phases to explain the restructuring of the nanoparticles. $Ni(CO)_x$ species can be formed in rich CO environments, which can then redisperse and reconstruct the Ni nanoparticle. The Ni(211) surface edge has enough space to accommodate more than one CO molecule, allowing the formation of $Ni(CO)_4$ complexes. We thus calculated the formation and elimination of $Ni(CO)_4$ with different CO coverages on that surface, where the elimination of this species leaves a vacancy at the edge of the Ni(211) steps. The $Ni(CO)_4$ formation enthalpy computed with PBE starting from CO is more exothermic than that experimentally reported, and the implications for this deviation are evaluated in the text.

For all the systems described before, we obtained the energies of the relevant intermediates in the electrochemical environment under $eCO_2RR$ conditions by considering the computational hydrogen electrode (CHE).[39,40] The intermediates' energies were corrected with calculated zero point and entropic contributions. Notice that for the first step where $CO_2$ adsorbs on the metals, it drags charge from the system, thus the notation then implies that it is activated. Notice that the calculations were done in boxes with zero net charge. Gas-phase molecules used as a reference were calculated with PBE functional. Zero-point, entropic, and heat capacity contributions are shown in Table S1.[41] Solvation effects were added to CO and COOH intermediates following the values employed in ref 41. We have tested and compared the results of our in-house implicit solvent model (VASP-MGCM)[42] to the values in the literature, Table S5−S6. Solvation of N-doped carbon systems are known to depend on the N-concentration, and we have evaluated these effects in our case.[43] However, in our models the N-doping occurs close to a single point in the cavity, and thus, the effect by changing the stoichiometry of the cavity is reduced, for the $NiN_3$ and $NiN_4$ models −0.39 and −0.35 eV, respectively. Further details on thermodynamic corrections are discussed in the Supporting Information. All structures can be retrieved from the database ioChem-BD[44] via the following link,[45] which contains a unique and labeled list of the DFT calculations in this project.

## 3. RESULTS AND DISCUSSION

**3.1. Computational Characterization of the Materials.** To understand the selectivity and activity of N-doped or N-free carbon materials, we modeled them under reaction conditions. The DFT simulations were performed on several N-doped defects where the Ni atoms can be anchored and Ni nanoparticles can be supported, to represent the species characterized in experiments.[20] In Figure 1, we show three families of models: (a) saturated N-doped carbon materials ($NiN_xC$) representing $NiN_4$ and similar undefined N-doped materials made at low doping temperature; (b) unsaturated N-doped ($NiNC_x$) and N-free materials ($NiC_x$) typically occurring for carbons at high doping temperatures, when the nitrogen content decreases; and (c) Ni metal surfaces composing the supported nanoparticles on the unsaturated N-doped supports ($Ni_{NP}$−$NC_x$). This approximation allows us to provide a holistic chain of models that accounts for the complexity of the N-doped carbon support and the metallic nature of the nanoparticle. The ultimate aim is to show the role of the speciation (charge, oxidation state, and coordination environment) on the electrochemical activity and the dynamic behavior or the different synthetic preparations. We simulated EXAFS spectra for all catalysts (Figure S1), where $NiN_xC$ (saturated N-doped materials) agreed well with experimental data.[20] DFT structural parameters are presented in Table S4.

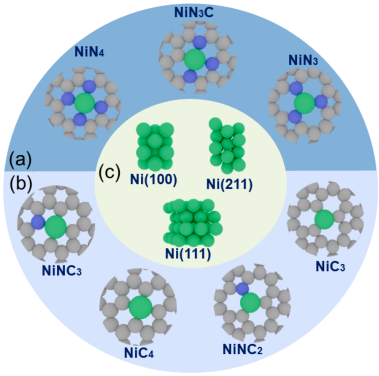


**Figure 1.** Computational models for different systems. (a) Saturated N-doped carbon material. (b) Unsaturated N-doped or N-free carbon material. (c) Metal surfaces. C in gray spheres, N in blue, and Ni in green.

**3.2. Activity and Selectivity of the Materials.** The activity and selectivity of the modeled catalysts can be discussed in terms of the corresponding Gibbs free-energy profiles, presented in Figure 2. The electrochemical activity was analyzed by calculating the binding energies of the intermediates according to the most agreed mechanism for $CO_2$ to CO reduction (Figure 2a−c). The process requires only a two-electron transfer, and the steps are (i) $CO_2 + e^- \rightarrow *CO_2$, (ii) $*CO_2 + H^+ \rightarrow *COOH$ (also, the first two steps in the literature are combined into: $CO_2 + H^+ + e^- \rightarrow *COOH$), (iii) $*COOH + H^+ + e^- \rightarrow *CO + H_2O$ and (iv) $*CO \rightarrow CO_{(g)} + *$. Notice that once $CO_2$ is adsorbed, activated, and polarized with partial charge transfer (see Table S10) from the host material, step (i) does not correspond to any extra electron added to the simulation box.



https://dx.doi.org/10.1021/acscatal.0c01909
ACS Catal. 2021, 11, 88−94

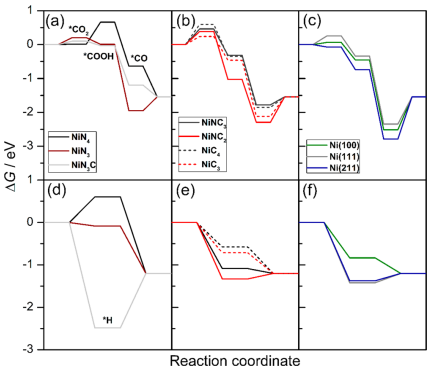


**Figure 2.** Gibbs free-energy profiles for (a, b, and c) $eCO_2RR$ and (d, e, and f) HER over different model sites at $U = -0.6$ V vs RHE (for reference the experimental pH was 7). (a,d) Saturated nitrogen-doped carbon materials. (b,e) Unsaturated or free N-doped carbon materials. (c,f) Metal surfaces.

In agreement with previous results, we can see that the highest activity toward CO is shown by unsaturated N-doped materials[7] and metal surfaces, as they bind CO strongly. Regarding selectivity, it can be discussed by comparison to the competing HER (Figure 2d–f). Saturated N-doped materials reach the highest selectivity toward CO, where $NiN_4$ and $NiN_3$ are representative models, while $NiN_3C$ model binds *H strongly. Therefore, based on the experimental selectivity[20] of single-atom catalysts, the $NiN_3C$ model is not representative. For a catalyst to be selective toward CO, the binding of *COOH and $*CO_2$ intermediates need to be strong to reduce the onset potential. Also, selectivity can be compared with *H binding energy and CO desorption energy. The correlation between the adsorption energies of *COOH and *H is shown in Figure 3a. We can see that $NiN_4$ and $NiN_3$ bind *H weakly, and therefore, saturated N-doped materials are selective. $NiN_4$ binds $*CO_2$ and *COOH weakly, which means it has a higher onset potential, while the opposite trend is seen for $NiN_3$. The computed onset potentials are presented in Table S11, where

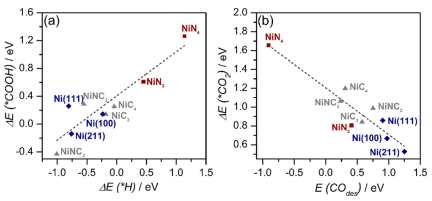


**Figure 3.** Linear scaling relationships. (a) Linear dependence for the COOH binding energy scaling as a function of the adsorption of a H atom. (b) $CO_2$ binding energy and corresponding linear-scaling relationships for desorption of the CO molecule. Saturated N-doped carbon materials are represented with red symbols, unsaturated N-doped carbon materials with gray symbols, and metal surfaces with blue symbols.

$NiN_3$ has a lower onset potential than $NiN_4$ because it binds *COOH stronger. Ni(211) and $NiNC_2$ bind strongly *H and *COOH, which means they will not be selective toward CO. Ni(100) would be the best candidate among the metal surfaces as it binds *H weakly and *COOH relatively strongly. Figure 3b represents a correlation between adsorption energies of $*CO_2$ and desorption of CO, where $CO_2$ activation can relate to Bader charges of the adsorbed $CO_2$ molecule (see Table S10). $NiN_3$, $NiNC_3$, and Ni(100) bind $*CO_2$ relatively strongly, where Ni(100) binds *CO strongly (see Figure S3), which means the rate of CO formation would be low. The strong adsorption energy of *H for Ni(100) and $NiNC_3$ can be related to low selectivity, where HER and $eCO_2RR$ compete. The most interesting system is $NiN_3$ because of the optimal *CO binding and the weakly *H binding. From an electronic structure point of view, the Ni atom in the $NiN_4$ square planar confinement is in the $Ni^{2+}$ oxidation state, while that in the $NiN_3$ trigonal planar configuration is in the $Ni^{+}$ oxidation state (see Figure S4). This special role of $Ni^{+}$ is long known in organometallic chemistry[46] and even in thermal catalysis.[47] The change in the oxidation state has an impact on the geometries of the activated $CO_2$ intermediate as both the O–C–O angle and Ni–C($CO_2$) distance indicate the degree of activation of the $CO_2$ molecule in the N-doped saturated materials. In Figure S5, the linear scaling relationship of $CO_2$ geometry and adsorption of *CO shows that the activation in $NiN_3$ correlates with the medium binding of *CO, while the lowest activation appears in $NiN_4$ with a C–O–O angle of 170.2°. All these fingerprints point out the relevance of understanding the organometallic structures when trying to identify the most suitable defects for a given metal and the importance of the charge state for the encapsulated metal ions.

## 4. RECONSTRUCTION OF NI NPS ON N-DOPED CARBON MATERIALS

Electrocatalysts can be affected by the presence of different variables. In our case, the reconstruction of Ni NPs and the disintegration of $Ni(CO)_2$ complexes change the activity and selectivity. Once the reconstruction happens experimentally, the partial current density of $H_2$ drastically drops compared with that of CO, thus favoring the disintegration process. Such dynamic behavior of electrocatalysts is crucial for their performance, and thus, we here address these aspects by simplified models.

To investigate the role of the reaction products in the stability of the Ni NPs, we model a nanoparticle-based on the lowest-energy surfaces through a Wulff construction. This is straightforward for metal nanoparticles and can be extended when adsorbates, like CO, are present.[37,48] In addition, we apply the atomistic version of Ostwald ripening theory[49,50] by the formation of $Ni(CO)_2$ complexes to show when the disintegration of nanoparticles can occur on such N-doped carbon materials.

**4.1. Nanoparticle Shape.** To address the role of nanoparticles, we first focus on their structure. The size of the synthesized Ni NPs was 2.5 to 7 nm, and thus, they can be represented via the Wulff construction (Figure 4), which corresponds to the equilibrium structure for a medium-to-large nanoparticle and is obtained from the surface energies. We calculated the surface energies for three orientations Ni(111), Ni(100), and Ni(211), and, employing the Wulff construction, we then extracted the corresponding areas for each facet. The average surface energy for the nanoparticle is 0.126 eV/Å. All


https://dx.doi.org/10.1021/acscatal.0c01909
ACS Catal. 2021, 11, 88–94

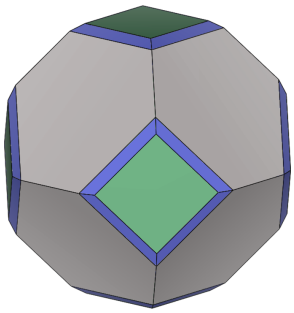

**Figure 4.** Wulff construction based on the surface energies calculated by DFT. Surface legend: Ni(100) in green, Ni(111) in gray, and Ni(211) in blue.

surface energies and ratios of the corresponding facets are presented in Table S17.

To assess the change in the nanoparticle that is induced by the environment, we consider CO adsorption on all three facets separately.[37] We calculated average binding energies $E'_{CO}$, for a range of coverages 1/12 to 12/12 ML for Ni(100) and Ni(211) facets, and Ni(111) from 1/16 to 16/16 ML (Figure S7). In all cases, at low to medium coverages, all the modified surface energies ($\gamma_x'$) are smaller, but the reduction in surface energies depends on the particular facet orientation. The detailed balance between adsorption sites and CO−CO repulsion contributes to the surface energy in a nonlinear way, as to achieve higher CO densities the molecules need to go to rather unstable sites. At 0.25 ML, we are left with Ni(100) and Ni(111) surfaces, while at full coverage of 1 ML the extent of Ni(211) facet in the nanoparticle increases and Ni(111) reconstructs (see Figure S6). In summary, the average surface energy for the decorated nanoparticle ($\gamma'$) at CO coverage 0.25 ML is 0.095 eV/Å$^2$, which is 0.031 eV/Å$^2$ less than for the bare one (Table S16). Therefore, the nanoparticle under product-rich conditions has more surface Ni atoms with less Ni−Ni average coordination. This could be the first step toward disintegration. In addition, this high product coverage influences the selectivity as it limits the HER reaction. The effect can be explained with the Gibbs free energies of the *H intermediate for the clean and on the CO covered ($\theta$ = 0.92 ML) Ni surfaces (see Figure S10). Once Ni surfaces are covered with CO, *H binds more weakly, thus lowering the selectivity for HER (see Figure S11). This agrees with the experimental observations showing a drastic drop of $H_2$ partial current density. Thus, selectivity is triggered by minimizing the HER path.

**4.2. Gibbs Free Energy of Disintegration Ni(CO)$_x$ Complexes on N-Doped Carbon Materials.** We applied the energetic formalism from Ouyang and co-workers[30] to evaluate whether the disintegration of Ni(CO)$_x$ from Ni NPs is possible on N-doped carbon materials. We followed the criteria of reactant induced dynamics, where feasibility can be explained by the Gibbs free energy of disintegration ($\Delta G^{dis}_{NP}$). First, we compute the formation energy of isolated metal adatom ($E^f_{Ni}$) with respect to Ni bulk reference supported on the different carbon defects (Table S18). From these results, we can see that formation energies are exothermic, as Ni atoms are anchored to a defect. Second, we calculate the Gibbs free energy for the CO-decorated nanoparticle, $\Delta G^{dis}_{NP}$, following the equation:

$$\Delta G^{dis}_{NP}(R, T, p) = E^f_{surf\text{-}nCO} - n \times \Delta\mu_{CO}(T, p) - \Delta E'_{NP}(R) - TS \quad (1)$$

where $E^f_{surf\text{-}nCO}$ is the energy of the Ni atom coordinated to the N-doped carbon substrate and $n$ remaining CO molecules, $\Delta E'_{NP}(R)$ is the energy of the CO-covered nanoparticle with radius $R$, and $\Delta\mu_{CO}(T,p)$ is the excess chemical potential of CO $(T,p)$. In our case, the configurational entropy $S$ was not included because the number of cavities is difficult to assess; however, it will favor dispersed species. Therefore, the values obtained here for the transition correspond to a maximum threshold. The excess chemical potential was set to $\Delta\mu_{CO}(T,p)$ = −0.76 eV,[51] corresponding to experimental conditions of 300 K and 0.10 mbar. The binding energy of nCO ($E^f_{1CO}$) needs to be negative and lower than $\Delta\mu_{CO}(T,p)$ = −0.76 eV. When both requirements are fulfilled, nanoparticle disintegration is thermodynamically possible.

The nature of the cavities in the support provides a large versatility regarding the stability against disintegration. In our investigations, we have considered all 7 types of defects in Figure 1. The anchored Ni atom in saturated N-doped models is coordinated either to pyridinic or pyrrolic N atoms, which are strong ligands able to easily trap metal atoms. This is in line with experiments where they do not observe nanoparticles on those materials. We observe an opposite trend for the unsaturated N-doped materials, where Ni NPs can redisperse into single-atom cavities. The reason for that is the decreased N-content and increased C-content in the materials, which makes Ni dynamic and prone to aggregate and disintegrate in the presence of dense CO phases and electrochemical conditions. Therefore, single Ni metal atoms with little aggregation are expected in agreement with experiments.[10] Finally, we show that the redispersion of Ni NPs on the $NC_2$ defect (unsaturated N-doped model) is thermodynamically possible. $NiNC_2$ is also one of the most active and nonselective $eCO_2RR$ configurations, with strong bindings for *CO, *COOH, and *H intermediates. Once Ni NPs are supported on $NC_2$, they can disintegrate, as the experimentally partial current density drops drastically compared with CO partial current densities. That is how the combination of the two results (activity and stability against dispersion) can support the fact that enhanced Faradaic efficiency was observed when the reaction was performed five times in a row for nanoparticles supported on unsaturated N-doped carbon materials.[20] Redispersion is thus possible on unsaturated materials; however, depending on the nature of the carrier that would imply a different performance. As the performance of the single atoms depends on the properties of the cavity, redispersion would only be more favorable provided that the right cavity exists, and it is occupied. The electrochemical cycling from the nanoparticles does enhance the selectivity in unsaturated hosts but not up to the levels found for the saturated materials.

To investigate the size ($R$) dependence of the disintegration induced by CO, we have used $Ni_{NP}$-$NC_2$ as cavity and have calculated the $\Delta G^{dis}_{NP}(R, T, p)$ considering the formation of $Ni(CO)_2$ sitting at these pockets at experimental temperature and pressure. Figure 5 presents the $\Delta G^{dis}_{NP}$ corresponding to



https://dx.doi.org/10.1021/acscatal.0c01909
ACS Catal. 2021, 11, 88−94

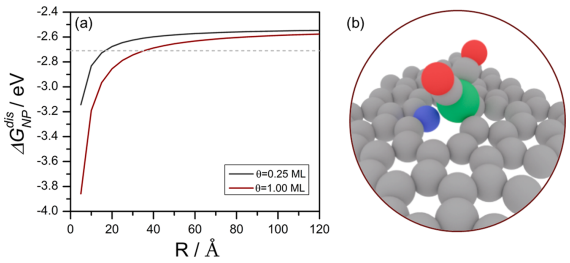


**Figure 5.** (a) Size dependence of the Gibbs free energy ($\Delta G^{dis}_{NP}$) of $Ni(CO)_2$, when $Ni_{NP}$ is supported on $NC_2$ at 300 K and 0.1 mbar. The horizontal dashed line indicates the limit for stability. (b) Schematic representation of $Ni(CO)_2$ bound to the $NC_2$ cavity.

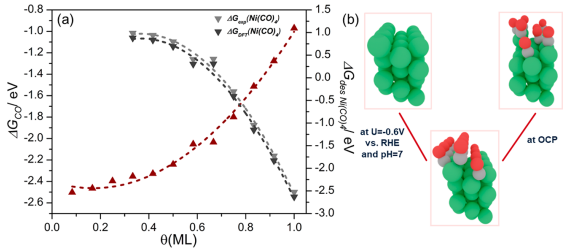


**Figure 6.** Process of Ni(211) metal surface reconstruction. (a) CO coverage dependence of the average Gibbs free energy (red curve) of CO adsorption at U = −0.6 V vs RHE (pH = 7) and (gray curves) desorption of $Ni(CO)_4$. (b) Schematic process of clean Ni(211) metal surface fully adsorbing CO at electrochemical conditions. When the reaction is stopped at the open circuit potential (OCP) to assess the material recyclability, $Ni(CO)_4$-like complexes can desorb.

$Ni(CO)_2$ versus the radius $R$ of a Ni nanoparticle at two different coverages, 0.25 and 1 ML (nonwetting conditions for the nanoparticle were considered, thus the Young angle was set to 180°). We found that $\Delta G^{dis}_{NP}$ decreases at smaller $R$ and crosses the reference level (−2.7 eV, energy of an isolated Ni atom in the cavity) at about 40 Å for 1 ML and 20 Å for 0.25 ML. The lower value found for lower coverage is a direct consequence of the simplicity of the model and shall be taken with caution as kinetic constraints related to the need of concentrating CO molecules to extract the surface atoms could play an important role. At high coverage, our results imply that Ni NPs smaller than 4 nm will disintegrate into $Ni(CO)_2$ when supported on the $NC_2$ at 300 K and 0.1 mbar.

**4.3. Mechanism for Ni Nanoparticle Reconstruction.** The dense layers that we have identified in Section 4.1 show that after $eCO_2RR$, CO extensively covers the surface and over long times has the potential to increase the fraction of Ni atoms in low-coordinated sites as stepped Ni(211) surfaces. Moreover, the thermodynamic models in Section 4.2 indicate that below a certain size, $Ni(CO)_x$ clusters can be stable in some particular motifs of the N-doped carbons. To merge these two scenarios, a viable route for decomposition needs to be described. Ni can form volatile species with CO in the form of $Ni(CO)_4$ that can be soluble under the reaction conditions. We have calculated the energy needed for the formation of these species.

On nanoparticles, $CO_2$ is reduced to CO at −0.6 V vs RHE and pH 7, and the resulting CO drives the reconstruction toward Ni(211). Once the reaction is stopped at open circuit potential (OCP), $Ni(CO)_4$ species can be formed as the CO coverage is very high. Thermodynamically, the formation energy of a metal vacancy (with respect to Ni bulk) in Ni(100), Ni(111), and Ni(211) surfaces are 0.59, 1.04, and 0.33 eV, respectively. Strong kinetic limitations can likely appear due to geometric constraints on Ni(111) and Ni(100), but for the fully CO adsorbed Ni(211) surface, the step edges can present very high CO concentration. Thus, $Ni(CO)_4$ can be formed in this face with concomitant elimination of Ni atoms. Figure 6a presents the average adsorption energy for CO at different coverages (red curve) on the Ni(211) facet and it is compared to the formation-elimination of the $Ni(CO)_4$ complex (gray curves). The crossing between these two lines can be interpreted as the coverage at which the elimination of Ni atoms in the form of the species becomes viable. Therefore, high CO coverages would affect the stability of the edge sites starting around 0.78 ML coverage (when using DFT or experimental value for $Ni(CO)_4$), promoting the formation of the species that can then redisperse on the cavities of the N-doped carbon. The process of reconstruction is sketched in Figure 6b. All the data is presented in Tables S21−23. Once the reaction is under electrochemical potential again, these complexes react with nonoccupied defects on the unsaturated N-doped carbon ($Ni_{NP}$-$NC_2$) and effectively redisperse. This process could potentially lead to higher activity, as shown in the experiments.[20]



https://dx.doi.org/10.1021/acscatal.0c01909
ACS Catal. 2021, 11, 88−94

## 5. CONCLUSIONS

Electrocatalysts based on Ni supported on N-doped carbon materials have been computationally analyzed for the reduction of $CO_2$ considering both nanoparticles and single atoms. The optimal activity and selectivity are found for the $NiN_3$ model, in which Ni is in $Ni^{1+}$ oxidation state. $NiN_3$ exhibits theoretically low onset potential in agreement with experiments and a high rate toward CO. However, rather, saturated N-doped materials are more selective toward CO formation. As single atoms can be prepared from nanoparticles, we show through the Ostwald formalism that disintegration of $Ni(CO)_x$ can happen if Ni nanoparticles are supported on N-doped unsaturated support such as $NC_2$. We present a mechanism of Ni(211) surface reconstruction that is possible only at high CO coverages around 8/12 ML by the formation of $Ni(CO)_4$ species, which then redisperse into active single atoms. The complete understanding of the Ni−N−C materials points toward a very dynamic behavior where considering the full complexity of the material in terms of Ni nuclearity and environment is needed. This is likely a common feature for such type of electrocatalysts.

## ■ ASSOCIATED CONTENT

### Supporting Information

The Supporting Information is available free of charge at https://pubs.acs.org/doi/10.1021/acscatal.0c01909.

Additional notes on the energy corrections and the modeling for the Ni nanoparticles for this article (PDF)

## ■ AUTHOR INFORMATION

### Corresponding Author

**Núria López** − *Institute of Chemical Research of Catalonia, ICIQ, The Barcelona Institute of Science and Technology, 43007 Tarragona, Spain*; orcid.org/0000-0001-9150-5941; Email: nlopez@iciq.es

### Author

**Paulina Prslja** − *Institute of Chemical Research of Catalonia, ICIQ, The Barcelona Institute of Science and Technology, 43007 Tarragona, Spain*

Complete contact information is available at: https://pubs.acs.org/10.1021/acscatal.0c01909

### Funding

ELCOREL, European Union's H2020 Programme under Grant Agreement No.722614.

### Notes

The authors declare no competing financial interest.

## ■ ACKNOWLEDGMENTS

The research leading to these results has received funding from the predoctoral grant ELCOREL, which is funded by the European Union's H2020 Programme under Grant Agreement No.722614. We would like to thank Dr. M. A. Ortuño and Dr. A. J. Martin for critically discussing the results. We thank the BSC-RES for providing generous computational resources.

## ■ REFERENCES

(1) Kornienko, N.; Zhao, Y.; Kley, C. S.; Zhu, C.; Kim, D.; Lin, S.; Chang, C. J.; Yaghi, O. M.; Yang, P. Metal-Organic Frameworks for Electrocatalytic Reduction of Carbon Dioxide. *J. Am. Chem. Soc.* **2015**, *137*, 14129−14135.

(2) Ju, W.; Bagger, A.; Hao, G. P.; Varela, A. S.; Sinev, I.; Bon, V.; Roldan Cuenya, B.; Kaskel, S.; Rossmeisl, J.; Strasser, P. Understanding Activity and Selectivity of Metal-Nitrogen-Doped Carbon Catalysts for Electrochemical Reduction of $CO_2$. *Nat. Commun.* **2017**, *8*, 944.

(3) Tripkovic, V.; Vanin, M.; Karamad, M.; Björketun, M. E.; Jacobsen, K. W.; Thygesen, K. S.; Rossmeisl, J. Electrochemical $CO_2$ and CO Reduction on Metal-Functionalized Porphyrin-like Graphene. *J. Phys. Chem. C* **2013**, *117*, 9187−9195.

(4) Li, J.; Pršlja, P.; Shinagawa, T.; Martín Fernández, A. J.; Krumeich, F.; Artyushkova, K.; Atanassov, P.; Zitolo, A.; Zhou, Y.; García-Muelas, R.; López, N.; Pérez-Ramírez, J.; Jaouen, F. Volcano Trend in Electrocatalytic $CO_2$ Reduction Activity over Atomically Dispersed Metal Sites on Nitrogen-Doped Carbon. *ACS Catal.* **2019**, *9*, 10426−10439.

(5) Varela, A. S.; Ranjbar Sahraie, N.; Steinberg, J.; Ju, W.; Oh, H. S.; Strasser, P. Metal-Doped Nitrogenated Carbon as an Efficient Catalyst for Direct $CO_2$ Electroreduction to CO and Hydrocarbons. *Angew. Chem., Int. Ed.* **2015**, *54*, 10758−10762.

(6) Varela, A. S.; Ju, W.; Bagger, A.; Franco, P.; Rossmeisl, J.; Strasser, P. Electrochemical Reduction of $CO_2$ on Metal-Nitrogen-Doped Carbon Catalysts. *ACS Catal.* **2019**, *9*, 7270−7284.

(7) Möller, T.; Ju, W.; Bagger, A.; Wang, X.; Luo, F.; Ngo Thanh, T.; Varela, A. S.; Rossmeisl, J.; Strasser, P. Efficient $CO_2$ to CO Electrolysis on Solid Ni-N-C Catalysts at Industrial Current Densities. *Energy Environ. Sci.* **2019**, *12*, 640−647.

(8) Zheng, T.; Jiang, K.; Ta, N.; Hu, Y.; Zeng, J.; Liu, J.; Wang, H. Large-Scale and Highly Selective $CO_2$ Electrocatalytic Reduction on Nickel Single-Atom Catalyst. *Joule* **2019**, *3*, 265−278.

(9) Jiang, K.; Siahrostami, S.; Zheng, T.; Hu, Y.; Hwang, S.; Stavitski, E.; Peng, Y.; Dynes, J.; Gangisetty, M.; Su, D.; Attenkofer, K.; Wang, H. Isolated Ni Single Atoms in Graphene Nanosheets for High-Performance $CO_2$ Reduction. *Energy Environ. Sci.* **2018**, *11*, 893−903.

(10) Wen, C. F.; Mao, F.; Liu, Y.; Zhang, X. Y.; Fu, H. Q.; Zheng, L. R.; Liu, P. F.; Yang, H. G. Nitrogen-Stabilized Low-Valent Ni Motifs for Efficient $CO_2$ Electrocatalysis. *ACS Catal.* **2020**, *10*, 1086−1093.

(11) Koshy, D. M.; Chen, S.; Lee, D. U.; Stevens, M. B.; Abdellah, A. M.; Dull, S. M.; Chen, G.; Nordlund, D.; Gallo, A.; Hahn, C.; Higgins, D. C.; Bao, Z.; Jaramillo, T. F. Understanding the Origin of Highly Selective $CO_2$ Electroreduction to CO on Ni,N-Doped Carbon Catalysts. *Angew. Chem.* **2020**, *132*, 4072.

(12) Yang, H.; Lin, Q.; Zhang, C.; Yu, X.; Cheng, Z.; Li, G.; Hu, Q.; Ren, X.; Zhang, Q.; Liu, J.; He, C. Carbon Dioxide Electroreduction on Single-Atom Nickel Decorated Carbon Membranes with Industry Compatible Current Densities. *Nat. Commun.* **2020**, *11*, 593.

(13) Yan, C.; Li, H.; Ye, Y.; Wu, H.; Cai, F.; Si, R.; Xiao, J.; Miao, S.; Xie, S.; Yang, F.; Li, Y.; Wang, G.; Bao, X. Coordinatively Unsaturated Nickel−Nitrogen Sites towards Selective and High-Rate CO2 Electroreduction. *Energy Environ. Sci.* **2018**, *11*, 1204−1210.

(14) Li, X.; Bi, W.; Chen, M.; Sun, Y.; Ju, H.; Yan, W.; Zhu, J.; Wu, X.; Chu, W.; Wu, C.; Xie, Y. Exclusive Ni-N4 Sites Realize Near-Unity CO Selectivity for Electrochemical CO2 Reduction. *J. Am. Chem. Soc.* **2017**, *139*, 14889−14892.

(15) Su, P.; Iwase, K.; Nakanishi, S.; Hashimoto, K.; Kamiya, K. Nickel-Nitrogen-Modified Graphene: An Efficient Electrocatalyst for the Reduction of Carbon Dioxide to Carbon Monoxide. *Small* **2016**, *12*, 6083−6089.

(16) Yang, H. B.; Hung, S. F.; Liu, S.; Yuan, K.; Miao, S.; Zhang, L.; Huang, X.; Wang, H. Y.; Cai, W.; Chen, R.; Gao, J.; Yang, X.; Chen, W.; Huang, Y.; Chen, H. M.; Li, C. M.; Zhang, T.; Liu, B. Atomically Dispersed Ni(I) as the Active Site for Electrochemical $CO_2$ Reduction. *Nat. Energy* **2018**, *3*, 140−147.

(17) Ma, S.; Su, P.; Huang, W.; Jiang, S. P.; Bai, S.; Liu, J. Atomic Ni Species Anchored N-Doped Carbon Hollow Spheres as Nanoreactors for Efficient Electrochemical $CO_2$ Reduction. *ChemCatChem* **2019**, *11*, 6092−6098.

(18) Zhao, C.; Dai, X.; Yao, T.; Chen, W.; Wang, X.; Wang, J.; Yang, J.; Wei, S.; Wu, Y.; Li, Y. Ionic Exchange of Metal-Organic

Frameworks to Access Single Nickel Sites for Efficient Electroreduction of $CO_2$. *J. Am. Chem. Soc.* **2017**, *139*, 8078−8081.
(19) Yang, J.; Qiu, Z.; Zhao, C.; Wei, W.; Chen, W.; Li, Z.; Qu, Y.; Dong, J.; Luo, J.; Li, Z.; Wu, Y. In Situ Thermal Atomization To Convert Supported Nickel Nanoparticles into Surface-Bound Nickel Single-Atom Catalysts. *Angew. Chem., Int. Ed.* **2018**, *57*, 14095−14100.
(20) Büchele, S.; Martín, A. J.; Mitchell, S.; Krumeich, F.; Collins, S. M.; Xi, S.; Borgna, A.; Pérez-Ramírez, J. Structure Sensitivity and Evolution of Nickel-Bearing Nitrogen-Doped Carbons in the Electrochemical Reduction of $CO_2$. *ACS Catal.* **2020**, *10*, 3444−3454.
(21) Chen, Y.; Ji, S.; Chen, C.; Peng, Q.; Wang, D.; Li, Y. Single-Atom Catalysts: Synthetic Strategies and Electrochemical Applications. *Joule* **2018**, *2*, 1242−1264.
(22) Yan, C.; Li, H.; Ye, Y.; Wu, H.; Cai, F.; Si, R.; Xiao, J.; Miao, S.; Xie, S.; Yang, F.; Li, Y.; Wang, G.; Bao, X. Coordinatively Unsaturated Nickel-Nitrogen Sites towards Selective and High-Rate $CO_2$ Electroreduction. *Energy Environ. Sci.* **2018**, *11*, 1204−1210.
(23) Wang, L.; Sofer, Z.; Pumera, M. Will Any Crap We Put into Graphene Increase Its Electrocatalytic Effect? *ACS Nano* **2020**, *14*, 21.
(24) Liu, S.; Yang, H. B.; Hung, S. F.; Ding, J.; Cai, W.; Liu, L.; Gao, J.; Li, X.; Ren, X.; Kuang, Z.; Huang, Y.; Zhang, T.; Liu, B. Elucidating the Electrocatalytic CO2 Reduction Reaction over a Model Single-Atom Nickel Catalyst. *Angew. Chem., Int. Ed.* **2020**, *59*, 798−803.
(25) Shen, J.; Kolb, M. J.; Göttle, A. J.; Koper, M. T. M. DFT Study on the Mechanism of the Electrochemical Reduction of $CO_2$ Catalyzed by Cobalt Porphyrins. *J. Phys. Chem. C* **2016**, *120*, 15714−15721.
(26) Shen, J.; Kortlever, R.; Kas, R.; Birdja, Y. Y.; Diaz-Morales, O.; Kwon, Y.; Ledezma-Yanez, I.; Schouten, K. J. P.; Mul, G.; Koper, M. T. M. Electrocatalytic Reduction of Carbon Dioxide to Carbon Monoxide and Methane at an Immobilized Cobalt Protoporphyrin. *Nat. Commun.* **2015**, *6*, 8177.
(27) Chen, Z.; Mitchell, S.; Vorobyeva, E.; Leary, R. K.; Hauert, R.; Furnival, T.; Ramasse, Q. M.; Thomas, J. M.; Midgley, P. A.; Dontsova, D.; Antonietti, M.; Pogodin, S.; López, N.; Pérez-Ramírez, J. Stabilization of Single Metal Atoms on Graphitic Carbon Nitride. *Adv. Funct. Mater.* **2017**, *27*, 1605785.
(28) Kresse, G.; Furthmüller, J. Efficiency of Ab-Initio Total Energy Calculations for Metals and Semiconductors Using a Plane-Wave Basis Set. *Comput. Mater. Sci.* **1996**, *6*, 15−50.
(29) Kresse, G.; Joubert, D. From Ultrasoft Pseudopotentials to the Projector Augmented-Wave Method. *Phys. Rev. B: Condens. Matter Mater. Phys.* **1999**, *59*, 1758−1775.
(30) Perdew, J. P.; Burke, K.; Ernzerhof, M. Generalized Gradient Approximation Made Simple. *Phys. Rev. Lett.* **1996**, *77*, 3865−3868.
(31) Grimme, S.; Antony, J.; Ehrlich, S.; Krieg, H. A Consistent and Accurate Ab Initio Parametrization of Density Functional Dispersion Correction (DFT-D) for the 94 Elements H-Pu. *J. Chem. Phys.* **2010**, *132*, 154104.
(32) Blöchl, P. E. Projector Augmented-Wave Method. *Phys. Rev. B: Condens. Matter Mater. Phys.* **1994**, *50*, 17953−17979.
(33) Pack, J. D.; Monkhorst, H. J. special Points for Brillouin-Zone Integrations"-a Reply. *Phys. Rev. B* **1977**, *16*, 1748−1749.
(34) Barmparis, G. D.; Lodziana, Z.; Lopez, N.; Remediakis, I. N. Nanoparticle Shapes by Using Wulff Constructions and First-Principles Calculations. *Beilstein J. Nanotechnol.* **2015**, *6*, 361−368.
(35) Wulff, G. XXV. Zur Frage Der Geschwindigkeit Des Wachsthums Und Der Auflösung Der Krystallflächen. *Z. Kristallogr. - Cryst. Mater.* **1901**, *34*, 449−530.
(36) Momma, K.; Izumi, F. VESTA 3 for Three-Dimensional Visualization of Crystal, Volumetric and Morphology Data. *J. Appl. Crystallogr.* **2011**, *44*, 1272−1276.
(37) Barmparis, G. D.; Remediakis, I. N. Dependence on CO Adsorption of the Shapes of Multifaceted Gold Nanoparticles: A Density Functional Theory. *Phys. Rev. B: Condens. Matter Mater. Phys.* **2012**, *86*, 1−7.
(38) Loffreda, D.; Simon, D.; Sautet, P. Dependence of Stretching Frequency on Surface Coverage and Adsorbate-Adsorbate Interactions: A Density-Functional Theory Approach of CO on Pd(111). *Surf. Sci.* **1999**, *425*, 68−80.
(39) Peterson, A. A.; Abild-Pedersen, F.; Studt, F.; Rossmeisl, J.; Nørskov, J. K. How Copper Catalyzes the Electroreduction of Carbon Dioxide into Hydrocarbon Fuels. *Energy Environ. Sci.* **2010**, *3*, 1311−1315.
(40) Nørskov, J. K.; Rossmeisl, J.; Logadottir, A.; Lindqvist, L.; Kitchin, J. R.; Bligaard, T.; Jónsson, H. Origin of the Overpotential for Oxygen Reduction at a Fuel-Cell Cathode. *J. Phys. Chem. B* **2004**, *108*, 17886−17892.
(41) Chan, K.; Tsai, C.; Hansen, H. A.; Nørskov, J. K. Molybdenum Sulfides and Selenides as Possible Electrocatalysts for $CO_2$ Reduction. *ChemCatChem* **2014**, *6*, 1899−1905.
(42) Garcia-Ratés, M.; López, N. Multigrid-Based Methodology for Implicit Solvation Models in Periodic DFT. *J. Chem. Theory Comput.* **2016**, *12*, 1331−1341.
(43) Reda, M.; Hansen, H. A.; Vegge, T. DFT Study of Stabilization Effects on N-Doped Graphene for ORR Catalysis. *Catal. Today* **2018**, *312*, 118−125.
(44) Álvarez-Moreno, M.; De Graaf, C.; López, N.; Maseras, F.; Poblet, J. M.; Bo, C. Managing the Computational Chemistry Big Data Problem: The ioChem-BD Platform. *J. Chem. Inf. Model.* **2015**, *55*, 95−103.
(45) Prslja, P. NiNx-NiCx-Ni_nanoparticle-CO2r Collection home page. DOI: 10.19061/iochem-bd-1-168.
(46) Beley, M.; Collin, J.-P.; Ruppert, R.; Sauvage, J.-P. Electrocatalytic Reduction of $CO_2$ by Ni Cyclam2+ in Water: Study of the Factors Affecting the Efficiency and the Selectivity of the Process. *J. Am. Chem. Soc.* **1986**, *108*, 7461−7467.
(47) Millet, M.-M.; Algara-Siller, G.; Wrabetz, S.; Mazheika, A.; Girgsdies, F.; Teschner, D.; Seitz, F.; Tarasov, A.; Levchenko, S. V.; Schlögl, R.; Frei, E. Ni Single Atom Catalysts for CO2 Activation. *J. Am. Chem. Soc.* **2019**, *141*, 2451−2461.
(48) Li, Q.; Rellán-Piñeiro, M.; Almora-Barrios, N.; Garcia-Ratés, M.; Remediakis, I. N.; López, N. Shape Control in Concave Metal Nanoparticles by Etching. *Nanoscale* **2017**, *9*, 13089−13094.
(49) Voorhees, P. W. The Theory of Ostwald Ripening. *J. Stat. Phys.* **1985**, *38*, 231−252.
(50) Ouyang, R.; Liu, J. X.; Li, W. X. Atomistic Theory of Ostwald Ripening and Disintegration of Supported Metal Particles under Reaction Conditions. *J. Am. Chem. Soc.* **2013**, *135*, 1760−1771.
(51) Berkó, A.; Solymosi, F. Adsorption-Induced Structural Changes of Rh Supported by $TiO_2$(110)-(1 × 2): An STM Study. *J. Catal.* **1999**, *183*, 91−101.


https://dx.doi.org/10.1021/acscatal.0c01909
*ACS Catal.* 2021, 11, 88−94